Dublin City University
Ollscoil Chathair Bhaile Átha Cliath

NMR Studies of Membrane-Bound Nanoparticles and Nanoparticle Assemblies

Carla Meledandri, B.Sc.

Thesis submitted for the Degree of
Doctor of Philosophy

Supervisor: Dr. Dermot Brougham

School of Chemical Sciences December 2008

I hereby certify that this material, which I now submit for assessment on the programme of study leading to the award of doctor of philosophy is entirely my own work, that I have exercised reasonable care to ensure that the work is original, and does not to the best of my knowledge breach any law of copyright, and has not been taken from the work of others save and to the extent that such work has been cited and acknowledged within the text of my work.

Signed: _____ (Candidate) ID No.:_____

Date: _____

This thesis is dedicated to my parents with love.

Acknowledgements

I would like to gratefully acknowledge the guidance, advice, and encouragement of my supervisor, Dr. Dermot Brougham. His knowledge and experience have been invaluable to me throughout my research. I appreciate the opportunity to work in his group, and his efforts to ensure my funding for the duration of my research.

I would like to sincerely thank Dr. Jacek Stolarczyk for the many helpful technical discussions, advice, suggestions, and his endless patience. Additionally, special thanks are due to all my past and present lab colleagues and friends, Dr. Michael Gottschalk, Dr. Darren Carty, Dr. Galya Ivanova, Dr. Swapankumar Ghosh, Dr. Eoin Murray, Ms. Sarah Kebbell, and Ms. Sarah Clarke.

My work has greatly benefited from the contributions of our collaborators, and I would like to thank Prof. Yurii Gun'ko and his group in Trinity College Dublin, Ireland, and Prof. Esteban Anoardo and his group in the National University of Córdoba, Argentina. Furthermore, this work would not have been possible without the assistance of the DCU technical staff, and I truly appreciate their ongoing efforts to quickly accommodate all of my research needs and requests. Many thanks.

In addition to professional support, I cannot overemphasise the value of the support and encouragement I have received from the many friends I have made in Ireland over the last four years. While there are too many people to list here, at the very least I must offer my most heartfelt thanks to Sue, Hazel, Michaela, Eimear, Emma, and Sarah, who dragged me out of the lab when I needed it the most, listened to me complain, helped me keep things in perspective, but most importantly, provided me with endless laughs and entertainment, and the breaks I needed in order to stay focused. I would also like to thank the members and instructors of the DCU karate club and the Diamond Dogs softball team for helping me to relieve stress and maintain my fitness levels…and at least some level of sanity.

Last, but certainly not least, I am forever indebted to my family for their endless support, love, encouragement, understanding, and patience, and without whom this work truly would not have been possible. This thesis is dedicated to my parents who always encouraged us to pursue our interests, promoted education and independent thinking, and continually strive to improve the happiness and lives of their children and grandchildren. They have taught me by their daily example the value of making sacrifices in order to achieve a greater goal.

List of abbreviations

Abbreviation	Description	Units
AAS	Atomic absorption spectroscopy	
AMLs	Aqueous magnetoliposomes	
ATR-IR	Attenuated total reflectance - infrared	
ATRP	Atom transfer radical polymerisation	
BMPA	2-bromo-2-methylpropionic acid	
BMPB	2-bromo-2-methylpropionyl bromide	
C18	Total C18 surfactant comprising eqimolar amounts of oleic acid and oleylamine	
CA	Contrast agent	
CA/BMPA	Citric acid/2-bromo-2-methylpropionic acid	
CN-silica	Cyanopropyl-modified 30 – 70 μm silica particles	
CPMG	Carl-Purcell-Meiboom-Gill	
D	Diffusion	
DDT	Dodecanethiol	
DLS	Dynamic light scattering	
DMM	Defined motions model	
DMPC	1,2-Dimyristoyl-sn-glycero-3-phosphocholine	
D_{NMR}	NMR diameter	[nm]
DOPG	1,2-Dioleoyl-*sn*-glycero-3-[phospho-rac-(1-glycerol)] (sodium salt)	
DOPC	1,2-Dioleoyl-sn-glycero-3-phosphocholine	
D_{PCS}	Hydrodynamic diameter obtained from PCS measurements	[nm]
DPPC	1,2-Dipalmitoyl-sn-glycero-3-phosphocholine	
DSC	Differential scanning calorimetry	
D_{TEM}	TEM diameter	[nm]
ΔE_{anis}	Anisotropy energy	[GHz]

Ea	Activation energy	[KJ·mol^{-1}]
FFC-NMR	Fast field-cycling nuclear magnetic resonance	
FM	Fast motions	
FT-IR	Fourier transform infrared	
κ	Bending elastic modulus	[kg·m^2·s^{-2}]
k_B	Boltzmann constant	[kg·m^2·s^{-2}·K^{-1}]
LD	Lateral diffusion	
LMVs	Large multilamellar vesicles	
LUVs	Large unilamellar vesicles	
MFA	Model-free approach	
MR	Molecular rotations	
MRI	Magnetic resonance imaging	
M_s	Saturation magnetisation	
NMR	Nuclear magnetic resonance	
NMRD	Nuclear magnetic resonance dispersion	
NP	Nanoparticle	
NPC	Nanoparticle cluster	
OA	Oleic acid	
OAm	Oleylamine	
OF	Order fluctuations	
PC	Phosphatidylcholine	
PCS	Photon correlation spectroscopy	
PDI	Polydispersity index	
PEG	Poly(ethylene glycol)	
PEO	Polyethylene oxide	
PF127	Pluronic F127	
PPO	Polypropylene oxide	
PSSNa	Sodium polystyrene sulfonate	

R_1	Longitudinal (spin-lattice) relaxation rate ($1/T_1$)	[s^{-1}]
r_1	Relaxivity	[$mM^{-1} \cdot s^{-1}$]
RES	Reticuloendothelial system	
rf	radiofrequency	
RLCA	Reaction limited cluster aggregation	
ROP	Ring-opening polymerization	
σ	Standard deviation	
SEM	Scanning electron microscopy	
SML	Solid magnetoliposome	
SPIO	Superparamagnetic iron-oxide	
SPION	Superparamagnetic iron-oxide nanoparticle	
SUVs	Small unilamellar vesicles	
T_1	Longitudinal (spin-lattice) relaxation time	[s]
T_2	Transverse (spin-spin) relaxation time	[s]
T_C	Curie temperature	[K]
TE	Echo time	[ms]
TEM	Transmission electron microscopy	
Tm	Main phase transition temperature of phospholipid bilayers	[°C]
T_N	Néel temperature	[K]
TOAB	Tetraoctylammonium bromide	
TR	Repetition time	[ms]
τ_N	Néel correlation time	[ns]
USPIO	Ultra-small particles of iron-oxide	
UVs	Unilamellar vesicles	
UV-Vis	Ultraviolet-visible	
Z-Avg	Z-Average diameter	[nm]

Table of Contents

Abstract

NMR Studies of Membrane-Bound Nanoparticles and Nanoparticle Assemblies

Membrane-bound magnetic nanoparticles and nanoparticle assemblies are attracting increasing attention for biomedical applications as MRI contrast agents, hyperthermia mediators, and drug delivery vehicles. These applications require the particles to have the combined properties of high saturation magnetisation, colloidal stability, and effective biodistribution, all of which are highly dependent on particle size. Several approaches have been adopted in this work to control the particle size and the emergent size-dependent magnetic properties of a range of nanocomposite materials. These include control of the synthetic conditions, size separation using magnetic filtration, and controlled nanocluster growth. The first part of this thesis presents the preparation of stable aqueous and non-aqueous suspensions of membrane-bound nanoparticle systems of controlled size; the surfaces of the nanoparticles were functionalised with fatty acids, phospholipids, or polymers. Photon Correlation Spectroscopy and Transmission Electron Microscopy were used to measure particle size, and the magnetic properties of the dispersions were investigated using Nuclear Magnetic Resonance Dispersion.

The second part of this thesis presents an NMR and light-scattering study into molecular and collective motions in liposomes. Liposomes are a widely accepted model for complex biological membranes; thus this work may provide insight into the role of dynamics in determining the properties of cell membranes and of liposomal delivery vehicles. Different approaches were used to fit the relaxation data corresponding to different models for the spectral density of lipid motions. The physically significant parameters extracted from the data were interpreted in terms of known modes of motion in membranes. The effect of vesicle size, temperature and the addition of cholesterol on the overall relaxation rate were studied.

CHAPTER 1

Introduction

1.1 Thesis overview

Chapter 1 provides an introduction to magnetic resonance techniques including the physical background and principles of proton relaxation, fast field-cycling nuclear magnetic resonance spectroscopy (FFC NMR), and magnetic resonance imaging (MRI). The classification of magnetic materials and their related magnetic properties is discussed with specific emphasis placed on superparamagnetic iron-oxide nanoparticles. Applications of magnetic nanoparticles are reviewed, and their clinical applications are highlighted. A theory for proton relaxation induced by dispersed superparamagnetic particles is introduced, and iron-oxide nanoparticle preparation and stabilisation methods are surveyed.

Chapter 2 describes the main experimental techniques used throughout this thesis including FFC NMR, photon correlation spectroscopy (PCS), attenuated total reflectance infrared spectroscopy (ATR-IR), atomic absorption spectroscopy (AAS), and transmission electron microscopy (TEM). The relevant theory, experimental conditions, and practical considerations for each technique are discussed.

Chapter 3 presents the synthesis of monodisperse maghemite (γ-Fe_2O_3) nanoparticle suspensions in heptane. By modifying the synthetic conditions, precise control is exerted over both the nanocrystal core size and the magnetic properties of the resulting nanoparticle dispersions. Field-cycling ^{1}H NMR relaxation analysis allows estimation of the saturation magnetisation and magnetic anisotropy energy of the suspended particles. The anisotropy energy is found to increase significantly for the smaller particles, a finding which is interpreted as arising from an increase in shape anisotropy.

Chapter 4 presents strategies toward the development of water soluble nanocluster systems with controlled size and optimal magnetic properties. Iron-oxide nanoparticle clusters of controlled size are grown from primary nanoparticles synthesised by the thermal decomposition method. The kinetics of

cluster growth is discussed, as well as the effect of primary particle size and iron concentration on the rate of growth. A mechanism for cluster growth is presented which will progress this process towards general application. The second part of Chapter 4 describes the generalisation of the method for the controlled growth of nanoparticle clusters to include the preparation of mixed-metal FeO:Au clusters. This has opened a new pathway to size-controlled nanocomposite materials.

Chapter 5 reports the synthesis of magnetic iron-oxide nanoparticles and their subsequent stabilisation inside phospholipid vesicles by two different methods. The resulting magnetoliposome structures, termed solid magnetoliposomes (SMLs) and aqueous magnetoliposomes (AMLs), are compared and evaluated in terms of their physical properties and particle morphology. Aqueous suspensions of both types of magnetoliposomes are characterised by dynamic light scattering and infrared spectroscopy, and their magnetic resonance properties are assessed using NMRD. Significant differences are noted in the physical characteristics of the particles, suggesting differences in particle morphology. Specifically, we present evidence indicating that SMLs contain a solid iron-oxide core coated with a phospholipid bilayer, in which the inner phospholipid layer is chemisorbed directly onto the particle, while AMLs are liposomal structures in which solid iron-oxide particles are contained within the internal aqueous compartment of the liposome. We also demonstrate that AMLs appear to lose their aqueous lumen on ageing and dilution, and hence behave more like SMLs. A comparison study of the relaxivity behaviour of magnetoliposome suspensions as a function of particle size was undertaken. SMLs demonstrated a decrease in r_1 with an increase in D_{PCS}, which has been interpreted as a result of extended residence times of bulk water in the proximity of larger magnetoliposomes. The results underline the importance of good particle size control. Magnetic filtration is introduced as a means of selective particle size control; we demonstrate the utility of magnetic filtration to fractionate magnetoliposome suspensions into samples with average diameters ranging from 50 to 250 nm with a narrow size distribution. The benefits of magnetic filtration over other size-selection techniques are discussed.

Chapter 6 presents a field-cycling NMR and dynamic light-scattering investigation of membrane dynamics by studying the molecular and collective motions in liposomes. The broad NMR spectroscopic time scale available using this technique makes it a versatile approach for studying the numerous motional processes that occur within model membrane systems including order fluctuations, translational diffusion, and molecular rotations. Following the evaluation of several methods of nuclear magnetic relaxation data analysis, a physical model-based analysis was selected which relates the physically significant parameters extracted from the data in terms of known modes of motion in membranes. The relaxometric behaviour of two types of single-lipid liposomes was modelled with a good degree of accuracy for samples with different sizes. The effect of sample temperature and the addition of cholesterol on the overall relaxation rate were studied.

A predominant theme throughout this thesis is the application of NMR spectroscopy to study and develop nanoscale materials of biological and biomedical interest. Thus, knowledge of the underlying principles governing this technique is critical for a thorough understanding of the work presented here. It is therefore beneficial to begin the thesis with an introduction to nuclear magnetic resonance techniques and a survey of the related literature.

1.2 Principles and physical background of NMR

1.2.1 Spin

In quantum mechanics, spin is a fundamental property of all elementary particles, and individual protons, neutrons, and electrons all possess spin. The spin angular momentum is quantised with its magnitude, S, defined by Equation 1.1

$$S = \hbar\sqrt{s\,(s+1)} \qquad \text{Equation 1.1}$$

where $\hbar$ is the reduced Planck's constant, and s represents the spin angular momentum quantum number, which is a non-negative integer or half-integer (0, 1/2, 1 3/2, 2, …).

The concept of spin angular momentum was first introduced in the 1920's. In 1922 Stern and Gerlach presented experimental evidence of the deflection of an atomic beam of silver atoms in a magnetic field [1]. Their results could not be described by classical mechanics, or by the quantum mechanics formulated in the Schrödinger equation for a spinless particle. Four years later, Goudsmit and Uhlenbeck proposed the existence of an electron with spin angular momentum, characterised by a spin quantum number s, equal to ½ [2]. This work was then followed up by Dirac, who in 1928 published a relativistic theory to describe the electron spin [3].

1.2.2 Nuclear spin

Atomic nuclei also have a net intrinsic spin angular momentum that arises from the individual spin angular momentum of its constituent nucleons. The existence of nuclear spin was first proposed by Pauli in 1924 [4]. Quantum mechanical considerations show that nuclear angular momentum (P) is quantised, with a magnitude given by Equation 1.2

$$P = \hbar\sqrt{I(I+1)} \qquad \text{Equation 1.2}$$

where I is the nuclear spin quantum number. The spin quantum number can have zero, positive integral or half-integral values. Some examples of spin quantum numbers for common nuclei of interest for NMR spectroscopy are shown in Table 1.1.

Table 1.1. Spin quantum numbers for selected atomic nuclei.

Nucleus	Spin Quantum Number, I
^{1}H	1/2
^{2}H	1
^{12}C	0
^{13}C	1/2
^{19}F	1/2
^{31}P	1/2
^{10}B	3
^{11}B	3/2
^{14}N	1
^{17}O	5/2

All nuclei with angular momentum also have an associated magnetic moment, μ, the magnitude of which is given by Equation 1.3

$$\mu = \gamma I \qquad \text{Equation 1.3}$$

where γ is a proportionality constant, known as the gyromagnetic ratio, which is unique for a given nucleus. Thus, nuclei with spin I = 0 have no associated nuclear magnetic moment. The nucleus of interest for our studies, ^{1}H, has spin I = ½. Thus, the remainder of the discussion will concentrate on spin ½ nuclei.

1.2.3 Nuclear spin behaviour in a magnetic field

When a nucleus with angular momentum P and magnetic moment μ is placed in a uniform external magnetic field, B_0, the nuclear spins, which are otherwise randomly oriented, will align in definite directions relative to the direction of B_0. The number of possible orientations of the nuclear spin in the presence of a magnetic field is given by 2I + 1, referred to as Zeeman splitting. The allowed orientations are defined by the magnetic quantum number m_I where m_I = I, I – 1, I – 2, … – I. Thus, only two possible orientations of the magnetic moments are quantum mechanically allowed for a ^{1}H nucleus with spin ½; the moments can either be aligned parallel or antiparallel to the direction of B_0, corresponding to a lower energy α-state or a higher energy β-state, respectively (Figure 1.1). The population ratio between the number of nuclei in the higher and lower energy levels is described by the Boltzmann relationship (Equation 1.4) which is dependent upon the absolute temperature of the sample, T, the strength of the magnetic field, and the nuclear magnetic moment.

$$\frac{N_\alpha}{N_\beta} = e^{\frac{\Delta E}{k_B T}} \qquad \text{Equation 1.4}$$

The energy separation (ΔE) between the two states is given by $\gamma\hbar B_0$, given that

$$E_{m_I} = -\mu B_0 = -\gamma I B_0 = -\gamma m_I \hbar B_0 \qquad \text{Equation 1.5}$$

The value of ΔE is very low, at attainable magnetic fields, of the order of 10^{-25} J. The resulting slight excess of nuclei in the lower spin state produces a small net macroscopic nuclear magnetisation, M_0, aligned with B_0, called the equilibrium magnetisation.

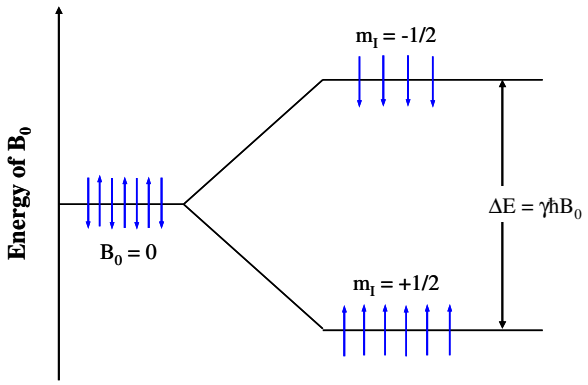

Figure 1.1. A schematic representation of the equilibrium distribution of nuclear spins with I = ½ in the presence of a magnetic field, B_0.

According to the classical picture, angular momentum of the nuclei can be visualised in terms of a vector model where the angular momentum vector rotates, or precesses, about an external magnetic field axis through its centre. By convention, the field axis direction is along the z-axis. Left undisturbed, the precession will continue indefinitely at a constant angle. The precession is caused by the torque exerted by the magnetic field in the perpendicular direction (Figure 1.2). The frequency of precession of the magnetic moments, known as the Larmor frequency (ω_L), is proportional to the field strength and the nuclear magnetic moment. This is known as the Larmor relation, Equation 1.6.

$$\omega_L = \gamma B_0 \qquad \text{Equation 1.6}$$

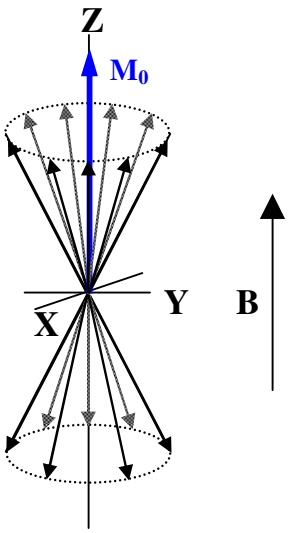

Figure 1.2. A depiction of an ensemble of nuclear spins in the presence of a magnetic field applied along the z-axis.

The vector sum of the z-components of all the ^{1}H magnetic moments in a sample results in a net macroscopic magnetic moment, M_0, oriented along the magnetic field direction. When a radiofrequency (rf) pulse is applied to the nuclei, transitions between the spin states are induced. The perturbation will rotate M_0 away from its original equilibrium position along the z-axis. When the excitation pulse is discontinued, the individual nuclei begin to undergo relaxation by releasing the absorbed rf energy, re-establishing the thermal equilibrium Boltzmann population of nuclear spins. Two different mechanisms by which M_0 can relax back to thermal equilibrium must be considered.

First, when the excitation pulse is discontinued, the individual nuclei can begin to undergo relaxation by releasing the absorbed rf energy to the surrounding lattice, which is known as longitudinal or spin-lattice relaxation (Figure 1.3). The magnetisation along the z-axis (that of the B_0 field) returns to its equilibrium value, due to a random process, thus it recovers exponentially as described by Equation 1.7 and shown in Figure 1.4.

$$M_z(t) = M_0(1 - e^{\frac{-t}{T_1}}) \qquad \text{Equation 1.7}$$

T_1 is the longitudinal, or spin-lattice relaxation time, and is the characteristic time required for M_0 to realign along the z-axis, and t is the time following the rf pulse.

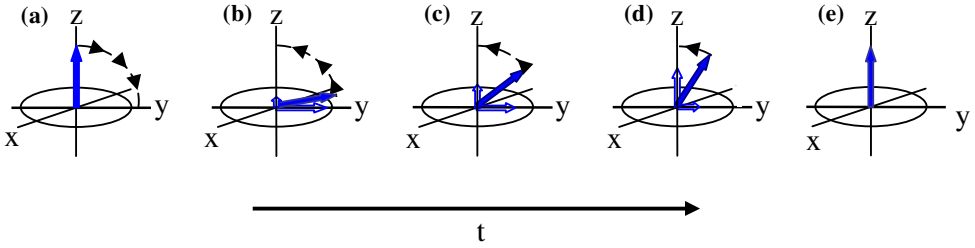

Figure 1.3. Schematic representation of M_0 undergoing longitudinal, or spin-lattice relaxation.

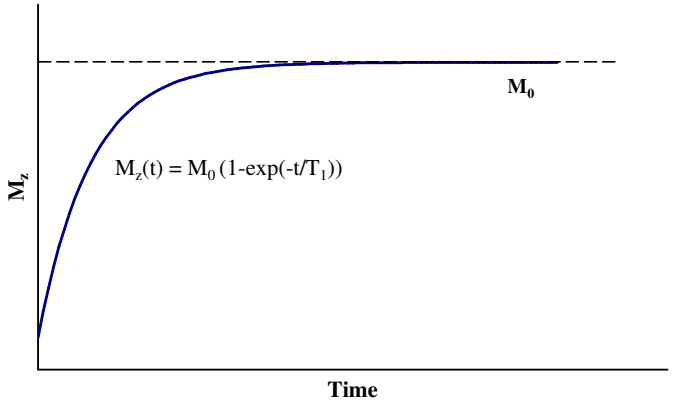

Figure 1.4. Diagram showing the exponential recovery of the longitudinal magnetisation component M_z.

A second type of relaxation mechanism is known as transverse relaxation, or spin-spin relaxation (Figure 1.5). Immediately following the end of the excitation pulse, all of the spins precess in-phase within the transverse xy-plane. As time passes, the individual nuclei spontaneously undergo relaxation by exchange of the absorbed rf energy within the spin system, resulting in an increase in entropy; the nuclear spins gradually lose their phase coherence and fan out, and the organisation of the spins is lost. This results in a decay of the total magnetisation

in the xy-plane, and can be described by Equation 1.8, where T_2 is the transverse, or spin-spin relaxation time, the characteristic time required for the spins to dephase in the transverse plane.

$$M_{xy}(t) = M_0 e^{\frac{-t}{T_2}} \qquad \text{Equation 1.8}$$

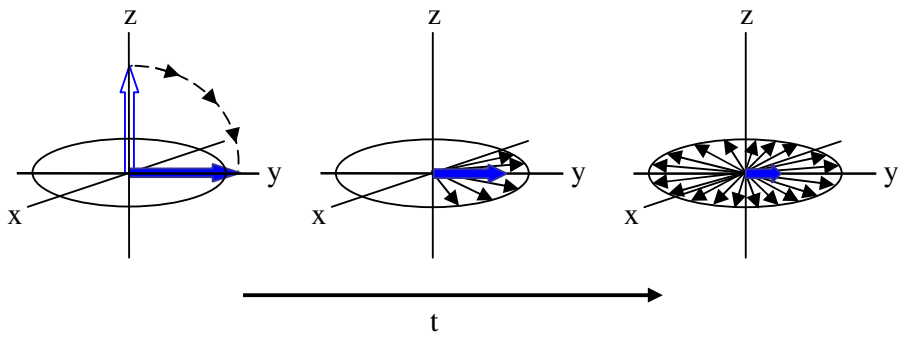

Figure 1.5. Schematic representation of transverse, or spin-spin relaxation.

In practice, there are actually two factors that contribute to the decay of the magnetisation in the transverse plane. In addition to the genuine T_2 effect, described above, any inherent inhomogeneity in B_0 can cause a variation in the magnetic field experienced by individual nuclei, causing them to precess at slightly different frequencies. This can result in a more rapid decay of the magnetisation than that due to T_2 effects alone. The actual decay of the transverse magnetisation is a combination of these two processes, characterised by a time constant T_2^*, which differs from the genuine T_2 by a contribution due to the inhomogeneity of B_0 ($1/T_{2\text{inhom}}$) as shown in Equation 1.9.

$$\frac{1}{T_2^*} = \frac{1}{T_2} + \frac{1}{T_{2in\,\text{hom}}} \qquad \text{Equation 1.9}$$

To eliminate the effect of field inhomogeneity, a spin-echo pulse sequence can be used in order to refocus the magnetisation in the presence of the magnetic

field gradients. In the Hahn spin-echo pulse sequence [5] (Figure 1.6), a spin echo is produced by applying a 180° pulse at a time τ after the initial 90° pulse. Following the 90° pulse, the nuclear spins gradually lose their phase coherence as a result of both genuine T_2 processes, as well as the magnetic field inhomogeneities. At time τ after the 90° pulse, a 180° pulse is applied which inverts the magnetisation vectors and reverses the dephasing due to field inhomgeneities (Figure 1.7). Those nuclear spins refocus to form an echo at a time 2τ. Dephasing due to true T_2 processes, which are random in nature, cannot be reversed, and as a result the phase difference between the first and second halves of the echo is not equal and the echo intensity is attenuated according to T_2. Thus, the magnetisation decay, evident in the decreasing intensity of successive echos, is solely due to the true T_2 of the sample.

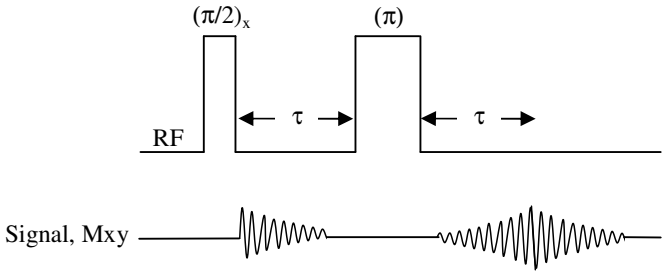

Figure 1.6. The spin-echo pulse sequence.

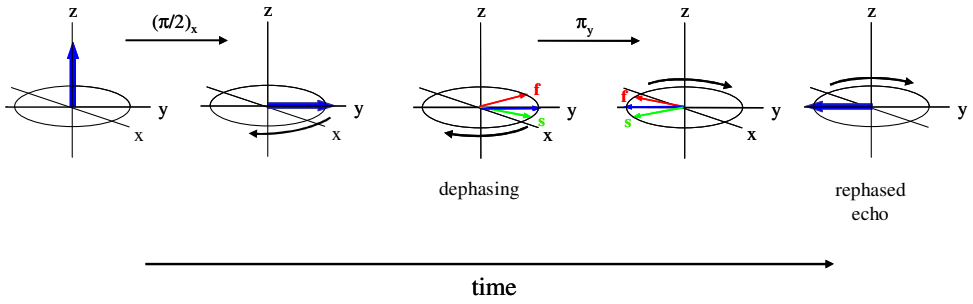

Figure 1.7. Vector diagram illustrating the evolution of the magnetisation during basic spin-echo pulse sequence.

The phase coherence that is restored at time 2τ in a basic spin-echo pulse sequence is gradually lost again as $t > 2\tau$. A train of 180° pulses, known as a multi-echo pulse sequence, can be used to generate a repeated chain of echos for successive phase recoveries. This was first suggested by Carr and Purcell in the 1950's [6]. The intensity of each echo decreases exponentially relative to the initial signal as shown in Figure 1.8.

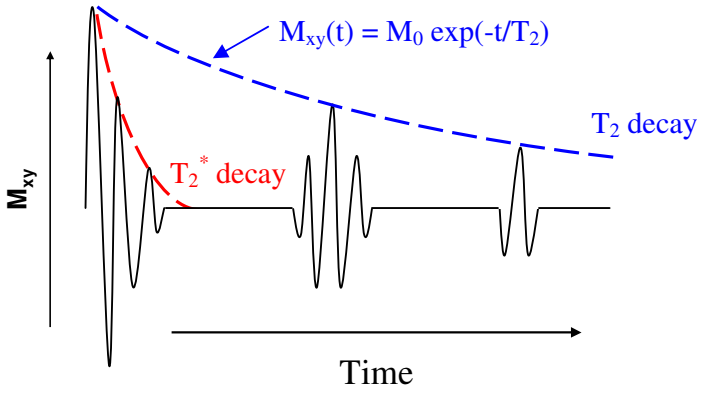

Figure 1.8. Schematic of the attenuation of echo signal amplitudes due to T_2 decay.

The phase of the inversion pulse in the spin-echo pulse sequence is significant. For instance, if the 180_x inversion pulse is replaced by a 180_y pulse, the result is an echo of a negative sign [7]. In 1958, Meiboom and Gill [8] introduced a modification of the Curr-Purcell multi-echo pulse sequence, resulting in a sequence that is currently referred to as the Curr-Purcell-Meiboom-Gill sequence, or CPMG. In the CPMG sequence, the successive 180° pulses are coherent, and the phase of the 90° rf pulse is shifted 90° relative to the phase of the 180° pulse. These modifications compensate for cumulative errors arising from small deviations in the exact angle of the 180° pulse, and hence improve measurement reproducibility. The CPMG pulse sequence was used for all T_2 measurements reported in this thesis. The multi-echo spin-echo pulse sequence is the basis of the sequences most commonly used in clinical imaging [9].

1.3 Fast field-cycling NMR

Fast Field-Cycling NMR (FFC NMR) is a technique used to obtain longitudinal relaxation times, T_1, (or equivalently, relaxation rates, $1/T_1 = R_1$) over a wide range of magnetic field strengths. A plot of R_1 as a function of frequency is known as a nuclear magnetic relaxation dispersion (NMRD) profile. The profile provides a great deal of information concerning the details of the molecular dynamics that occur within a system. The profiles can be interpreted according to theories developed for the particular systems of interest.

The fluctuations that stimulate the transitions that drive relaxation arise due to modulation of the $^1H - {}^1H$ (or $^1H - e^-$) dipolar interaction driven by dynamic processes on a time scale that matches ω. NMRD profiles provide information concerning the molecular motions of a system in the form of the spectral density function, J(ω). For a system where relaxation is driven by a single motion, the spin-lattice relaxation rate is given by

$$\frac{1}{T_1} = \frac{9}{8}\left(\frac{\mu_0}{4\pi}\right)^2 \gamma^4 \left(\frac{h}{2\pi}\right)^2 \frac{1}{r^6}\left[\frac{4}{15} J(\omega) + \frac{16}{15} J(2\omega)\right] \qquad \text{Equation 1.10}$$

where μ_0 is the vacuum permeability, h is Planck's constant, and r is the distance between the ^1H nuclei. J(ω) and J(2ω) are the spectral density functions evaluated at the Larmor frequency and twice the Larmor frequency, as they are the only allowed frequencies for induced single- and double-spin flip transitions between the energy levels of the spin system. The efficiency of the local fluctuating fields to induce transitions is given by the spectral density function, which is defined by Equation 1.11.

$$J(\omega) = \int_{-\infty}^{\infty} G(\tau)\, e^{-i\omega\tau}\, dt \qquad \text{Equation 1.11}$$

The fluctuations of the local magnetic fields arising from random motions of the sample give rise to exponential time correlation functions of the form shown in Equation 1.12.

$$G(\tau) = G(0)\, e^{\frac{-\tau}{\tau_c}} \qquad \text{Equation 1.12}$$

The correlation time, τ_c, is the time constant for decay of $G(\tau)$. It is a measure of the mean time between the reorientation of a molecule. Slow motions result in long correlation times, whereas short correlation times are a result of faster motions (Figure 1.9).

The Fourier transform of an exponential time correlation function is a Lorentzian spectral density function (Equation 1.13).

$$G(\tau) \xrightarrow{FT} C(0)\, \frac{\tau_c}{1+(\omega\tau_c)^2} = J(\omega) \qquad \text{Equation 1.13}$$

The rate of random motion, τ_c^{-1}, can be obtained directly from the half width of the Lorentzian spectral density function. Figure 1.10 is a simulation of spectral density functions resulting from three different τ_c values.

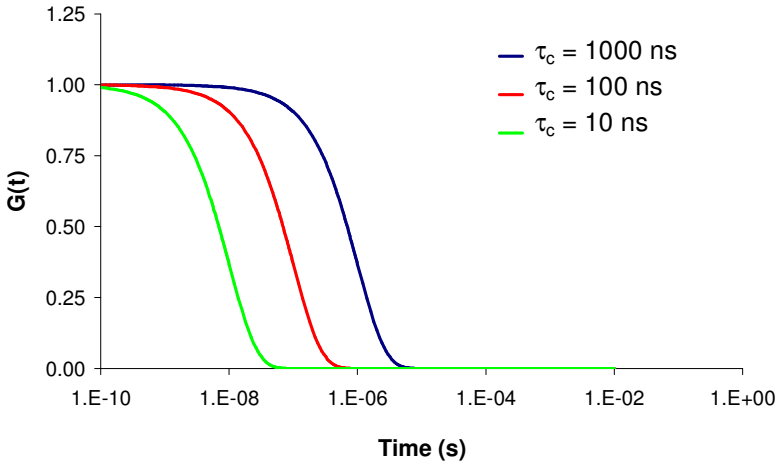

Figure 1.9. Representative correlation functions $G(\tau)$ resulting from three values of rotational correlation time, τ_c.

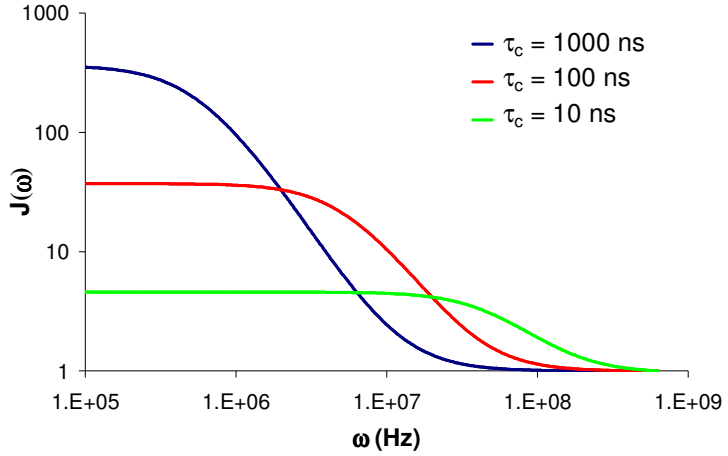

Figure 1.10. Three simulated spectral density functions J(ω) resulting from three values of rotational correlation time, τ_c.

Thus the NMRD profile maps out the spectral density of the motional system under study. In the case of relaxation due to a single random dynamic process, the profile is the superposition of two Lorentzian functions.

In Figure 1.11, a representative plot of the spin-lattice relaxation time as a function of correlation time is shown for a given Larmor frequency, assuming dipole-dipole relaxation. There are three distinct ranges which can be identified from this plot.

(i) $\tau_c\omega \ll 1$; this is known as the extreme or motional narrowing limit. In this range, the rate of fluctuations is much higher than the resonance frequency, this is typical for small molecules in non-viscous solvents. The fast motions of molecules averages out the interactions between molecules and $T_1 = T_2 \approx \sim 1/5K\tau_c$, where K is a constant equal to $3\mu_0^2\hbar^2\gamma^4/160\pi^2r^6$, and the relaxation times are frequency independent [10]. This corresponds to the low frequency plateaus in Figure 1.10.

(ii) $\tau_c\omega \approx 1$; At this point, there is a T_1 minimum, and relaxation is most efficient. The fluctuations occur on an intermediate time scale. This is typical for medium sized molecules or viscous solvents.

(iii) $\tau_c\omega >> 1$; this is known as the slow-motion limit. The rate of fluctuations is slow, typical for slowly tumbling molecules or macromolecules in viscous media. There is no strong spectral density contribution to the relaxation near the Larmor frequency, corresponding to the high frequency limit in Figure 1.10. Thus, the T_1 value is high.

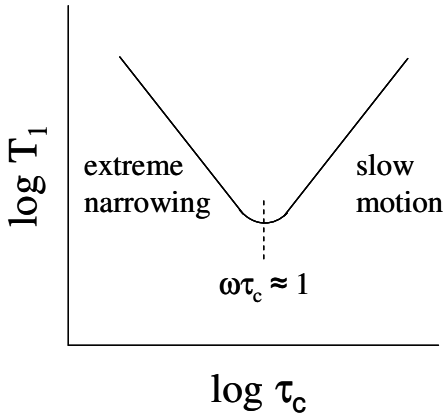

Figure 1.11. A typical plot of log T_1 as a function of log τ_c which maps out the extreme narrowing and spin diffusion limits.

The advantage of the field-cycling approach over conventional T_1 measurements as a function of temperature is that the dynamics can be characterised at a single temperature, and if Lorentzian spectral density functions are not appropriate, this will be immediately apparent from the profile.

1.4 Magnetic resonance imaging

Magnetic resonance imaging (MRI) is a non-invasive medical diagnostic technique used primarily in medical settings due to its capability to enhance the differentiation between normal and pathological tissues. Several key

developments led to the routine clinical applications of NMR [11]. Damadian identified a difference in the nuclear magnetic relaxation times of normal and cancerous tissues and he published his findings in Science in 1971 [12]. The first demonstration of MRI imaging was in 1973 when Lauterbur produced a 2-D MR image of a test tube sample [13]. This was quickly followed by reports by Moon et al. [14] and Hoult et al. [15] where biochemical information was obtained from cells and tissues in 1973 and 1974, respectively. In 1975, Richard Ernst's group in Zurich invented 2-D fourier transform imaging [16,17] which forms the basis of almost all modern MRI techniques.

The signal intensity in MRI is directly related to the longitudinal or transverse relaxation times of the ^{1}H in water molecules contained within tissues. The values for T_1 and T_2 are dependent upon the chemical and magnetic environment, which differs depending on the tissue. The difference in the relaxation times in different parts of tissue is what generates the contrast in the image.

The sensitivity of the MRI signal to the T_1/T_2 values, and therefore the image contrast, can be enhanced by adjusting pulse sequence parameters [18]. The spin-echo pulse sequence contains two important adjustable parameters: i) the time between consecutive 90° rf pulses, known as the repetition time (TR), and ii) the time between the initial 90° pulse and the echo, known as the echo time (TE). Variation of TR and TE can modulate image contrast. An image obtained using a short TR and a short TE is known as a T_1-weighted image. In this case, the image contrast is based primary on the T_1 characteristics of the tissues while T_2 contributions are minimised [19]. The T_1 of a tissue determines the amount of longitudinal magnetisation available to generate a measurable signal in the transverse plane following the excitation pulse. Under T_1-weighted conditions, tissues with a short T_1, such as fat tissue, will undergo rapid longitudinal decay, therefore generating a strong signal, i.e., bright contrast, upon subsequent excitation pulses. Conversely, tissues with a longer T_1, such as muscle tissue, will only undergo slight longitudinal relaxation before the next 90-degree pulse is applied, and therefore offer little longitudinal magnetisation. The signal intensity is decreased compared with tissues with a short T_1, and these tissues appear dark within the T_1-weighted images.

T_2-weighting, on the other hand, is designed to produce higher signals (brighter contrast) from tissues with longer transverse relaxation times, while regions with short T_2 appear dark under these conditions. A T_2-weighted image can be obtained by utilising a spin-echo pulse sequence with a long TR to minimise T_1-weighting, and long TE to maximise T_2-weighting. When TE >> than T_2, the magnetisation can decay completely and thus there is little to no transverse signal left to measure [18].

The image contrast can be enhanced even further through the use of contrast agents (CAs). Magnetic nanoparticles form an important class of contrast agents. Iron-oxide nanoparticles, in particular, have attracted significant attention due, in part, to their unique size-dependent magnetic properties. Before further discussing the benefits of iron-oxide nanoparticles as MRI contrast agents, however, it will be useful to first introduce the different classes of magnetic materials and their associated magnetic properties.

1.5 Magnetism and magnetic classification of materials

All materials can be categorised based on the magnetisation (M) induced in response to an externally applied magnetic field (H). Their bulk magnetic susceptibility (χ) is given by Equation 1.14.

$$\chi = \frac{M}{H} \qquad \text{Equation 1.14}$$

Five classes of magnetic behaviour have been observed: diamagnetism, paramagnetism, ferromagnetism, antiferromagnetism, and ferrimagnetism.

Diamagnetic materials have no intrinsic magnetic properties in the absence of an applied field. They have no unpaired electrons in their orbital shells, and therefore no net magnetic dipole moment. A dipole moment is induced upon the application of an external magnetic field, however, due to the perturbation of the orbital motion of the electrons. The result is the induction of a magnetic moment

oriented in the opposite direction to that of the applied external field (Figure 1.12 (a)). The bulk magnetic susceptibility of a diamagnetic material is small and negative (Figure 1.12 (b)). When placed in a magnetic field, diamagnetic materials are actually repelled by the field, though the force of repulsion is relatively weak compared to ferromagnetism and paramagnetism [20]. Thus, induced diamagnetism is usually masked by the larger and more permanent ferromagnetism or paramagnetism, if present.

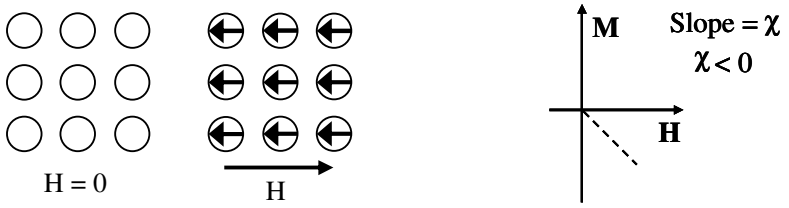

Figure 1.12. (a) Schematic representation of the dipole moment ordering in a diamagnetic material in the presence and absence of an external magnetic field. (b) Typical magnetisation curve showing sample magnetisation as a function of applied magnetic field for a diamagnetic material.

Paramgnetism occurs in materials which have a net magnetic moment due to unpaired electrons in partially filled orbitals. In the absence of a magnetic field, the individual magnetic moments are randomly oriented as a result of thermal motion, and there is no coupling between neighbouring magnetic moments. Thus, paramagnetic substances do not exhibit any net magnetic moment in the absence of a field [21]. The application of an external field, however, causes the moments to partially align with the field, and a low magnetisation is induced in the same direction as the applied field. The magnetic susceptibility of the material is therefore classified as small and positive (Figure 1.13 (b)). The fraction of the spins oriented by the field is proportional to the field strength (Figure 1.13 (a)). A paramagnetic material exhibits magnetism for as long as the external field is applied [20,22]. When the magnetic field is removed, the magnetisation is lost as the magnetic moments return to their normal random alignment.

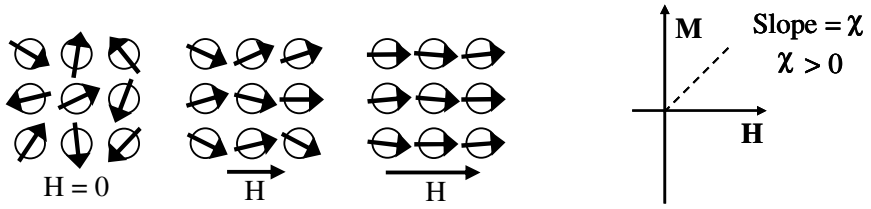

Figure 1.13 (a). Schematic representation of the dipole moment ordering in a paramagnetic material in the presence and absence of an external magnetic field of varied field strength. (b) Typical magnetisation curve for a paramagnetic material.

The tendency of the field to align the moments must overcome the thermal agitation caused by an increase in temperature to produce magnetisation. This results in a temperature dependent magnetic susceptibility in paramagnetic materials (Figure 1.14). The inverse relationship between χ and T is described by the Curie Law (Equation 1.15), where C is the Curie constant, which is specific to a given material.

$$\chi = \frac{C}{T} \quad or \quad M = C\left(\frac{H}{T}\right) \qquad \text{Equation 1.15}$$

The Curie law only holds for high temperatures or weak magnetic fields because it predicts that the magnetisation will increases indefinitely with an increase in the externally applied field; however, once the material is saturated, with all the moments aligned, any further increase in H or T will have a minimal effect on the sample magnetisation.

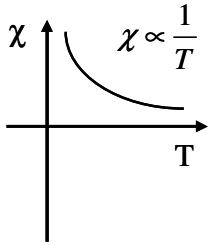

Figure 1.14. Temperature dependence of the magnetic susceptibility of a paramagnetic material.

Ferromagnetic materials are known as permanent magnets, as they are inherently magnetic regardless of whether or not they are placed in a magnetic field [20]. The inherent magnetism of ferromagnetic materials is attributed to the long-range ordering at the atomic level which causes the unpaired electron spins to line up parallel with each other within a local region known as a magnetic domain. In the absence of an external magnetic field, the local magnetisation within each domain is saturated, but the domains are randomly oriented with respect to one another (Figure 1.15 (a)); when the sample is placed in a magnetic field all of the magnetic domains align in one direction (Figure 1.15 (b)) so the material is magnetised.

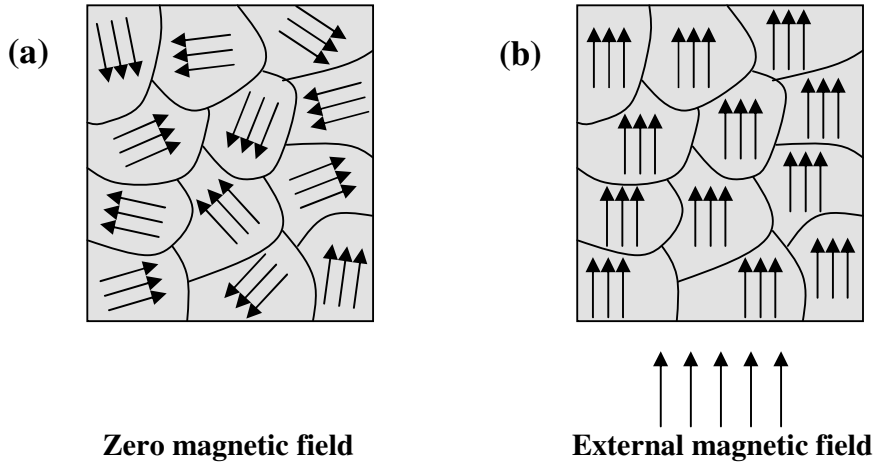

Figure 1.15. Schematic representation of the magnetic ordering characteristic of ferromagnetic materials.

Ferromagnetic materials tend to retain a fraction of their magnetisation upon removal from an external magnetic field. This “magnetic memory” is known as hysteresis. A plot of the relationship between the induced magnetisation of a sample and the strength of the applied external magnetic field is known as a hysteresis loop, and it shows the “history dependent” nature of the magnetisation. A number of basic magnetic parameters can be derived from the magnetisation curve, an example of which is shown in Figure 1.16.

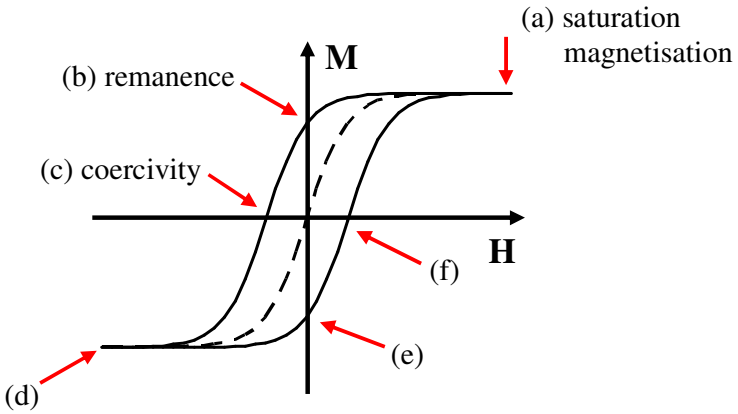

Figure 1.16. A hysteresis loop showing the relationship between the magnetisation of the sample (M) and the strength of the external magnetic field (H).

When a previously unmagnetised ferromagnetic material is placed in magnetic field, the material is driven to magnetic saturation, M_s, (Figure 1.16 (a)) in which all of the magnetic domains are rotated away from the easy axis and align with the applied field. Upon reducing the field to zero, some of the magnetic domains remain aligned with the field, while others have returned to their easy direction of magnetisation. The residual magnetisation remaining when the external field is zero is known as the remanence magnetisation (M_r) of the sample (Figure 1.16 (b)). Upon reversing the direction of the applied field, some of the magnetic domains are flipped resulting in a net magnetisation of zero within the sample (Figure 1.16 (c)). The field required to remove the residual magnetisation and drive the magnetisation to zero after saturation is called the coercivity of the sample. By increasing the field in the negative direction, the material is driven to magnetic saturation in the negative direction, in which all of the magnetic domains are aligned against the field (Figure 1.16 (d)). Reducing the strength of field to zero will again result in remanence magnetisation, this time in the negative direction (Figure 1.16 (e)). Finally, upon an increase of the magnetic field in the positive direction, the sample magnetisation will return to zero (Figure 1.16 (f)). If the magnetic field is repeatedly cycled, the magnetisation of

the sample will also cycle around the hysteresis loop in a counter-clockwise direction, as described. The hysteresis parameters are dependent on different factors including particle size, domain character (single- or multi-domain), stresses, and temperature.

When a ferromagnetic material is heated above a critical temperature, known as the Curie temperature (T_C), the long range ordering, and therefore the magnetisation, is lost as a result of thermal agitation. Below T_C, the ferromagnet is ordered, while above T_C, it is disordered. Thus, the Curie temperature, an intrinsic property of the material, gives an indication of the amount of energy necessary to break up the long range ordering in the ferromagnet.

Antiferromagnetism arises due to strong coupling between the magnetic moments of adjacent atoms or ions, but in contrast to ferromagnetism, the neighbouring magnetic moments are equal in magnitude and aligned antiparallel to one another, resulting in a net moment of zero [21]. Antiferromagnetic materials do not exhibit any bulk magnetisation, but they have a small and positive magnetic susceptibility. The susceptibility reaches a maximum at a critical temperature known as the Néel temperature (T_N). Above T_N, anti-ferromagnetic materials are paramagnetic.

Ferrimagnetism, which can be considered as a form of antiferromagnetism, is observed when the magnetic moments of the ions in a material are aligned in an antiparallel arrangement, but the magnitude of the opposing moments are unequal, thus resulting in an overall net magnetisation when the material is placed in an external field. Ferrimagnetism occurs in compound materials, and is common in magnetic oxides. Some common oxides that exhibit ferrimagnetic behaviour are shown in Table 1.2.

Table 1.2. Magnetic properties of common bulk ferrimagnetic materials; T_C is the Curie temperature and M_s is the saturation magnetisation [23].

Material	**T_C (°C)**	**M_s (kA/m)**
Chromium dioxide (CrO_2)	117	410
Maghemite (γ-Fe_2O_3)	590	414
Cobalt ferrite ($CoFe_2O_4$)	520	422
Magnetite (Fe_3O_4)	585	470

An important example of a commonly used ferrimagnetic magnetic oxide is magnetite, Fe_3O_4 [23]. The ionic arrangement of magnetite is responsible for the net magnetic moment and the ferrimagnetic behaviour. The magnetic structure of magnetite consists of two distinct ferromagnetic sublattices, a tetrahedral site (A site) occupied by Fe^{3+} and an octahedral site (B site) occupied by Fe^{2+} and Fe^{3+} [24]. This cation arrangement on the A and B sublattice sites defines an inverse spinel structure and the structural formula can be written as $[Fe^{3+}]_A[Fe^{3+},Fe^{2+}]_BO^{2-}{}_4$. At the tetrahedral site, Fe is surrounded by 4 oxygen ions, and it is surrounded by 6 oxygen ions at the octahedral site. A representation of the crystal structure of magnetite is shown in Figure 1.17. Below T_C, the magnetic moments on the A and B sites are opposite in direction and unequal in magnitude, resulting in ferrimagnetic behaviour.

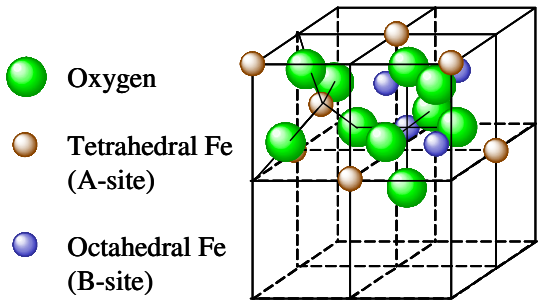

Figure 1.17. Schematic of the crystal structure of magnetite. The spins of the A sublattice are antiparallel to the spins of the B sublattice. Figure is adapted from Banerjee and Moskowitz, 1985 [25].

Maghemite (γ-Fe_2O_3) is also ferrimagnetic at room temperature and has a structure similar to that of magnetite. It has an inverse spinel structure with a cubic unit cell; however, as all the Fe cations in maghemite are in the trivalent state, the cation arrangement on the A and B sublattice sites differs from that of magnetite. The Fe^{3+} cations in maghemite occupy both tetrahedral A-sites and octahedral B-sites, and there are cation vacancies, confined to octahedral sites, in order to compensate for the increased positive charge [24,26]. A representation of the crystal structure of maghemite is shown below in Figure 1.18. Below T_C, the magnetic moments of the Fe^{3+} ions in the tetrahedral A sites and the octahedral B sites are opposite in direction and unequal in magnitude, resulting in ferrimagnetic behaviour.

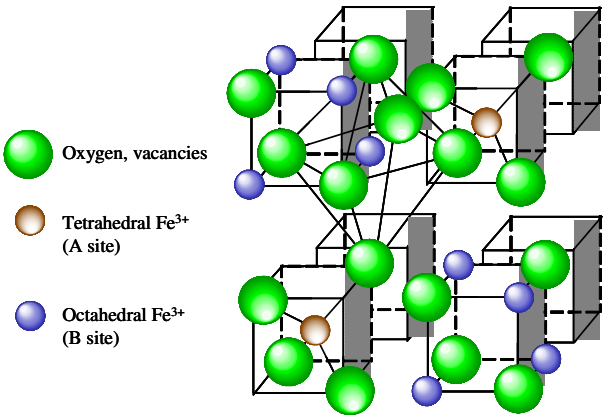

Figure 1.18. Schematic representation of the nonequivalent tetrahedral and octahedral sites of Fe^{3+} in the structure of maghemite. Figure is adapted from Zboril et al., 2002 [26].

1.5.1 Superparamagnetism in magnetic nanoparticle systems

The magnetic properties of individual nanoparticles are highly dependent on both temperature and volume. When the diameter of a ferro- or ferrimagnetic object is decreased below a critical diameter, the formation of domains becomes energetically unfavourable due to the increased relative domain wall energy, and the particle consists of a single, uniformly magnetised domain. The critical

diameter, D_{crit}, below which a particle behaves as a single domain particle is given by Equation 1.16.

$$D_{crit} \approx 18 \frac{(AK_{eff})^{1/2}}{\mu_0 M_s^2} \qquad \text{Equation 1.16}$$

where A is the exchange constant, K_{eff} is the uniaxial anisotropy constant, μ_0 is called the constant of permeability, and M_s is the saturation magnetisation. Typical values for D_{crit} for some relevant materials are reported in Table 1.3.

Table 1.3. Estimated single-domain diameters for common magnetic materials [27,28].

Material	D_{crit} (nm)
hcp Co	15
fcc Fe	7
Ni	55
Fe	15
$SmCo_5$	750
Fe_3O_4	128
γ-Fe_2O_3	166

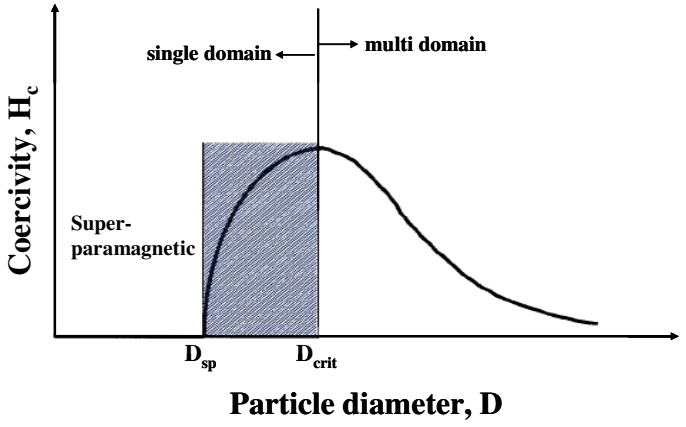

Figure 1.19. Coercivity as a function of particle size; D_{sp} is the superparamagnetic size limit and D_{crit} is the single domain particle size limit.

A further decrease in the size of a single-domain particle results in a transition from the ferromagnetic to the superparamagnetic state. Below the superparamagnetic size limit, D_{sp} (Figure 1.19), the thermal energy (k_BT) is greater than the energy required to reverse the direction of the magnetic moments. The magnetisation can then spontaneously fluctuate between two energetically equivalent magnetisation directions, either parallel or anti-parallel to an "easy axis" of magnetisation. The anisotropy energy is the energy barrier for the rotation of the magnetisation between the two easy axis directions, and can be expressed by Equation 1.17 where V is the particle volume, K_{eff} is the anisotropy constant, and θ is the angle between the magnetisation and the easy axis.

$$\Delta E_{anis}(\theta) = K_{eff} V \sin^2 \theta \qquad \text{Equation 1.17}$$

A plot of the energy as a function of magnetisation direction for single domain particle is shown in Figure 1.20. Two energy minima are indicated at θ = 0 and θ = π, corresponding to a magnetisation direction parallel and antiparallel to the easy axis, respectively.

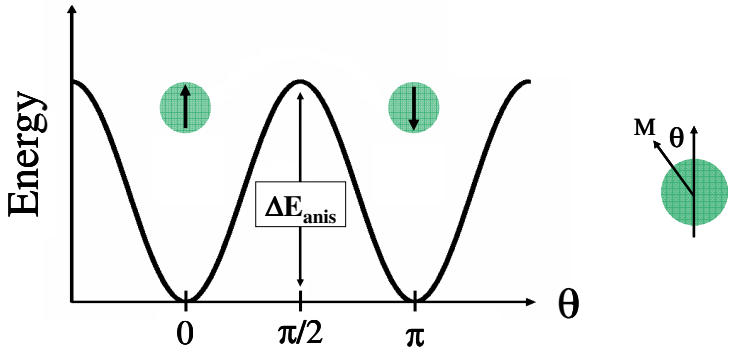

Figure 1.20. Schematic plot of the energy as a function of magnetisation direction for a single-domain particle with uniaxial anisotropy. ΔE_{anis} is the energy barrier for the rotation of the magnetisation, and θ is the angle between the magnetisation, M, and the easy axis.

In an assembly of isotropic single domain ferromagnetic particles, in which there are no inter-particle interactions, when $k_BT >> K_{eff}V$, the system behaves as a paramagnet, except its magnetic moment is not that of a single atom. Instead, the total magnetisation of each single domain particle is a sum of the moments of all the atoms in the particle [29]. The macroscopic magnetisation is known as a super-spin, which fluctuates coherently.

When the magnetic field is turned off, a distribution of moment orientations is re-established, resulting in a time-averaged remanent moment of zero. Thus, the cooperative alignment of magnetic moments is no longer observed and superparamagnetic materials do not retain magnetisation once the magnetic field is removed.

The characteristic time of the fluctuation of the magnetisation of a particle with uniaxial anisotropy is known as the Néel correlation time, τ_N, which is given by the Néel-Brown expression (Equation 1.18) where k_B is the Boltzmann constant, and $\tau_0 \sim 10^{-9}$ s.

$$\tau_N = \tau_0 \exp\left(\frac{K_{eff}V}{k_BT}\right) \qquad \text{Equation 1.18}$$

The rate of fluctuations is temperature dependent, and slows as the sample is cooled. If the fluctuation rate slows to a point in which the particle moments appear static within the time scale of the experiment and superparamagnetic behaviour ceases to be observed, the particle is said to be blocked. The temperature, T_B, below which the particle moments appear static within the time scale of the experiment, is known as the "blocking" temperature. The blocking temperature is described by Equation 1.19 for uniaxial particles.

$$T_B = \frac{KV}{25k_B} \qquad \text{Equation 1.19}$$

1.5.2 Applications of magnetic nanoparticles

Magnetic nanoparticles and nanoparticle assemblies have found widespread use with applications that extend into many areas of science and technology including magnetic storage media [30], catalysis, magnetic ink for jet printing [31], and use in high-frequency electrical circuits for portable communication devices [32]. Recently, Ceylan et al. provided the first account of the use of magnetic nanoparticles for inductive heating for performing chemical synthesis [33].

Since the mid-1970's, there has been increasing interest in the use of magnetic nanoparticles in the areas of bioscience and medicine. Iron-oxide nanoparticles, specifically, Fe_3O_4 and γ-Fe_2O_3, have proven to be very promising for biomedical applications because they are relatively easy to form, have low toxicity [34], are well tolerated by the human body [35], and suspensions of single-domain nanocrystals of these oxides exhibit favourable magnetic properties; (i) they are superparamagnetic at room temperature with moderately high saturation magnetisation; (ii) a large magnetic moment on each particle allows them to be guided with external magnetic fields; (iii) they do not retain any magnetisation upon removal of a magnetic field, which eliminates the potential complication of aggregation, such is observed for larger, multi-domain paramagnetic materials [36].

1.5.2.1 Magnetic drug targeting

One of the major obstacles underlying drug therapy, particularly anticancer drug therapy, is the delivery of the drugs to a particular site in the body. Conventional chemotherapy agents are relatively non-specific, and current treatments involve the distribution of these agents throughout the body. This course of treatment exposes otherwise healthy cells and tissues to the potentially cytotoxic effects of the drugs. Thus, there is a critical need to achieve selective delivery of drugs to specific targets, thereby maximising drug action, and minimising the dosage and potential side effects. This can be achieved through drug targeting, in which the distribution of drugs throughout the body is altered so that the majority of the administered dose interacts specifically with the target tissue [37].

A common drug targeting strategy is active or physical drug targeting [35,38] in which normal drug distribution patterns are circumvented through the use of external influences. One particular type of active drug targeting with widely recognised benefits is magnetic drug targeting (MDT). This technique utilises magnetic particles combined with an external magnetic field for the delivery of chemotherapeutic agents to the desired target area. Anticancer drugs can be grafted onto magnetic nanoparticles via physical adsorption [35,39], ionic bonding [40], and covalent bonding [41,42] or encapsulated with magnetic nanoparticles inside a polymeric shell [43,44] or phospholipid vesicle [45-47]. External magnetic fields, localised around the appropriate region of the body, can then be used to guide the nanoparticles to the chosen site, and hold them there until therapy is complete [35,37,40,48]. Drug release from nanoparticle surfaces has been achieved by hydrolytic bond degradation [49] or pH-triggered bond cleavage [41], and drug release from encapsulated systems have been triggered by lasers [45], temperature [50,51], light [52], ultrasound [53], and EMF pulses [54,55].

Phase I clinical trials of magnetic drug targeting in human patients with advanced and unsuccessfully pretreated tumours were reported by Lübbe et al. in 1996 [35]. It was found that while the magnetic drug targeting was generally well tolerated, some modifications would be necessary for improved effectiveness of the treatment.

1.5.2.2 Hyperthermia

Hyperthermia is a therapeutic procedure designed to kill cancer cells by exposing affected organs or tissues to elevated temperatures. Temperatures between 41 – 46°C, known as mild or classical hyperthermia [56,57] are used to stimulate an immune response to reject and destroy tumours. The use of higher temperatures, from 46 – 56°C, known as thermoablation, initiates tumour destruction by cell necrosis, coagulation, or carbonisation [56,57]. Thermal therapy offers numerous advantages over more conventional treatments such as surgery, chemotherapy, and radiation. It is a simple, minimally or non-invasive technique that has the potential of treating tumours embedded in critical regions of the body, which are

not suitable for surgical removal. Additionally, thermal therapy eliminates the painful side effects resulting from chemotherapy and radiation.

The use of heat in the treatment of cancer is not a new concept, and many studies have been reported over the course of several centuries. A wide range of heating sources have been investigated including externally applied microwaves [58], ultrasound [59] and infrared radiation [60]. The limitations of these sources, including limited heat conduction through some tissues and an inhomogeneous temperature distribution [38,61], led some researchers to attempt to improve the localisation of heating through the use of implantable heating devices that convert electromagnetic energy into heat upon application of an external magnetic field. Such devices have involved heat delivery by optical fibres [62], radiofrequency electrodes [63] and microwave antennas [64]. While this strategy does improve heat localisation, it is an invasive procedure that requires surgical intervention.

Magnetically mediated hyperthermia (MMH) was first introduced by Gilchrist et al. in 1957 [65], and the ongoing advances in nanotechnology have provided a renewed interest in hyperthermia. Nanoparticles offer the distinct advantage of more uniform heating and non-invasive delivery to the target area. Presently, the MMH technique involves the injection of colloidal dispersions of magnetic nanoparticles and localisation of the particles within tumour tissues through the use of external magnetic fields. Alternating magnetic fields are then used to generate energy in the form of heat through the oscillation of the magnetic moment inside the nanoparticles located at the tumour site. The heat is then conducted to the surrounding environment [38]. The origin of heating depends on the size and magnetic properties of the particles [57]. Ultra-small particles of iron-oxide (USPIO) have been shown to generate an exceptionally high amount of heat compared to micron-sized particles when exposed to AC magnetic fields [56,57,66]. The difference is due to the single domain nature of USPIO.

Heat can be generated in USPIO as a result of two relaxation mechanisms, Néel relaxation and rotational Brownian motion [67]. In Néel relaxation, the heat generation is due to rotation of the magnetic moments within the particle core

[66]. The characteristic time of relaxation, τ_N, is given by Equation 1.18, above. The frequency ν_N for maximal heating via Néel relaxation is given by Equation 1.20.

$$\nu_N = \frac{1}{2\pi\tau_N} \qquad \text{Equation 1.20}$$

The second mechanism for heat generation is Brownian motion of the particle within a carrier liquid. In this case, heat is generated due to the rotation of the entire magnetic particle because of the torque exerted by the external field [57]. The energy barrier for particle reorientation is determined by rotational friction within the carrier liquid, and the rotation is characterised by the Brown relaxation time, τ_B [57], defined by Equation 1.21

$$\tau_B = \frac{3\eta V_B}{k_B T} \qquad \text{Equation 1.21}$$

where V_B is the hydrodynamic volume of the particle [57]. The frequency for maximal heating via Brown rotation ν_B is given by Equation 1.22 [57].

$$\nu_B = \frac{1}{2\pi\tau_B} \qquad \text{Equation 1.22}$$

The amount of heat delivered by a magnetic material, is given by its specific absorption rate (SAR), Equation 1.23, which is a measure of the power of heating of the material per gram [57].

$$SAR = C\frac{\Delta T}{\Delta t} \qquad \text{Equation 1.23}$$

In Equation 1.23, C is the specific heat capacity of the sample in J g^{-1} K^{-1}, and $\Delta T/\Delta t$ is the initial slope of the temperature versus time dependence [57]. The SAR of a material is dependent on a large number of parameters including

particle size [68], size distribution, shape, chemical composition, frequency, and the amplitude of the magnetic field [57]. Clinically, a larger SAR value of a hyperthermia mediator lowers the dose required for administration to the patient [68].

Phase I/II clinical trials conducted in human patients with brain tumours showed promising results when combined with chemotherapy, as reported by Jordan et al in 2001 [69].

1.5.2.3 Contrast agents

The use of contrasts agents (CAs) further expands the versatility and diagnostic ability of MRI by increasing sensitivity and enhancing the image contrast between healthy and pathological tissues. The origin of contrast enhancement lies in the ability of the contrast agent to shorten the T_1 or T_2 relaxation times of the water protons within the surrounding tissue (termed a T_1- or T_2- agent). The effectiveness of the contrast agent to do so can be quantified by the concentration independent relaxivity, r_1 or r_2, which is defined as the change in the longitudinal or transverse relaxation rate per unit concentration of the contrast agent, given by

$$r_1 = \frac{\left(R_{1\_obs} - R_{1\_tissue}\right)}{[CA]} \qquad \text{Equation 1.24}$$

$$r_2 = \frac{(R_{2\_obs} - R_{2\_tissue})}{[CA]} \qquad \text{Equation 1.25}$$

where R_{1_obs} and R_{2_obs} are the observed relaxation rates in the absence of enhancement, and [CA] is the concentration of the contrast agent in mM. Thus, for our work, r_1 and r_2 have units of $mM^{-1}s^{-1}$ of iron.

Contrast agents can be classed into two groups. Positive contrast agents reduce T_1 and generate a brighter signal (positive contrast) under T_1-weighted conditions. Also known as T_1-agents, they typically consist of paramagnetic complexes of Gd^{3+} or Mn^{2+} ions and have a low r_2/r_1 ratio in the range of 1-2

[70-73]. The overall relaxation rate enhancement by paramagnetic contrast agents is due to both inner- and outer-sphere relaxation mechanisms; both mechanisms contribute approximately equally to the overall relaxivity. An inner-sphere contribution is a result of the chemical exchange between water protons from water molecules bound within the inner coordination sphere of the metal ion and the bulk water, and an outer-sphere contribution is a result of water protons diffusing past the unpaired electrons in the outer sphere environment of the metal ion.

Negative contrast agents (or T_2-agents) have a much higher r_2/r_1 ratio and generate a darker signal (negative contrast) in MR images recorded under T_2-weighted conditions. They are usually based on small particles of iron-oxide (SPIO), particles containing multiple ferrite nanocrystals within a water permeable shell. The relaxation enhancement is due solely to the outer-sphere relaxation mechanism [74].

Some currently available commercial contrast agents are reported in Table 1.4 [75].

Table 1.4. A summary of some commercially available contrast agents.

Trade name	**Lumirem®**	**Endorem®**	**Sinerem®**	**Resovist®**
Manufacturer	AMAG Pharmaceuticals	AMAG Pharmaceuticals, Guebert	AMAG Pharmaceuticals	Bayer Schering Pharma AG
Composition	Silicone-coated iron-oxide particles	USPIO	USPIO; fractionation of Endorem®	SPIO
Crystal size (nm)	8.5	4.5	4.5	
Particle diameter (nm)	300	150	30	
Contrast effect	T_2-agent	T_2-agent	T_1-, T_2-agent	T_1-, T_2-agent
Application	gastro-intestinal tract imaging	liver and spleen disease detection	MR-angiography and vascular staging of RES-directed liver disease	MR-angiography and vascular staging of RES-directed liver disease

1.6 SPM theory applied to USPIO

NMRD profiles are commonly used to gain insight into the relaxation behaviour of magnetic colloidal dispersions, which are known to determine the MRI response [76]. There have been several relaxometric studies published which validate the approach as a general purpose tool for characterising magnetic nanoparticle dispersions [77,78]. The generally accepted theory for solvent relaxation due to the presence of dispersed superparamagnetic nanoparticles (SPM theory) was developed by Muller and co-workers [79]. In summary, the theory extends the classical outer-sphere theory of relaxation to include the presence of a high Curie component, even at moderate fields, and the presence of strong magneto-crystalline anisotropy. The high-frequency relaxation is driven by diffusion of the solvent, with the position of the r_1 maximum sensitive to the primary particle size, as it is determined by the characteristic diffusion time, $\tau_D = d^2/(4D)$, where d is the particle diameter and D is the diffusion coefficient. The position of the maximum shifts to lower frequencies as the size of the primary particles increases, and higher frequencies as the size decreases. This is shown in the simulated relaxivity curve, or NMRD profile, in Figure 1.21.

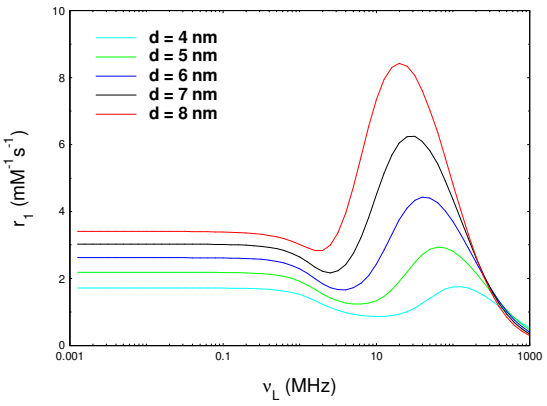

Figure 1.21. Simulated relaxivity curves showing the effect of increasing the particle diameter. The values of the diameter are shown in the legend; the remaining parameters are M_s = 40 emu/g, τ_N = 2 ns, ΔE_{anis} = 2 GHz, D_{H2O} = 4.02e-5 cm^2s^{-1}

The overall amplitude of the profiles is scaled by the saturation magnetisation (M_s), or the maximum magnetisation achieved in a magnetic field. Simulated r_1 profiles demonstrating the effect of increasing M_s are shown in Figure 1.22.

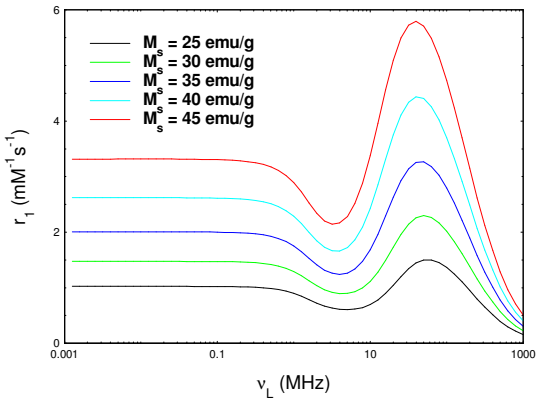

Figure 1.22. Simulated relaxivity curves showing the effect of increasing the saturation magnetisation. The values of the saturation magnetisation are shown in the legend; the remaining parameters are d = 6 nm, τ_N = 2 ns, ΔE_{anis} = 2 GHz, D_{H2O} = 4.02e-5cm^{2}s^{-1}

The characteristic time for fluctuation of the magnetisation of a particle with uniaxial anisotropy, the Néel correlation time (τ_N), is given by the Néel-Brown expression (Equation 1.26) where ΔE_{anis} is, k_B is the Boltzmann constant, and T is the temperature. The relaxation at low fields is primarily caused by such fluctuations of the particle moment. Simulations of the effect of τ_N are shown below in Figure 1.23.

$$\tau_N = \tau_0 \exp\left(\frac{\Delta E_{anis}}{k_B T}\right) \qquad \text{Equation 1.26}$$

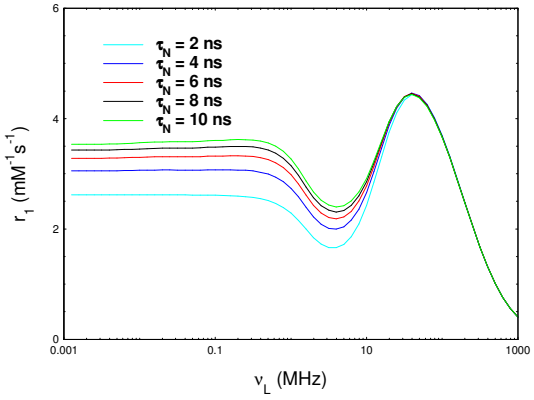

Figure 1.23. Simulated relaxivity curves showing the effect of increasing the Neel correlation time. The values of τ_N are shown in the legend; the remaining parameters are d = 6 nm, M_s = 40 emu/g, ΔE = 2 GHz, D_{H2O} = 4.02e-5cm^2s^{-1}

The position of the mid-frequency dip of the NMRD profile is determined by the anisotropy energy (ΔE), the amount of energy required to invert the particle spin orientation. The depth of the dip is influenced by both ΔE (Figure 1.24) and nanoparticle diameter (Figure 1.21). The anisotropy energy for a single-domain particle is proportional to its volume, and is therefore expected to increase with an increase in particle diameter.

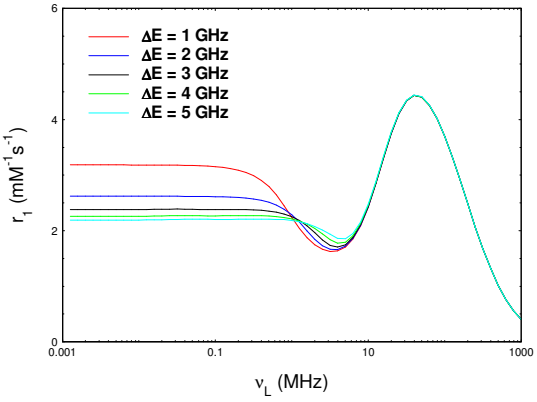

Figure 1.24. Simulated relaxivity curves showing the effect of increasing the anisotropy energy. The values of ΔE are shown in the legend; the remaining parameters are d = 6 nm, M_s = 40 emu/g, τ_N = 2 ns, D_{H2O} = 4.02e-5 cm^2s^{-1}

Because of the obvious influence of the magnetic parameters on the shape of the simulated profiles, application of SPM theory to experimental data can provide information on the saturation magnetisation, magnetic anisotropy energy, Néel correlation time, and the magnetic diameter of the suspended particles.

1.7 Synthesis of iron-oxide nanoparticles

Because the magnetic properties of iron-oxide nanoparticles are strongly dependent on their size, the ability to synthesise uniform particles of a controlled size is critical. Many methods are available for the preparation of magnetic iron-oxide nanoparticles including alkaline coprecipitation [80-84], laser pyrolysis [85], microemulsion methods [86-89], and organic phase high-temperature decomposition [90,91]. A full review of the synthetic methods is beyond the scope of this thesis, and the interested reader is directed to some recent and comprehensive reviews [92-95]. Instead, only the preparation methods relevant to the work presented in this thesis will be described in more detail.

1.7.1 Alkaline coprecipitation

One of the most widely used methods of preparing SPIO nanoparticles is the alkaline coprecipitation of Fe(II) and Fe(III) salts. The procedure involves the addition of ammonia to an aqueous solution of the iron salts, typically in a Fe^{2+}:Fe^{3+} molar ratio of 1:2. The overall reaction is shown in Equation 1.27 [92,93].

$$Fe^{2+} + 2Fe^{3+} + 8OH^- \rightarrow Fe_3O_4 + 4H_2O \qquad \text{Equation 1.27}$$

The reaction is often carried out at elevated temperatures in the range of 60-80°C [82]. A complete precipitation should occur within a pH range of 7.5-14 [96], and an oxygen-free environment is desired to prevent oxidation of the Fe^{2+} ion.

In the absence of any stabilisers during a coprecipitation synthesis, the uncoated magnetite nanoparticles in suspension are unstable with respect to agglomeration. Due to their large surface area-to-volume ratio, they tend to

aggregate, or cluster, in order to reduce their surface energy [82]. *In-situ* stabilisation by steric repulsion has proven to be an effective means of preventing particle aggregation during coprecipitation synthesis. Many types of stabilisers have been incorporated into the synthesis including fatty acids such as oleic acid [81] and lauric acid [84]; polymers such as poly(acrylic acid) [97], dextran [98], and polyvinyl alcohol [98]; and phospholipids [99].

The coprecipitation method is convenient and straightforward, and allows some control of the mean particle size through adjustment of the pH and the ionic strength of the precipitation medium [100]. Additionally, the average size of the particles produced by this method is fairly reproducible. The main disadvantage of the coprecipitation method, however, is that the particle size distribution is generally quite broad, and control of the distribution is limited [92].

1.7.2 Organic phase high-temperature decomposition

A well-known synthetic procedure for the synthesis of very small (below 10 nm) iron-oxide nanoparticles with a high level of monodispersity is the thermal decomposition of an iron precursor in organic solvent in the presence of alcohol and stabilising surfactants [77,90,91,101].

While the mechanism of particle formation resulting from the organic phase decomposition has yet to be fully understood, it is widely accepted that the formation of highly uniform iron-oxide nanocrystals takes place in two phases: nucleation and growth. A critical requirement for producing a narrow size distribution is the complete separation of these two phases [91,95]. There are two general strategies for separating nucleation and growth, known as homogeneous nucleation and heterogeneous nucleation.

The objective of homogenous nucleation is to generate a single nucleation event ("burst nucleation") followed by a slow, controlled growth phase. One type of homogeneous nucleation is known as the 'heating-up' process [102]. In this process, the precursor, solvent, and surfactants are mixed at room temperature, then heated to the reflux temperature of the solvent. During heating, the iron acetylacetonate decomposes to generate iron ions in the solution. When the ion

concentration exceeds the supersaturation limit, a single, homogeneous nucleation event, or "burst nucleation," is thought to occur, thus reducing the ion concentration and preventing secondary nucleations. Ostwald ripening takes place during the growth stage, focusing and narrowing the size distribution, and the final result is a monodisperse suspension of nanoparticles with nearly identical growth history and uniform physical and magnetic properties.

During heterogeneous nucleation, the nucleation is physically separated from the growth by utilising preformed nanocrystals to act as seeds (nuclei) for the subsequent growth of larger nanoparticles. The preformed nanocrystals are introduced into the reaction solution containing additional monomers; the concentration of the monomers is kept low to prevent additional homogeneous nucleation. Metal atoms are deposited onto the surface of the seed nanocrystals, thus resulting in the growth of larger nanoparticles.

1.8 Surface modification of superparamagnetic iron-oxide nanoparticles

The stabilisation of magnetic nanoparticles in physiological environment is critical for biomedical, applications. Stabilisation can be achieved by coating nanoparticle surfaces with ligands that increase the hydrophilic properties of the particles and facilitate the transfer into aqueous solutions. Several nanoparticle coating strategies have been proposed. One common strategy involves ligand exchange. For instance, Jun et al. [103] reported the development of a multifunctional ligand system for the exchange of hydrophobic surfactant ligands on Fe_3O_4 nanoparticle surfaces with 2,3-dimercaptosuccinic acid (DMSA), which formed carboxylic chelate bonds on the Fe_3O_4 surface, therefore providing a stable coating around the particles. The DMSA-coated Fe_3O_4 nanocrystals were shown to be stable in both water and PBS. Lee et al. [104] have presented an interfacial ligand exchange in which the oleate unit of the oleic acid molecules on Fe_2O_3 nanoparticle surfaces was replaced with the carboxylate unit of betaine·HCl, resulting in a more hydrophilic surface.

A more general method for the phase transfer and stabilsation of surfactant coated nanoparticles from organic into aqueous solutions was presented by Wang and co-workers [105]. The surface of oleic acid coated iron-oxide and silver

nanoparticles dispersed in hexane was modified by the formation of an inclusion complex between α-cyclodextrin (α-CD) and the surface-bound oleic acid molecules, allowing the transfer into aqueous solutions.

Several groups have utilised Pluronic F127 (PF127) for surface modification and phase transfer of oleic acid coated iron-oxide nanoparticles from organic to aqueous phase [106,107]. PF127, a triblock copolymer made from two A-chains of polyethylene oxide (PEO) and one B-chain of polypropylene oxide (PPO) in an ABA configuration, has been shown to surround surface-bound oleic acid molecules, forming a hierarchical surface structure [106]. The hydrophobic PPO chains are thought to interact with the hydrocarbon chains of the C18 surfactant coating on the iron-oxide particles, while the hydrophilic PEO chains extend away from the core to stabilise the particles in aqueous suspension.

A large number of techniques have been developed for the preparation of aqueous suspensions of polymer-stabilised magnetic nanoparticles [108-112]. Recently, Hatton et al. [113] developed an original multi-step, surface functionalisation procedure in which surface-bound oleic acid (OA) and oleylamine (OAm) surfactant molecules are first replaced with citric acid and 2-bromo-2-methylpropionic acid (CA/BMPA) ligands containing reactive hydroxyl groups through a ligand exchange reaction. The hydroxyl groups are then reacted with an acylating agent, 2-bromo-2-methylpropionyl bromide (BMPB), in the presence of triethylamine, forming ester bonds and transforming the hydroxyl groups into ester moieties containing a highly efficient initiator (α-haloester) for atom transfer radical polymerisation (ATRP) [113]. Finally, the initiator induces polymerization through the generation of radicals, and the sodium polystyrene sulfonate (PSSNa) polymer brush is grown from, or "grafted from," the NP surface. This strategy will be investigated further in Appendix B.

CHAPTER 2

Experimental Section

2.1 Introduction

The purpose of this chapter is to describe the main experimental techniques that are used frequently throughout this thesis. For each technique, when applicable, the relevant theory, governing equations, experimental conditions, and practical considerations will be described. Techniques that are only relevant to a single chapter, and all synthetic procedures will be described in the experimental sections of the appropriate chapters.

2.2 Fast Field-Cycling NMR (FFC NMR)

2.2.1 Principles of the technique

In contrast to conventional NMR, field-cycling NMR relaxometry involves the rapid switching of magnetic fields throughout the experiment in order to measure T_1 over a wide range (several orders of magnitude) of low magnetic field strengths. The interest in T_1 relaxation experiments lies in the fact that molecular motions drive the relaxation of the ^1H spin system back to its equilibrium state due to coupled magnetic interactions, be they dipolar $^1H - ^1H$ or paramagnetic $^1H - e^-$. A plot of the spin-lattice relaxation rate R_1 ($1/T_1$) as a function of magnetic field, and hence resonance frequency, is known as a Nuclear Magnetic Resonance Dispersion (NMRD) profile. The profile can provide detailed insight into the molecular dynamics that occur within a system in the form of spectral density functions. To achieve this, the profiles are analysed using theories for the spectral densities of the relevant motions.

There are two field-cycling sequences commonly employed to measure T_1. The first is used to measure T_1 below ~6 MHz, and is known as the prepolarised (PP) sequence, outlined in Figure 2.1. The ^1H magnetisation of the sample is first polarised in a high polarisation field (B_{POL}, typically 10 – 14 MHz), to induce a larger equilibrium magnetisation, for improved signal-to-noise ratio (S/N). The polarisation time (T_{POL}) should be longer than 4 times T_1, at B_{POL}, to ensure the magnetisation reaches saturation. The field is then very rapidly switched (in milliseconds) to a much lower value (B_{RLX}) where the relaxation process takes place for a variable time τ. The signal remaining after this variable relaxation

interval is detected in a third, homogenous intermediate field (B_{ACQ}, typically 9.25 MHz) [114,115] when its magnitude is measured through a $\pi/2$ rf pulse magnetisation which generates a free induction decay which is detected in the xy plane. Thermal equilibrium is then restored during a delay period, at zero field, of five times T_1 (known as the recycle delay, RD). This process is repeated as a function of τ to sample the magnetisation recovery at the given relaxation field. Commonly, the signal intensity is measured at 16 τ-values, ranging from 1 ms to approximately 5 x T_1. The value of T_1 is extracted by least squares fitting of the exponential decay function at each relaxation field (AcqNMR, v.2.1.0.60, Stelar; Mede, Italy). All the magnetic recovery curves of all the samples studied in this thesis were mono-exponential within experimental error. All fitting errors in T_1 were less than 1% for magnetic fluids, and in the range of 5 – 10% for liposome samples.

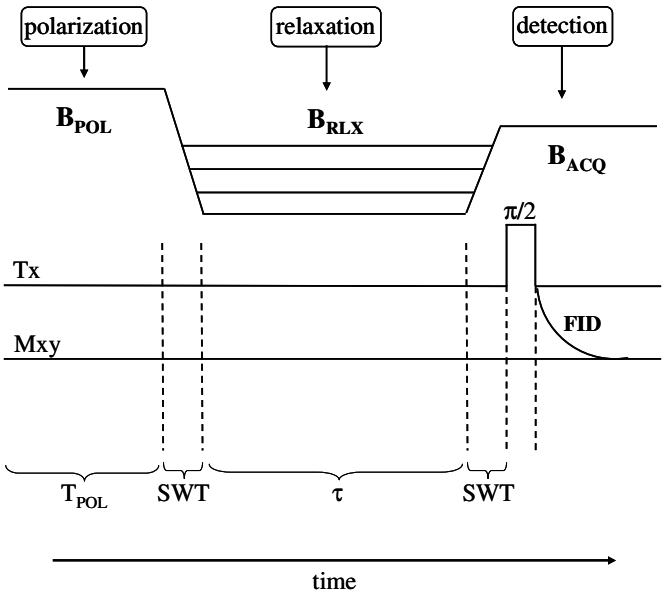

Figure 2.1. The basic pre-polarised (PP) FFC NMR pulse sequence. The switching time (SWT) is the time required by the field to switch between the different levels. Tx displays the transmitter output, and Mxy is the magnetisation in the xy plane. The multiple lines drawn for B_{RLX} represent various relaxation fields [114].

When the frequency of the relaxation field approaches that of the polarisation field (typically > 6 MHz), it is preferable to use the non-polarised (NP) sequence in which the magnetisation is allowed to grow from a value of zero. The details of the NP sequence are outlined in Figure 2.2. By using a $B_{POL} = 0$, i.e., no polarisation, this sequence maximises the field difference between B_{pol} and B_{rlx} [115], thus it maximises the difference in the sample magnetisation at short and long τ, and hence provides a more accurate value for T_1.

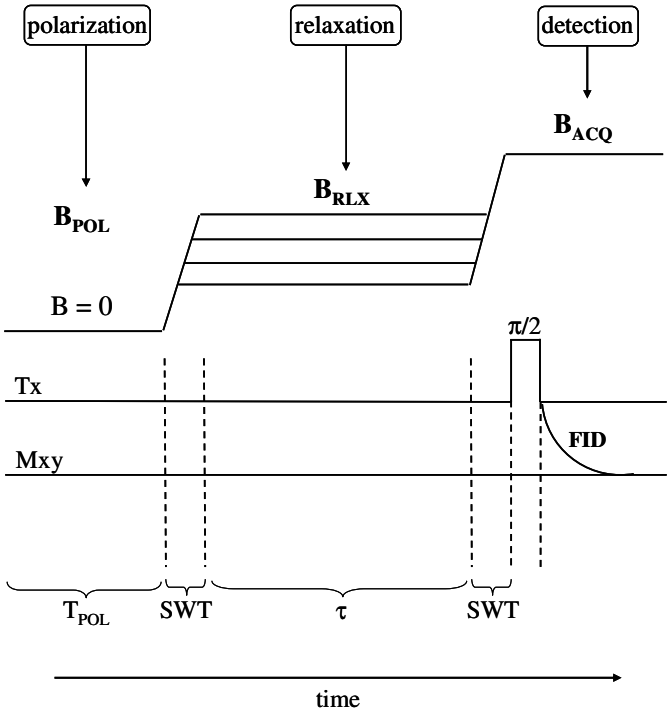

Figure 2.2. The basic non-polarised (NP) FFC NMR pulse sequence. T_{POL} is the polarisation time, and B_{POL} is the polarisation magnetic field. The relaxation field is represented by B_{RLX}, and B_{ACQ} is the detection field. The switching time (SWT) is the time required by the field to switch between the different levels. Tx displays the transmitter output, and Mxy is the magnetisation in the xy plane. The multiple lines drawn for B_{RLX} represent various relaxation fields [114].

2.2.2 Experimental conditions

All field-cycling relaxometry experiments were performed on a Spinmaster FFC-2000 Fast Field-Cycling NMR Relaxometer (Stelar; Mede, Italy) using a sample volume of 0.5 - 1 mL. The use of a Spinmaster Variable Temperature Controller

allowed sample temperatures to be controlled within about 0.1°C, and a minimum temperature equilibration time of 20 min preceded all measurements. Measurements were carried out at 25°C, unless noted otherwise within the relevant chapters.

Typical acquisition parameter ranges, optimised for each type of sample, are reported in Table 2.1.

Table 2.1. Typical FFC NMR acquisition parameter ranges utilised for the samples studied in this thesis.

B_{POL}	= 12 - 14 MHz
T_{POL}	= 0.3 - 0.5 s
B_{ACQ}	= 9.25 MHz
Slew rate	= 12 - 18 MHz/ms
Switching time	= 0.0015 - 0.003 s
TAU delay	= 0.001 s
Block size	= 256 – 512
Sweep width	= 1000000 Hz
FLTR	= 270000 – 930000 Hz
90° pulse duration	= 6 - 7 ms

2.2.3 Practical considerations

Practically, we must consider the boundaries of the frequency range. The highest measurable frequency on the Stelar is 20 MHz. At higher frequencies, the current through the magnet coil results in strong magnet heating that cannot be sufficiently dissipated by the cooling system. To measure T_1 at frequencies higher than 20 MHz, we used a reconditioned Bruker WP80 variable field magnet. This allows us the ability to measure T_1 from 35 – 75 MHz at ~ 5 MHz frequency intervals using an Aperiodic-Pulse-Sequence Saturation Recovery (APSR/S) pulse sequence.

2.3 Photon Correlation Spectroscopy

2.3.1 Theory

Photon Correlation Spectroscopy (PCS) is a light scattering technique which measures the Brownian motion of dispersed sub-micron sized particles and relates it to particle size [116]. A laser is used as a light source to illuminate a sample in a cuvette; some of the light is scattered by the particles within the fluid at various angles, and is measured by the detector. Due to the constant motion of the particles, the signal intensity of the scattered light fluctuates as a function of time. A digital auto correlator measures the signal intensities at successive time intervals in order to determine the time scale of the fluctuations [117]. Due to their slower diffusion, larger particles will cause the signal intensity to change more slowly than smaller, faster moving particles, and therefore the intensity correlation will extend over a longer period of time. Conversely, the correlation of the signal will reduce much more rapidly for smaller particles. Monodisperse particles in random, Brownian motion give rise to an exponential correlation function, G(t), of the form shown in Equation 2.1;

$$G(\tau) = G(0)\, e^{\frac{-|\tau|}{\tau_c}} \qquad \text{Equation 2.1}$$

where τ is the sample time of the correlator, and τ_c is a "correlation time," the time constant for decay of $G(\tau)$. The correlation time is defined as the mean time between diffusional steps; the inverse of the correlation time is the diffusional rate, τ_c^{-1}. Figure 2.3 presents a typical correlogram for a sample containing dispersed particles with an average hydrodynamic diameter of 100 nm.

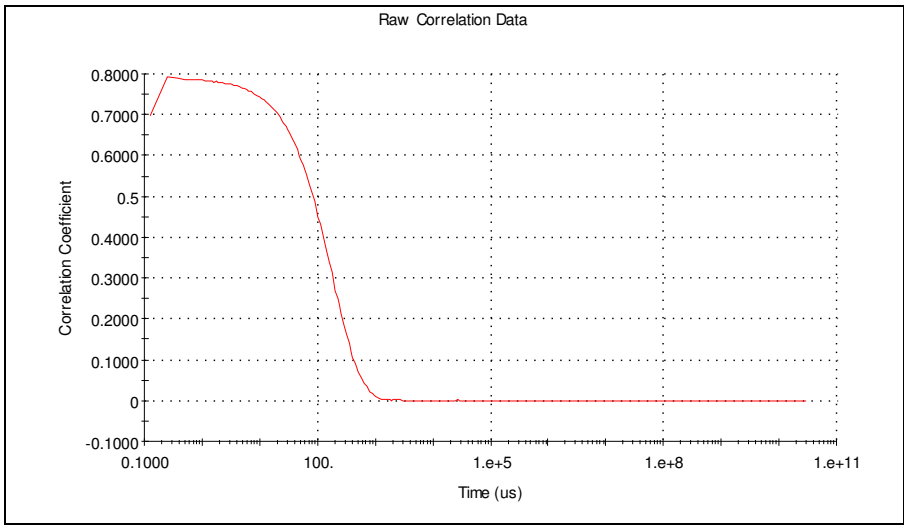

Figure 2.3. A sample correlogram for dispersed 100 nm particles.

This time dependence of scattered light intensity can be related to the particles' diffusion coefficient, D, using Equation 2.2, where k is the magnitude of the scattering vector, given by Equation 2.3.

$$D = \frac{1}{2\tau_c k^2} \qquad \text{Equation 2.2}$$

$$k = \frac{2\pi\eta}{\lambda} \sin\frac{\theta}{2} \qquad \text{Equation 2.3}$$

In the equation above, η is the refractive index of the solvent, λ is the wavelength of the incident light, and θ is the scattering angle. From D, the particles' hydrodynamic diameter, d(H), can be calculated using the Stokes-Einstein equation (Equation 2.4), where k_B is Boltzmann's constant and T is the absolute temperature. The term hydrodynamic diameter is used because it is not necessarily the true dimension of the particle; rather, the diameter obtained by this technique is the diameter of a sphere with the same diffusion coefficient as the particle plus any associated solvent layers [116].

$$d(H) = \frac{k_B T}{3\pi\eta D}$$ Equation 2.4

The correlation function of the light scattered by a polydisperse sample cannot be described by a single exponential function. There are several approaches to the analysis of polydisperse samples (Laplace inversion, etc.), but the most general approach [118], known as cumulants analysis, involves a fit of the experimental estimates of ln G(t) to a polynomial function of the form shown in Equation 2.5.

$$\frac{1}{2}\ln G(\tau) = a_0 + a_1\tau + a_2\tau^2 + a_3\tau^3 + ...$$ Equation 2.5

The Z-average (Z-Avg) diffusion coefficient is given by the value of a_1, and it can be converted to size by utilising the dispersant viscosity and instrumental constants [119]. A measure of the skewness and kurtosis of the distribution are provided by a_2 and a_3. [118]. The relative width of the size distribution, known as the polydispersity index (PDI), is defined as $2a_2/a_1^2$ [119]. PDI values range from 0 to 1 with values closer to zero being indicative of a more monodisperse suspension, and larger values being indicative of a broader particle size distribution. A PDI value of 1 corresponds to a polydisperse suspension which is often a multimodal distribution. In practice, we find reasonable distributions have a PDI value around 0.2 or below.

An alternative approach is to obtain the intensity size distributions from correlation function analysis using the Multiple Narrow Modes algorithm based upon a non-negative least squares fit [120,121] using commercially available software (Dispersion Technology Software, v. 4.10, Malvern Instruments; Worcestershire UK). A typical intensity distribution is shown in Figure 2.4. The intensity distribution is the fundamental size distribution made available by the Dispersion Technology software, but the results of the measurement can be converted to volume or number distributions.

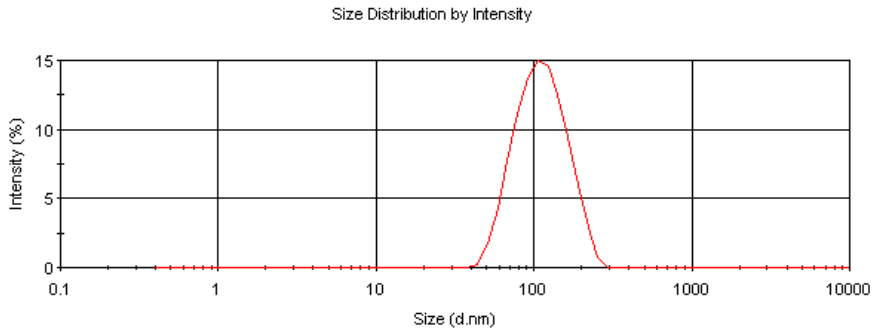

Figure 2.4. The size distribution by intensity plot for a liposome sample; Z-Avg = 99.1 nm, PDI = 0.152.

2.3.2 Analysis procedure

PCS measurements were carried out on a High Performance Particle Sizer, HPPS (Malvern Instruments; Worcestershire UK). Light from a 3mW He-Ne laser operating at a wavelength of 633 nm was focused onto the sample held in a 12.5 x 12.5 x 45 mm sizing cuvette. Aqueous samples were placed in plastic cuvettes, and all non-aqueous magnetic fluids were placed in quartz cuvettes. A thermal equilibration time of 5 – 10 minutes preceded all measurements. Sample temperature was maintained constant, at 25°C, throughout the measurement with the internal heating system of the instrument. The intensity of the scattered light was detected at 173° to the incident beam, known as backscatter detection. This optical configuration results in an 8-fold increase in the detected scattering volume when compared with classical 90° scattering detection, resulting in an 8-fold increase in the count rate observed at the detector [122]. The count rate is directly related to instrument sensitivity; thus, the use of 173° backscatter detection allows measurements of smaller particle sizes down to lower sample concentrations [122]. Figure 2.5 illustrates a simplified block diagram of the components involved in PCS measurements.

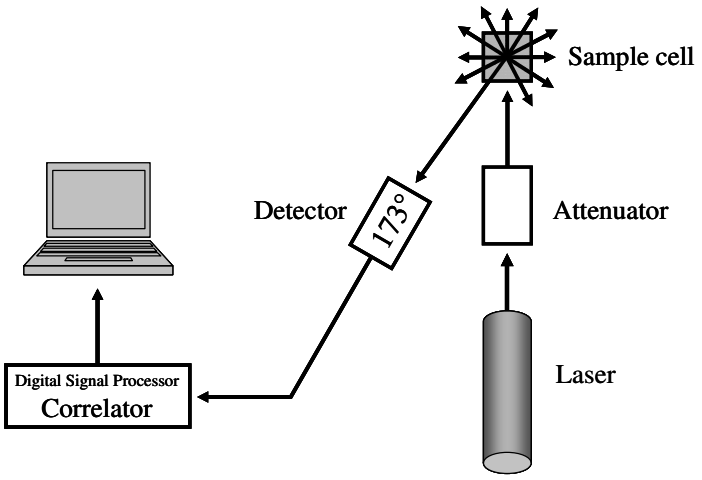

Figure 2.5. Diagram of the components of a PCS machine.

2.3.3 Practical considerations

Generally speaking, PCS is useful for measuring the diameter of particles ranging in size from a few nanometres to a few microns. In practice, however, accessing the lower end of this size range is dependent on the ability to detect scattering fluctuations over experimental noise such as environmental disturbances, electronic noise, and thermal fluctuations. The high end of the range is dependent on dispersion stability limit. The particles must remain stable throughout the measurement with no sedimentation. In practice, with standard instrumentation, the signal is usually only recorded for 1 x 10^{11} μs, which sets the upper limit for particle size.

The concentration of the samples should be low enough to avoid multiple scattering, which can produce systematic underestimation of particle size, but high enough to provide a sufficiently high number of particles for statistical significance, i.e., the total number of scatterers should not change as a function of time during the measurement. Additionally, samples should be free from foreign particles (such as dust), as their presence will dominate smaller, more weakly scattering particles of interest.

An accurate and stable temperature is crucial in PCS measurements. Convection currents in the sample can be caused by an unstable temperature, therefore

causing non-random motions and an incorrect interpretation of the particle size. A particle's surface structure can also affect its apparent hydrodynamic diameter. Any surface characteristic that reduces a particle's rate of diffusion can result in a larger apparent size. Similarly, any conformation or shape change in non-spherical particles that alters its diffusion speed will be detected by PCS, and the hydrodynamic diameter will be affected accordingly. Finally, at higher volume fractions, restricted diffusion can cause systematic errors, compounded in this case by multiple scattering.

Despite these limitations, PCS offers many benefits over other size-determination techniques. It is non-destructive and relatively economic. Additionally, with little or no sample preparation required, and typical measurement times of around 2-5 minutes, PCS is a rapid technique, and hence it has potential for monitoring changes in particle size. Minimal sample volumes are required, of the order of 0.75 - 1 mL. Dispersed particles can be studied by PCS in their actual fluid environment, which is not the case for other size-determination techniques, such as electron microscopy.

2.4 Attenuated Total Reflectance (ATR) – Infrared Spectroscopy

2.4.1 Principles of ATR

ATR is a non-destructive technique which measures the changes in an internally reflected infrared beam caused by contact with a sample. An infrared beam is directed onto an optically transparent internal reflectance element (the crystal, or IRE) of higher refractive index than that of the contacting sample at an angle exceeding the critical angle (θ_c) for internal reflection. Just beyond the IRE/sample interface, an electromagnetic field (E) is established in the sample, generating an evanescent wave, even under conditions of total reflection at the boundary with the sample. The evanescent wave has the same frequency as the incoming light, but decays exponentially with distance (z) from the crystal surface (Equation 2.6) [123,124]. This exponential decay of the field is depicted in Figure 2.6. The depth of penetration (d_p) of the evanescent wave can be defined as the distance into the sample required for the intensity of the wave to

decay to 1/e its initial value at the interface, and is given by Equation 2.7, where η_{IRE} and η_{sample} are the refractive index of the IRE and sample, respectively, θ is the angle of incidence, and λ is the wavelength of the incident radiation [125].

$$E = E_0 e^{\frac{-z}{d_p}} \qquad \text{Equation 2.6}$$

$$d_p = \frac{\lambda}{2\pi\eta_{IRE}\left(\sin^2\theta - \left(\frac{\eta_{sample}}{\eta_{IRE}}\right)^2\right)^{\frac{1}{2}}} \qquad \text{Equation 2.7}$$

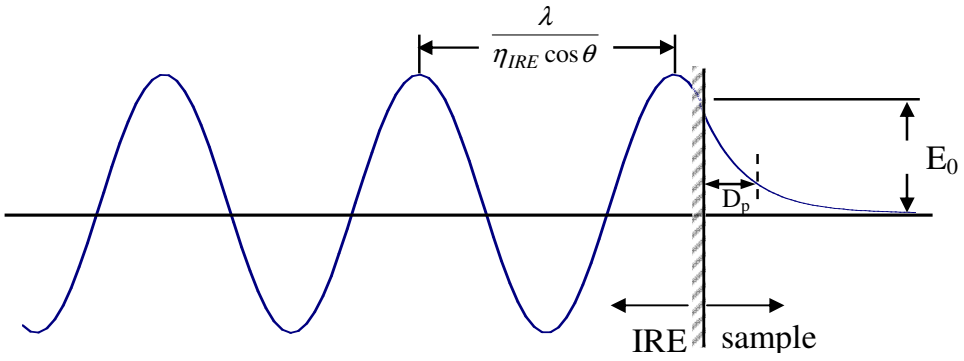

Figure 2.6. Exponentially decaying electromagnetic field of an evanescent wave at the sample/IRE interface.

The sample selectively absorbs the energy of the infrared beam, resulting in a loss of energy at the wavelength where the material absorbs, and a reflectivity less than unity. The attenuated reflected radiation is measured by the detector and plotted as a function of inverse wavelength giving rise to the sample spectrum.

2.4.2 Practical considerations

The ATR sampling accessory utilised in the work presented in this thesis was a Horizontal ATR (HATR) accessory with a horizontally oriented ZnSe IRE

(Figure 2.7). The sample is placed horizontally on top of the crystal allowing forced contact between the IRE and the sample. Thin films can be formed directly on the crystal by placing a liquid sample on the crystal and allowing the solvent to evaporate. A significant advantage of this solvent evaporation ATR technique over more conventional transmission methods is the elimination of strong, broad O-H vibrational bands typically present in spectra of aqueous samples. These bands often overlap a considerable portion of the spectral range and can mask weaker bands and hinder sample analysis.

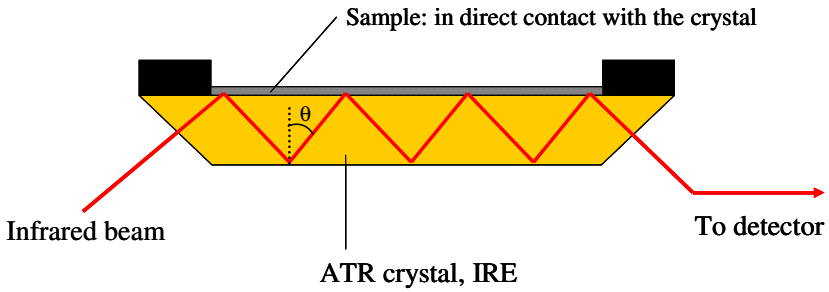

Figure 2.7. Schematic of a multiple reflection, horizontal ATR system.

ATR measurements can be carried out with small sample volumes. According to Equation 2.7, d_p decreases as θ increases; d_p also decreases with an increase in η_{IRE}. Optimising these conditions allows IR measurements of very thin layers, decreasing sample volume requirements.

For internal reflectance to occur, the refractive index of the crystal must be significantly greater than that of the sample; if this condition is not met, light will be transmitted. Typical refractive index values for ATR crystals range from 2.38 to 4.01 at 2000 cm^{-1}; the refractive index of ZnSe is 2.4 [126], which in most cases provides sufficient sample/IRE separation. ZnSe has a limited working pH range of 5 – 9, and it scratches easily, so care must be taken when cleaning. It has a very broad spectral range, however, with the useful range spanning 20,000 to 500 cm^{-1} [126].

2.4.2.1 ATR correction

One of the most significant differences between transmission and ATR measurements is the path of the infrared beam and its interaction with the sample. In transmission, the path length is only dependent on the thickness of the sample. In ATR measurements, however, the path length is dependent on d_p, which in turn is dependent on the wavelength of the radiation (Equation 2.7). Thus, the resultant ATR spectrum is wavelength dependent; absorbance bands are more intense at lower frequencies relative to those at higher frequencies. This is easily corrected by applying an ATR correction algorithm (usually incorporated in commercial FT-IR software packages) which scales the ATR absorbance values by a d_p function in order to compensate for the wavelength dependence.

2.5 Atomic Absorption Spectroscopy

2.5.1 Theory

Atomic Absorption Spectroscopy (AAS) is a technique routinely used for the detection and analysis of trace metals in a liquid sample. Metals include Fe, Cu, Al, Au, Rb, Pb, Ca, and Zn. The sample is aspirated, aerosolised, then introduced into a high temperature, high enthalpy flame with a temperature ranging from 2100 – 2800°C. The flame atomises the analyte and produces ground state atoms. The atoms absorb radiation at a characteristic wavelength from an external light source, a hollow cathode lamp, which stimulates a transition to an excited state energy level (E_j), allowing the quantitative measurement of the amount of absorbed radiation. [127,128]. The reduction of the light intensity, due to absorption by the analyte, is detected by a photomultiplier and can be related to the concentration of the element being analysed using the Beer-Lambert law.

In the work presented in this thesis, AAS was used to determine the amount of iron in magnetic fluids at the millimolar level. Spectra were recorded on a Varian SpectrAA Spectrometer fitted with a single slit burner. The light source was a Fe-cathode lamp with a wavelength of 248.3 nm. A single slit burner was used to increase the path length of the beam through the flame, and a high temperature air/acetylene flame was used, which can reach a maximum temperature of

2200°C. To prepare the samples for analysis, five drops of 6N analar grade HCl and 1 mL H_2O were added to small aliquots (approximately 0.3-0.5 mL) of the magnetic fluid. Suspensions containing phospholipid-coated nanoparticles were mixed with an equal volume of 5% (v/v) Triton X-100 solution to dissolve the lipid membrane. The solutions were heated to boiling, which was allowed to continue until the volume was reduced to a few drops. H_2O (25 mL) was then added and the solutions were again heated to boiling. The solutions were cooled to room temperature, then diluted appropriately into the 0.5 – 2.5 mg/L linear working range.

It was necessary to carry out a calibration with iron standards of known analyte concentration. An iron standard solution (0.5 M $Fe(NO_3)_3$ in HNO_3; Merck Chemicals, Darmstadt, Germany) was diluted to 0.5, 1.0, 1.5, 2.0, and 2.5 mM Fe. A calibration curve was generated, and a linear fit to the data was used to calculate the iron content of the samples. A typical calibration curve is presented in Figure 2.8. The R^2 value of 0.9995 is typical of those obtained using this technique, allowing an estimation of a lower limit for detection better than 1%.

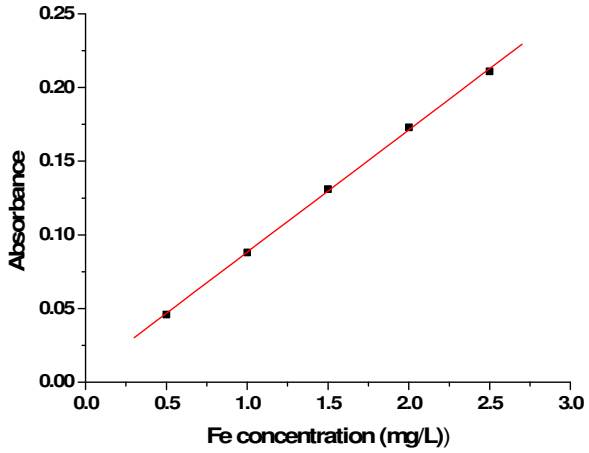

Figure 2.8. A typical AAS standard calibration curve for iron using standards of known Fe concentration on the range of 0.5 – 2.5 mg/L; — y = 0.083x + 0.0053, R^2 = 0.9995.

2.5.2 Practical considerations

Analyte levels in solution should be at least 10 times the detection limit (0.006 µg/mL for Fe [128]), and below the upper limit of the linear working range (5 mg / L for Fe [128]).

2.6 Transmission electron microscopy (TEM)

2.6.1 Theory

TEM is a versatile analytical technique used to investigate the structure of micro- and nano-materials. An energised beam of electrons, generated by an electron gun, is focused by electromagnetic condenser lenses and transmitted through a very thin sample specimen. The incident electrons can interact with the specimen during transmission; the electrons are deflected or scattered from their original path by direct collisions (less likely) or electrostatic interactions with the atomic nuclei or surrounding electrons of the specimen. The result is a transmitted, non-uniform distribution of electrons which contains information regarding the specimen structure and chemistry. The electrons are refocused by an objective lens and an image is formed when the transmitted electrons are magnified and projected on a fluorescent screen and/or digitally processed by a computer. A schematic diagram of the components of a typical transmission electron microscope is shown in Figure 2.9.

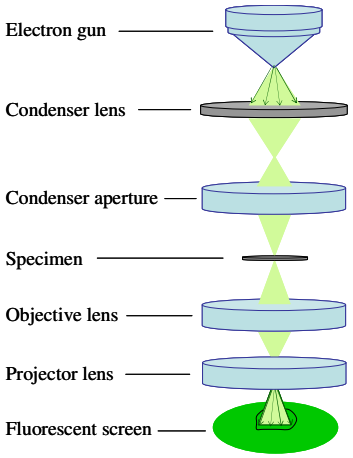

Figure 2.9. Schematic of a transmission electron microscope.

All the information obtained about a specimen from TEM analysis is a result of some form of electron scattering [129]. If an electron that passes through a solid specimen is scattered only once, the process is known as single scattering. If it is scattered more than once, it is known as plural scattering. Multiple scattering is the term used for an electron that is scattered > 20 times. A higher number of scattering events complicates the interpretation of images and diffraction patterns. In general, the number of backscattered electrons increases as the thickness of the sample increases [129], hence the importance of preparing thin specimens for TEM analysis. Scattering events within the specimen can be elastic, in which there is no loss of energy of the incident beam of electrons, or inelastic, in which there is a transfer of energy from the electron beam to the electrons of the specimen atoms. Scattered electrons are most likely scattered in the forward direction, i.e., parallel to the direction of the incident beam. It is these forward scattered electrons which generate the images in TEM.

The resolution of an image is typically limited by contrast as opposed to the resolving power of the microscope [130]. The main source of contrast in an electron image is the loss of amplitude from the electron beam due to elastic scattering, known as amplitude contrast. In general, amplitude contrast varies as a function of sample thickness as well as the atomic number of the specimen. Heavy elements with high atomic numbers and high electron densities result in the highest degree of scattering. Thus, the intensity distribution of electrons that reaches the fluorescent screen is lower from such regions [131]. The converse is true for atoms with lower atomic numbers, such as iron, which generally generate low contrast images.

2.6.2 Practical considerations

Specimens for imaging must be very thin to allow the transmission of high-energy electrons. Typical sample thickness is < 100 nm when possible, but in general, this requirement is a function of both electron energy and atomic number of the specimen. If the dimensions of a specimen are so small that the sample is essentially ‘electron transparent’, then a dilute dispersion of the sample can be deposited on support grids and the solvent can be evaporated through open air drying. The disadvantage of this technique, however, is the potential for

introducing artefacts during the drying process. Additional considerations are required when imaging objects only a few nanometres in size. For example, it is necessary to increase the magnification, but this limits the field of view, thus limiting the number of objects or structures that can be analysed in each image.

2.6.3 Analysis procedure

All transmission electron microscopy (TEM) images were obtained using a JEOL 2000 FX TEMscan instrument (at an accelerating voltage of 80 kV), courtesy of the Electron Microscopy Laboratory at the University College Dublin Conway Institute of Biomolecular and Biomedical Research, Belfield. Samples were prepared for microscopy by placing a drop of each dilute heptane suspension onto carbon-coated (400 mesh) copper grids and allowing the solvent to evaporate prior to imaging.

CHAPTER 3

Non-aqueous magnetic nanoparticle suspensions with controlled particle size and nuclear magnetic resonance properties

3.1 Introduction

Magnetic nanoparticles are an important component of a wide range of functional materials due to their unique size-dependent optical, electronic, and magnetic properties which differ from those of their bulk counterparts. Stable suspension of magnetic iron-oxide nanoparticles have important biomedical applications; for instance as contrast agents for MRI [103,132,133], as hyperthermia mediators for cancer ablation [66,134], and as drug delivery vehicles [35,135]. Control of the nanoparticle size, and of the emergent size-dependent magnetic properties [136-138], is critical to the performance of magnetic materials and is also of fundamental scientific interest.

Because the magnetic properties of iron-oxide nanoparticles are strongly dependent on their size, the ability to synthesise uniform particles of a controlled size is critical. Many strategies have been developed to prepare iron oxide nanoparticles, including aqueous coprecipitation [81,82], microemulsion methods [87,139], and laser pyrolysis [140], however the crystallinity and uniformity of the particles produced using these methods are currently quite poor. A commonly used synthetic procedure for producing very small (sub 10 nm) nanoparticles is the thermal decomposition of an iron precursor in organic solvent in the presence of alcohol and stabilising surfactants. Biomedical applications require nanoparticle stability in physiological media, and several methods currently exist for the phase transfer and stabilisation of hydrophobic iron-oxide cores into water [106,113]. There have been significant recent advances [141,142] which suggest that for the preparation of stable aqueous magnetic fluids, synthesis via the organic route and subsequent phase transfer may be preferred over more direct aqueous coprecipitation methods due to the greater control of nanoparticle size and dispersity which it offers. However, the phase transfer of hydrophobic nanocrystals has proven to be non-trivial; the transfer process can often lead to the formation of aggregates, compromising the benefits of non-aqueous synthesis. Thus, characterisation of the magnetic properties of well dispersed single particles in organic solvents prior to phase transfer can be extremely advantageous.

In the work reported here we have utilised methods published by Sun et al. [90,101] to prepare monodisperse magnetic iron-oxide nanoparticles, but we have modified the standard procedure by varying the mole ratio of C18 surfactants to Fe precursor. The effect of changing the synthetic conditions on the particle size of the stable maghemite suspensions in heptane was investigated using the complementary techniques of PCS and TEM. These studies demonstrate excellent control of particle size, dispersity and dispersability down into an unusually low size range. The magnetic resonance properties were assessed using, for the first time, NMRD of the heptane suspensions. This has established the validity of SPM theory for non-aqueous suspensions, it has allowed us to confirm that our method also provides good control of the magnetic properties, and for the first time we have observed, by NMR, the influence of reduced surface area on the magnetic properties of the suspended nanoparticles, at the lower end of the size range.

3.2 Experimental

3.2.1 Synthesis

The appropriate amount of oleic acid (≥99.0%, Fluka Chemicals) and oleylamine (≥70.0% GC, Fluka) (Table 3.1) were weighed into a 100 mL 3-neck round-bottomed flask. Iron (III) acetylacetonate (2 mmol; 99.9%, Aldrich) and 1,2-hexadecanediol (10 mmol; Technical grade 90%, Aldrich) were weighed into a weigh boat, then transferred to the round-bottomed flask. Diphenyl ether (20 mL; 99%, Aldrich) was added, and the system was degassed by purging nitrogen through the flask for 15 minutes prior to the start of the reaction. A 3-neck flask was required to simultaneously attach to the system a nitrogen flow, a water-cooled condenser, and a high-temperature (350°C) thermometer. The reaction was started by turning on the heating mantle to its highest setting and the N_2 flow was reduced. In all cases, the reaction reached its reflux temperature (~268°C) in 15 minutes, and was then allowed to reflux for an additional 15 minutes. The entire reaction was carried out in the absence of stirring.

Table 3.1. The amounts and ratios of C18 surfactant and Fe precursor used for the entire series of preparations. Note that the total C18 surfactant used = oleic acid + oleylamine.

Total surfactant/Fe precursor molar ratio	Fe source used (mmol)	Oleic acid (mmol)	Oleylamine (mmol)
3	2	3	3
6	2	6	6
9	2	9	9
12	2	12	12
15	2	15	15

During the reflux, a colour change from red to black was observed, which suggests the formation of iron-oxide nanoparticles. The reaction was quite vigorous and the suspension would occasionally 'bump' strongly, sometimes dislodging the thermometer from the flask. Precautions were taken to prevent the thermometer from breaking by padding the area surrounding the heating mantle.

Following the reflux, the suspension was allowed to cool naturally to room temperature. Ethanol (50 mL) was added to the flask to precipitate the iron-oxide, and the flask was placed over a bar magnet to isolate the nanoparticles. This was a slow process and required the flask to remain over the magnet overnight. The solvent was decanted from the iron-oxide and the nanoparticles were suspended in 15 mL heptane in the absence of additional surfactants (in contrast to the method described by Sun and Zeng). Following one additional reprecipitation with ethanol which was carried out overnight, the magnetic nanoparticles were suspended in 15 mL heptane to produce the final magnetic suspension which appeared dark brown in colour.

The magnetic fluids were centrifuged for 35 minutes at 13,000 rpm using a tabletop Eppendorf Centrifuge 5415 D in order to sediment and remove any larger or aggregated particles. The dark brown supernatant was collected and utilised for all characterisation.

3.2.2 Characterisation

The ferrofluids were characterised by PCS and NMRD as described in Chapter 2.

Transverse relaxation time (T_2) measurements were carried out at 9.25 MHz on a Spinmaster FFC-2000 Fast Field Cycling NMR Relaxometer (Stelar; Mede, Italy), and at 40 MHz on a reconditioned Bruker WP80 variable field magnet. The Carr-Purcell-Meiboom-Gill (CPMG) pulse sequence was used in all cases with 512 echoes and an echo delay of 50 μs. The sample temperature was 25°C; temperature control within ~0.1°C was ensured using the Spinmaster Variable Temperature Controller.

All transmission electron microscopy (TEM) images were obtained using a JEOL 2000 FX TEMscan instrument (at an accelerating voltage of 80 kV), courtesy of courtesy of the Electron Microscopy Laboratory at the University College Dublin Conway Institute of Biomolecular and Biomedical Research, Belfield. Samples were prepared for microscopy by placing a drop of each dilute heptane suspension onto carbon-coated (400 mesh) copper grids and allowing the solvent to evaporate prior to imaging.

Total iron content was determined by AAS as described in Chapter 2.

The amount of ferrous iron present in the samples was determined through colourimetric techniques. Concentrated HCl (5 drops), 1 mL deionised water, and 2.5 mL 1,10-phenanthroline was added to a small aliquot (0.3-0.5 mL) of the iron-oxide suspension. Phenanthroline forms an orange complex with Fe(II) within a pH range of 2 – 9 [143], and prevents oxidation to Fe(III) during the dissolution procedure [144]. The mixture was heated on a hot plate until only 1 drop of liquid remained, at which time 25 mL deionised water was added. The solution was heated to boiling, then immediately removed from heat and allowed to cool to room temperature. The volume was adjusted to 100 mL, and the pH was adjusted from 1 to ~7.0 with dilute NH_3 solution; a pink-orange colour appeared as the pH was increased. A set of six standards with known ferrous iron

concentrations in the range of 0.003 – 0.084 mM were prepared, and digested using the procedure described above to ensure that no oxidation from Fe^{2+} to Fe^{3+} took place during the process. Experiments were also conducted to ensure that phenanthroline could withstand high temperature and low pH conditions, though it is reported in the literature that it remains highly stable under these conditions [143]. UV-Vis analysis of Fe(II)-o-phenanthroline complexes of the six standard solutions as well as all sample solutions was carried out at room temperature on a Cary 50 Scan UV-Vis Spectrophotometer (Varian, Inc., CA, USA) at a wavelength of 496 nm. A standard calibration curve was generated by plotting the absorbance values of the standard solutions as a function of ferrous iron concentration in mM. The calibration curve was linear in the 0.003 – 0.084 mM concentration range. A straight line fit to the data (R^2 = 0.9978) was generated and used to determine the Fe^{2+} concentration of the sample solutions.

3.3 Results

3.3.1 Redox distribution of iron in iron-oxide nanoparticles

Visually, the heptane suspensions appeared red-brown in colour, which is characteristic of dispersed maghemite particles [145]. UV-Vis spectrophotometric analysis of the Fe^{2+} -phenanthroline complexes confirmed this observation, as no significant amount of Fe^{2+} was detected in any of the magnetic fluids. The distribution of ferrous and ferric iron in the preparation series is reported in Table 3.2. The results indicate the absence of Fe_3O_4. It should be noted that although it is not possible to discriminate between maghemite and hematite (α-Fe_2O_3) using wet chemistry methods, based on a review of published literature, we have assumed that there are only two types of iron-oxide present in nanoparticles synthesised through our thermal decomposition method, magnetite (Fe_3O_4: $2Fe^{III}Fe^{II}$) and maghemite (Fe_2O_3: $2Fe^{III}$). Thus we can assume maghemite (γ-Fe_2O_3) is the predominant crystalline phase in all samples. This is confirmed by the magnetic character of the suspensions, described below.

Table 3.2. Redox distribution of iron in a series of iron-oxide nanoparticle preparations synthesised by the high temperature decomposition method with varied C18/Fe precursor mole ratios.

Molar ratio	Prep	Total [Fe] (mM)	[Fe^{2+}] (mM)	[Fe^{3+}] (mM)	% Fe^{3+} of total Fe
3	1	98.20	3.67	94.53	**96.3**
6	4	89.07	3.91	85.16	**95.6**
9	1	75.37	2.15	73.22	**97.2**
9	2	73.08	5.07	68.01	**93.1**
12	1	109.6	4.53	105.1	**95.9**
15	1	40.20	1.20	38.99	**97.0**
15	2	35.17	1.56	33.61	**95.6**

3.3.2 Particle size as determined by transmission electron microscopy

Transmission electron microscopic images for representative samples of C18-stabilised maghemite nanoparticles with C18/Fe precursor mole ratios of 3, 6, 9,

12, and 15 are shown in Figures 3.1(a), 3.2(a), 3.3(a), 3.4(a), and 3.5(a), respectively. The micrographs show rather spherical, monodisperse, and well-formed primary nanoparticles with no evidence of agglomerates. No differences in particle morphology were apparent in any of the samples at the magnification used (300 k).

A statistical sample of the particle sizes was obtained by direct measurement of the diameters of more than 190 particles in all cases. From these measurements, particle size distribution histograms were prepared for all samples which are shown in Figures 3.1(b) – 3.5(b). The distributions were fitted successfully to a log-normal size distribution; this approach is widely adopted as a Gaussian distribution would permit negative values [82,146,147]. The mean particle size and standard deviations were derived from the log-normal distribution function shown in Equation 3.1 [82,147,148]:

$$P(x) = \frac{1}{\sqrt{2\pi}\sigma x} e^{\frac{-(\ln x - \mu)^2}{2\sigma^2}} \quad (x > 0) \qquad \text{Equation 3.1}$$

P(x) is the probability density of the distribution, x = D/D_p is the reduced diameter, D_p is the median diameter, D is the particle diameter, and μ and σ are the mean and standard deviation of ln x, respectively. Once values for μ and σ were obtained, the mean particle diameter and standard deviation were calculated using Equations 3.2 and 3.3, respectively:

$$D_{TEM} = D_p\left(e^{\mu+\sigma^2/2}\right) \qquad \text{Equation 3.2}$$

$$\sigma_{TEM} = D_p\sqrt{(e^{\sigma^2}-1)e^{2\mu+\sigma^2}} \qquad \text{Equation 3.3}$$

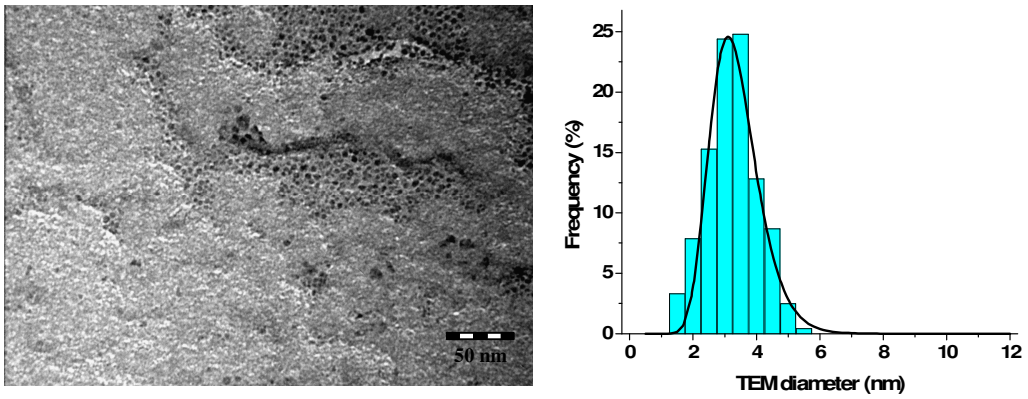

Figure 3.1. (a) TEM image of monodisperse maghemite nanoparticles with a C18/Fe precursor mole ratio of 3. (b) Particle size distribution histogram and lognormal distribution.

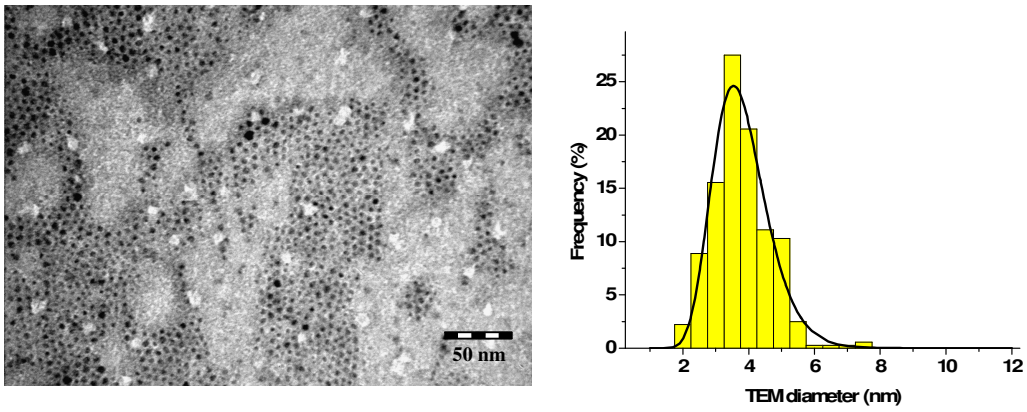

Figure 3.2. (a) TEM image of monodisperse maghemite nanoparticles with a C18/Fe precursor mole ratio of 6. (b) Particle size distribution histogram and lognormal distribution.

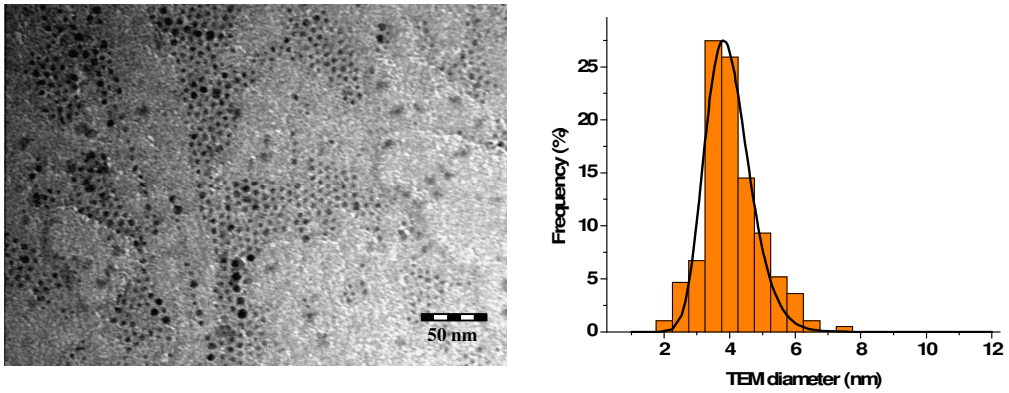

Figure 3.3. (a) TEM image of monodisperse maghemite nanoparticles with a C18/Fe precursor mole ratio of 9. (b) Particle size distribution histogram and lognormal distribution.

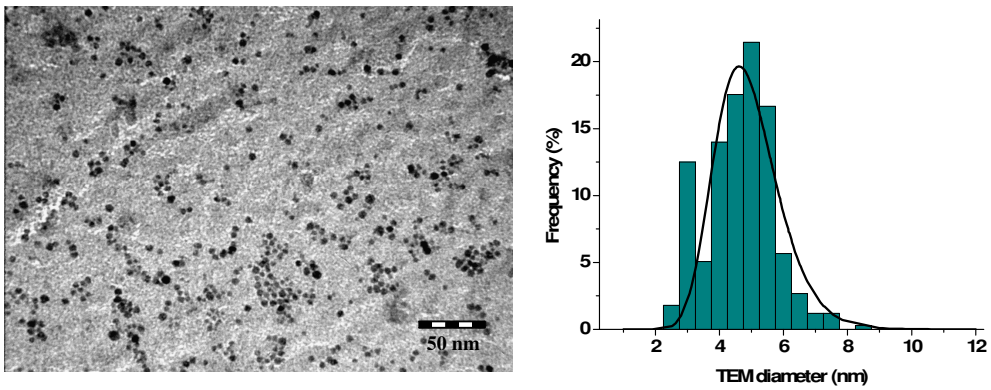

Figure 3.4. (a) TEM image of monodisperse maghemite nanoparticles with a C18/Fe precursor mole ratio of 12. (b) Particle size distribution histogram and lognormal distribution.

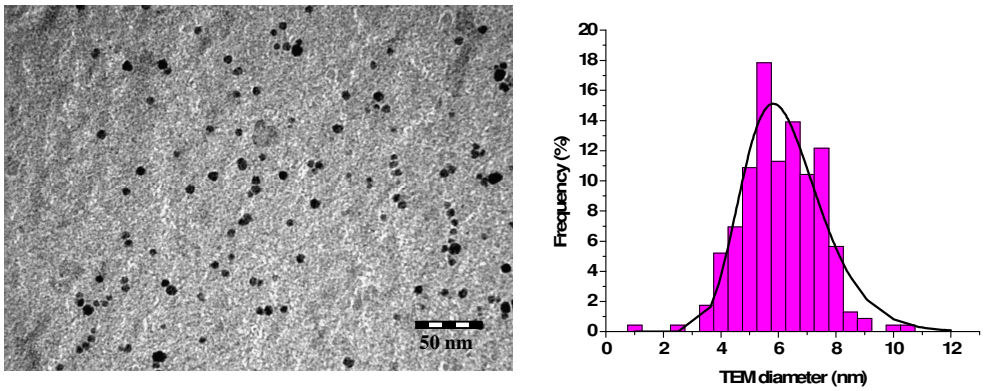

Figure 3.5. (a) TEM image of monodisperse maghemite nanoparticles with a C18/Fe precursor mole ratio of 15. (b) Particle size distribution histogram and lognormal distribution.

A comparison of the TEM particle size distribution as a function of C18/Fe precursor mole ratio is shown in Figure 3.6. Shown in this way, it is clear that the mean TEM diameter increases as the C18/Fe precursor increases. The TEM diameter and corresponding standard deviation derived from Equations 3.1 – 3.3 for each preparation in the series is reported in Table 3.3. A linear increase in the TEM diameter (D_{TEM}) with mole ratio was observed with $R^2 = 0.897$ (Figure 3.9). The width of the size distributions are comparable to those to those previously reported using thermal decomposition approach for producing iron-oxide nanoparticles. For instance, Roig and coworkers [77] report $D_{TEM} = 4.9 \pm 0.7$ nm. Our approach allows control, using a single technique, over a broad particle size range and down to smaller size than has previously been reported [149,150].

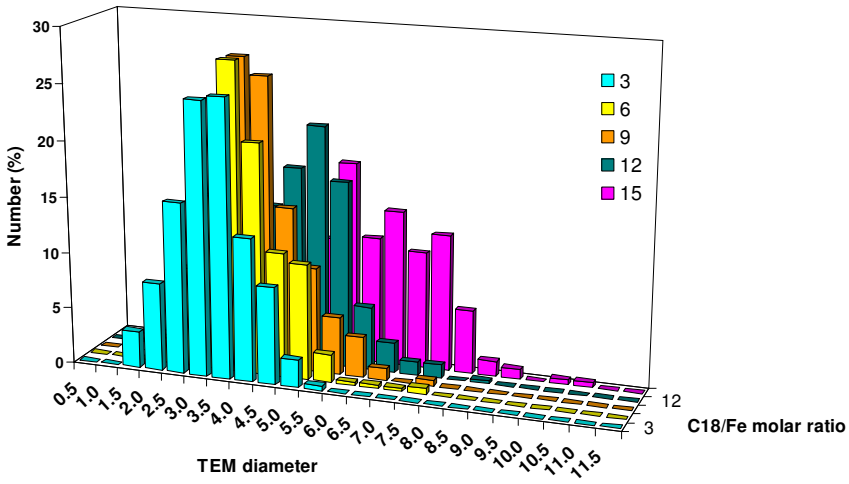

Figure 3.6. TEM particle size distribution as a function of C18/Fe precursor mole ratio.

Table 3.3. The average TEM diameter and standard deviation of oleate-coated maghemite nanoparticles with increasing surfactant concentration.

C18/Fe ratio	No. of particles counted	D_{TEM}, nm (σ_{TEM})
3	242	3.4 (0.8)
6	360	3.8 (0.9)
9	193	4.0 (0.7)
12	336	4.9 (1.0)
15	230	6.3 (1.4)

3.3.3 Particle size as determined by photon correlation spectroscopy

The results of PCS measurements carried out on the entire series of preparations are shown below in Table 3.4. These findings were reproducible, within error, at all mole ratios. All of the suspensions were relatively monodisperse; the analysis indicated the presence of unimodal size distributions and low PDI values (< 0.190 in all cases, and usually < 0.125). The suspensions obtained were stable, by PCS, for periods of months.

Table 3.4. The average hydrodynamic diameter and polydispersity index, at 25°C, of all C18-coated iron-oxide nanoparticle preparations in the series.

C18/Fe ratio	Z-Avg, nm (std dev)	PDI	Peak 1 intensity (nm)	Peak 2 intensity (nm)
3	7.4 (0.2)	0.105	100	0
6	7.7 (0.2)	0.102	100	0
9	8.9 (0.2)	0.187	98.1	1.9
12	9.0 (0.3)	0.108	100	0
15	10.4 (0.3)	0.123	100	0

An increase in hydrodynamic diameter (D_{PCS}) was observed with increasing C18/Fe precursor mole ratio, and the increase was once again linear over the range studied, with $R^2 = 0.94$ (Figure 3.9). The slope obtained was the same as was obtained for the TEM data, but the PCS intercept was 4.3 nm higher.

3.3.4 Nuclear magnetic resonance relaxometry

All the magnetic recovery curves recorded were mono-exponential, within experimental error. All fitting errors in T_1 were less than 1%. The relaxivity profiles of representative samples of each mole ratio in the series are shown in Figure 3.7. The appearance of the profiles is broadly as expected for suspensions of superparamagnetic iron-oxide. A high field r_1 maximum is observed in the frequency range of 10-80 MHz for mole ratios 6-15, but not for the mole ratio of 3. For this suspension the maximum presumably lies above our highest measurable frequency, 80 MHz. Clear systematic changes in the profile were observed for the suspension prepared with different mole ratios, the implications of which are discussed in the discussion section of this chapter.

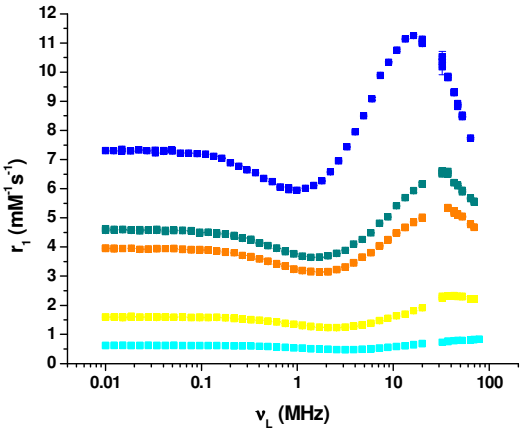

Figure 3.7. Relaxivity profiles, measured at 25°C, of heptane suspensions of C18-stabilised maghemite nanoparticles synthesised with a C18/Fe precursor mole ratio of ■ 3, ■ 6, ■ 9, ■ 12, and ■ 15.

The relaxivity profiles are consistent with SPM theory, developed by Muller and co-workers [151] (described in Chapter 1), which predicts the presence of an r_1 maximum at high frequency. The position of the r_1 maximum is sensitive to primary particle size; a higher frequency maximum indicates a smaller primary particle size, and a lower frequency maximum indicates a larger primary particle size.

Figure 3.7 shows a clear shift in the r_1 maximum to lower frequencies with an increase in C18/Fe mole ratio, consistent with an increase in the diameter of the primary particle. These results are consistent with the PCS and TEM results which also show an increase in particle size with an increase in the mole ratio. Application of SPM theory, to be discussed in greater detail in the discussion section, permitted estimation of the NMR diameter (D_{NMR}) from the NMRD analysis. The results are reported in Table 3.5. An increase in D_{NMR} was observed with increasing C18/Fe precursor mole ratio, and the increase was once again linear over the range studied, with $R^2 = 0.977$.

Table 3.5. The average NMR diameters of oleate-coated iron-oxide nanoparticles synthesised with increasing surfactant concentration.

Molar Ratio	D_{NMR}, nm
3	4.8
6	5.8
9	6.3
12	6.9
15	8.1

Relaxivity measurements were performed for repeat syntheses with C18/Fe mole ratios of 6 and 9, and the results are shown in Figure 3.8 (a) and (b). The preparation to preparation reproducibility of the profiles was good, and was certainly greater than the difference, measured for the different mole ratios used. For instance, at 0.01 MHz, the variation in r_1 was always less than 7%. The difference in the PCS parameters for these repeat preparations was even better, ranging from 3.5 – 6.5%. The stability of the suspensions was tested by repeating the relaxation time measurements after ageing the samples for at least 30 days. No significant change in the relaxivity profiles was observed. The relaxation rates increased somewhat, due to the loss of heptane over time, but it was always possible to overlay the R_1 NMRD profile of the original sample with that recorded for the aged sample scaled down by a factor corresponding to the increase in the iron concentration over time.

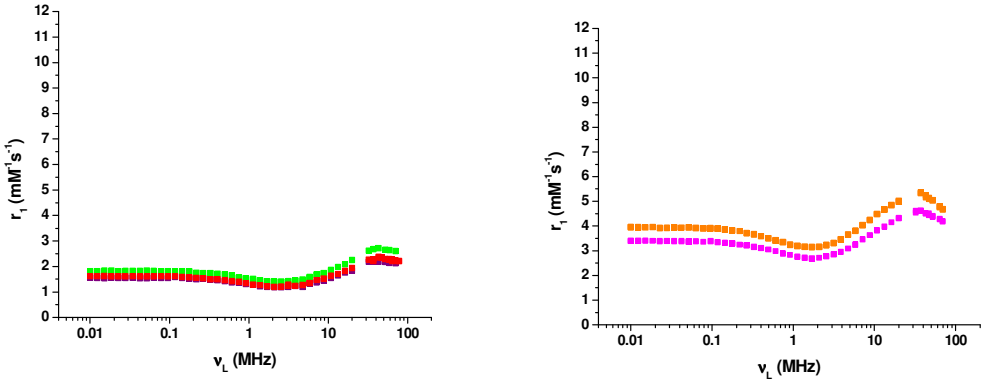

Figure 3.8. Relaxivity profiles, measured at 25°C, for repeat preparations of oleate-stabilised maghemite nanoparticles suspended in heptane with a C18/Fe precursor mole ratio of (a) 6: ■ prep 1, ■ prep 2, ■ prep 4; and (b) 9: ■ prep 1, ■ prep 2. For comparison, the profiles are shown on the same scale as used in Figure 3.7.

3.3.5 Relaxivity ratios

The individual r_1 and r_2 relaxivities measured at 9.25 and 37 MHz, as well as the corresponding r_2/r_1 ratios, measured for the entire series of preparations are reported in Table 3.6. In almost all cases, r_2/r_1 ratios measured for the maghemite suspensions ranged between 1 and 2. The ratios were found to increase with an increase in the mole ratio, corresponding to an increase in r_2/r_1 as a function of the nanoparticle core size.

Table 3.6. The measured r_2/r_1 ratios at 25°C for the series of maghemite suspensions; in all cases, the fitting errors in T_1 and T_2 were less than 2%, and in most cases, less than 1%.

C18/Fe ratio	9.25 MHz			37 MHz		
	r_1 ($mM^{-1}s^{-1}$)	r_2 ($mM^{-1}s^{-1}$)	r_2/r_1	r_1 ($mM^{-1}s^{-1}$)	r_2 ($mM^{-1}s^{-1}$)	r_2/r_1
3	0.54	0.66	**1.23**	0.78	1.22	**1.56**
6	1.56	2.04	**1.24**	2.17	3.65	**1.69**
9	4.33	5.81	**1.34**	5.23	10.19	**1.95**
12	5.18	6.88	**1.33**	6.41	11.77	**1.84**
15	10.55	19.99	**1.90**	9.62	30.43	**3.16**

3.4 Discussion

3.4.1 Particle size

Considering the PCS and TEM results firstly; both techniques demonstrate a straight line dependence of average particle size on mole ratio, with the same slope of 0.248, Figure 3.9. Unconstrained fits to the size data obtained from each technique produce the same value. That is, a difference in slope which is less than the standard errors on the slopes when either data set is fitted individually.

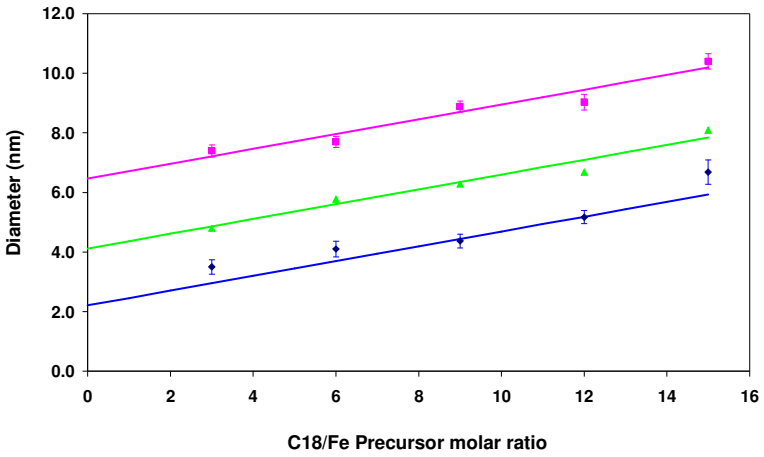

Figure 3.9. Relationship between the nanoparticle size (as measured with different techniques) and the C18/Fe precursor mole ratio. The solid lines are straight line fits, with fixed slope = 0.248, through the: D_{PCS} data (■), intercept = 6.47 nm; D_{NMR} data (▲), intercept = 4.12 nm; D_{TEM} data (♦), intercept = 2.21 nm.

PCS indicates an average hydrodynamic size ~4.3 nm greater than the core size for all the suspensions. Larger values are expected from PCS measurements which yield "hydrodynamic" information (Figure 3.10). The alkyl capping molecules are expected to coat the γ-Fe_2O_3 particles with the non-polar C18 chains extending away from the cores providing efficient steric stabilisation. As D_{PCS} is a measure of the hydrodynamic size, its value will reflect the presence of the C18 coating as well as any solvent molecules bound to the tumbling particle. The C18 coating on each nanoparticle is expected to add ~3.6 nm to the particle diameter, assuming that one monolayer of approximately 1.8 nm [152] is present. The larger values suggest the retention of significant numbers of solvent molecules, on relatively long time-scales compared to particle diffusion. We have confirmed that this effect is a factor for our suspensions by performing PCS measurements at elevated temperature, where some of the solvent shell is apparently lost. A suspension from a preparation with mole ratio 9 was found to have D_{PCS} = 8.95 nm at 298 K, this decreased to 8.40 nm, on increasing the temperature to 313 K.

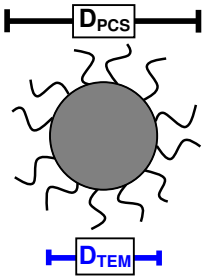

Figure 3.10. Schematic representation of the suspended particles; the illustrated D_{PCS} is the minimum hydrodynamic size, i.e. associated solvent shells are omitted.

PCS/TEM size discrepancies could also arise because larger particles scatter light more strongly than smaller particles, so the upper end of the PCS size distribution might contribute more strongly to the scattering, resulting in a systematically high measure of the mean particle size. However, this effect would be anticipated to be more important for the suspensions of larger particles. The position of the mode of the intensity size distributions, derived from the fit to the correlation function, is expected to be particularly sensitive to the larger particles in the distribution. When the mole ratio dependence of this parameter is examined a proportional relationship is also observed, with a higher slope = 0.301 as expected, as shown in Figure 3.11. Thus we have used the Z-average diameter, derived from the cumulants analysis, as a measure of the hydrodynamic size, as it is less susceptible to this type of error and shows the same slope as D_{TEM}, which is a number average.

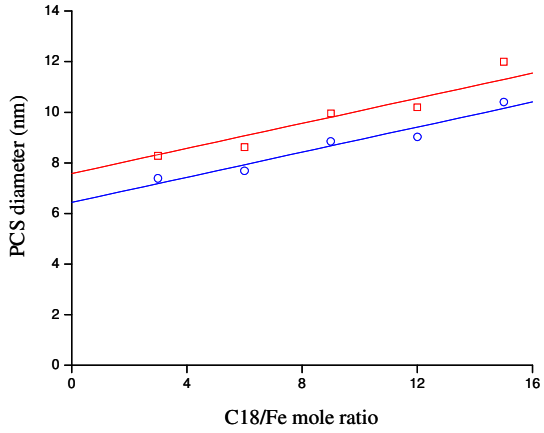

Figure 3.11. The relationship between the nanoparticle size determined from PCS and the C18/Fe precursor mole ratio. When the PCS size is determined: (i) by Cumulants analysis (Z-Average) (O), slope = 0.248; (ii) from the mode of the intensity distribution (□), which is determined by analysis of the correlation functions by non-negative least squares fitting, slope 0.301.

The simplest interpretation of Figure 3.9 is that there are no systematic, or size-dependent, errors associated with the D_{TEM} and D_{PCS} parameters obtained for these suspensions. Two conclusions can be drawn; (*i*) given the dependence of light scattering intensity on particle volume, the observation of the same slope demonstrates that the contribution to light scattering from aggregates is negligible, i.e. the suspensions are 100% dispersed, and (*ii*) D_{PCS} and D_{TEM} can be taken to be good measures of the hydrodynamic and iron-oxide core sizes, respectively.

The slope of the NMR size data was the same as we obtained for the PCS and TEM, Figure 3.9. The intercept was ~2.4 nm lower than that obtained from PCS and surprisingly ~1.9 nm higher than the TEM result. Despite this systematic overestimate of the core size when compared to microscopy, the D_{NMR} values quantitatively reproduce the size dependence on mole ratio, obtained using the more direct sizing techniques. This numerical consistency, which we can only achieve because the suspensions are highly monodisperse, validates our interpretation of the trends in the other parameters derived from the NMRD analysis, to be discussed below. In recent studies of aqueous suspensions of

citrate-coated and uncoated- γ-Fe_2O_3 nanoparticles, similar systematic differences between the particle size obtained from TEM, NMRD and PCS were reported by Roig and coworkers [77]. For uncoated Fe_2O_3 in water these authors reported; D_{TEM} = 4.9 nm, D_{NMR} = 5.7 nm and D_{PCS} = 8 ± 2 nm. Thus our D_{NMR} values are not unusual for magnetic iron-oxide suspensions, the high values presumably arise due to the limitations of SPM theory.

3.4.2 Nuclear magnetic resonance properties and particle morphology

Clear systematic changes in the NMRD profiles were observed for suspensions prepared with different mole ratios (Figure 3.7). The frequency of the relaxivity maximum, ν_{max}, is observed to decrease as the mole ratio is increased, Figure 3.12. SPM theory shows that this effect arises from the larger core size of these suspensions. The most remarkable difference between the profiles is the strong increase in r_1 with mole ratio at all frequencies measured. This difference is greater than expected, particularly in the low-frequency (sub MHz) part of the profile, for particles in this core size (and associated M_s) range. The dependence of the low frequency r_1 plateau on mole ratio is also shown in Figure 3.12.

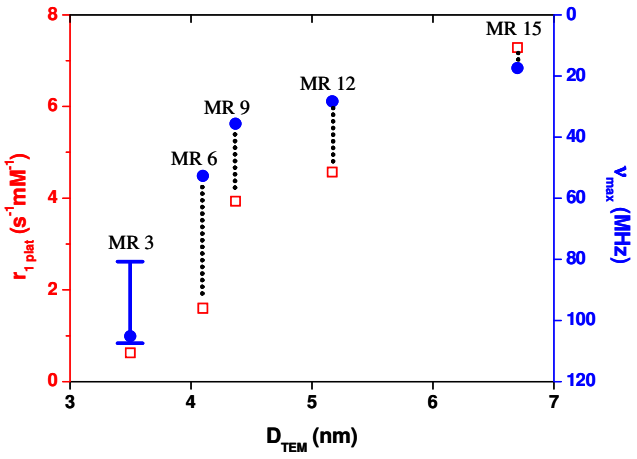

Figure 3.12. Low field relaxivity at the plateau, r_{1plat} (□), and frequency of the high field relaxivity maximum, ν_{max} (●), as a function of iron-oxide core size, D_{TEM}. The ν_{max} value for the suspension prepared with mole ratio = 3 was above our measurable range (if present). The value estimated from the unconstrained simulation to the NMRD profile is indicated, the maximum uncertainty in this ν_{max} value is included as an error bar.

In general for magnetic nanoparticle suspensions, the shape of the NMRD profile is determined by; (i) the size and crystallinity of the magnetic cores, as they affect the saturation magnetisation; (ii) the accessibility of the cores to the diffusing solvent molecules; and (iii) inter-core interactions, as they affect the anisotropy energy. The latter is known to be a potentially strong contributor in the low MHz range, in particular [151]. The suspensions that we have produced are very size-monodisperse and as we have shown PCS, which is very sensitive to the presence of larger aggregates, indicates that there are none present. In fact the suspensions are stable with respect to aggregation for periods of months. Furthermore, over the iron concentration range studied, 1.5 – 97.5 mM, the R_1 values are linearly dependent on concentration (Equation 1.24). We conclude that the contribution of inter-particle interactions to the magnetocrystalline anisotropy is negligible. Therefore, since the nature of the C18 coating does not change across the mole ratio range, the differences in the profiles can be attributed solely to changes in the γ-Fe_2O_3 cores.

It was possible to simulate relaxivity profiles, using Muller's SPM theory [151], which conform reasonably well to the data, Figure 3.13. If we assume that heptane tumbles isotropically on a timescale faster than those of all the other relevant processes, including the diffusion time, τ_D (Chapter 1, section 1.5), which we estimate between $0.9 \cdot 10^{-9}$ and $3.6 \cdot 10^{-9}$ s for particles in this size range, and the Néel correlation time, τ_N (Chapter 1, section 1.5), which is also in the nanosecond range, then SPM theory should be directly applicable to heptane suspensions. This approach is justified given that $D_{heptane} = 3.12 \cdot 10^{-5}$ $cm^2 \cdot s^{-1}$ at 298 K,[38] which by the Stokes Einstein relation, corresponds to a diffusional timescale of $1.03 \cdot 10^{-11}$ s. Finally, the ^1H concentration of pure heptane at room temperature is 109.2 M, a value only 1.6% lower than that of water, so the simulated r_1 values of heptane suspensions do not need to be scaled for ^1H content, given the precision of the model. Ultimately, SPM theory predicts that, for monodisperse iron-oxide nanoparticles of a given size, the NMRD profiles of fully dispersed heptane suspensions will have r_1 values approximately 15% higher than the equivalent water suspensions, in the range below 100 MHz. It should be noted that the scaling is only approximately linear across this

frequency range. This confirms that SPM theory, which was formulated to interpret aqueous suspensions of iron-oxide, can be extended to non-aqueous suspensions. To our knowledge, there are no published reports of the application of SPM theory to the interpretation of NMRD profiles of non-aqueous magnetic iron-oxide suspensions.

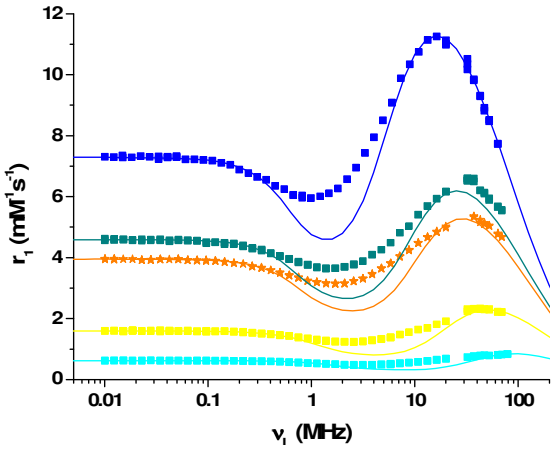

Figure 3.13. The fitted profiles for oleate-stabilised iron-oxide nanoparticles suspended in heptane synthesised with C18/Fe precursor mole ratios of ■ 3, ■ 6, ■ 9, ■ 12, and ■ 15.

Given the number of parameters in the model (D_{NMR}, M_s, ΔE_{anis} and τ_N), two simulation strategies were investigated: (i) an unconstrained simulation in which the parameters were allowed to adopt any value; (ii) a core-shell model, which reduces the number of parameters by fixing the M_s value for a given value of D_{NMR}, using the relationship described by Lu et al [153], Figure 3.14. These authors explained the size-dependent magnetic properties of nanoparticulate iron-oxide by assuming the core has a magnetically dead outer oxide layer of width 0.6 nm, corresponding to one stoichiometric unit.

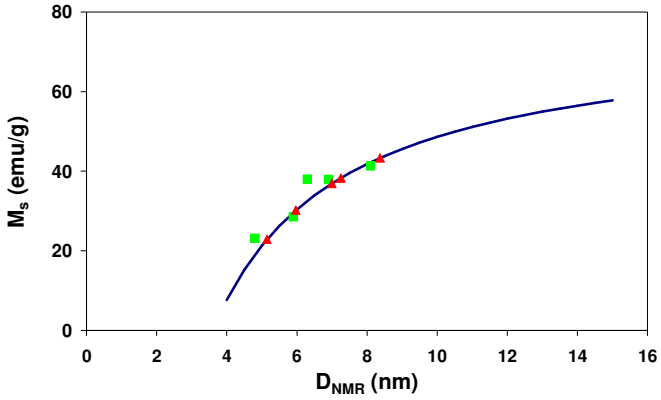

Figure 3.14. Graph showing agreement of the M_s value obtained from ■ the unconstrained NMRD simulations, and ▲ the core-shell model NMRD simulation with ─ the fit to the published data from Lu et al. [153] using the equation $M_s = M_{s0}(1-(6t/D))$with bulk saturation magnetism M_{S0} = 76 emu/g [77,154,155] and t = 0.60 nm [156].

For our suspensions the core-shell approach gives D_{NMR} values on average only ~0.3 nm higher (including the dead layer, Figure 3.15) than the unconstrained approach.

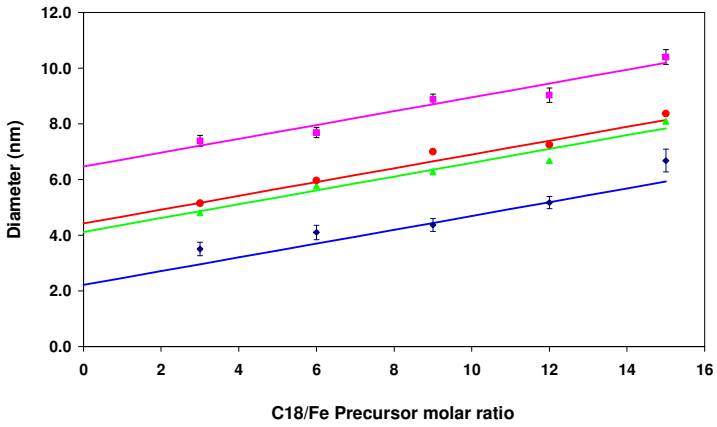

Figure 3.15. Relationship between the nanoparticle size (as measured with different techniques) and the C18/Fe precursor mole ratio. The solid lines are straight line fits, with fixed slope = 0.248, through the: D_{PCS} data (■), intercept = 6.47 nm; D_{NMRLU} data (●), intercept = 4.42 nm, D_{NMR} data (▲), intercept = 4.12 nm; D_{TEM} data (♦), intercept = 2.21 nm.

The two approaches to the simulations produce very similar values for the parameters, and nearly indistinguishable profiles. Therefore, we have preferred the unconstrained approach as it makes no assumptions about the nanoparticle structure. The remainder of this discussion will focus on the results of the unconstrained simulations. The parameters obtained from unconstrained simulations of the NMRD profiles (Figure 3.13) are shown in Table 3.8.

Table 3.8. The parameters obtained from unconstrained simulations of the NMR profiles of C18-stabilised γ-Fe_2O_3 heptane suspensions. The diffusion coefficient of heptane was taken to be $3.12 \cdot 10^{-5}$ $cm^2 \cdot s^{-1}$ [157].

Mole ratio	**D_{NMR} (nm)**	**M_s ($emu \cdot g^{-1}$)**	**ΔE_{anis} (GHz)**
3	4.8	23	2.0
6	5.8	29	1.2
9	6.3	38	1.1
12	6.9	38	0.9
15	8.1	41	0.75

The systematic deviation of the fits in the mid-frequency range, Figure 3.13, on the low frequency side of the r_1 maxima, is noteworthy. The parameters D_{NMR} and M_s do not strongly influence the simulated r_1 values in this frequency range. D_{NMR} determines the frequency of the r_1 maximum and M_s scales the r_1 values at all frequencies. The effect of ΔE_{anis} is significant in both in the mid- and low-frequency parts of the profile. It is not possible to remove the mid-frequency discrepancy and to simultaneously reproduce the low-frequency plateau using simulations from SPM theory (Figure 3.16). Furthermore, it is only possible to produce the reasonable agreement shown in Figure 3.13 by significantly increasing the value of ΔE_{anis} for the smaller cores (Figure 3.17). It is likely that the discrepancy in the mid-frequency range arises from the assumption, made in SPM theory, that the magnetic symmetry of the particles moment is uni-axial.

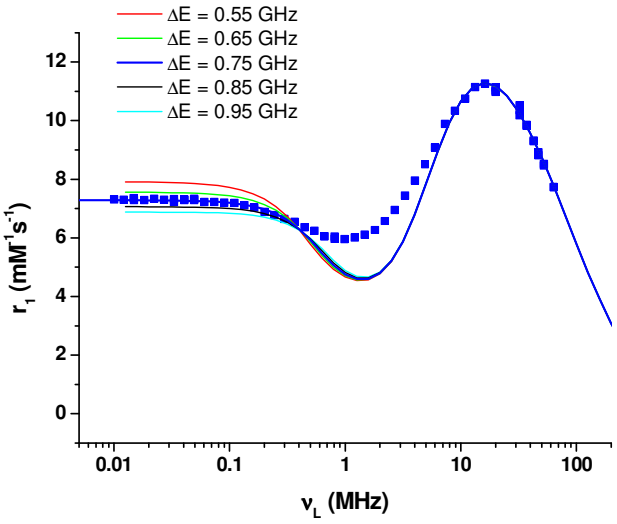

Figure 3.16. The sensitivity of fitted profiles to changes in ΔE. D_{Lu} = 8.37 nm, M_s = 43.3 emu/g, τ_N = 6.5 ns, ΔE is as indicated in the legend. ■ Experimental relaxivity profile of oleate-stabilised maghemite nanoparticles synthesised with a C18/Fe precursor mole ratio of 15.

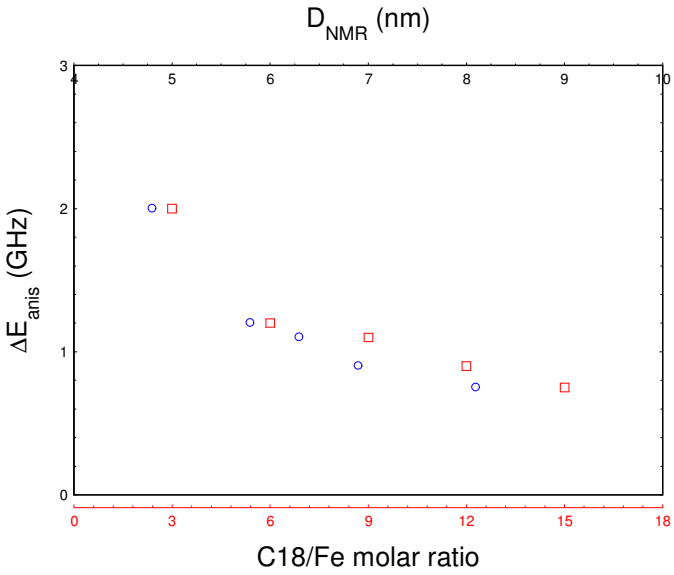

Figure 3.17. The effect of C18/Fe precursor mole ratio and magnetic diameter on the anisotropy energy of the maghemite nanoparticles.

For larger single-domain quasi-spherical particles ΔE_{anis} is usually found to be approximately proportional to the core volume [151]. Since anisotropic inter-particle interactions have been discounted for our suspensions, we attribute the reversal of the expected behaviour to a progressive increase in energy anisotropy associated with increased surface area to volume ratio, in this very low size range. For particles of such small dimensions, it is not expected that minor geometric deviations would be identifiable by TEM, despite their marked effect on the magnetic properties of the suspensions, Figure 3.13.

For particles in this size range increased energy anisotropy, due to surface effects, is not surprising. For the sake of illustration, if we assume ideal spherical particles formed of identical stoichiometric units, with the bulk density of γ-Fe_2O_3; a 3.5 nm core (mole ratio 3) would contain ~465 stoichiometric (γ-Fe_2O_3) units of which ~57% would be on the surface, while a 4.37 nm particle (mole ratio 9) would contain ~905 units with ~48% exposed, and a 6.68 nm particle (mole ratio 15) would contain would contain ~3231 units of which only ~33% would be on the surface. Thus minor surface defects will become increasingly important in determining the orientation and relative energies of the easy-axes of magnetisation for smaller γ-Fe_2O_3 nanoparticles. This view is in contrast to the picture of a featureless "dead-layer", one stoichiometric unit across, that might be inferred from the study of Lu et. al. [153] although our data agree with the findings of that study.

3.4.3 Effect of reaction conditions on nanoparticle properties

It is generally accepted that temporal separation of the nucleation and growth phases is critical for the preparation of uniform, monodisperse nanoparticles [95]. The "heating up" process is a common approach to achieve homogeneous nucleation, where a single nucleation event, or "burst nucleation", is followed by a growth phase. In the 'heating up' process reagents are mixed at room temperature and then heated to reflux. In the preparation of nanoparticulate γ-Fe_2O_3, during heating iron acetylacetonate decomposes to generate iron ions in solution. When the ion concentration exceeds the supersaturation limit, a single, homogeneous nucleation event is thought to occur, rapidly reducing the ion

concentration and preventing secondary nucleation. During the process, the surfactant molecules are believed to form intermediate complexes with the iron ions, reducing the concentration of free metal ions, so delaying supersaturation and hence nucleation [136]. For our preparations with higher mole ratios (higher C18 concentration) a greater fraction of the ion content would be complexed, which presumably reduces the number of nucleation sites during the burst. This results in an extended growth phase and hence larger particles with higher saturation magnetisation and lower magnetocrystalline anisotropy energy.

Iron determination was carried out both before and after the final centrifugation step during the suspension preparation. This revealed that the amount of iron removed from suspension, in the form of sedimented particles or larger agglomerates, broadly increased as the C18/Fe ratio increased (Table 3.9). The results suggest that at higher surfactant concentrations, consistent with the formation of larger particles, inter-particle interactions leading to agglomeration become increasingly relevant. Attractive inter-particle interactions in nanoparticle systems include van der Waals and magnetic dipolar interactions; both of which are known to be stronger for larger than for smaller particles [158]. It should be noted that it is unlikely that aggregation is due to an insufficient amount of C18 surfactant to stabilise the particles as a large excess of surfactant was present in all the preparations. The total amount of C18 surfactant used during the synthesis ranged from 0.3 – 1.5 M, for C18/Fe precursor ratios of 3-15. The amount of surfactant necessary to form a single monolayer around 4-8 nm spherical iron-oxide nanoparticles (the size range relevant to this chapter) is 0.02 – 0.04 M, using a value of 38 $Å^2$ for the 'footprint' of oleic acid/oleylamine [159], and assuming total conversion of iron (III) acetylacetonate to iron-oxide.

Ultrasonic treatment of the samples resulted in even further aggregation. We found centrifugation to be the most effective method of removing the aggregates from all of the samples in the preparation series.

Table 3.9. The effect of centrifugation on the iron concentration of the maghemite suspensions in the entire series of preparations.

C18/Fe ratio	Prep	[Fe] before centrifugation (mM)	[Fe] after centrifugation (mM)	% Fe removed by centrifugation
3	1	104.8	97.5	7.0
6	4	114.8	96.8	15.7
9	1	107.5	63.0	41.4
9	2	122.7	81.2	33.8
12	1	102.9	84.1	18.3
15	1	125.1	37.9	69.7
15	2	115.7	36.0	68.9

3.4.4 Evaluation of effectiveness as magnetic resonance contrast agents

Table 3.6 shows r_2/r_1 ratios for all preparations at 9.25 and 37 MHz (0.22 and 0.87 T). The r_2/r_1 ratio is commonly used to determine the character of a potential nanoparticulate contrast agent and classify a magnetic fluid as either a positive (T_1-reducing), or negative (T_2-reducing) contrast agent. Traditionally, positive contrast agents with a low r_2/r_1 ratio in the range of 1-2 are paramagnetic complexes of Gd^{3+} or Mn^{2+} ions, while negative contrast agents with a much higher r_2/r_1 ratio are based on aggregated or partially aggregated iron-oxide particles [77,106,160]. More recently, however, ultra-small particles of iron-oxide have been evaluated as potential T_1 contrast agents [77] due to improvements in the ability to prepare monodisperse suspensions of a controlled particle size. The authors report a r_2/r_1 ratio of 1.38 and 2.03 at 20 and 60 MHz, respectively, at a temperature of 310 K.

The r_2/r_1 ratio is known to be sensitive to particle size, agglomeration, and magnetic field strength. Due to the broad range of field strengths used in published studies, a direct comparison of our experimental r_2/r_1 ratios with those reported in the literature is difficult. Furthermore, below 37 MHz, our instrumentation limits us to the measurement of T_2 at 9.25 MHz. For the purposes of illustration a simulation of the transverse relaxivity as a function of field strength is shown in Figure 3.18 [151]. According to SPM theory, the transverse (r_2) NMRD profile has broadly the same shape as the longitudinal

profile at low and mid-range frequencies. The main difference occurs at higher frequencies, where the r_2 profile does not decrease towards zero. This is a result of a frequency-dependent secular term, which contributes to the transverse relaxation rate, but not to the longitudinal relaxation rate [151].

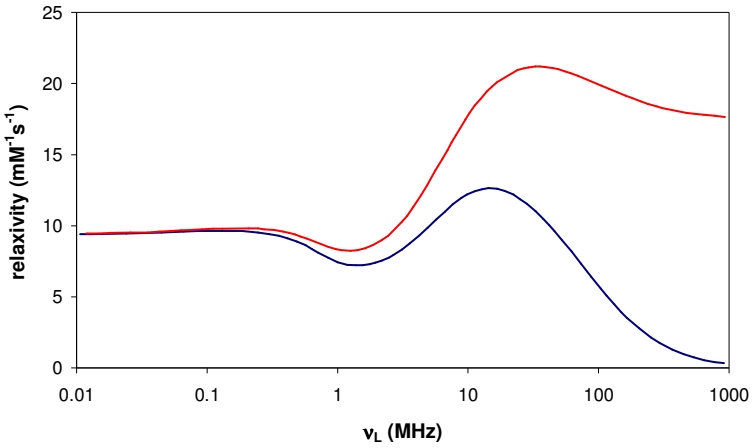

Figure 3.18. Comparison of example longitudinal (—) and transverse (—) NMRD profiles as defined by SPM theory for D_{NMR} = 10 nm, τ_N = 9 ns, ΔE_{anis} = 1 GHz, M_s = 2.07 x 10^5 emu/g, D = 3.4 x 10^{-5} cm^2/s, T = 310 K [151].

Table 3.6 shows that almost all the r_2/r_1 ratios measured for the entire series of maghemite heptane suspensions, with core sizes from 3-6 nm, ranged between 1 and 2, irrespective of the field strength used. This confirms their potential for use as effective T_1- contrast agents, should it be possible to phase transfer into aqueous suspensions without inducing aggregation.

3.5 Conclusions

We have successfully developed a method to easily and reproducibly control the primary particle size of γ-Fe_2O_3 nanoparticles by controlling the reaction conditions. This in turn permits selection of the magnetic properties of the resulting nanoparticle suspensions. Particle size information obtained from three different sizing techniques was successfully compared, validating our interpretation of the properties of the monodisperse suspensions. The NMRD

profiles of the suspensions, which are usually measured to assess the MRI efficacy of aqueous suspensions, have been shown to be a valid approach for magnetic characterisation of non-aqueous magnetic nanofluids using SPM theory. We have found that as the size of the suspended particles is reduced, their magnetic properties are increasingly determined by the high surface area to volume ratio.

CHAPTER 4

Toward the preparation of stabilised suspensions of magnetic nanoparticle clusters of controlled size

4.1 Introduction

In Chapter 3 we demonstrated the ability to control the primary particle size and the emergent magnetic properties of γ-Fe_2O_3 nanoparticles (NPs) over a broad range, and down to a smaller size than has previously been reported. Ultra-small iron-oxide particles have been shown to generate an exceptionally high amount of heat compared to micron-sized particles when exposed to AC magnetic fields [56,57,66], making them ideal for use as hyperthermia mediators. Furthermore, smaller particles have a lower r_2/r_1 ratio making them suitable for use as positive MRI contrast agents [77]. However, *in vivo* application of these particles is currently limited by two important factors. (i) The biodistribution and accumulation in target organs is highly dependent on particle size [161-163]. So while the 5 – 8 nm particles synthesised in Chapter 3 exhibit a broad range of controllable and well-defined magnetic properties, recent research [164] suggests that upon administration, their ultra-small size may promote rapid removal through renal clearance. (ii) Biomedical applications require particle stability in physiological media, but the as synthesised particles are coated with long chain hydrophobic capping molecules and can therefore only be dispersed in non-polar organic solvents. The aim of this chapter is to present an investigation into strategies to resolve these two issues in an attempt to progress the methods presented in Chapter 3 toward the development of water stable nanoparticle cluster suspensions with controlled size for physical targeting, and with optimal magnetic properties for magnetic-mediated hyperthermia, and possibly MRI, applications.

Nanoparticle clusters (NPCs), i.e., clusters of NPs, have shown great promise for biomedical applications, as they combine the size-dependent magnetic properties of the individual nanoparticles with the ability to target specific structures *in vivo* due to their larger physical size [165]. While several methods currently exist for the preparation of nanoparticle clusters including the reaction of primary nanoparticles with polymers [165,166] and the *in-situ* formation of nanoparticles in the presence of polymers [109,110,166,167], the cluster size is not usually

controlled, or is not controllable over a broad size range. This is because the cluster size is determined by the surface chemistry of the reaction.

Recently, a process for the controlled growth of NPCs through competitive stabiliser desorption was developed by the group [168,169]. Heptane suspensions of oleic acid coated iron-oxide NPs, prepared by the coprecipitation method, were exposed to cyanopropyl-modified silica particles, resulting in the *in-situ*, continuous growth of NPCs due to the gradual depletion of oleic acid from the nanoparticle surface. As the surfactant is partially depleted, the particles become destabilised, and hence activated toward interaction with other destabilised NPs or NPCs (Figure 4.1). Initially, small clusters are formed through an N → N+1 aggregation by addition of single, destabilised nanoparticles from the suspension. Upon the partial or complete depletion of the primary particles from the suspending medium, it is believed that any further surfactant desorption results in the activation of the NPCs, leading to an aggregation of clusters, or a 'clustering of clusters'. The key point, which distinguishes this process from uncontrolled colloid destabilisation and aggregation, is that the size dispersity of the original NP suspension is preserved during NP growth. It was also shown [169] that the process can be stopped at any time, allowing the preparation of NPCs of a specific size between 20 – 400 nm. Thus, the process offers significant advantages over other published methods of nanoparticle cluster formation.

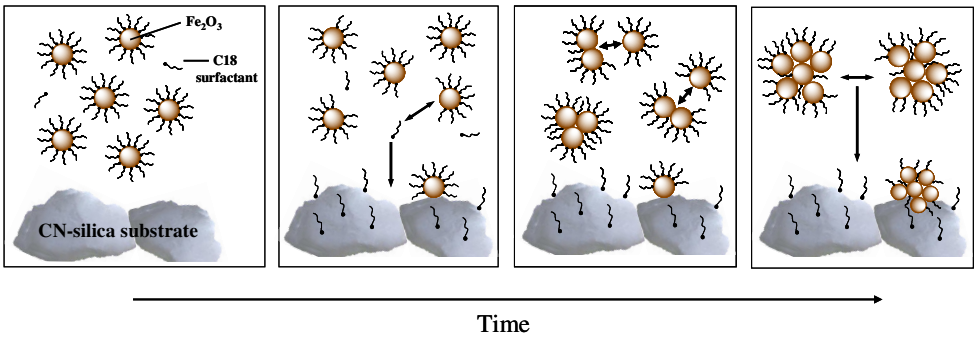

Figure 4.1. Schematic representation of the mechanism proposed by Stolarczyk et al. [169] for the growth of iron-oxide NPCs of controlled size from primary particles synthesised from coprecipitation methods.

In the first part of this chapter, we describe the application of these techniques using primary NPs synthesised by the thermal decomposition method. We have also investigated the kinetics of cluster growth; specifically, the effect of primary particle size and iron concentration on the rate of growth are discussed in some detail. Finally, we propose a reasonable mechanism for cluster growth based on both current experimental observations as well as previous studies from our group which will progress this process towards general application [168,169].

Biomedical applications of NPs and NPCs require colloidal stability in physiological media, and several methods currently exist for the phase transfer and stabilisation of iron-oxide cores with hydrophobic surfaces into water [77,106,113,141]. Recently, there has been an increased interest in utilising gold as a coating for magnetic NPs, as the well-established surface chemistry of gold can impart surface tunability to the cores for improved aqueous stability and biocompatibility [170,171]. Gold nanoshells offer additional advantages that extend beyond stability in aqueous media. For instance, the optical properties of the gold, combined with the magnetic properties of the core allow the use of these core@shell particles for simultaneous optical and magnetic resonance imaging [172]. Additionally, gold nanoshells have been utilised for near-infrared mediated thermal therapy of solid tumours [173,174].

A current challenge is the synthesis of gold-coated magnetic nanoparticles with a desired size and composition. There are many reports of different approaches to coat iron-oxide NPs with gold including thermally-activated hetero-interparticle coalescence of gold and iron-oxide nanoparticles [175], the attachment of 2 – 3 nm gold nanoparticles onto 10 nm magnetite nanoparticles via 3-aminopropyltriethylsilane [176], and the deposition of gold onto the surface of 9 nm iron-oxide NPs via iterative hydroxylamine seeding in aqueous solution [177]. While the Au shell thickness and the particle size can be manipulated in some cases, control of the final particle size has only been demonstrated for a narrow range of sizes. Additionally, the formation of a complete layer of gold around iron-oxide nanoparticles can greatly reduce their saturation magnetisation [178], which in turn can diminish their efficacy as MRI contrast agents.

In the second part of this chapter, we describe the generalisation of the method for cluster growth to include the preparation of mixed-metal iron-oxide:gold (FeO:Au) clusters. This has opened a new pathway to size-controlled nanocomposite materials and has provided further insight into the mechanism of nanoparticle cluster growth.

Finally, as a step toward the transfer of these NPCs into aqueous media, we have evaluated two distinct methods of polymer-mediated stabilisation of dispersed NPs, and have characterised the resulting aqueous suspensions by dynamic light scattering and relaxivity measurements. It should be noted that the approaches assessed were a limited success. The surface chemistries were demonstrated to be compatible with iron-oxide; however, some aggregation could not be avoided. These results will not be discussed in this chapter; the interested reader can find the full details in Appendix B.

4.2 Experimental

4.2.1 Materials

Hydrogen tetrachloroaurate (≥ 99.9%), dodecanethiol (DDT; ≥ 98%), and sodium borohydride ($NaBH_4$; ≥ 98.5%), were purchased from Sigma-Aldrich. Tetraoctylammonium bromide (TOAB; ≥ 98%) was obtained from Fluka, and cyanopropyl-modified 30-70 μm silica particles (CN-silica) were purchased from Alltech Associates.

4.2.2 Synthesis

4.2.2.1 Iron-oxide NPs

Stable heptane suspensions of monodisperse C18-stabilised γ-Fe_2O_3 NPs were prepared using a modification of published methods, as described in Chapter 3.

4.2.2.2 Gold NPs

Dodecanethiol-derivatised gold NPs were synthesised in a two-phase liquid-liquid system as described by Brust et al [179]. A solution of TOAB in toluene

(26.7 mL, 50 mM) was added to a 100-mL round-bottomed flask and stirred with a magnetic stir bar to completely dissolve the solid. An aqueous solution of hydrogen tetrachloroaurate (10 mL, 30 mM), appearing bright yellow in colour, was added to the organic phase in the flask. The two-phase mixture was vigorously stirred until the tetrachloroaurate was completely transferred into the organic layer (~10 – 15 min). The mixture turned red-brown during mixing, and separated into two phases when mixing was temporarily discontinued; the upper toluene phase appeared red-brown in colour, and the lower aqueous phase was colourless. Magnetic stirring was resumed, and 67 μL dodecanethiol was added to the mixture. A freshly prepared aqueous solution of sodium borohydride (8.3 mL, 0.4 mM) was then added dropwise to the flask with continual and vigorous stirring. The colour changed from red-brown to dark purple upon reduction. The two phase mixture was covered and stirred at room temperature for 3 hours. The stirring was discontinued, the two phases separated, and the dark purple organic phase was removed and transferred to a separate glass flask. Ethanol (~ 50 mL) was added to the flask to precipitate the gold nanoparticles. This required the mixture to be kept in the freezer at -20°C for at least 4 hours, but this step was usually carried out overnight. After at least 4 hours in the freezer, a dark purple-brown precipitate had settled to the bottom of the flask. The precipitate was filtered under reduced pressure using a buchner funnel, washed with ethanol, and suspended in 40 mL heptane to produce the final suspension, which appeared dark purple in colour. The suspension was centrifuged for 45 minutes at 13,000 rpm using a tabletop centrifuge (Eppendorf 5415 D) to sediment and remove any larger or aggregated particles. The dark purple supernatant was collected, characterised by PCS, and utilised for nanocluster growth experiments.

4.2.3 NPC growth experiments

(i) Iron-oxide cluster growth

CN-silica (50.2 mg) was placed in a quartz cuvette and spread evenly to form a thin layer at the bottom. A small amount (3-4 drops) of heptane was carefully dripped down the side of the cuvette to pre-wet the silica and prevent agitation when the nanoparticle dispersions were later added on top of the silica. The iron-oxide nanoparticle dispersion was diluted as necessary to 1.0 mM – 5.0 mM with

heptane. The nanoparticle dispersion (1.2 mL) was carefully placed in the cuvette over the thin silica layer, taking care not to agitate the silica at the bottom. The average hydrodynamic diameter of the growing clusters in suspension was continuously monitored by dynamic light scattering on one of two instruments: a High Performance Particle Sizer, HPPS, or a Zetasizer NanoZS (Malvern Instruments; Worcestershire UK). Visually, over time, a gradual nanoparticle deposition was observed on the surface of the silica, and there was an obvious increase in light transmission through the sample.

(ii) Cluster growth for co-suspensions

The gold nanoparticle dispersion was diluted to 0.71 mM, and the dilute dispersion was combined with the 1.0 mM iron-oxide dispersion to produce a broad range of [FeO]:[Au] ratios: 111:1, 91:1, 77:1, 47:1, and 10:1. The nanoparticle co-suspensions (1.2 mL) were placed in the cuvette as described previously, and the average hydrodynamic diameter of the growing clusters in suspension was continuously monitored on either the HPPS or the Zetasizer NanoZS.

(iii) Cluster growth attenuation by addition of gold NPs

An iron-oxide nanoparticle dispersion (1.2 mL) was carefully placed in the cuvette over the thin silica layer, and the average hydrodynamic diameter of the growing clusters in suspension was continuously monitored by dynamic light scattering, as described above. The NPC growth was allowed to proceed for a desired amount of time (5 – 7 hours), after which, the measurement was temporarily terminated and the cuvette was carefully removed from the instrument. A small volume (typically 50 μL) of the 0.71 mM gold nanoparticle suspension was slowly and carefully added to the suspension of iron-oxide clusters. The cuvette was replaced in the instrument, and the light scattering measurements were resumed for an additional 2 – 20 hours.

4.2.4 Characterisation

Total iron content of all the suspensions was determined by AAS as described in Chapter 2.

Gold concentration was determined by AAS in the same way as described for the iron in Chapter 2. It was first necessary to carry out a calibration with standards of known Au concentration. A 15 mg/L stock solution was prepared by dissolving 0.0076 g $HAuCl_4 \cdot 3H_2O$ in 500 mL DI H_2O. A serial dilution was carried out to prepare standards with [Au] = 12, 7.5, 4.5, and 1.5 mg/L.

Transmission electron microscopy (TEM) images were obtained using a JEOL 2000 FX TEMscan instrument (at an accelerating voltage of 80 kV), courtesy of the Electron Microscopy Laboratory at the University College Dublin Conway Institute of Biomolecular and Biomedical Research, Belfield. Samples were prepared for microscopy by depositing a drop of the relevant dilute heptane suspension onto carbon-coated (400 mesh) copper grids and allowing the solvent to evaporate prior to imaging.

High-resolution scanning electron microscopy (SEM) images were obtained using a Hitachi S-5500 instrument (at an accelerating voltage of 30.0 kV). Samples were prepared for imaging as described above for TEM microscopy.

All gold and iron-oxide suspensions were characterised by PCS as described in Chapter 2. Iron-oxide-, gold-, and mixed-metal cluster growth was monitored by PCS by measuring the average hydrodynamic diameter of the suspended clusters over time. A total of up to 200 measurements were recorded at a rate of one measurement every 15 minutes. The temperature was held constant at 25°C for all measurements.

4.3 Results

4.3.1 Controlled growth of iron-oxide NPCs

Typical growth data, obtained by PCS, for the formation of iron-oxide NPCs from primary particles synthesised by the thermal decomposition method is shown in Figure 4.2. Included in the figure is the value of the Z-Avg diameter, derived from the cumulants analysis, plotted as a function of time. The particle size distributions were obtained from correlation function analysis and were unimodal for all samples. The mean of the distribution peak shifted to larger diameters over time, and a typical example is shown in Figure 4.3. The mean count rate, a measure of the backscattered light intensity, and the PDI values were also plotted as a function of time and are included in Figure 4.2. The gradual increase in the intensity of the backscattered light up to about 16 hours is a result of an increase in the number of larger particles in suspension, formed through the slow growth of clusters by the addition of primary NPs. The inflection point and subsequent decrease in the mean count rate after 16 hours indicates a loss of larger particles from suspension, most probably caused by the precipitation of large aggregates. A fairly unimodal size distribution (PDI $\leq$ 0.3) is maintained up to the point of inflection in the mean count rate, indicating that during the NPC growth phase, the suspension remained monodisperse. This trend is consistent for all of the controlled iron-oxide NPC growth data presented in this chapter. The preservation of a monodisperse size distribution is indicative of controlled cluster growth, as normal particle destabilisation and precipitation results in a rapid increase in the PDI values to 0.5 – 1.0 [169].

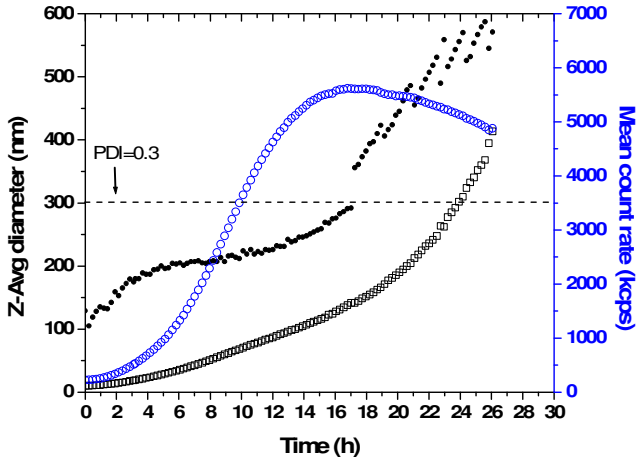

Figure 4.2. Typical growth data, obtained by PCS, for the formation of iron-oxide NPCs in heptane in the presence of silica-CN. □ Z-Avg (nm), ○ mean count rate (kcps), ● PDI.

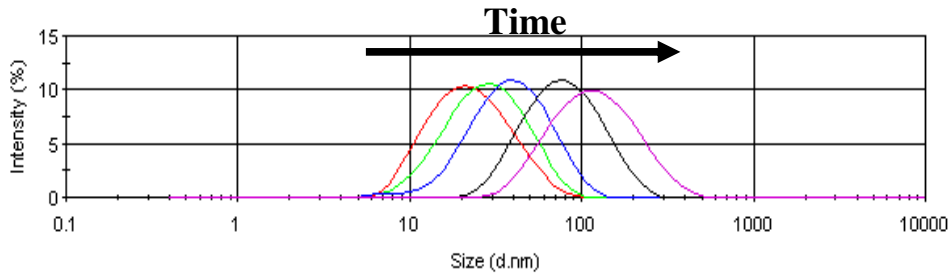

Figure 4.3. The particle size distribution of growing iron-oxide NPCs in heptane over silica-CN as a function of time.

Transmission electron microscopy confirmed that the observed increase in the PCS diameter (D_{PCS}) over time is due to the aggregation of primary NPs rather than the growth of individual particles. TEM images for typical samples of primary particles of C18-stabilised maghemite NPs (a), and NPCs (b), are shown in Figure 4.4. The micrograph of the primary particles shows evidence of rather spherical, monodisperse nanoparticles with no evidence of agglomerates before cluster growth. A statistical sample of the particle sizes was obtained by direct measurement of the diameters of 360 particles. From these measurements, particle size distributions were prepared and fitted to a lognormal distribution,

yielding an average diameter of 3.8 nm. The micrograph of the nanocluster suspension, typical of the images obtained for NPC suspensions, clearly shows a large cluster formed by individual primary particles similar in size to those shown in (a). The average value of D_{PCS} for the NPCs in suspension was 52 nm. The purpose of the TEM image is to demonstrate the incidence of clustering; we did not measure the diameter of a sufficient number of NPCs to determine the average cluster diameter or standard deviation.

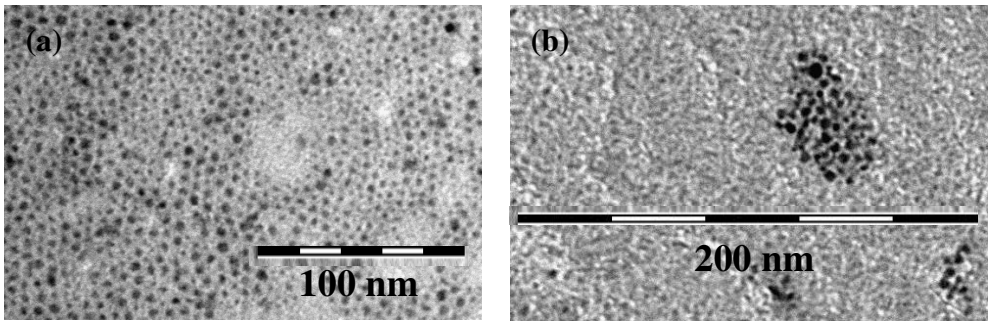

Figure 4.4. TEM images of (a) monodisperse C18-stabilised maghemite NPs, and (b) maghemite NPCs with a measured D_{PCS} = 52 nm.

The gradual deposition of the orange-brown coloured solid NPs onto the surface of the silica during a typical NPC growth experiment is shown in Figure 4.5. An increase in light transmission through the sample over time can also be observed.

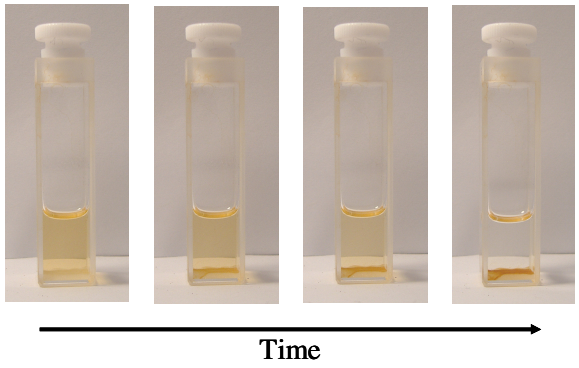

Figure 4.5. Representative photographs showing the gradual deposition of iron-oxide NPs on the surface of silica-CN during a typical NPC growth experiment.

4.3.1.1 Optimisation of NPC growth conditions

4.3.1.1.1 Primary particle size

Growth curves for iron-oxide clusters grown from primary γ-Fe_2O_3 NPs of different core sizes but the same total iron concentration are shown in Figure 4.6. TEM analysis indicated average primary particle core sizes (D_{TEM}) of 3.36, 3.80, 3.98, and 4.92 nm, corresponding to C18/Fe mole ratios during synthesis of 3, 6, 9, and 12, respectively (see Chapter 3). The interruption in the data observed in Figure 4.6 for one experiment (D_{TEM} = 4.92 nm) is due to the removal of the sample from the PCS machine in order to make the instrument available to other users. During this time, the cuvette was removed carefully to prevent agitation of the silica, and placed in a 25°C water bath to maintain it at a constant temperature. When the cuvette was replaced in the PCS machine, no visible disruption was observed, as indicated by stable Z-Avg and PDI values. A significant increase in the rate of cluster growth was observed with a decrease in the primary particle size from 3.98 – 3.36 nm. No growth was observed for the largest particles for up to 40 hours.

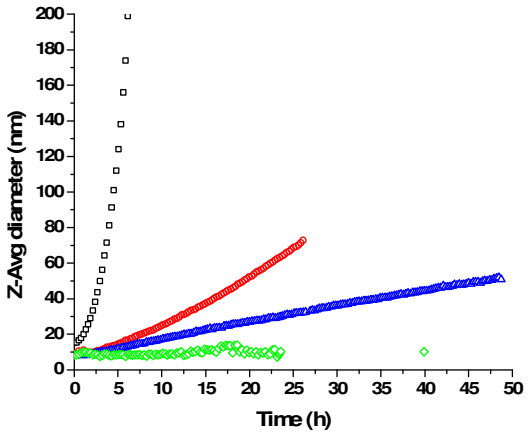

Figure 4.6. Curve of NPC growth grown from primary γ-Fe_2O_3 NPs with D_{TEM} of □ 3.36 nm, ○ 3.80 nm, Δ 3.98 nm, ◊ 4.92 nm. The total iron concentration was 0.82 mM in all cases, and the heptane suspensions were each placed over 50.2 mg silica-CN.

4.3.1.1.2 Iron concentration

Growth curves for a single suspension of iron-oxide NPs as a function of iron concentration are shown in Figure 4.7. The primary particle size was not measured by TEM for this sample, but PCS analysis indicated a hydrodynamic diameter of ~ 8.0 nm at the start of the growth experiment at all concentrations; this corresponds to a D_{TEM} of ~ 3.7 nm (Chapter 3). The rate of growth over the entire curve was found to decrease with an increase in the total iron concentration of the sample.

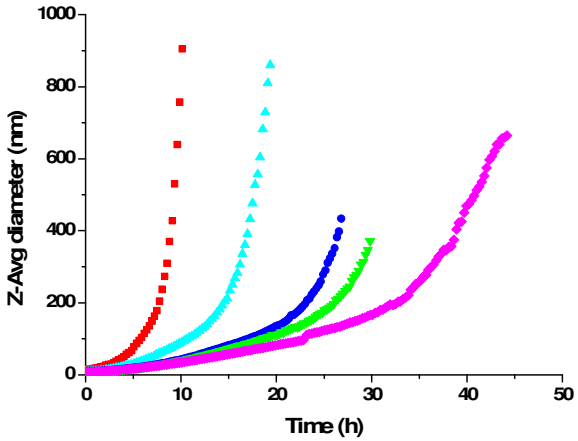

Figure 4.7. Curve of nanocluster growth in the presence of silica-CN (50.2 mg) as function of iron concentration. [Fe] = ■ 1.0 mM, ▲ 2.0 mM, ● 3.0 mM, ▼ 4.0 mM, ♦ 5.0 mM. The primary particle core size at all concentrations = 3.7 nm.

4.3.2 NPC growth from mixed-metal FeO:Au co-suspensions

The individual growth data for two single-metal suspensions, of C18-stabilised iron-oxide NPs, and of DDT-stabilised gold NPs, are compared in Figure 4.8. As seen previously, there is an obvious increase in the Z-Avg diameter with time for the suspension of iron-oxide nanoparticles, consistent with the formation of NPCs. The primary particle size was not measured by TEM for this sample, but PCS analysis indicated a hydrodynamic diameter of 7.9 nm at the start of the growth experiment, corresponding to a core diameter of ~ 3.6 nm (Chapter 3). Interestingly, there is no evidence of aggregation of the DDT-stabilised gold NPCs. It should be noted that the size distribution for the gold nanoparticles was

not completely unimodal. A small population of larger aggregates (> 4 μm) was present in the sample, and could not be removed by centrifugation or sonication. Because larger particles scatter light more strongly than smaller particles, the presence of these aggregates resulted in a high value for the Z-Avg diameter; therefore, the mean diameter of the primary peak (Peak 1 mean; 7.5 nm at the onset of the experiment) is presented as a measure of the gold nanoparticle diameter in Figure 4.8 (a). This is justified because the absolute value of the diameter is not important in this case; the key result is that there was no change in the PCS response indicating the absence of any growth over 19 hours.

Typical growth data for a mixed-metal dispersion containing FeO and Au NPs (FeO:Au) is also shown in Figure 4.8. The overall shape of the mixed-metal growth curve is distinctly different from that of the iron-oxide dispersion. For the co-suspension, the growth over the first ~ 5 hours is broadly similar to that of the pure iron-oxide sample. After 5 hours, however, the rate of growth significantly decreases. While the PDI of the single-metal FeO suspension gradually increased from ~ 0.12 – 0.30 up to the point of inflection in the mean count rate (over the course of ~ 17 hours), the PDI of the co-suspension gradually decreased from ~ 0.25 – 0.14 (Figure 4.8 (b)). The total iron concentration was 3.6 mM for both the iron-oxide suspension, and the mixed FeO:Au suspension.

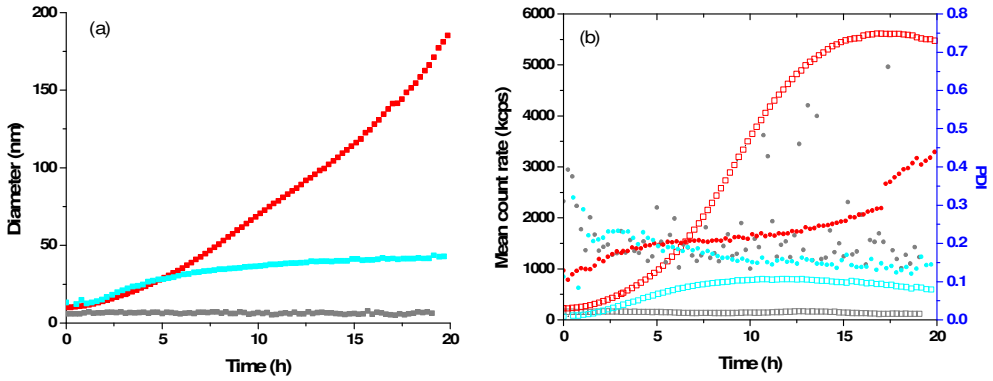

Figure 4.8. Comparison of (a) Z-Avg and (b) mean count rate (□) and PDI (●) over time for ■ 3.6 mM C18-stabilised maghemite NP dispersion (D_{TEM} = 3.6 nm), ■ 0.71 mM DDT-stabilised gold NP dispersion (D_{PCS} = 7.5 nm, based on the peak 1 mean), and ■ mixed FeO:Au NP dispersion with an FeO:Au ratio of 5:1 and an iron concentration of 1.8 mM.

Nanoparticle cluster growth curves for mixed FeO:Au NP dispersions as a function of FeO:Au ratio at very similar Fe concentrations are shown in Figure 4.9. In all cases, the growth curves for the co-suspensions exhibit two growth phases, an initial period of faster growth, followed by a period of slower, almost linear growth. Clear systematic changes in the growth characteristics are observed for increasing FeO:Au ratios; notably, the initial growth rate increases with FeO:Au ratio, allowing the growing clusters to reach larger diameters. Thus, the slower growth, in the later stage, occurs at larger diameters for higher FeO:Au ratios. The PDI values remained below 0.25 for up to 20 hours for all co-suspensions, and in most cases the PDI values remained below 0.2.

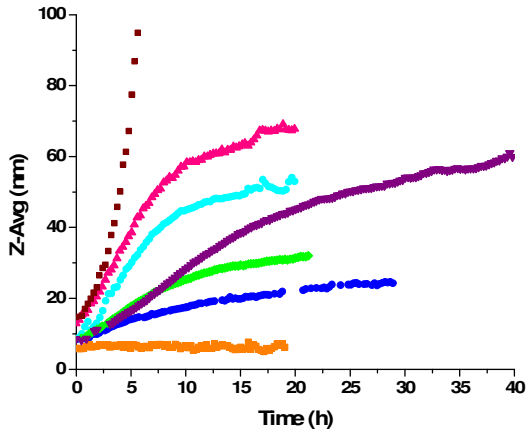

Figure 4.9. NPC growth curves in the presence of silica-CN (50.2 mg) for ■ a single-metal C18-FeO NP dispersion, ■ a single-metal DDT-Au NP dispersion, and mixed FeO:Au NP dispersions with an FeO:Au ratio of ▲ 111:1, ● 91:1, ▼ 77:1, ♦ 47:1, and ● 10:1. [Fe] ranges from 0.88 mM to 0.99 mM. At all concentrations, D_{TEM} = 3.7 nm for iron-oxide NPs and D_{PCS} = 7.72 nm for gold NPs.

The gradual deposition of the solid NPs onto the surface of the silica during a typical mixed-metal FeO:Au NPC growth experiment is shown in Figure 4.10. An increase in light transmission through the sample over time can also be observed. The final colour of the solid particles deposited on the surface of the silica from the co-suspension is distinctly darker than the particles that precipitated from the single-metal iron-oxide suspension.

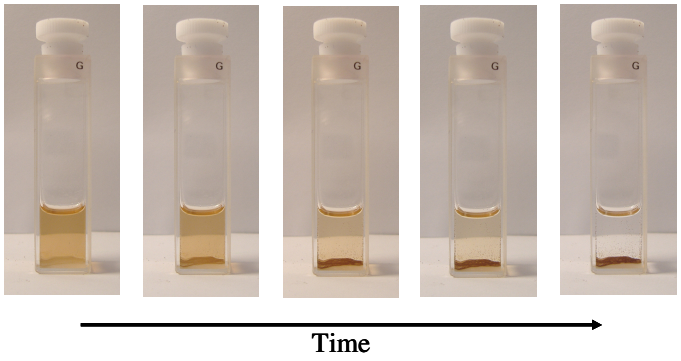

Figure 4.10. Representative photographs showing the gradual deposition of solid NPs on the surface of silica-CN from a heptane co-suspension of FeO:Au NPs during a typical NPC growth experiment.

4.3.3 Controlled iron-oxide cluster growth attenuation by addition of gold NPs

A small volume of a DDT-stabilised Au NP suspension was added to a suspension of growing iron-oxide NPCs in the presence of silica-CN. The concentration of Au added was 0.030 mM. The exact FeO concentration at the time of Au addition is not known, due to ongoing FeO precipitation, but the ratio of initial FeO concentration to Au concentration was 33:1. The introduction of the Au NPs caused an immediate and significant decrease in the rate of cluster growth (Figure 4.11 (a)). The results are compared with those obtained for a suspension of iron-oxide NPs, with the same iron concentration, which were allowed to grow without the addition of Au NPs. Although the figure suggests that the growth may have stopped completely, in fact growth did continue at a very slow rate. The Z-Avg increased by 5 nm over 15 hours from (10 h – 25 h) while maintaining a constant low PDI, at or below 0.2.

The presence of the Au NPs also had a significant effect on the count rate (Figure 4.11 (b)). In the absence of Au NPs, the count rate dropped rapidly from 1540 – 150 kcps over three hours, but upon the addition of Au NPs the count rate slowly decreased from 1600 – 100 kcps over the course of 22 hours.

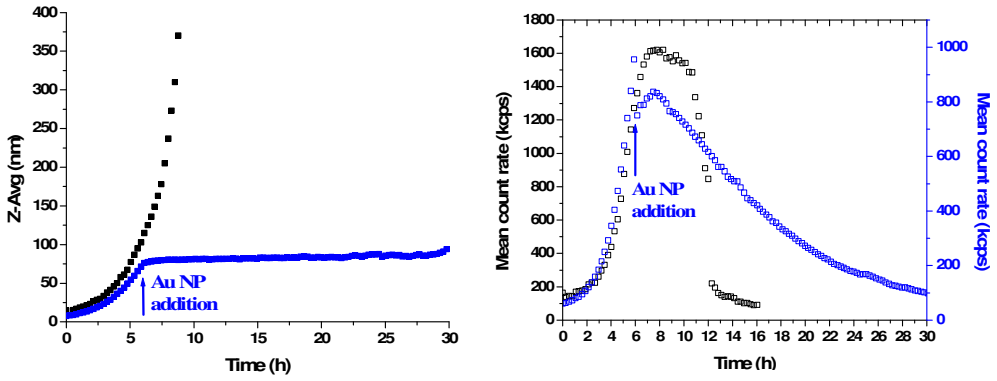

Figure 4.11. The effect of Au NP addition on the (a) Z-Avg and (b) mean count rate of growing iron-oxide NPCs. The initial [Fe] = 1.0 mM in both cases. Black data: no Au addition; blue data, 0.030 mM Au NP addition after 6 hours. D_{PCS} at the start of the experiment was 7.61 nm and 7.72 nm for the iron-oxide and Au NPs, respectively.

The experiment was repeated, and the results were found to be very reproducible (Figure 4.12). The initial growth rate and mean count rate before Au NP addition was nearly identical for two trials, as expected. Importantly, in both cases, the introduction of Au NPs caused an immediate decrease in the rate of cluster growth.

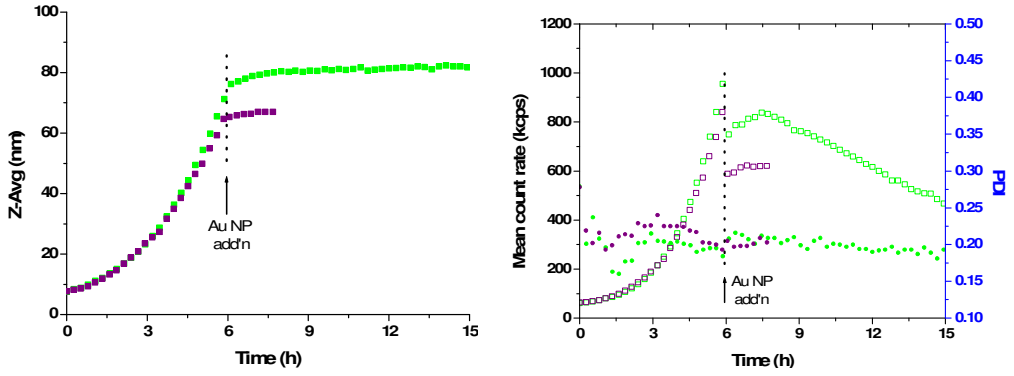

Figure 4.12. The effect on the growth data of the addition of a heptane suspension of DDT-stabilised primary Au NPs (0.030 mM, D_{PCS} = 7.72 nm) to a heptane suspension of growing iron-oxide NPCs placed over silica-CN. The initial [Fe] of the suspension before exposure to silica-CN was 1.0 mM. ■ Trial 1; ■ Trial 2.

There was a noticeable drop in the mean count rate (22 – 30%) immediately after the Au NP addition, and this was observed in all experiments in which gold NPs were added to iron-oxide suspensions. The iron concentration of the suspension

containing the growing FeO clusters was determined by AAS immediately before and after Au nanoparticle addition in this case, and was found to be unchanged, at 0.5 mM. This corresponds to a loss of ~ 50% from the initial iron concentration at this time. The decrease in measured light intensity does not arise due to changes in the cuvette position or photomultiplier tube attenuation, hence we ascribe it to a change in the refractive index of the medium.

As the addition of a DDT-stabilised Au NP suspension was found to attenuate the growth of FeO clusters in the presence of silica-CN, this approach was used to prepare clusters of four different sizes. A small volume of the Au NP suspension was added to suspensions of growing iron-oxide NPCs at different times during the growth, resulting in an immediate attenuation of the growth, in all cases, at cluster sizes of 40, 71, 110, and 131 nm (Figure 4.13). Following the Au nanoparticle addition, the Z-Avg values of the clusters slowly increased by an additional 7 – 20 nm over the course of 30 hours, and the PDI values, in general, steadily decreased (Figure 4.14).

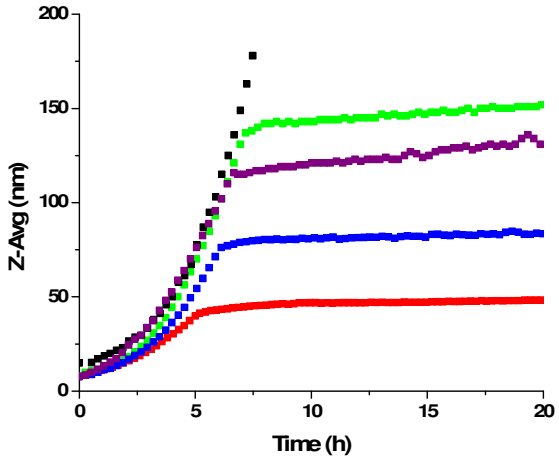

Figure 4.13. The effect of the addition of ~ 0.030 mM heptane suspension of DDT-stabilised Au NPs (D_{PCS} = 7.72 nm) to 1.0 mM heptane suspensions of growing iron-oxide NPCs placed over silica-CN. Au addition took place after ■ 5 hours, ■ 6 hours, ■ 6.5 hours, ■ 7 hours. The Z-Avg size of the FeO clusters at the time of Au addition was ■ 40 nm, ■ 71 nm, ■ 110 nm, and ■ 131 nm. The growth curves are compared with that obtained for a suspension of iron-oxide NPs (1.0 mM, D_{PCS} = 7.61 nm) allowed to grow without the addition of Au NPs (■).

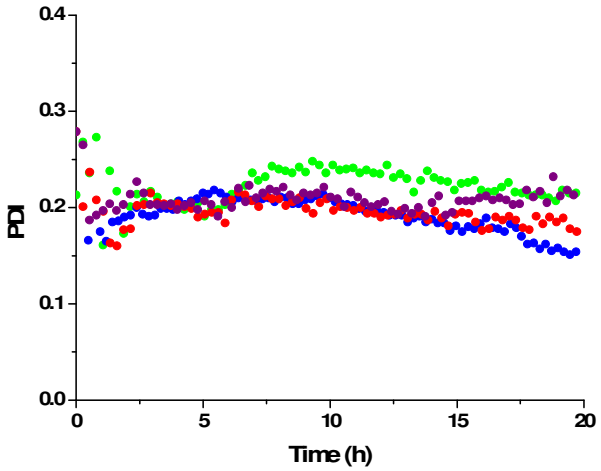

Figure 4.14. The effect on the PDI values of the addition of a heptane suspension of DDT-stabilised Au NPs (~ 0.030 mM, D_{PCS} = 7.72 nm) to heptane suspensions of growing iron-oxide NPCs placed over silica-CN. Au addition took place after ■ 5 hours, ■ 6 hours, ■ 6.5 hours, ■ 7 hours.

4.4 Discussion

4.4.1 Controlled growth of iron-oxide NPCs

4.4.1.1 Mechanism of cluster growth

The growth curves of iron-oxide NPs, as illustrated in Figure 4.15, appear to exhibit at least two distinct stages. The rate of initial growth can be described as an exponential function of time; this initial stage is followed by a stage of slower, approximately linear growth. If the measurements are continued for a sufficiently long time, a second stage of exponential growth is observed, forming the third stage. It was not possible to interpret any of the growth curves as a single exponential function (Figure 4.16), and fitting with three different functions provided a significant improvement in the quality of the overall fits.

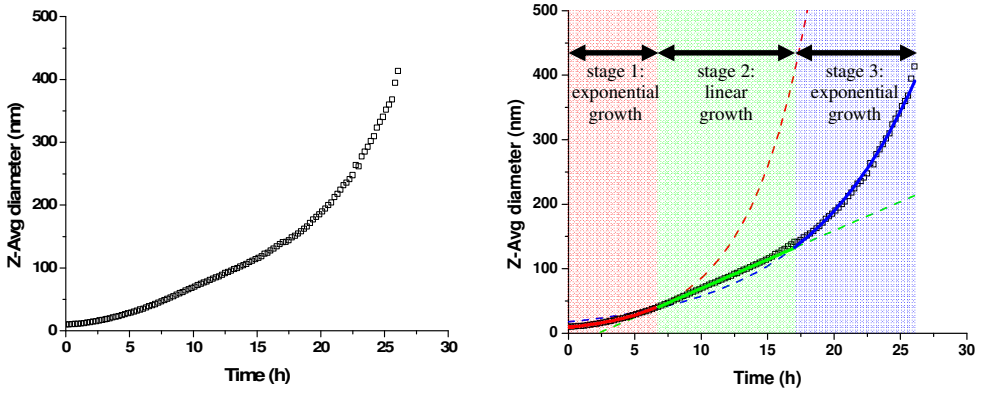

Figure 4.15. A typical growth curve for the formation of iron-oxide NPCs divided into 3 growth stages and fitted with growth functions: — $y = 9.31e^{0.22x}$, $R^2 = 0.997$; — $y = 9.43x - 24.87$, $R^2 = 0.997$; — $y = 17.48e^{0.12x}$, $R^2 = 0.996$.

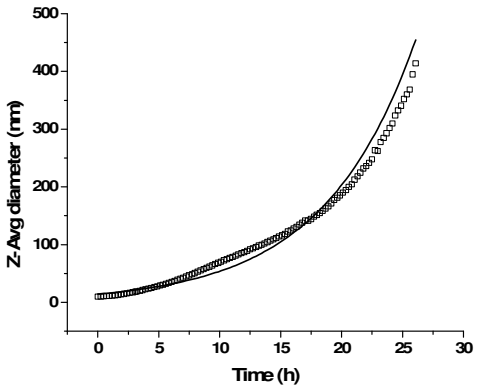

Figure 4.16. A typical growth curve for the formation of iron-oxide NPCs fitted with a single exponential function: — $y = 14.33e^{0.13x}$, $R^2 = 0.971$.

The apparent separation of the growth curve into these different stages provides further insight into the underlying mechanism of cluster formation when considered in conjunction with the fundamental principles of particle aggregation. Uncoated iron-oxide NPs in solution are unstable with respect to agglomeration and are known to cluster in order to reduce their surface energy. Stabilisation by steric repulsion has proven to be an effective means of preventing particle aggregation [82,168,180,181]. If the stabilising surfactant is partially depleted from the nanoparticle surface, the NPs become destabilised, and hence activated toward interaction with other destabilised NPs or NPCs [168,169].

Direct contact of the stabilised NPs with the silica substrate is not necessary to generate activated particles in suspension. We carried out dialysis experiments in which heptane suspensions of OA-coated iron-oxide NPs were introduced into dialysis tubing, and the tubing was then placed inside a vial containing pure heptane over a thin layer of silica (Figure 4.17 (a)). The small pores in the dialysis tubing restrict the passage of the solid iron-oxide NPs through the semi-permeable membrane, but permit diffusion of the OA molecules. After ~ 36 hours, precipitation of iron-oxide particles was observed at the bottom of the dialysis tubing (Figure 4.17 (a)), resulting from the destabilisation of the particles upon partial depletion of the OA surface coating. This indicates that direct contact between OA and silica is not necessary for OA desorption from the surface of the iron-oxide NPs.

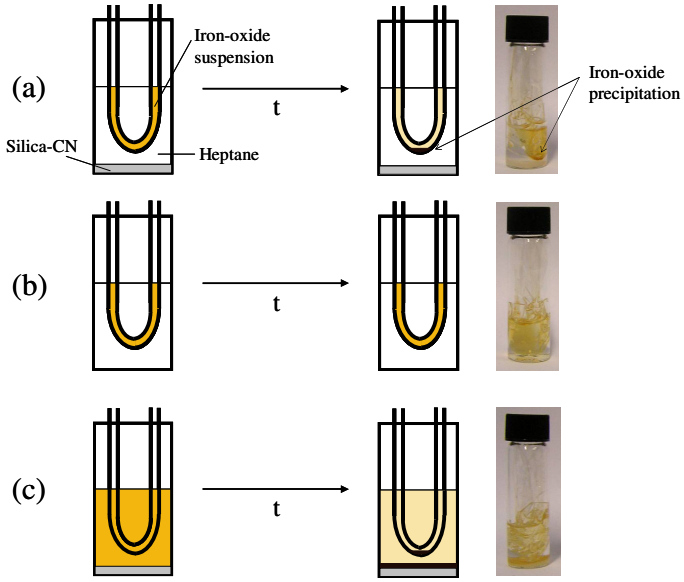

Figure 4.17. An illustration of the results of the dialysis experiments carried out to assess the necessity of contact between iron-oxide and silica-CN for the generation of activated NPs and NPCs. (a) Precipitation was observed in the absence of direct contact between iron-oxide and silica. (b) No precipitation was observed in the absence of silica. (c) Precipitation was observed due to direct contact between iron-oxide and silica.

Two control experiments were also carried out; in the first experiment, the vial did not contain any silica (Figure 4.17 (b)), and the second, the vial contained a heptane suspension of iron-oxide NPs placed over a thin layer of silica (Figure 4.17 (c)). In the first control experiment, there was no visible evidence of precipitation in the absence of silica over the course of 36 hours, and the stability of the particle size was confirmed by PCS at the end of the experiment. This experiment demonstrated that the particles were stable to precipitation at these concentrations, and that the silica is required for the destabilisation of OA-coated iron-oxide NPs. In the second control experiment, visible precipitation was noted both inside the dialysis tubing, as well as on the surface of the silica on the outside of the tubing. This suggests that both direct and indirect contact between OA and silica can result in OA desorption from the surface of the iron-oxide NPs.

Direct contact of the stabilised NPs with the silica substrate may not, in fact, generate activated particles, but instead result in the irreversible binding of the OA-coated NPs or NPCs to the silica surface. A similar situation has been reported by van Ewijk [182] in which an unexpectedly strong attraction between small oleic acid-coated magnetite NPs and larger octadecanol-grafted silica spheres in nonpolar solvents was observed. This lead to the irreversible adsorption of the magnetite particles onto the silica spheres.

On the basis of the results presented here, and the previous work in our group, we can now propose a mechanism for the formation of NPCs due to the aggregation of highly uniform NPs prepared by the thermal decomposition method. During the initial growth phase, stage 1, small clusters are formed through an $N \rightarrow N+1$ aggregation by addition of single, destabilised NPs from the suspension. Because the initial diameter of the clusters is so small, the addition of a single particle to a cluster significantly increases the overall diameter of the cluster. This results in an initial exponential growth rate, as seen in Figure 4.15. Once the clusters have reached a critical diameter, the addition of a single particle no longer increases the overall diameter by an appreciable amount. The rate of increase in the mean diameter decreases and can then be described by a linear function (stage 2). When the primary particles have been

depleted from the suspending medium, any further activation of the NPCs results in an aggregation of clusters, or a 'clustering of clusters'. The Z-Avg then increases exponentially (stage 3), and the aggregation of clusters continues until a sedimentation limit is reached and the clusters fall from suspension and deposit on the surface of the silica (Figure 4.1).

4.4.1.2 The effect of primary particle size on NPC growth rate

The results in Figure 4.6 demonstrate that there is very sensitive dependence of the growth rate on the initial particle size between 3.36 and 4.92 nm, at a constant iron concentration. Indeed, under the conditions used, no growth was observed for 4.92 nm NPs. While the absolute difference in the diameters of 3.36 – 4.92 nm particles is quite small, the surface area-to-volume ratio of the smallest particles is 46% higher than that of the largest particles. At an iron concentration of 0.82 mM, there are ~ 7.6×10^{14} 3.36 nm primary particles, resulting in a total surface area of 0.027 m^2, or ~ 2.4×10^{14} 4.92 nm primary particles, associated with a total surface area of 0.018 m^2. A 46% increase in the iron concentration of the suspension containing the 4.92 nm particles would result in the same total surface area, but Figure 4.7 suggests that this would not be sufficient to account for the significant change in growth rate.

It is also unlikely that the faster rate of clustering observed for the smaller particles is due to incomplete surfactant coverage at the onset of the experiment. The amount of surfactant necessary to form a single monolayer around 4 – 8 nm spherical iron-oxide NPs, synthesised from 2 mmol iron (III) acetylacetonate (Chapter 3), is 0.02 – 0.04 M, and the total amount of C18 surfactant used during the synthesis ranged from 0.3 – 1.5 M. Thus, a large excess of surfactant was present during the synthesis of all the samples.

The increased rate of clustering for the smaller particles is probably the result of an increase in the rate of desorption of the surfactant molecules from the fully-coated NP surface. A decrease in particle size results in an increase in surface curvature, which can lead to a higher prevalence of surface defects. Such surface defect sites may decrease the strength of the bond between the iron-oxide surface and the C18 surfactant, resulting in a faster desorption of the surfactant

molecules and an increased rate of clustering. An additional factor that may be relevant is that the volume associated with the activated sites on the NP surface, where the surfactant has been lost, is larger for smaller particles, due to the greater curvature.

We can quantify the dependence of the growth rate on particle size by examining the three growth stages individually. For the initial and final exponential growth stages, we can plot ln (D_0/D_t) as a function of time, and extract the rate constants from the slope of the straight line; the rate of linear growth in the second stage can be determined directly. The 3.80 nm sample will be used as an initial example. The kinetics plot for stage 1 and stage 3 are shown in Figures 4.18. The full curve, separated into its three growth stages, is also included.

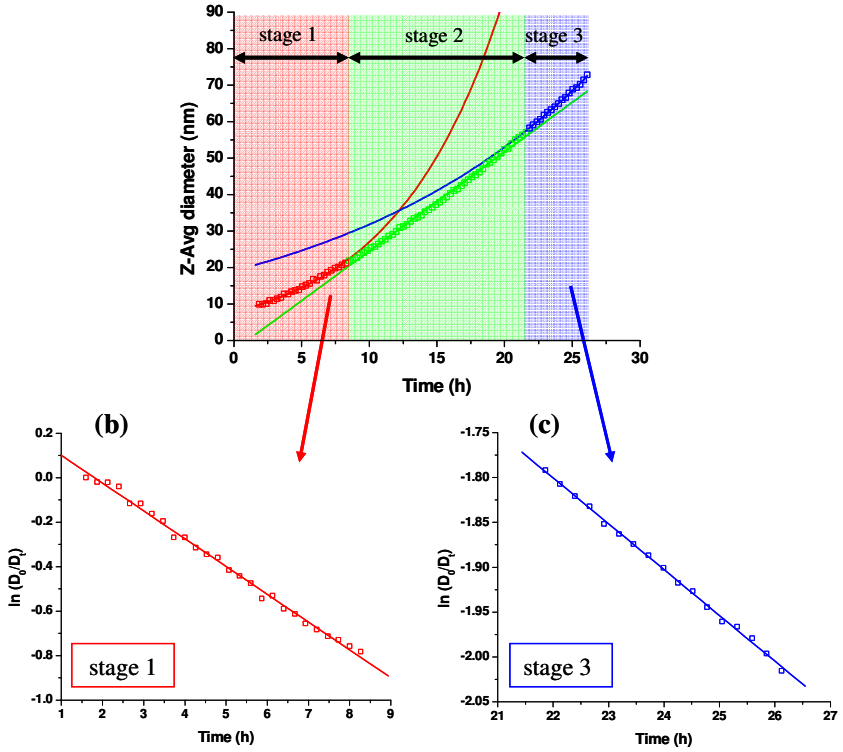

Figure 4.18. (a) Growth curve for the formation of iron-oxide NPCs from primary particles with D_{TEM} = 3.80 nm. The curve is divided into 3 growth stages and fitted with growth functions. — $y = 7.74e^{0.125x}$, $R^2 = 0.995$; — $y = 2.72x - 2.70$, $R^2 = 0.997$; — $y = 19.09e^{0.05x}$, $R^2 = 0.999$. (b) First-order plot for stage 1; — straight line fit to the data: $y = -0.125x + 0.226$; $R^2 = 0.995$. (c) First-order plot for stage 3; — straight line fit to the data: $y = -0.0511x - 0.6764$; R^2=0.998.

It should be noted that this is not a first order kinetics plot, as diameter is not proportional to concentration. We could take the cube of radius to produce a volume which would be proportional to concentration, but this would require the assumption that the clusters have a fractal dimension of 3. Microscopy does strongly indicate that the clusters are densely packed and hence the kinetics of NPC growth are not diffusion limited [183]. Thus, the growth process must be reaction limited, a situation usually termed 'reaction limited cluster aggregation' (RLCA) [184]. It should also be noted that transforming diameter to volume and taking the log would still result in linear time dependence, but with a different slope.

The growth curves for the dispersions containing γ-Fe_2O_3 particles with D_{TEM} of 3.36 nm and 3.98 nm (Figure 4.6) were analysed in the same way and rate constants (k_{s1}, k_{s2}, k_{s3}) were derived for each of the three stages, for each of the three samples. The results are summarised below in Table 3.1. By plotting the natural log of the rate against the reciprocal of size for stages 1 and 2, we obtain a straight line (Figure 4.19). This suggests that the surfactant coverage decreases for smaller particles in the presence of silica (i.e. coverage is a function of size). As mentioned before, this could arise due to (i) higher curvature of the smaller "spherical" particles, reducing both ΔE_{ads}, and/or the steric repulsion between particles, or (ii) an increased number of defects associated with the increased curvature and/or surface area to volume ratio (i.e. the number of defects is inversely related to particle size).

In Chapter 3 we observed increased magnetic anisotropy for the smaller particles, which we attributed to 'shape anisotropy.' Those observations suggest the latter explanation for the change in cluster growth rate applies. Confirmation for this interpretation might be possible from HR-TEM, however, this technique is not currently available to us.

Finally, it is interesting to note that these observations confirm an implicit assumption of our model for the growth process; that is vacancies on the iron-

oxide NP surface arising due to the presence of the silica result in a reduction of the particles' steric stabilisation, which drives aggregation. The magnetic force between two particles is attractive [185,186], but is a function of both the volume and M_s, hence it is far weaker for smaller particles. Nonetheless, we observe faster aggregation for these particles, confirming that the magnetic contribution to the interaction energy is minor.

Table 4.1. Summary of the rate constants derived for the three growth stages as a function of particle size.

D_{TEM} (nm)	k_{s1}, hr^{-1} (R^2)	k_{s2}, nm/hr (R^2)	K_{s3}, hr^{-1} (R^2)
3.36	0.446 (0.998)	470 (0.960)	N/A
3.80	0.125 (0.995)	2.72 (0.997)	0.051 (0.999)
3.98	0.081 (0.991)	0.884 (0.998)	N/A
4.92	N/A	N/A	N/A

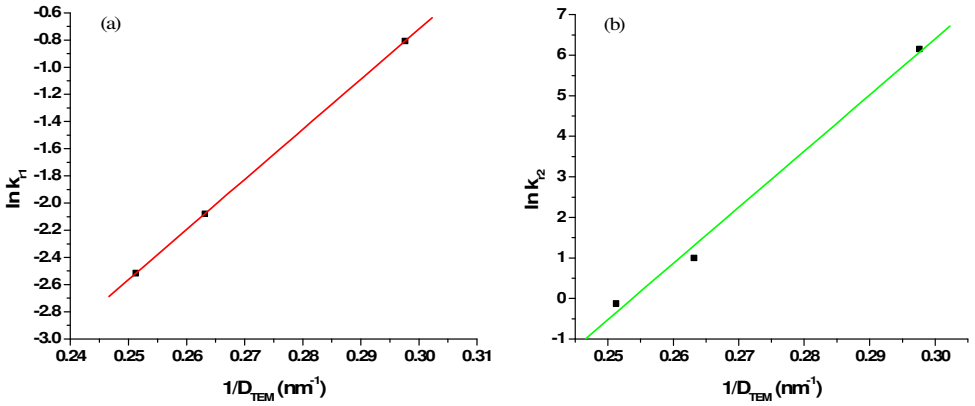

Figure 4.19. A plot of ln k as a function of inverse particle size for three suspensions of iron-oxide NPs. (a) stage 1: — Straight line fit to the data: y = 36.87x – 11.78, R^2 = 0.999; (b) stage 2: — Straight line fit to the data: y = 138.5x – 35.15, R^2 = 0.994.

To confirm the straight line dependence of ln k_{s1} on inverse particle size, suggested by Figure 4.19, more data is required. At present, however, these initial results indicate that knowledge of the primary particle size of iron-oxide

NPs at a given concentration may permit the calculation of the cluster growth rate, and therefore allow us to achieve better control over the cluster size.

4.4.1.3 Effect of concentration on NPC growth rate

The effect of iron concentration on the NPC growth curve was presented in Figure 4.7. The results demonstrate a significant decrease of the cluster growth with an increase in iron concentration, over the 1.0 mM – 5.0 mM concentration range, with a constant primary particle size. A decrease in the NPC growth rate is observed with an increase in iron concentration.

We can again attempt to quantify the dependence of the growth rate on iron concentration by examining the three growth stages at five different concentrations. The 4.0 mM sample can be used as an example, its growth curve, separated into three stages (exponential, linear, exponential), is shown in Figure 4.20.

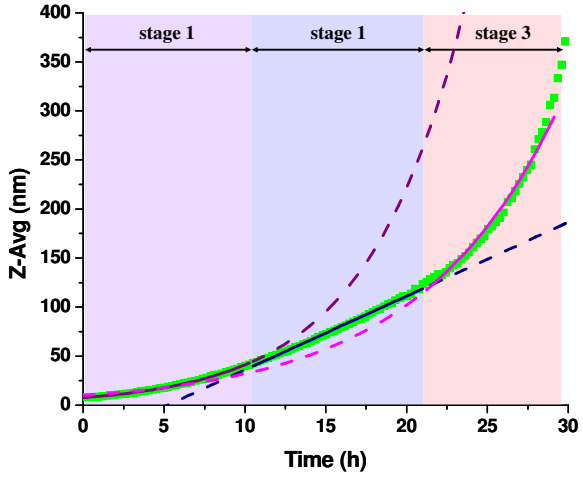

Figure 4.20. Growth curve for the formation of iron-oxide NPCs from 3.7 nm (core size) primary particles. The iron concentration of the FeO suspension = 4.0 mM. The profile is divided into 3 growth stages and fitted with growth functions. – $y = 7.64e^{0.168x}$, $R^2 = 0.999$; – $y = 7.52x - 39.27$, $R^2 = 0.996$; – $y = 10.03e^{0.116x}$, $R^2 = 0.986$.

The growth curves for the dispersions with initial [Fe] = 1.0, 2.0, 3.0, and 5.0 mM (Figure 4.7) were analysed in the same way and rate constants (k_{s1}, k_{s2}, k_{s3}) were derived for each of the three stages for each of the three samples. R^2 values ranged from 0.986 – 0.999, and in most cases, $R^2 > 0.99$. The results are summarised below in Table 3.2. With the exception of one obvious outlier in stage 1, in general, the natural log of the rate constant increases as a function of concentration for stages 1 and 2, as shown in Figure 4.21. The observed concentration dependence is much weaker than the NP size dependence. However, the results suggest that for samples with the same primary particle size, a desired growth rate in the initial stage of growth can be achieved by optimising the iron concentration of the sample.

Table 4.2. Summary of the rate constants derived from the three growth stages as a function of concentration; R^2 values are in parentheses. The primary particle core size in all cases was 3.7 nm.

Initial [Fe] (mM)	**k_{s1}, hr^{-1} (R^2)**	**k_{s2}, nm/hr (R^2)**	**k_{s3}, hr^{-1} (R^2)**
1.0	0.369 (0.995)	406 (0.990)	
2.0	0.266 (0.997)	16.5 (0.992)	0.284 (0.991)
3.0	0.155 (0.998)	8.92 (0.998)	0.133 (0.991)
4.0	0.168 (0.999)	7.52 (0.995)	0.116 (0.986)
5.0	0.158 (0.998)	4.79 (0.999)	0.064 (0.997)

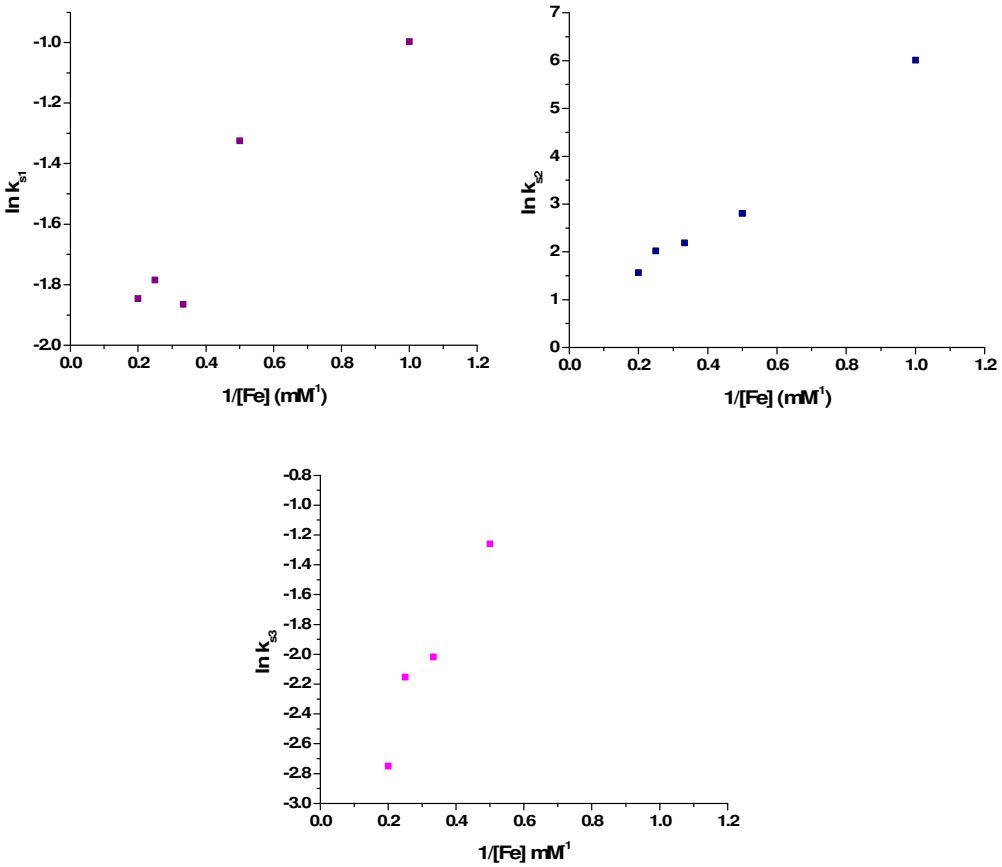

Figure 4.21. A plot of ln k as a function of inverse concentration for five suspensions of iron-oxide NPs.

The concentration dependence can be interpreted as a result of a shift in the equilibrium of surfactant molecules in suspension. The total concentration of C18 surfactant (OA + OAm) in suspension is the sum of both free and bound surfactant molecules. It should be noted that it is currently not known whether OAm is desorbed from NP and NPC surfaces as has previously been observed for OA [169]. In order to simplify the present discussion, we will temporarily overlook this point, and assume that both OA and OAm molecules are desorbed from NP and NPC surfaces.

A heptane suspension of FeO NPs undoubtedly contains residual free C18 molecules originating from the synthesis. It is assumed that while there may be some exchange between the NP-bound and free C18 in suspension, the overall concentration of free C18 is maintained at a constant, equilibrium value. When

the suspension is placed over silica, the binding of the free C18 molecules to the silica surface results in a decrease in the concentration of free C18 in suspension (Equation 4.1), and a therefore a shift in the equilibrium between bound and free C18.

$$SiO_2 + C18 \rightarrow SiO_2 - C18 \qquad \text{Equation 4.1}$$

As C18 binding to SiO_2 is thought to be irreversible [182], the only way to re-establish the equilibrium is through desorption of C18 ligands from the FeO NPs and NPCs, as shown in Equation 4.2, where the star (*) denotes an activated FeO NP or NPC.

$$FeO - C18 \leftrightarrow FeO^* + C18 \qquad \text{Equation 4.2}$$

As the iron concentration of the suspension increases, since the quantity and available surface of silica does not change, there is a corresponding decrease in ratio of activated NPs to non-activated NPs at a given time. This results in a decreased rate of cluster growth.

The kinetics of cluster growth have been presented in some detail, and we have shown that the NPC growth rate is sensitive to both the primary NP core size, and the initial NP to silica ratio. The observed size dependence is much stronger than the concentration dependence. The results suggest that the optimisation of these starting conditions will allow precise control of the growth rate, and thus allow the preparation of NPCs of a desired size and optimal size dispersity.

4.4.2 Controlled NPC growth from mixed-metal FeO:Au co-suspensions

4.4.2.1 DDT-stabilised gold NP suspensions

No evidence of NPC growth was detected for the dispersion of 7.72 nm DDT-stabilised gold NPs (0.71 mM) placed over silica for 19 hours (Figure 4.8). Gold is known to have a strong affinity for sulfur, resulting in the formation of a strong Au-S bond (~ 40 - 45 kcal/mol [187,188]) between the NP surface and the

DDT ligand. The silica cannot compete with the strong thiolate bond and the DDT stabilising ligand is not desorbed from the Au surface. As a result, the Au particles are not activated toward clustering and remain stable in the heptane suspension as single NPs during the time of the experiment.

4.4.2.2 Mixed-metal FeO:Au nanoparticle co-suspensions

The kinetics of mixed-metal NPC growth from the co-suspensions is significantly different from that of iron-oxide NPC growth. The curves for the mixed-metal dispersions reveal an initial period of fast growth, followed a by a stage in which the rate significantly decreases, after which, very little increase in diameter is observed (Figure 4.9). The total iron concentration of the single-metal iron-oxide suspension shown in Figure 4.8 was identical to the iron concentration in the mixed FeO:Au suspension (3.6 mM). The same iron-oxide sample was used to prepare the mixed suspension, so the primary particle size of the iron-oxide NPs was the same in both experiments.

The addition of OA to a heptane suspension of growing iron-oxide NPCs in the presence of silica almost immediately terminates all growth [169]. The free surfactant molecules block adsorption sites on both the silica and the NPs, thereby re-stabilising the activated particles and preventing further growth. The possibility that free DDT surfactant molecules in the FeO:Au co-suspensions could act in the same manner was tested by performing an experiment in which DDT was added to a suspension of growing iron-oxide NPCs. The experiment was performed twice; in the first instance, 116 mg DDT was added to 5 mL of heptane, and 1 drop of the DDT/heptane solution was added to the NPC suspension. In the second experiment, 1 drop of DDT (11.6 mg) was mixed with 4 drops of heptane, and the mixture was carefully added to the suspension of growing NPCs. In the second case, the amount of DDT added was in excess of the amount present in a typical suspension of DDT-stabilised Au NPs and equivalent to the amount of oleic acid that has been shown to terminate iron-oxide cluster growth.

In Figure 4.22, the average hydrodynamic diameters of the iron-oxide particles before and after DDT addition for both trials are presented. In both cases, the

addition of DDT did not have a significant effect on the rate of iron-oxide NPC growth. These results suggest that DDT is not adsorbed onto the surface of the iron-oxide clusters, and even when in great excess, it does not block adsorption sites on the surface of the silica substrate. Thus, it is unlikely that free DDT prevents or slows the cluster growth in mixed-metal FeO:Au suspensions.

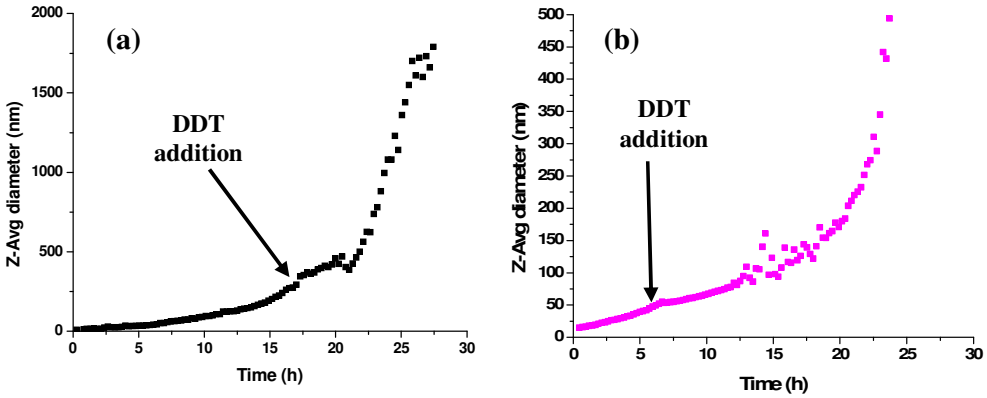

Figure 4.22. The effect of DDT addition to heptane suspensions of growing iron-oxide NPCs placed over silica-CN. (a) 0.3 mg DDT was added after ~17 hours; (b) 11.6 mg DDT was added after 6.7 hours.

It follows that the decrease in the rate of cluster growth for the FeO:Au co-suspensions (Figure 4.9) is caused by the presence of Au NPs. It appears that the growth curves, in all cases, can be described in terms of two separate growth stages, an initial period of faster growth, followed by a period of much slower growth. The growth data obtained for the first 6 – 8 hours could be approximately fitted to a straight line for FeO:Au ratios of 111:1, 91:1, 47:1, and 10:1, with R^2 values ranging from 0.986 – 0.999, as shown in Figure 4.23 (a). The growth curve obtained for the FeO:Au ratio of 77:1 appears to be anomalous, as the initial fast growth stage continued for over 16 hours. The fits were generated in order to investigate the general trend in the growth rate as a function of gold concentration. While at first glance it appears that the data can be described reasonably well by a straight line, closer inspection reveals systematic deviations from the fit. Therefore, the resulting parameters have only been only used to compare the rates in general terms. The fitting parameters obtained from the straight line fits to the fast growth stage of the curves obtained

for the co-suspensions of FeO:Au with concentration ratios ranging from 10:1 to 111:1 are summarised in Table 4.3.

The data in the slower growth rate stage could also be approximated as a linear time dependence for all FeO:Au co-suspensions, as shown in Figure 4.23 (b). This stage generally began after 9 – 12 hours and continued for at least 9 hours for FeO:Au ratios of 111:1, 91:1, 47:1, and 10:1. For the 77:1 ratio sample it did not begin until 21 hours. The fitting parameters and R^2 values obtained from the fits in this growth stage are also summarised in Table 4.3. For both growth stages, the R^2 values were reasonably good.

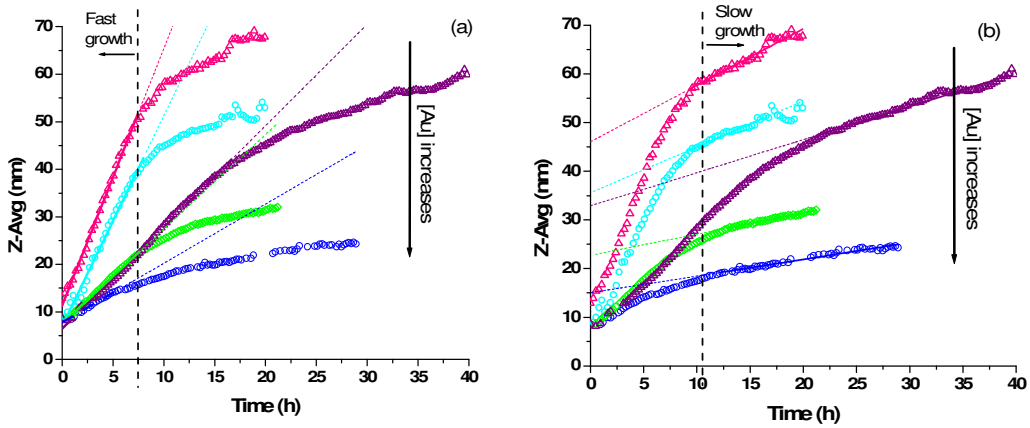

Figure 4.23. NPC growth curves in the presence of silica-CN (50.2 mg) for mixed FeO:Au NP dispersions with an FeO:Au ratio of ▲ 111:1, ○ 91:1, ▼ 77:1, ◊ 47:1, ○ 10:1. The iron concentration ranges from 0.88 to 0.99. The primary particle size of iron-oxide and gold at all concentrations = 3.7 nm (core size) and 7.72 nm (hydrodynamic size), respectively. The dashed lines are straight line fits to the (a) fast and (b) slow linear stages, the details are reported in Table 4.3.

Table 4.3. Summary of the fitting parameters of the straight line fits to the fast and slow linear regions of the growth curves obtained for heptane co-suspensions of FeO:Au with concentration ratios ranging from 10:1 to 111:1.

[FeO]:[Au] ratio	Fast growth stage			Slow growth stage		
	Slope	Intercept	R^2	Slope	Intercept	R^2
10:1	1.24	7.81	0.986	0.343	15.0	0.970
47:1	1.99	7.56	0.999	0.438	22.7	0.989
77:1	2.13	6.46	0.997	0.681	32.9	0.981
91:1	4.42	7.04	0.989	0.942	35.6	0.969
111:1	5.41	11.3	0.997	1.16	46.1	0.962

The amount of Au NPs present in the co-suspensions had a clear effect on the rate of cluster growth. In both growth stages, there was a clear decrease in the slope, and therefore in the cluster growth rate, with an increase in the amount of Au present in the co-suspensions. The initial number of FeO and Au NPs at the start of the growth experiments for each concentration ratio can be estimated from the size of the primary particles and the known concentration of iron and gold in the suspensions. The values are reported in Table 4.4.

Table 4.4. The ratio of the initial number of FeO primary particles to the number of Au primary particles at the start of the co-suspension growth experiment for each concentration ratio.

FeO:Au ratio	
Concentration	Number
10:1	35:1
47:1	164:1
77:1	275:1
91:1	318:1
111:1	394:1

In order to explain the effect of Au NPs on the rate of cluster growth in the FeO:Au co-suspensions, it is necessary to consider four possible types of interactions that can take place between the NPs and NPCs in the suspensions, represented by Equations 4.3 – 4.6. In these equations, an activated NP or NPC is

denoted with a star (*), FeO_1 and FeO_1* refer to single NPs, and FeO_n and FeO_n* signify a NPC composed of more than one NP. We will assume that there are only interactions between FeO particles, and between FeO and Au particles, as we previously demonstrated (Figure 4.8) that Au NPs in suspension in the presence of silica remain stable as single NPs over the relevant timescale.

$$FeO_1^* + FeO_1^* \rightarrow FeO_n \qquad \text{Equation 4.3}$$

$$FeO_n^* + FeO_{1\,or\,n}^* \rightarrow FeO_n \qquad \text{Equation 4.4}$$

$$FeO_1^* + Au \leftrightarrow FeO_1 - Au \qquad \text{Equation 4.5}$$

$$FeO_n^* + Au \leftrightarrow FeO_n - Au \qquad \text{Equation 4.6}$$

The first two types of interactions have been discussed previously; single, activated nanoparticles can aggregate irreversibly to form a small NPC containing two NPs (Equation 4.3), and activated NPCs can grow through the addition of single NPs, or NPCs (Equation 4.4). The presence of Au NPs in suspension offers two additional types of interactions. First, an Au NP may interact with an activated FeO NP (Equation 4.5), or an activated FeO NPC (Equation 4.6), thereby physically blocking the activated site on the FeO surface, rendering it unavailable to other activated FeO NPs and NPCs. This obstruction may be temporary and reversible, as shown by the double-sided arrow, or it may be permanent. If it is permanent, then it can be assumed that as cluster growth proceeds, the DDT-stabilised Au NPs are incorporated into the growing NPC, forming a mixed-metal cluster.

The possibility of a mixed-metal cluster is supported by the data in the initial fast growth stage, but the significant slowing of the growth after time suggests otherwise. If the Au NPs are indeed incorporated into the FeO clusters, it follows that the suspension would be depleted of primary Au NPs much faster than it is depleted of FeO NPs due to the high ratio of FeO:Au NPs at the start of the

experiment (Table 4.4). Once the supply of Au NPs in suspension is exhausted, any further cluster growth would be a result of FeO NP or NPC addition to the growing cluster, and therefore an increase in the growth rate after an initial slow growth stage would be expected. However, this was not observed at any Au NP concentration.

The fact that we observe a slowing of the growth rate in the second stage suggests that after some time, the DDT-stabilised Au NPs present in a FeO:Au co-suspension coat the surface of the growing iron-oxide nanoclusters by forming a protective "shell" around the clusters through physisorption, by interdigitation and entanglement of the surfactant fatty acid chains. This would cause a decrease in the rate of cluster growth by; (i) reducing the number of exposed activated sites on the surface of the FeO clusters, and (ii) protecting the C18 surfactant from further desorption by the silica-CN by providing a physical barrier, thus slowing the generation of further activated sites. Implicit in this explanation of an Au NP shell is the assumption that during the initial fast growth stage, the interaction of DDT-stabilised Au NPs with either an activated FeO NP (Equation 4.5), or small NPCs (Equation 4.6), results in a temporary blockage of the activated site on the FeO surface. This would have to occur on a time scale long enough to slow down the growth rate from that observed for a suspension of pure FeO NPs. The Au would be subsequently 'released' back into suspension making it available for interaction with NPCs at a later stage. The frequency of the Au + FeO* collisions increases with an increase in the number of Au NPs, hence a decrease in the growth rate with an increase in Au concentration in the initial fast growth stage is observed.

We can then interpret the decrease in the growth rate with an increase in Au concentration in the later slow growth stage (Figure 4.23) as a result of an increase in the partial Au nanoparticle surface coverage of the FeO clusters with an increase in the amount of DDT-stabilised Au NPs present in the suspension.

We interpret the apparent transition between the fast and slow growth stages as the time at which the Au NPs begin to adsorb irreversibly to the surface of the FeO NPCs. The fact that this occurs at very different cluster sizes for FeO:Au

ratios of 111:1, 91:1, 47:1, and 10:1 suggests that irreversible binding does not arise due to geometric effects, such as the formation of cavities on the cluster surface. Instead it appears that it begins when the total SA ratio of FeO NPCs to Au NPs decreases to a certain value, Figure 2.24 (a). The ratios presented in this figure were calculated by converting the NPC sizes in Figure 4.9 into (spherical) surface areas, multiplying by the estimated number of clusters in suspension, and dividing by the total surface area of Au NPs available (surface area of sphere), at each Au concentration. This figure is in agreement with our general view that faster growth is associated with higher FeO to Au relative surface area and slower growth occurs as more of the NPC surface is coated. It is very interesting that at lower Au concentrations (FeO:Au ratios of 111:1, 91:1, 77:1, and 47:1) the ratio stabilises at the same value of about 20, even for the anomalous case. We could speculate that this represents a limiting packing density of Au NPs on the NPC surface. By this reasoning, the curve obtained for the ratio of 10:1 would represent a different packing density, associated with higher Au NP concentration at the start of NPC formation. However, this graph was generated assuming that there is no precipitation of FeO over time of the experiment. If we assume a loss of 50% of the FeO NPs after 6 hours, Figure 4.24 (b), the situation is much simpler. Slow growth is associated with NPCs that are almost blocked. At the present time, we do not have sufficient data to distinguish between these two possibilities.

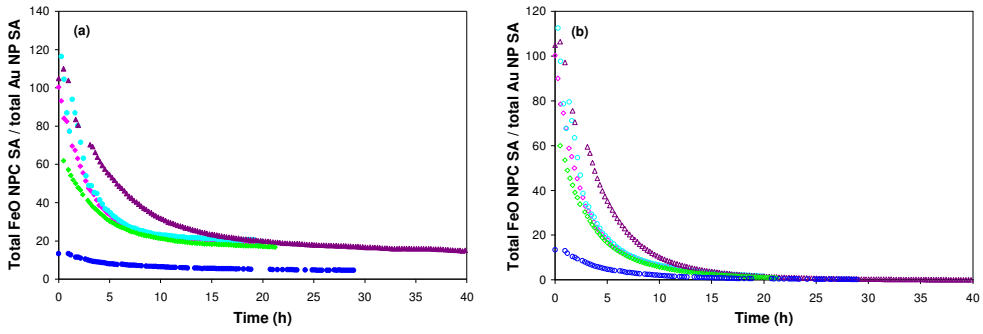

Figure 4.24 The total SA ratio of FeO/Au as a function of time for mixed FeO:Au NP dispersions with an FeO:Au ratio of ▲ 111:1, ● 91:1, ▼ 77:1, ♦ 47:1, ● 10:1. (a) FeO loss due to precipitation is neglected. (b) Gradual precipitation is simulated, at an exponential rate, based on a 50% FeO concentration loss after 6 hours.

The realisation that the Au NPs probably form a shell around the FeO NPCs led us to consider the use of Au NPs to attenuate the growth of growing FeO clusters.

4.4.3 NPC growth attenuation by addition of gold NPs

Attenuation of the growth of FeO clusters by addition of DDT-stabilised Au NPs was demonstrated in Figure 4.13. To further probe the mechanism responsible for this attenuation, an additional iron-oxide growth experiment was performed with three points of intervention (Figure 4.25); (1) A small volume of a DDT-stabilised Au nanoparticle suspension was added to the growing FeO NPCs. (2) After ~ 2 hours, the suspension was removed from the silica, placed in a clean cuvette in the absence of silica, and the size measurements were resumed. (3) After ~ 2 hours, the suspension was placed over fresh silica, and the size measurements were continued for an additional 10 hours. The effect on the Z-Avg, PDI, and mean count rate is shown in Figure 4.25.

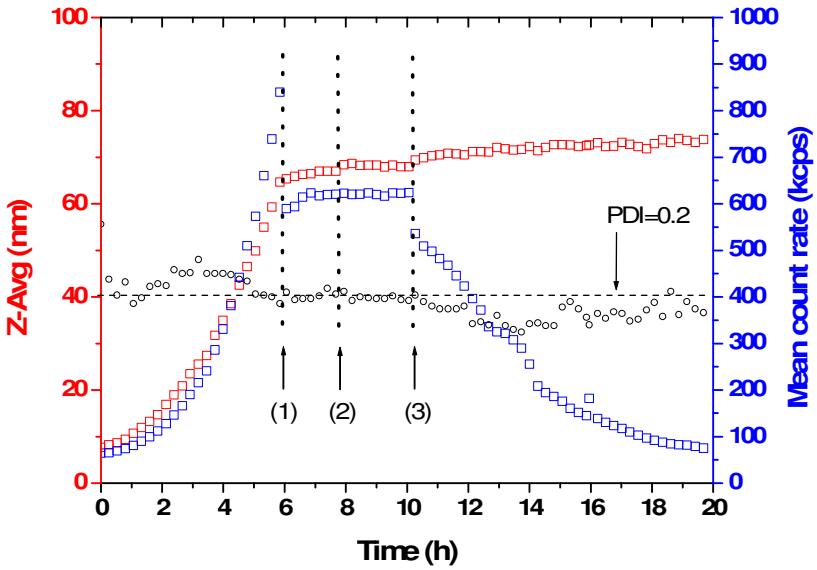

Figure 4.25. The effect of the addition of a heptane suspension of DDT-stabilised primary Au NPs (0.030 mM, D_{PCS} = 7.72 nm) to a suspension of growing iron-oxide NPCs placed over silica-CN. The initial [Fe] of the suspension before exposure to silica-CN was 1.0 mM. The actions performed at times (1) – (3) are described in the text.

The introduction of the Au NPs (1) caused an immediate and significant decrease in the rate of cluster growth, as was observed previously. When the suspension was removed from the silica (2), the growth stopped completely. This further demonstrates that the silica is critical for cluster growth, as it continuously generates the required low concentration of activated particles. It also reveals that the clusters are stable to agglomeration in the absence of silica-CN. Finally, when the suspension was placed over fresh silica (3), cluster growth resumed at approximately the same, slow rate that was observed before the suspension was first removed from the silica. This is an important result, as it indicates that the attenuation of the NPC growth is not simply caused by a blockage of the adsorption sites on the surface of the silica substrate by the gold NPs. Instead, it suggests that the gold NPs actually stabilise the FeO clusters and prevent further aggregation and growth.

These results further confirm that when growing FeO NPCs are exposed to DDT-stabilised Au NPs, the Au nanoparticles coat the growing iron-oxide nanoclusters, forming a core@shell structure. We now proposed a mechanism for the attenuation of FeO NPC growth by the addition of DDT-stabilised Au NPs, and it is shown below in Figure 4.26.

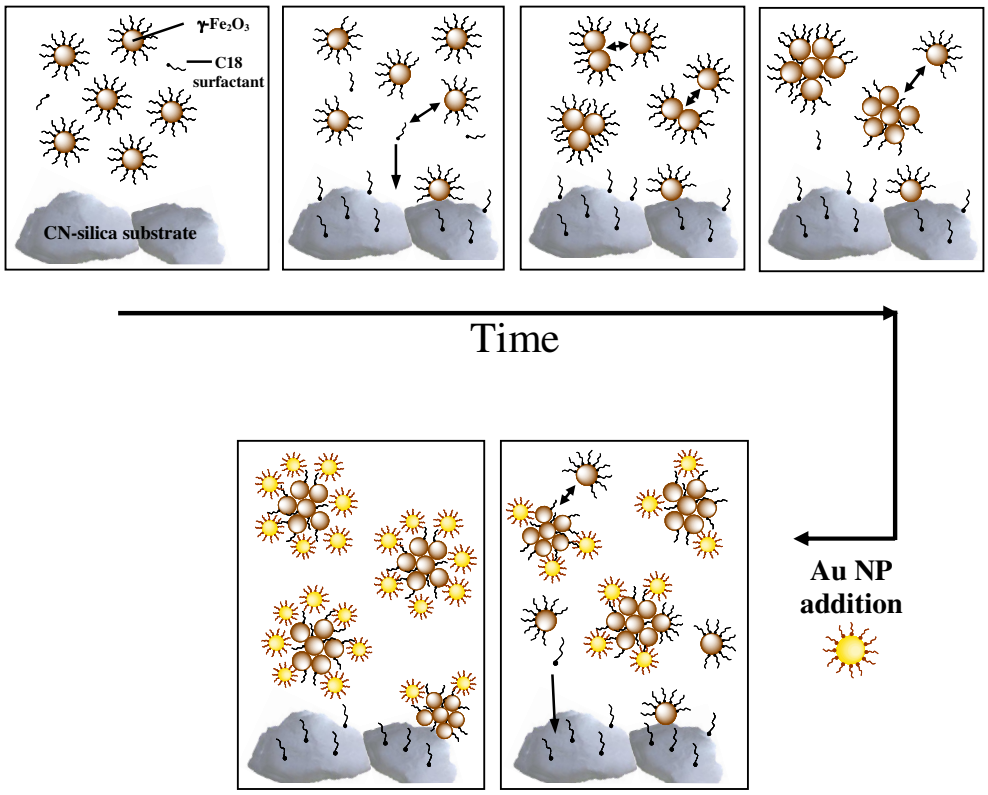

Figure 4.26. The proposed mechanism of the attenuation of FeO NPC growth by the addition of DDT-stabilised Au NPs.

Further evidence of a core@shell FeO@Au structure was provided by scanning electron microscopy (SEM) images (Figure 4.27). These images were obtained following the attenuation of FeO cluster growth by the addition of Au NPs to the suspension. The brighter contrast is generated by the Au NPs, and the darker contrast is due to the FeO NPs. The Au nanoparticles appear to be fairly evenly distributed over the majority of the cluster, though it is clear that there is a higher concentration of Au NPs around the edge of the clusters. There are obvious regions of the cluster where the gold nanoparticles appear to occlude the FeO nanoparticles. On the other hand, there does not appear to be any region of the cluster where FeO nanoparticles can be observed to occlude any Au nanoparticles. This suggests that the Au NPs are indeed located on the surface of the FeO NPC.

The SEM micrographs indicate a cluster diameter of ~ 170 – 210 nm, based on visual inspection of the images. The hydrodynamic diameter was ~ 71 nm. The discrepancy in the diameters measured by the two techniques is probably due to a flattening of the cluster on the TEM grid during the preparation of the samples for imaging, therefore resulting in an apparent larger cluster diameter measured by SEM. It is possible that because the size distribution is not entirely monodisperse, larger clusters may be present in dispersions with a smaller average hydrodynamic size. However, PCS measurements indicated a relatively monodisperse suspension with a reasonable PDI value of 0.20 at the time the sample was removed for SEM.

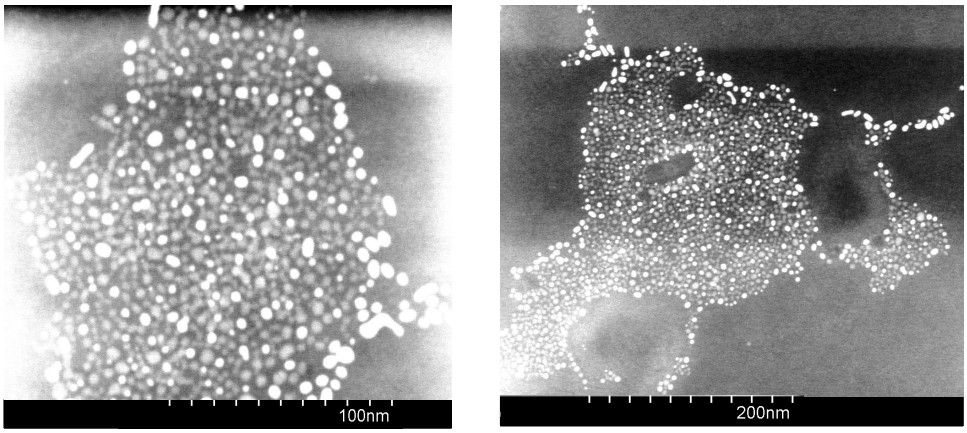

Figure 4.27. Dark-field STEM images of FeO:Au NPCs, recorded on a Hitachi S5500. A suspension of DDT-stabilised Au NPs was added to a heptane suspension of 71 nm FeO NPCs in the presence of silica-CN.

TEM images were also obtained for the same sample following the attenuation of FeO cluster growth by the addition of Au NPs (Figure 4.28). In this case, the dark contrast is generated by the Au NPs, and the lighter contrast is due to the FeO NPs. Once again, the Au nanoparticles appear to be fairly evenly distributed over the majority of the cluster. The TEM micrographs indicate a cluster diameter of ~ 300 nm.

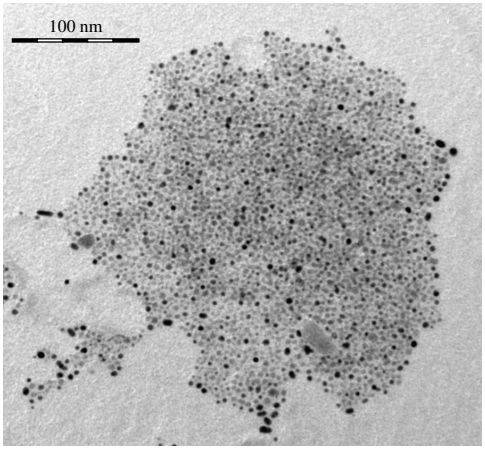

Figure 4.28. TEM image of a FeO:Au NPC recorded on a JEOL 2000 FX TEMscan instrument. A suspension of DDT-stabilised Au NPs was added to a heptane suspension of 71 nm FeO NPCs in the presence of silica-CN.

We have presented substantial experimental evidence and microscopy images suggesting the successful preparation of FeO@Au core@shell NPCs of controlled size, though the results are still preliminary. At present we are waiting for further instrument availability for additional microscopy.

4.5 Conclusions

We have presented strategies toward the development of water stable magnetic nanocluster systems with controlled size and optimal magnetic properties. Iron-oxide NPCs of controlled size were grown from primary NPs synthesised by the thermal decomposition method. The effect of primary particle size and iron concentration on the rate of growth were studied, and provided insight into the kinetics of cluster growth. This has laid the groundwork for further kinetic investigations within the group, and a mathematical model is currently under development to describe the observed aggregation behaviour (manuscript in preparation). The basic principles of the model will be introduced in Section 4.6.

The method for cluster growth was extended to include the preparation of mixed-metal iron-oxide:gold NPCs, which we believe assemble into FeO@Au core@shell structures. The preparation method offers significant advantages over

current strategies for gold-coated magnetic NP and NPC synthesis, including controlled cluster size over a very wide range, and partial Au surface coverage, which is necessary to maintain high M_s values. Furthermore, the successful preparation of mixed-metal iron-oxide:gold NPCs may open up a new pathway to size-controlled nanocomposite materials of various compositions.

While the polymer-mediated phase transfer and aqueous stabilisation of dispersed NPs was of limited success (Appendix B), the proposed core@shell FeO@Au structure provides a wealth of new possibilities to increase the hydrophilicity of the iron-oxide NPCs, especially by ligand exchange, due to the well-established surface chemistry of gold.

4.6 Future work

In order to further analyse the results presented in this chapter, a mathematical model is currently being developed in the group. This work will be briefly described here as, in our opinion, it offers the most likely route to a detailed, and perhaps quantitative, understanding of the kinetics of NPC growth. Our aim is to describe the aggregation behaviour of C18-stabilised iron-oxide NPs in the presence of silica-CN, and to correlate this with surface phenomena, specifically with the extent of surfactant coverage. An important feature of the growth data presented in this chapter is the self-preservation of the particle size distributions (Figure 4.3). We have adopted a Smoluchowski approach [189,190] to model this behaviour and simulate the evolution of the NPC size distribution over time. The Smoluchowski equation is shown in Equation 4.7.

$$\frac{\partial n_k(t)}{\partial t} = \frac{1}{2}\sum_{i+j=k} K_{ij}^{A} n_i(t) n_j(t) - n_k(t)\sum_{i=1}^{\infty} K_{ik}^{A} n_i(t) \qquad \text{Equation 4.7}$$

In this equation, $n_k(t)$ is the number concentration of aggregates composed of k primary particles at time t. The first summation on the right side of the equation expresses the formation of k aggregates from collisions of smaller aggregates composed of i and j primary particles, where K_{ij} is the rate constant (or kernel)

for aggregation. The second summation accounts for the rate of loss of k aggregates as they are incorporated into larger aggregates. The Brownian aggregation kernel (K_{ij}^{BA}), i.e. for non-interacting particles in random motion, can be calculated by Equation 4.8.

$$K_{ij}^{BA} = 4\pi(D_i + D_j)(R_{c,i} + R_{c,j}) \qquad \text{Equation 4.8}$$

In this equation, D_i and D_j are the diffusion coefficients of the aggregates, and $R_{c,i}$ and $R_{c,j}$ are the collision radii of the two NPCs. The fact that the NPC structures are dense, not dendritic or fractal (as determined by TEM), indicates that they are formed by reaction limited colloidal aggregation (RLCA), in which very few collisions are actually successful [183,191]. To take this into account, the Brownian aggregation kernel is divided by W_{ij}, known as the Fuchs stability ratio [186], which is a ratio of the frequency of collisions between particles to the frequency of collisions leading to aggregation (Equation 4.9).

$$K_{ij}^{A} = \frac{K_{ij}^{BA}}{W_{ij}} \qquad \text{Equation 4.9}$$

This ratio is dependent upon the colloidal interactions between aggregates. The ratio can be calculated as a function of the total interaction potential energy, $\Phi_{total}(a)$, using Equation 4.10, where a is the surface-to-surface closest distance between the aggregates ($a + R_{ci} + R_{cj}$ is the centre-to-centre separation).

$$W = 0.5\left(R_{ci} + R_{cj}\right)\int_0^{\infty} \frac{\exp\left(\Phi_{total}(a)/k_B T\right)}{\left(0.5(x_{ci} + x_{cj}) + a\right)^2} da \qquad \text{Equation 4.10}$$

The total interaction potential, Φ_{total}, is usually expressed as a sum of three attractive and repulsive forces (Equation 4.11), namely the attractive van der Waals forces (ϕ_{vdW}) [186,192], and both osmotic (ϕ_{osm}) [192,193] and elastic (ϕ_{elas}) [192] repulsive forces. The electrostatic double-layer repulsion, which is described by the DLVO model, is not relevant in our case.

$$\Phi_{total} = \Phi_{vdW} + \Phi_{osm} + \Phi_{elas} \qquad \text{Equation 4.11}$$

The osmotic and elastic repulsive forces, which act between the stabilising ligand chains, are dependent on ligand coverage. Thus, the total force, and therefore W (Equation 4.10), is a function of surfactant coverage.

The results of the model will be compared with the experimental data. An accurate model of the evolution of the NPC size distribution will allow us to predict the growth behaviour and extract the degree of surface coverage of the clusters at any point in time.

CHAPTER 5

Preparation and characterisation of size specific magnetoliposome suspensions

5.1 Introduction

Liposomes, or lipid vesicles, were introduced by A. D. Bangham in 1965 [194] and were quickly recognised as good candidates for use as drug delivery vehicles. They consist of an aqueous body within a lipid bilayer, and they resemble cell membranes in both structure and composition. Their colloidal stability, biocompatibility, microencapsulation potential and surface properties also make liposomes attractive candidates for use as carrier systems for MRI contrast agents [160], and hyperthermia mediators [160,195-197]. Liposomes can facilitate concurrent diagnosis and therapy by offering the ability to encapsulate both an MRI contrast agent and a water soluble pharmaceutical agent within the aqueous interior. Additionally, the phase transitions and membrane dynamics of liposomes can be exploited to trigger release of encapsulated contents and control leakage, allowing a more efficient delivery into target tissues [198-200]. Hence the ongoing efforts of researchers to study these processes with a view toward actively controlling permeability [201-203]

Liposomes which contain solid iron-oxide particles are of particular interest as contrast agents for MRI and drug delivery vehicles due to their low toxicity and favourable magnetic properties. For instance, iron-oxide nanocrystals encapsulated within PEG-grafted liposomes have been reported to be efficient MRI contrast agents for *in-vivo* imaging following a mouse model imaging study [195]. Additionally, rhodamine-labeled magnetic fluid-loaded liposomes have been assessed for potential magnetic targeting to select intravascular areas of the brain by *in vivo* imaging in mice [204]. The term “magnetoliposome” was first used by De Cuyper and Joniau [205] to describe structures in which the interior of the phospholipid vesicle is entirely packed with magnetic material, and the inner phospholipid layer is adsorbed directly onto the nanoparticle surface. The preparation method described by De Cuyper involves the incubation and dialysis of surfactant stabilised magnetic particles with preformed phospholipid vesicles. The phospholipids are thought to displace the surfactant molecules and arrange in a bilayer configuration around the iron-oxide core [205,206]. Since its introduction, the term “magnetoliposome” has also been widely adopted by other groups and used to describe liposomal structures in which solid iron-oxide

particles are thought to be contained within the internal aqueous compartment of the liposome [195,207]. The preparation method, in this case, commonly involves the hydration of a lipid film with a magnetic fluid followed by extrusion to homogenise the dispersion [195,208].

While these two distinct preparative procedures are widely accepted and routinely used in the preparation of liposomal iron-oxide nanocomposites, to the best of our knowledge, no attempt has been made to compare and evaluate the physical properties and particle morphology of the resulting assemblies. In this work, we aim to investigate whether the properties and morphology of magnetoliposomes depend on the method of preparation.

The first part of this chapter describes the synthesis of magnetic iron-oxide nanoparticles and the subsequent stabilisation inside phospholipid vesicles by two different methods, a 'solid'-type method, and an 'aqueous'-type method, forming what will be referred to as solid magnetoliposomes (SMLs) and aqueous magnetolipsomes (AMLs), respectively. As a first attempt at a SML preparation, the De Cuyper method was used, but the resulting suspensions did not exhibit the expected superparamagnetic properties. Therefore, the SML preparation method utilised in the work reported here is a modification of a procedure introduced by Shen et al. [81,82] for the preparation of stable, water-based suspension of bilayer fatty acid-coated magnetic nanoparticles. In this two-step method, an alkaline coprecipitation of ferrous and ferric salts is carried out in the presence of phospholipid molecules, which are believed to chemisorb onto the magnetite surface [99]. This is followed by the physical adsorption of a secondary phospholipid layer, forming a stable bilayer around the iron-oxide core. The resulting magnetoliposome suspensions prepared by both the 'solid'-type and 'aqueous'-type methods were characterised by dynamic light scattering and infrared spectroscopy. The magnetic resonance properties were then assessed using NMRD.

The therapeutic and diagnostic potential of magnetoliposomes as potential contrast agents and drug delivery vehicles is determined by the combined properties of high saturation magnetisation, colloidal stability, and effective biodistribution, all of which are strongly dependent on particle size. There has been significant focus in the literature on control of nanoparticle size using different strategies [90,100,209], and in the previous two chapters we have discussed control of the synthetic and dispersion conditions as methods to control the particle size and the emergent size-dependent magnetic properties of fatty acid-stabilised nanocomposites. In this chapter we will also introduce the technique of magnetic filtration as a means of selective particle size control for magnetoliposomes. The advantage of magnetic filtration lies in its ability to separate particles based on their magnetic parameters, therefore allowing the fractionation of the suspension into samples with desired magnetic properties.

In a recent report in Science [210], Colvin and co-workers demonstrated the efficacy of low-field magnetic separation, on 4 – 12 nm Fe_3O_4 nanocrystals, which has potential for improved arsenic removal from water. Previous reports also exist on the separation of magnetoliposomes from non-adsorbed phospholipids by application of a high magnetic field gradient [204,205,211]. Similarly, Moeser and co-workers assessed the feasibility of high-gradient magnetic separation to remove phospholipid-coated magnetic nanoparticles from water for chemical processing and protein separations [212]. Although these authors studied the effect of flow velocity on the capture efficiency for different phospholipid-coated particles, in the size range of 25 – 50 nm, to the best of our knowledge the size-selection capabilities of magnetic filtration have yet to be explored. We have demonstrated the utility of magnetic filtration to fractionate magnetoliposome suspensions into samples with average particle sizes ranging from 50 to 250 nm with relatively narrow size distributions, by varying both the magnetic field and the flow rate. The benefits of magnetic filtration over other size-selection techniques will be discussed. Finally, magnetic filtration will be presented as a promising alternative to extrusion in the preparation of a homogenous suspension of AMLs.

5.2 Experimental

5.2.1 Materials

1,2-Dioleoyl-*sn*-glycero-3-[phospho-rac-(1-glycerol)] (sodium salt) (DOPG) was purchased as a lyophilised powder (> 99%) from Avanti Polar Lipids (Alabaster, AL, USA) and stored at -20°C. Iron (II) chloride tetrahydrate (> 99%) was purchased from Fluka (Buchs, Switzerland). Iron (III) chloride-6-hydrate (> 99%) was purchased from Riedel-de-Haën (Seelze, Germany). All reagents were used without further purification. Deionised water was deaerated before use.

5.2.2 Synthesis of iron-oxide cores

Two approaches were used to synthesise the iron-oxide cores. In the first approach, aqueous dispersions of uncoated magnetite were prepared by alkaline chemical coprecipitation of iron salts with ammonium hydroxide following a modification of the method described by Khalafalla and Reimers [80]. In a typical preparation, a mixture of $FeCl_3 \bullet 6H_2O$ and $FeCl_2 \bullet 4H_2O$ in a 2:1 molar ratio was added to 20 mL deoxygenated water, with stirring, in a 100 mL 3-neck round-bottomed flask placed in a sand bath. The salts dissolved in the water forming a yellow coloured solution. The system was degassed by purging nitrogen through the flask for 15 minutes prior to heating. A 3-neck flask was required to simultaneously attach a nitrogen flow, a water-cooled condenser, and a thermometer to the system. The solution was slowly heated to 80°C with strong magnetic stirring. The reaction temperature was reached in 15 – 20 minutes. After 30 minutes at 80°C, the stirring speed was increased to a maximum, and 1.5 mL of 33% ammonia was added to the flask. A black precipitate was immediately observed, indicating the formation of magnetite nanoparticles. Crystal growth was allowed to proceed for 15 minutes with vigorous stirring. The suspension was removed from the heat and allowed to cool naturally to room temperature. A solution of equal volumes of methanol and acetone (40 mL total volume) was added to precipitate the black magnetite from suspension, and the flask was placed over a bar magnet to isolate the nanoparticles. When the particles had settled over the magnet and the supernatant appeared clear, the solvent was decanted from the magnetite. The magnetite was washed again with

acetone and methanol (50/50 v/v). To produce a temporarily stable water suspension of uncoated particles, the magnetite was washed 2-3 times with DI H_2O to lower the pH. The suspension was then used in the formation of magnetoliposomes by the thin film-hydration method [213], described in section 5.2.3.

In the second approach, magnetite nanoparticles coated with DOPG, which for the purposes of this chapter will be referred to as mono-SML, were synthesised by carrying out the alkaline coprecipitation of iron salts in the presence of the phospholipid molecules. A mixture of $FeCl_3 \bullet 6H_2O$ and $FeCl_2 \bullet 4H_2O$ in a 2:1 molar ratio was added with stirring to 20 mL deoxygenated H_2O in a 3-neck round-bottomed flask as described above. The salts dissolved in the water forming a yellow coloured solution. The system was degassed by purging nitrogen through the flask for 15 minutes prior to heating. The solution was slowly heated to 80°C over 15 – 20 minutes with strong magnetic stirring. After 30 minutes at 80°C, the stirring speed was increased to a maximum. One fifth of the total phospholipid to be added (0.85 mM dissolved in 0.5 mL methanol) was added to the reaction mixture, immediately followed by the addition of 1.5 mL of 33% ammonia to precipitate the metal ions. A black precipitate was immediately observed, indicating the formation of magnetite nanoparticles. The remaining DOPG (3.41 mM dissolved in 1 mL methanol) was then slowly added to the mixture over a 5 minute period, and crystal growth was then allowed to proceed for 15 minutes with vigorous stirring at 80°C. The suspension was removed from the heat and allowed to cool naturally to room temperature. A solution of equal volumes of methanol and acetone (40 mL total volume) was added to precipitate the suspension, and the flask containing the black, DOPG-coated magnetite was placed over a bar magnet to isolate the nanoparticles. When the particles had settled over the magnet and the supernatant appeared clear, the solvent was decanted. The precipitate was washed an additional four times with methanol and acetone (50/50 v/v), and during the final wash, the sample was split into two fractions (A and B). The precipitate in both fractions was immobilised using a permanent magnet, and the methanol/acetone was decanted. The DOPG-coated magnetite of fraction A was dispersed in 10 mL $CHCl_3$ and reserved for PCS and NMRD characterisation. The DOPG-coated magnetite of fraction B was

resuspended in 10 mL DI H_2O in preparation for magnetoliposome formation through the addition of a secondary, physisorbed phospholipid layer, described in section 5.2.3.

5.2.3 Formation of magnetoliposomes

Magnetoliposomes were prepared by two methods:

(I) *Thin film-hydration method* [213]: DOPG (74 mg) was dissolved in $CHCl_3$, and the solvent was subsequently removed overnight under a gentle stream of N_2 to form a thin film. Four preparation steps followed and will be discussed in detail throughout this chapter:

(a) Preparation of the uncoated magnetite (described above).

(b) Hydration (H). Multilamellar magnetoliposomes were formed by hydrating the lipid film with the appropriate volume (generally 18 – 20 mL) of a previously prepared aqueous suspension of uncoated magnetite nanoparticles. The suspension was allowed to hydrate above the lipid gel-to-liquid crystalline phase transition temperature, Tm (-18° for DOPG [214]) for at least two hours with periodic vortex mixing.

(c) Freeze-thaw (FT). The multilamellar magnetoliposome suspensions were subjected to six freeze-thaw cycles with liquid N_2 and warm water (~40°C) to form unilamellar vesicles.

(d) Extrusion or Magnetic filtration (MF). To prepare samples with a homogeneous size distribution, samples were either extruded through two stacked polycarbonate membranes with a 0.2 μm pore size (Whatman Nuclepore; Clifton, NJ) using an Avanti Polar Lipids mini extruder (Alabaster, AL), or magnetically filtered (section 5.2.4). Both techniques provide suspensions of unilamellar vesicles of a desired size. All extruded and magnetically filtered samples were collected and retained for characterisation by PCS and NMRD.

(II) *'Solid'-type physisorption method*: Magnetite nanoparticles coated with a monolayer of DOPG and temporarily dispersed in H_2O were heated to 65°C under a steady stream of N_2 with vigorous stirring in a 3-neck round-bottomed flask fitted with a water-cooled reflux condenser. After 30 minutes at 65°C, 10 mM ammoniated DOPG was added slowly to form a secondary phospholipid

layer around the nanoparticles, and the suspension was stirred for an additional 25 minutes. Upon cooling to room temperature, the suspension was sonicated for 30 minutes in a bath – sonicator, then placed over a bar magnet for approximately 20 minutes. The supernatant containing the smallest DOPG magnetoliposomes was collected and retained for characterisation.

For clarity, the steps undertaken in the SML and AML preparations are illustrated in Scheme 5.1.

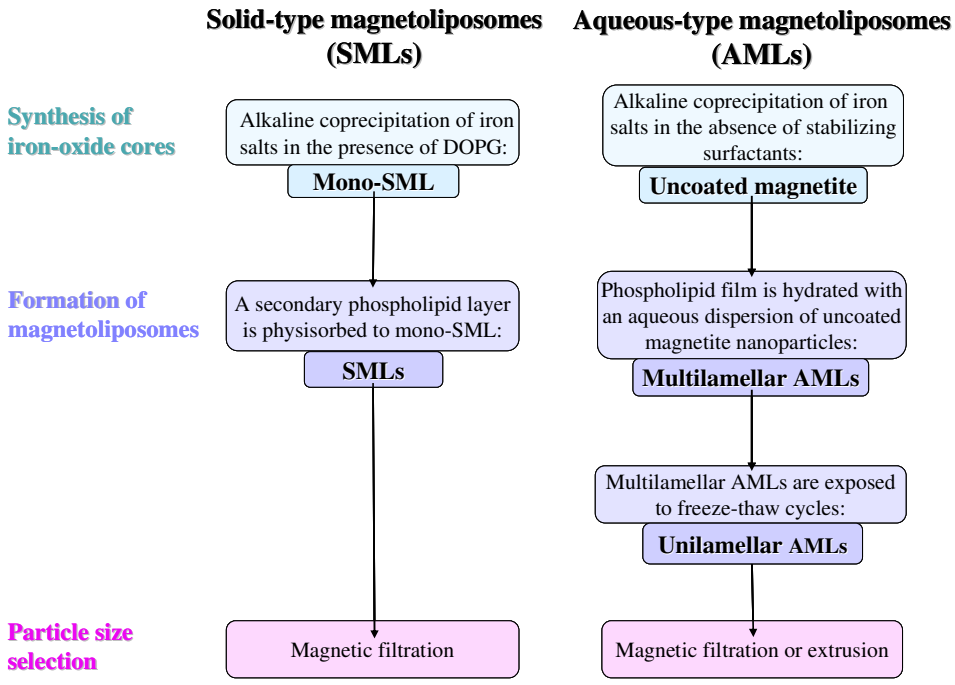

Scheme 5.1. Scheme of the steps involved in both the SML and AML preparations.

5.2.4 Magnetic filtration

Magnetic filtration was performed by using a variable flow peristaltic pump to pump aqueous magnetoliposome suspensions through 1/8 inch ID tubing packed with ~60 mg of steel wool, which was placed between the poles of an electromagnet. Flow rates were varied between 4 – 600 mL/hr and the magnetic field was varied between 0.01 and 1.64 T. A single aliquot of the

magnetoliposome suspension was pumped through the magnetic filtration system (Figure 5.1) at a rate of 4 mL/hour at a field of 0.47 T. At this field and flow rate, all the magnetic material was retained as solid particles on the magnetised steel wool (the retentate), and the non-magnetic material was eliminated from the sample. While continuing to apply a magnetic field, subsequent volumes of deionised water were pumped through the system at increasing flow rates. Each aliquot, or eluent, was collected and retained for characterisation. The magnet was switched off and the final retentate was collected by pumping water through the system to redisperse the retained, solid particles. Thus, this method produced multiple eluent samples and one final retentate sample.

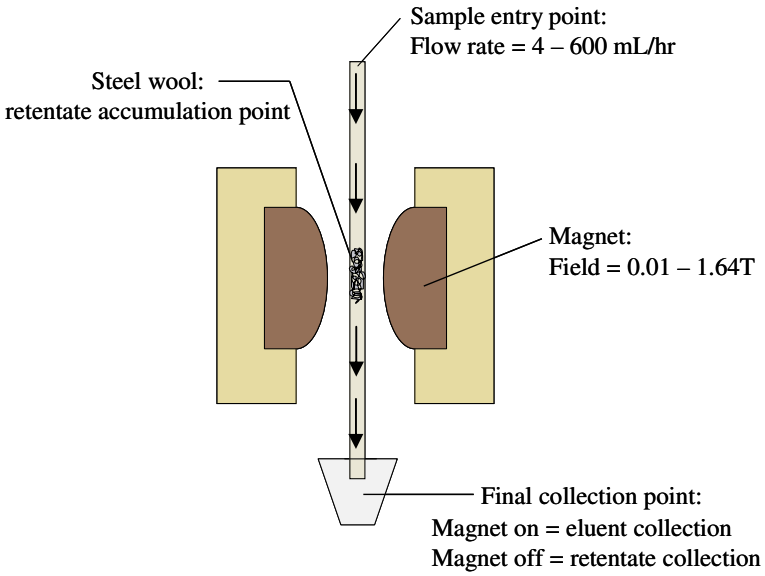

Figure 5.1. Schematic representation of magnetic filtration.

5.2.5 Characterisation

The magnetoliposome suspensions were characterised by PCS and NMRD as described in Chapter 2.

Total iron content was determined by AAS as described in Chapter 2. To prepare the samples for analysis, five drops of 6N analar grade HCl and 1 mL H_2O were added to small aliquots (approximately 0.3 – 0.5 mL) of the magnetic fluid.

Equal volumes of 1% (v/v) Triton X-100 solution were added to the magnetoliposome suspensions to dissolve the phospholipid membrane. The solutions were heated to boiling which was allowed to continue until the volume was reduced to a few drops. H_2O (25 mL) was then added and the solutions were again heated to boiling. The solutions were cooled to room temperature, then diluted appropriately into the 0.5 – 2.5 mg/L linear working range.

Attenuated total reflectance (ATR) infrared spectra were recorded on a Spectrum GX FT-IR System (Perkin Elmer; Norwalk, CT, USA). Liquid suspensions were placed on the face of a ZnSe trough plate crystal and the solvent was evaporated under N_2. Eight scans were recorded over a 4000-650 cm^{-1} spectral range with 2 cm^{-1} spatial resolution. ATR and baseline corrections were applied followed by 19-point smoothing (Spectrum software v.3.01; Perkin Elmer LLC; Norwalk, CT, USA).

5.3 Results

5.3.1 Formation of magnetoliposomes

5.3.1.1 Formation of SMLs

The ATR-IR spectrum of mono-SMLs is shown in Figure 5.2. To investigate the mode of interaction between DOPG and the iron-oxide nanoparticles, ATR-IR spectra of pure DOPG liposomes and uncoated magnetite were also recorded, and are included in Figure 5.2 for comparison. Considering first the spectrum of uncoated magnetite, it contains two bands at 3382 cm^{-1} and 1649 cm^{-1}, which can be attributed to the O-H stretching and H-O-H bending modes of adsorbed water molecules [215]. Considering next the spectrum of pure DOPG liposomes, it contains a strong band at 2487 cm^{-1} caused by O-D stretching of residual D_2O, present in the sample due to incomplete drying of the suspension on the ATR crystal. The remaining bands in the spectrum arise from vibrational modes of DOPG; bands at 2923 cm^{-1}, 2854 cm^{-1}, and 1459 cm^{-1} can be attributed to the asymmetric and symmetric C-H stretching and the C-H scissoring modes, respectively; the feature at 3362 cm^{-1} is due to O-H stretching of the hydroxyl groups of the phospholipid headgroup; the band at 1726 cm^{-1} is due to C=O stretching, and those at 1204 cm^{-1} and 1052 cm^{-1} are due to the asymmetric and symmetric PO_2^- stretching modes.

The mono-SML spectrum contains all of the characteristic bands of both magnetite and DOPG, with two notable exceptions; firstly, the asymmetric PO_2^- stretch (1211 cm^{-1} in pure DOPG), is completely absent from the mono-SML spectrum. Secondly, the broad hydroxyl group O-H stretching band is also absent from the mono-SML spectrum. The implication is that both the phosphate and hydroxyl groups of DOPG are involved in the bonding of phospholipid molecules to the iron-oxide surface in mono-SML samples.

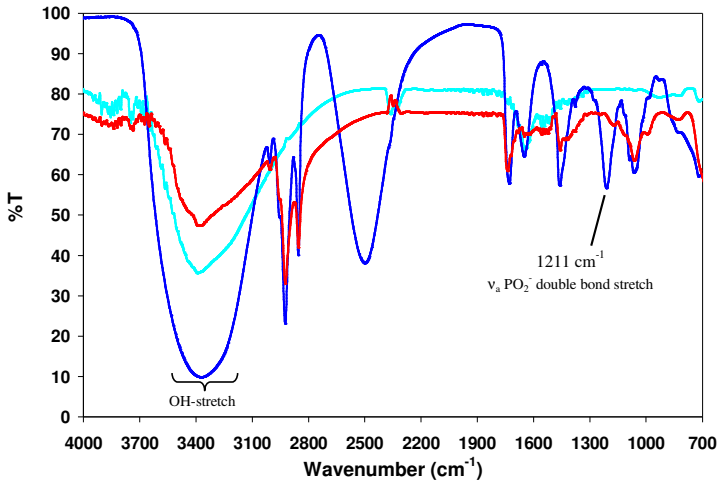

Figure 5.2. ATR-IR spectra of uncoated magnetite, pure DOPG, and mono-SMLs.

The spectrum of mono-SMLs is compared with the spectrum of SMLs in Figure 5.3. The asymmetric PO_2^- stretching mode, absent in the spectrum of mono-SML, appears at 1204 cm^{-1} in the SML spectrum. Additionally, there is a broadening of the O-H stretching band above 3000 cm^{-1} in the SML spectrum, consistent with the presence of hydroxyl group vibrations. This suggests the presence of non-bonded DOPG in the SML sample.

The IR band assignments for pure DOPG, mono-SMLs, and SMLs are summarised in Table 5.1. ATR-IR analysis confirms the presence of DOPG in both the mono-SML and SML samples, and further suggests bonding of DOPG to the surface of iron-oxide surface through hydroxyl and phosphate moieties. These results validate the utility of the SML preparation method to form DOPG magnetoliposomes.

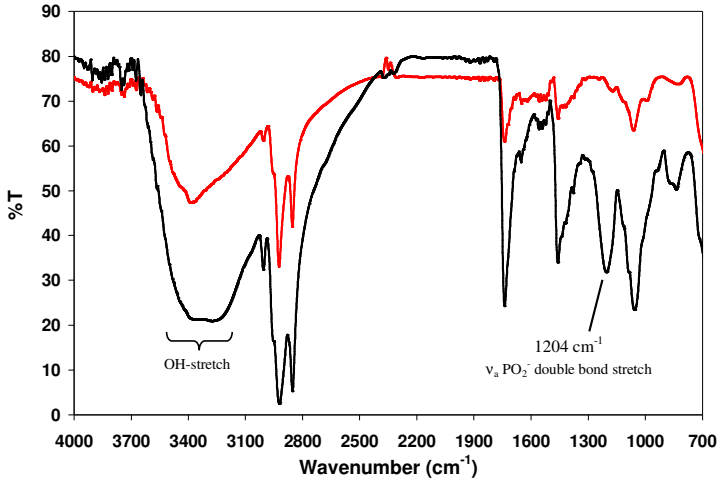

Figure 5.3. A comparison of the ATR-IR spectra of — mono-SMLs, and — SMLs.

Table 5.1. Summary of the infrared band assignments for pure DOPG liposomes, DOPG-magnetite, and SMLs. The structure of DOPG is also shown for reference.

Pure DOPG ν (cm^{-1})	**Mono-SML ν (cm^{-1})**	**SMLs ν (cm^{-1})**	**Assignment [216-218]**
3362	3390	3272	OH stretch
3003	3006	3005	sp^2 CH stretch
2923	2923	2922	ν_a CH_2 stretch
2854	2854	2853	ν_s CH_2 stretch
1726	1738	1739	C=O stretch
1459	1459	1459	ν_s CH_2 scissor
1211		1204	ν_a PO_2^- stretch
1052	1063	1057	ν_s PO_2^- stretch

DOPG 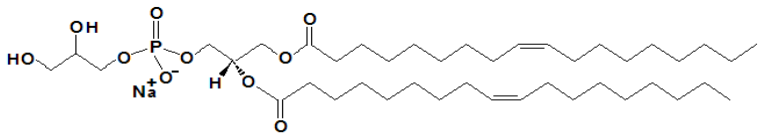

A cryo-TEM image for a representative sample of DOPG SMLs is shown in Figure 5.4. The micrograph reveals spherical, well dispersed, and uniform particles with an approximate diameter of 75 nm, based on visual observation of

the image. The average PCS diameter (D_{PCS}) of the same magnetoliposome suspension was 82.9 nm.

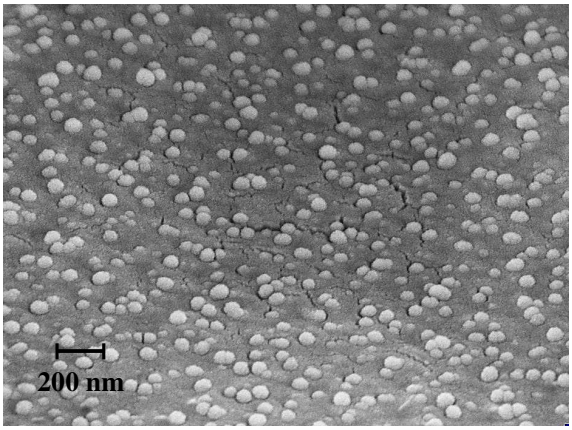

Figure 5.4. Cryo-TEM image of SMLs, courtesy of Carl Zeiss, Ltd.; WD = 6.0 mm InLens 10 kV; D_{PCS} = 82.9 nm, PDI = 0.284.

The results of PCS measurements for five, freshly prepared SML suspensions are summarised in Table 5.2. All of the suspensions contain relatively monodisperse particles, as indicated by the PDI values of around, or below, 0.2. The mean hydrodynamic size of the five preparations is 95.8 ± 5.6 nm, which demonstrates good reproducibility for a method with no size sorting process included. The application of magnetic filtration to further improve size control will be discussed below.

Table 5.2. The average hydrodynamic diameter and polydispersity index, at 25°C, of five SML preparations with no further size sorting process.

Sample name	Z-Avg	PDI
GML3	97.1	0.216
GML4	90.2	0.195
GML5	101	0.178
GML6	89.7	0.203
GML8	101	0.176

The hydrodynamic size of three SML preparations was monitored over time. The results of the PCS measurements are reported in Table 5.3. The liposome size was relatively unchanged (< 5% increase in D_{PCS}) for up to 88 days for samples stored in the laboratory without any particular precautions. After 4 – 5 months, there was a ~ 7% increase in the average diameter, and after 1 year, the diameter increased by ~ 14%.

Table 5.3. The average hydrodynamic diameter and polydispersity index measured over time, at 25°C, for a series of SML preparations with no further size sorting.

Sample name	Day	Z-Avg (nm)	PDI
GML4	0	90.4	0.195
	76	91.8	0.188
	88	93.9	0.183
GML5	0	101	0.178
	62	106	0.209
	137	109	0.223
GML8	0	101	0.176
	7	101	0.185
	11	101	0.179
	405	117	0.222

5.3.1.2 Formation of AMLs

The ATR-IR spectrum of DOPG AMLs is shown in Figure 5.5. Spectra of uncoated magnetite and pure DOPG liposomes are also included for comparison. The band assignments for pure DOPG liposomes were reported in section 5.3.1.1; all bands arising from DOPG vibrations are observed in the AML spectrum, confirming the presence of DOPG in the AML sample. The DOPG IR band assignments for the AML sample are summarised below in Table 5.4. The band assignments for SMLs (Table 5.1) are also included for comparison. Only subtle differences exist between the spectra of SMLs and AMLs (Figure 5.6); therefore, no significant conclusions can be reached regarding a difference in particle morphology from IR analysis alone.

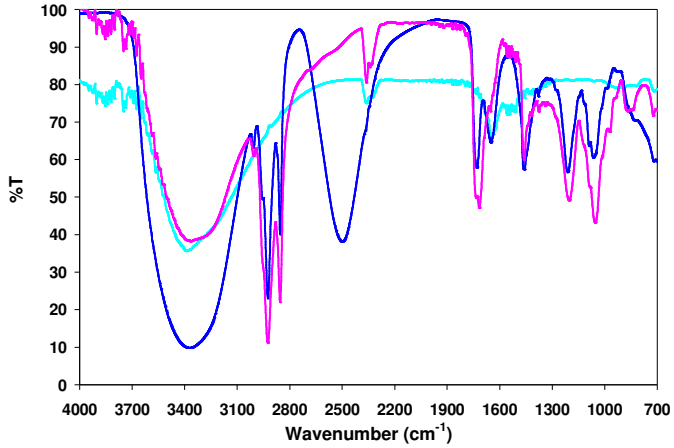

Figure 5.5. ATR-IR spectra of — uncoated magnetite, — pure DOPG liposomes, and — AMLs prepared by the thin film-hydration method.

Table 5.4. Summary of the infrared band assignments for pure DOPG liposomes and magnetoliposomes.

Pure DOPG ν (cm^{-1})	**AMLs ν (cm^{-1})**	**SMLs ν (cm^{-1})**	**Assignment [216-218]**
3362	3366	3272	OH stretch
3003	3006	3005	sp^2 CH stretch
2923	2925	2922	ν_a CH_2 stretch
2854	2855	2853	ν_s CH_2 stretch
1726	1727	1739	C=O stretch
1459	1461	1459	ν_s CH_2 scissor
1204	1203	1204	ν_a PO_2^- stretch
1052	1055	1057	ν_s PO_2^- stretch

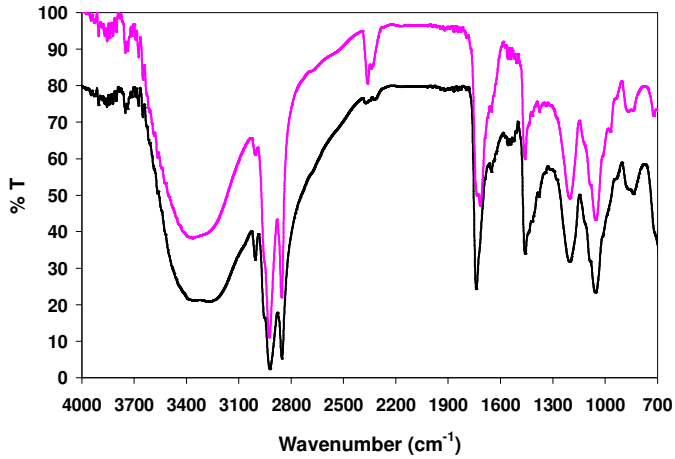

Figure 5.6. A comparison of the ATR-IR spectra of ─ SMLs and ─ AMLs.

PCS measurements were performed throughout the various stages of the AML preparation, and the results for three different preparations are presented in Table 5.5. In figure 5.7, the particle size distributions at each stage of the preparation of a typical sample are compared.

Table 5.5. The average hydrodynamic diameter and polydispersity index, at 25°C, of DOPG AMLs at different stages of the magnetoliposome preparation. U = uncoated magnetite, H = hydration, FT = freeze-thaw, E = extrusion, and MF = magnetic filtration

Sample Name	Preparation Stage	Z-Avg (nm)	PDI
AML3	(i) U	148	0.208
AML3	(ii) H	219	0.439
AML3	(iii) H/FT	280	0.636
AML3	(iv) H/FT/E	157	0.242
AML4	(i) U	157	0.146
AML4	(ii) H	200	0.354
AML4	(iii) H/FT	239	0.442
AML4	(iv) H/FT/E	148	0.194
AML13	(i) U	150	0.221
AML13	(ii) H	350	0.379
AML13	(iii) H/FT	238	0.375
AML13	(iv) H/FT/MF	158	0.156

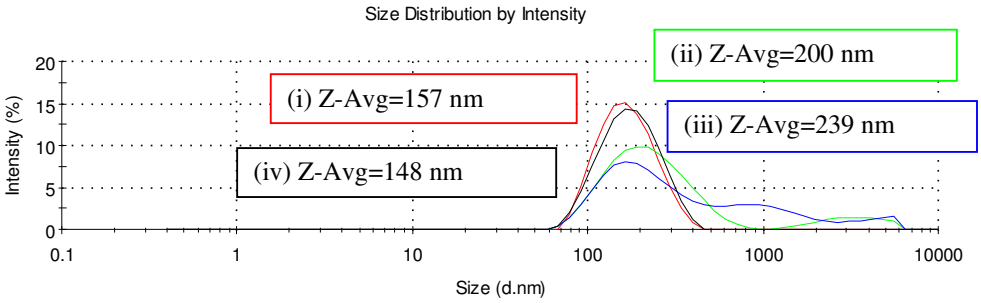

Figure 5.7. PCS results obtained during each of the four main steps of a typical AML preparation: — Uncoated magnetite (U), — Hydration only (H), — Hydration + freeze-thaw (H/FT), — Hydration + freeze-thaw + extrusion (H/FT/E).

A cryo-TEM image obtained after the freeze-thaw step in the thin film-hydration AML preparation method is shown in Figure 5.8. The image was obtained before the particle size and vesicle lamellarity were reduced by extrusion or magnetic

filtration; therefore, a polydisperse size distribution of multilamellar vesicles was expected, and was observed. PCS for this sample indicates an average diameter of 198 nm and a PDI value of 0.520. The micrograph reveals both spherical and non-spherical structures, in contrast to the image obtained for SMLs.

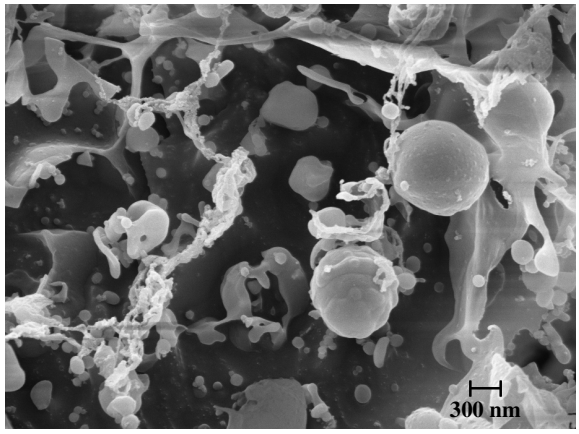

Figure 5.8. Cryo-TEM image, courtesy of Carl Zeiss, Ltd., of DOPG multilamellar AMLs prepared by the thin film-hydration method; WD = 4.5 mm InLens 5.0 kV; D_{PCS} = 198 nm (0.520).

The hydrodynamic size of three AML preparations was monitored over time. The results of the PCS measurements are reported in Table 5.6. In all cases, the hydrodynamic diameter decreased over time, and in general, the PDI improved. This behaviour is the reverse of that observed for SMLs.

Table 5.6. The average hydrodynamic diameter and polydispersity index measured over time, at 25°C, for a series of AML preparations.

Prep	Day	Z-Avg (nm)	PDI
AML4	0	149	0.187
	8	143	0.127
	85	123	0.122
	207	120	0.161
AML6	0	163	0.272
	25	140	0.154
AML13	0	158	0.228
	32	138	0.182

5.3.2 Nuclear magnetic resonance relaxometry

All the magnetic recovery curves were mono-exponential within experimental error. All fitting errors in T_1 were less than 1%. The temperature was maintained at 25°C with a maximum variation of ± 1°C for all measurements.

The relaxivity profiles for representative samples of SMLs and AMLs are shown in Figure 5.9. Both profiles exhibit features expected for dispersed superparamagnetic nanoparticles in suspension [151]; namely, a low frequency plateau, a high frequency maximum, and a rapid decrease toward zero at high frequencies. A mid-frequency dispersion, often present for suspensions of small crystals (typically < 20 nm) [151] does not appear in the magnetoliposome profiles. In general, the overall shape of the profile from preparation to preparation was more consistent for suspensions of SMLs than for AMLs.

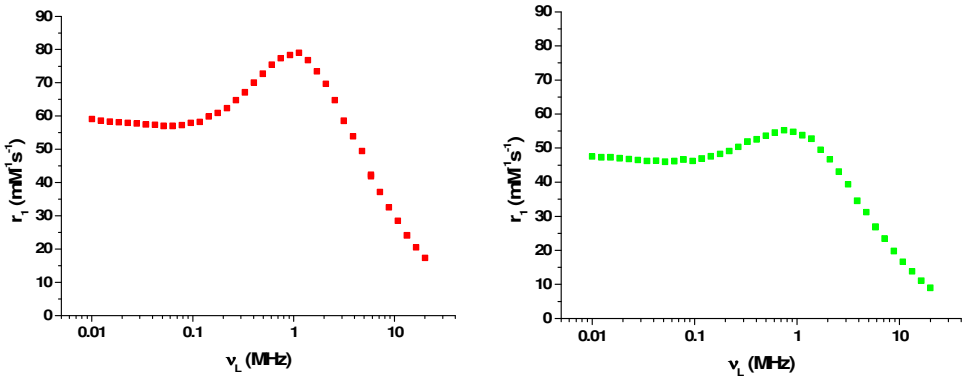

Figure 5.9. Relaxivity profiles at 295K of (a) ■ an aqueous suspension of SMLs; Z-Avg = 108 nm, PDI = 0.125 (b) ■ an aqueous suspension of AMLs; Z-Avg = 131 nm (0.248).

5.3.2.1 Effect of magnetoliposome size on the NMRD response

A series of experiments was conducted to investigate the effect of particle size on the NMRD response of aqueous suspensions of both SMLs and AMLs. Figure 5.10 shows the NMRD profiles for multiple SML samples with average PCS diameters ranging from 81 – 150 nm. Magnetic filtration allowed the division of

bulk SML samples into fractions which differed in mean particle size. Results are shown for suspensions which exhibited good PDI values. The 81.4 and 89.7 nm samples are magnetically filtered fractions of one bulk SML suspension, and the 128 and 150 nm samples are fractions of a second bulk suspension. The 96.2 nm sample was a separate preparation, and did not undergo magnetic filtration. The results indicate that there is a strong, systematic increase in r_1 with a decrease in hydrodynamic size, particularly at the mid and low frequency range. The shape of the profiles is broadly consistent for all particle sizes, with a slight variation in the shape of the profile for the 96.2 nm sample. This may be a result of the particular low PDI value of this suspension, or due to the presence of non-encapsulating vesicles.

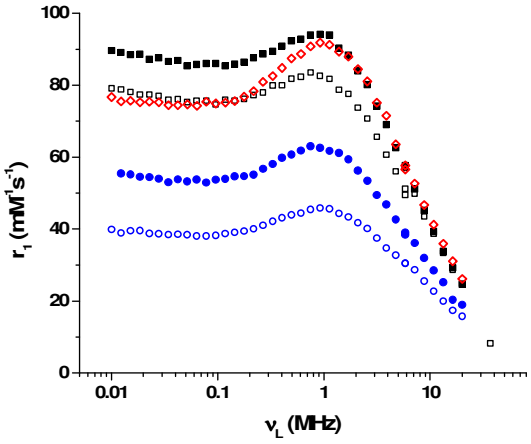

Figure 5.10. NMRD profiles, recorded at 295K, of SML samples with hydrodynamic diameters of ■ 81.4 nm (0.169), □ 89.7 nm (0.203), ◊ 96.2 (0.159), ● 128 nm (0.185), and ○ 150 nm (0.206).

NMRD profiles for three AML samples are presented in Figure 5.11. Two of the suspensions have nearly identical hydrodynamic diameters (D_{PCS} = 128 nm and 131 nm), and the third has an average diameter of 108 nm. Unlike SMLs, no apparent correlation exists between r_1 and D_{PCS}.

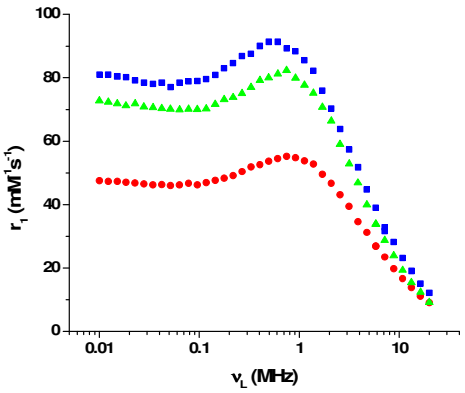

Figure 5.11. NMRD relaxivity profiles at 298 K of AMLs with a hydrodynamic diameter of ■ 128 nm (0.099), ■ 108 nm (0.097), ■ 131 nm (0.248).

5.3.3 Magnetoliposome stability to dilution

A series of dilutions was carried out on both SML and AML suspensions, and the effect of dilution on the NMRD and PCS response was investigated. The motivation behind the dilution study was a report by Muller and co-workers on the concentration dependence of the contrast enhancement of Gd-based MRI contrast agents arising from both inner- and outer-sphere relaxation mechanisms (Chapter 1, section 1.4.5.3) [72]. Table 5.7 shows the results of PCS measurements for SML samples with dilutions ranging from 1:1 to 1:8, corresponding to an iron concentration range of 3.13 – 0.35 mM. The Z-Avg and PDI values did not change upon dilution of the neat suspension. It should be noted that this sample was intentionally prepared with a high PDI for a future magnetic filtration experiment.

Table 5.7. Effect of dilution on the average hydrodynamic diameter and polydispersity index, at 25°C, of an aqueous suspension of SMLs.

Diluton factor to neat	Z-Avg (nm)	PDI
0	110	0.258
1	111	0.250
2	110	0.280
3	110	0.279
4	110	0.270
5	108	0.260
6	128	0.381
7	110	0.256
8	110	0.262

Relaxivity profiles for each of the samples in the dilution series are shown in Figure 5.12. The concentration of Fe in the neat sample was 3.13 mM; the concentrations for the diluted samples were calculated from neat. No significant variation in r_1 was observed upon dilution within the Fe concentration range of 3.13 – 0.35 mM. This result is consistent with the results of the PCS measurements; both techniques indicate the average particle diameter remains constant upon dilution of the suspension. This result indicates that during magnetic filtration a dilution of up to 1:8 will not affect the size or relaxivity of the suspended particles.

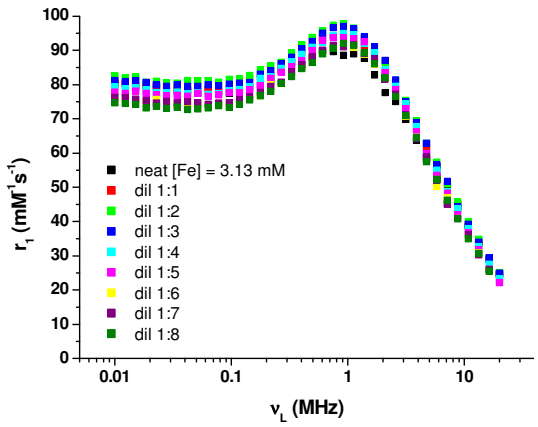

Figure 5.12. Relaxivity profiles, measured at 25°C, for 8 dilutions of an aqueous suspension of SMLs. The corresponding PCS sizes are shown in Table 5.7.

The results of PCS measurements for AML samples for dilutions ranging from 1:1 to 1:4 are shown in Table 5.8. The dilution series corresponds to an iron concentration range of 3.1 – 0.6 mM. The hydrodynamic diameter was found to decrease by > 20% upon dilution of the neat suspension. The decrease in the diameter is significant considering the reasonable PDI values, of 0.2 or below. The fact that the iron concentrations were the same for both SML and AML suspensions demonstrates that this is not an artefact of the PCS experiment.

Table 5.8. Effect of dilution on the average hydrodynamic diameter and polydispersity index, at 25°C, of an aqueous suspension of AMLs.

Dilution factor to neat	Z-Avg (nm)	PDI
0	209	0.159
1	182	0.236
3	160	0.167
4	161	0.188

Relaxivity profiles for each of the samples in the dilution series are shown in Figure 5.13. Again, no significant variation in r_1 was observed upon dilution within the Fe concentration range of 3.11 – 0.62 mM. This result demonstrates that the hydrodynamic diameter does not determine the relaxation profile of AMLs.

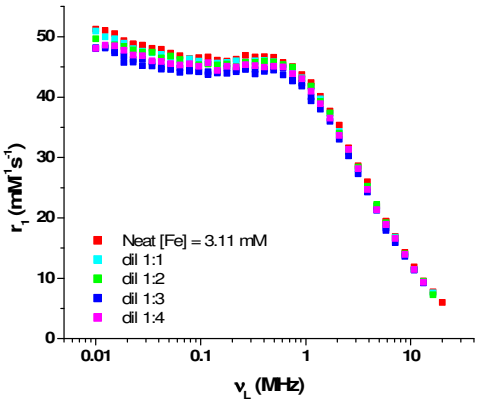

Figure 5.13. Relaxivity profiles, measured at 25°C, for 4 dilutions of an aqueous suspension of AMLs. Some of the corresponding PCS sizes are shown in Table 5.8.

5.3.4 Magnetic filtration

5.3.4.1 Size-separation of SMLs

Magnetic filtration was carried out on an aqueous suspension of SMLs with initial Z-Avg and PDI values of 102 nm and 0.182. PCS was used to measure the

average hydrodynamic diameter of the magnetoliposomes suspended in each fraction (eluent) after filtration. An increase in D_{PCS} was observed with an increase in flow rate from 8 – 600 mL/hr using a constant magnetic field of 0.5 T. A flow rate of 600 mL/hr was the highest obtainable with the available peristaltic pump. Once this limit was reached, further size separation was achieved by varying the magnetic field while using a constant flow rate. A summary of the PCS results is shown below in Table 5.9.

Table 5.9. The effect of magnetic filtration at different magnetic fields and flow rates on the average hydrodynamic diameter and polydispersity index, at 25°C, of a typical suspension of SMLs.

Flow Rate (mL/hr)	**Magnetic Field (T)**	**Z-Avg (nm)**	**PDI**
Original sample		102	0.182
8	1.6	52.6	0.224
8	1.2	56.9	0.205
8	0.7	58.5	0.176
8	0.5	71.8	0.163
15	0.5	74.6	0.163
30	0.5	81.5	0.158
40	0.5	80.0	0.125
50	0.5	84.9	0.131
100	0.5	91.3	0.135
200	0.5	92.4	0.136
400	0.5	96.6	0.114
600	0.5	104	0.153
600	0.1	110	0.103
600	0.02	116	0.118
final retentate	0	132	0.112

Magnetic filtration allowed the division of the bulk sample into several fractions which differed in mean particle size by up to 79 nm. The fractions containing the largest and the smallest particles with a PDI < 0.200 are compared in Figure 5.14 in the form an intensity size distribution plot. In this case, a separation of 73.5 nm in the average particle size was achieved, however PCS indicates that full

resolution was not accomplished. These results are typical of the size separation possible by magnetic filtration for SML suspensions.

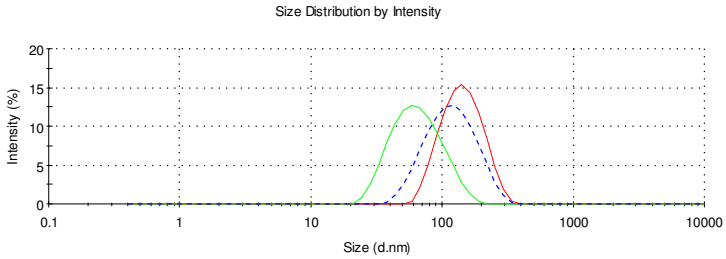

Figure 5.14. Intensity size distribution comparison of a SML sample – – unfiltered, Z-Avg = 102 nm (0.182); — magnetically filtered at 30 MHz at a flow rate of 8 mL/hour, Z-Avg = 58.5 nm (0.176); — the final retentate of the magnetic filtration, Z-Avg = 132 nm (0.112).

5.3.4.2 Size separation of AMLs

Magnetic filtration was carried out on an aqueous suspension of AMLs with initial Z-Avg and PDI values of 238 nm and 0.375. PCS was used to measure the average hydrodynamic diameter of the magnetoliposomes suspended in the eluent after filtration. The clear systematic change in D_{PCS} as a function of flow rate, observed for SMLs, was not as apparent for AMLs.

PCS measurements were repeated for the magnetically filtered suspensions after ageing the eluent samples for one month. In all cases, the average hydrodynamic diameter of the particles was smaller after ageing. The decrease in diameter from the initial measurements ranged from 2.6 – 34%, with no correlation in the extent of the change with particle size or the magnetic filtration parameters. Interestingly, a systematic increase in D_{PCS} with increased flow rate was now observed. The results of the PCS measurements obtained immediately after filtration and after ageing for one month are compared in Table 5.10.

Table 5.10. A comparison of PCS measurements of a magnetically filtered sample of AMLs obtained immediately after filtration and after ageing for one month.

Flow rate (mL/hr)	Field (MHz)	Z-Avg (nm) Initial	PDI Initial	Z-Avg (nm) Aged	PDI Aged	% Decrease
15	0.5	90.3	0.224	74.5	0.234	17
50	0.5	140	0.213	116	0.191	17
100	0.5	187	0.378	124	0.203	34
200	0.5	159	0.225	141	0.204	11
300	0.5	158	0.228	138	0.182	13
400	0.5	179	0.255	144	0.184	19
500	0.5	158	0.156	154	0.210	2.6
600	0.2	177	0.231	156	0.152	12
600	0.05	189	0.137	171	0.121	9.6
Final retentate	0	250	0.247	198	0.135	21

The combination of magnetic filtration followed by ageing for one month allowed the division of the bulk magnetoliposome sample into several fractions which differed in mean hydrodynamic size by up to 123.5 nm. The fractions containing the largest and the smallest particles are compared in Figure 5.15 in the form an intensity size distribution plot. PCS indicates that again full resolution was not achieved.

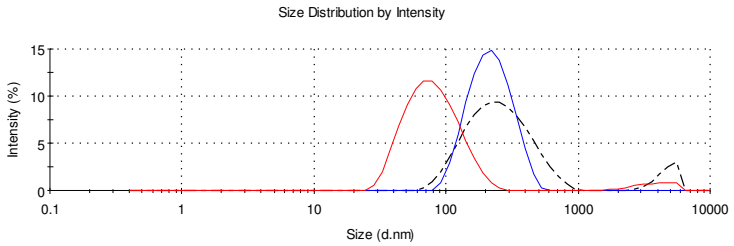

Figure 5.15. Intensity size distribution comparison of an 'aqueous'-type magnetoliposome sample – – unfiltered (FT only), — magnetically filtered at 20 MHz at a flow rate of 15 mL/hour and aged one month, Z-Avg = 74.5 nm (0.234); — the final retentate of the magnetic filtration, aged one month, Z-Avg = 198 nm (0.135).

5.4 Discussion

5.4.1 Formation of AMLs

Analysis by ATR-IR confirmed the presence of DOPG in the aqueous suspensions of AMLs prepared by the thin film-hydration method. This method is a commonly used procedure for the preparation of non-encapsulating phospholipid vesicles [219-221], and the mechanism of formation is quite well known. The procedure involves the hydration of a lipid film, a series of freeze-thaw cycles, and a size homogenisation step. We utilised this approach to prepare AMLs, but modified the procedure by using an aqueous magnetic fluid to hydrate the phospholipid film.

Based on what is known about the formation of unilamellar phospholipid vesicles using the thin film-hydration method, we can assume that upon hydration of the lipid film with a magnetic fluid, phospholipid vesicles form around the nanoparticles, encapsulating the particles within the aqueous core. The aqueous suspension of uncoated magnetite is only temporarily stable, and the particles usually agglomerate and begin to precipitate from suspension within 1 – 2 days. Following encapsulation, however, no precipitation of the magnetite was observed over a period of at least two months, suggesting that the iron-oxide is stable within the vesicles. The hydration step results in a suspension containing large, multilamellar vesicles (LMVs), which are macromolecular structures formed from a number of concentric bilayer membranes forming a single vesicle, with each bilayer separated by a narrow aqueous layer. Freeze-thaw cycling is known to reduce the number of bilayer lamellae surrounding each vesicle [221], eventually producing a suspension of large, unilamellar vesicles (LUVs) with a broad size distribution. The last step of AML preparation involves the homogenisation of the size distribution. The size and distribution of the particles can be reduced by a variety of techniques, one of the most common being extrusion [222]. During extrusion, the sample is passed through polycarbonate membranes of a defined pore size, typically 0.1 μm. The result is a reasonably monodisperse suspension of AMLs, which was verified by PCS measurements.

The results of all PCS measurements performed throughout the AML preparation (shown in Table 5.5) support the formation of AMLs by the expected process. All uncoated magnetite suspensions contained particles in the range of 148 – 157 nm, with PDIs ranging from 0.146 – 0.221. Upon hydration and freeze-thaw, PCS results indicated a heterogeneous distribution of large particles, as expected for the presumed multilamellar structures at this stage of the preparation. Finally, the average size and the size distribution of the particles decreased significantly upon extrusion through 200 nm polycarbonate membranes, indicating the successful preparation of a homogenous sample of vesicles with a unimodal size distribution.

A cryo-TEM image obtained after the freeze-thaw cycles (Figure 5.8) shows a heterogeneous distribution of structures including somewhat spherical particles ranging from ~100 – 1000 nm in addition to non-spherical structures distinctly different in size and shape from those observed in the TEM image for SMLs. The broad size distribution was expected considering the anticipated multilamellar structures at this stage, prior to any size homogenisation process.

5.4.2 Stability of AMLs

The hydrodynamic diameter of unilamellar AMLs decreased over time, as measured by PCS, and in general, the PDI improved. In Figure 5.16, the NMRD profile of a freshly prepared AML sample is compared with the profile after ageing the sample for 14 days. For this sample, the hydrodynamic diameter decreased from 164 nm to 153 nm in 14 days. There is a slight change in the r_1 value at low frequencies for the aged sample, but the magnitude of difference is certainly less than what would be expected for a decrease of 11 nm.

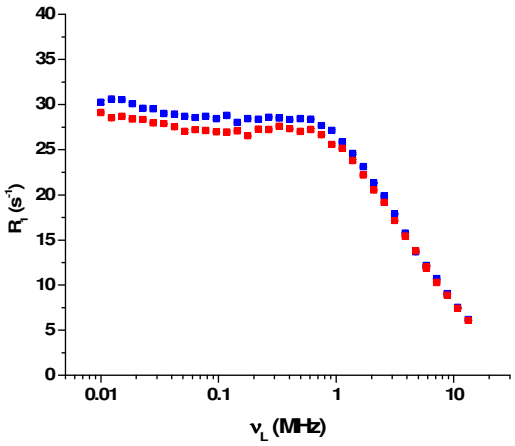

Figure 5.16. NMRD profiles at 298 K of a suspension of freshly prepared AMLs (Z-Avg = 164 nm), and the same suspension aged 14 days (Z-Avg = 153 nm).

This result highlights, again, the observation (Figure 5.11) that no apparent correlation exists between r_1 and D_{PCS} for AMLs. The discrepancy between D_{PCS} and r_1 suggests that the cluster does not occupy the entire interior volume formed by the lipid vesicle; instead it is encapsulated within a larger aqueous compartment.

The hydrodynamic diameter of AMLs was not stable to dilution, and was observed to decrease by > 10% upon a 1:1 dilution. The decrease in particle diameter observed by PCS was again not reflected in the corresponding NMRD profiles. Based on the constant position of the r_1 maximum, NMRD analysis indicates that the size of the core remains unchanged. The combined PCS and NMRD analysis suggests that the size of magnetic core of the AMLs remain constant, and the decrease in the hydrodynamic diameter is due to a decrease in the contribution to the diameter of the aqueous lumen. The shrinkage of the vesicle due to loss of the aqueous core results in a hydrodynamic diameter which probably more accurately reflects the core diameter. This is illustrated in Figure 5.17. The reason for the loss of the aqueous compartment over time and upon dilution has not been investigated. It is related to the affinity of phosphate for iron-oxide surfaces [205,223], and/or to the exchange of bulk water across the membrane. In summary, AMLs appear to lose their aqueous lumen on ageing and dilution, and hence to become like SMLs.

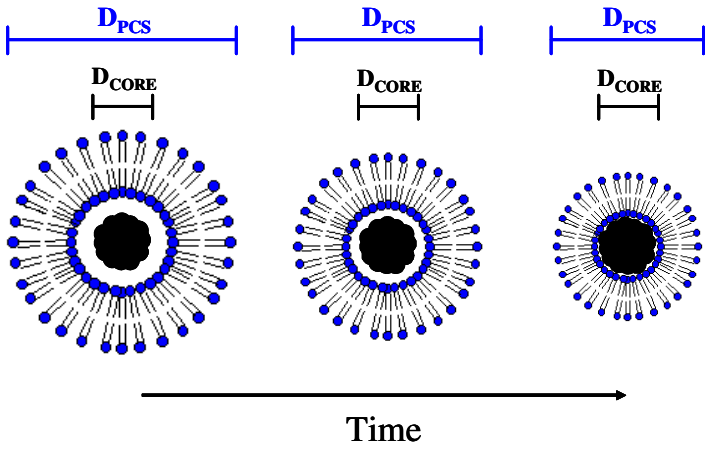

Figure 5.17. Schematic representation of the decrease of the hydrodynamic diameter of AMLs as a function of time.

5.4.3 Magnetic filtration of AMLs

The AML preparation method alone does not offer much control over particle size. Many size-sorting techniques are routinely used to fractionate magnetic fluids, including centrifugation [209] or size-exclusion chromatography [224], but these methods separate the particles based on their overall physical size. The hydrodynamic size and magnetic cluster size have been shown to differ significantly for AMLs, and while the fractionation of a magnetoliposome suspension based on hydrodynamic size may by useful for physical targeting *in vivo*, it cannot ensure the preparation of a sample with uniform magnetic properties. We have utilised magnetic filtration as a means of selective particle size control. The advantage of magnetic filtration lies in its ability to separate particles based on their magnetic size, therefore allowing the fractionation of the suspension into samples with desired magnetic properties.

Separation of particle sizes by magnetic filtration arises due to competition between two opposing forces, an applied magnetic force, and the force of flow as the sample is pumped through the magnetic field at a particular rate. The magnetic force on a single spherical particle (F_{mag}) due to an applied external magnetic field is proportional to particle volume, as described by Equation 5.1;

$$F_{mag} = \frac{4}{3}\pi r^3 M_s B \qquad \text{Equation 5.1}$$

Where r is the radius of the particle, B is the magnetic field strength and M_s is the saturation magnetisation of the material. Therefore, the magnetic force on a single particle is stronger for larger particles and weaker for smaller particles at a constant applied magnetic field.

At the slowest flow rate, the force exerted on the particles by the magnetic field is stronger than the force due to flow, for particles of all sizes. All of the magnetic material is retained on the steel wool (retentate), while any non-magnetic material, such as excess phospholipids, is flushed through and collected in the eluent (Figure 5.18 (a)). As a fresh aliquot of dispersant is then pumped through the system at a slightly faster flow rate, the force of the flow is now stronger than the magnetic force for the smallest particles; the largest particles remain on the magnetic steel wool, while the smallest magnetic particles are collected in the eluent (Figure 5.18 (b)). As aliquots of dispersant are pumped through the system at increasing rates, the force of the flow becomes stronger than the magnetic force for most particles; only the largest particles are retained on the steel wool, and all other particles are collected as the eluent (Figure 5.18 (c)). The flow rate can be increased gradually in order to selectively retain a sample of the desired particle size. When the maximum or minimum attainable flow rate is reached for a given pump, further size separation can be achieved by gradually adjusting the magnetic field to higher fields using a constant minimum flow rate, or to lower fields using a constant maximum flow rate.

The colour of the eluent fractions following magnetic filtration provides evidence for the successful separation of particles from the bulk sample, as shown in Figure 5.19. A distinct colour change is observed as the flow rate is increased due to an increase in the average size and concentration of the dispersed particles.

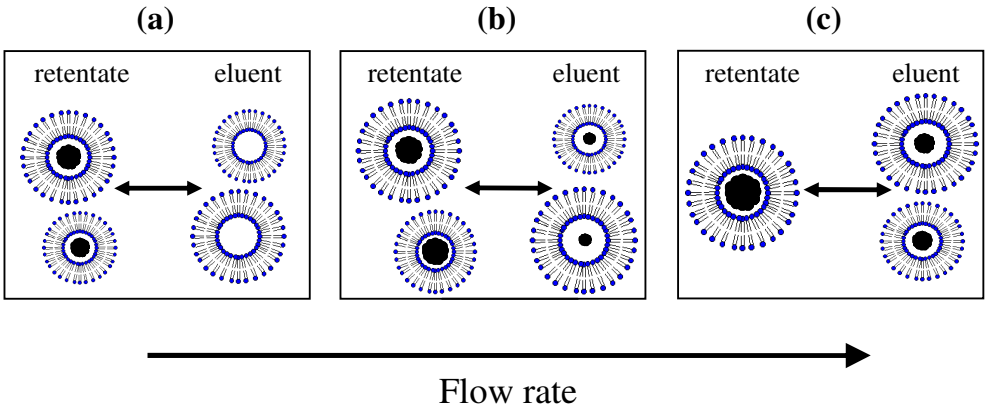

Figure 5.18. Schematic representation of magnetic filtration of SMLs as a function of flow rate.

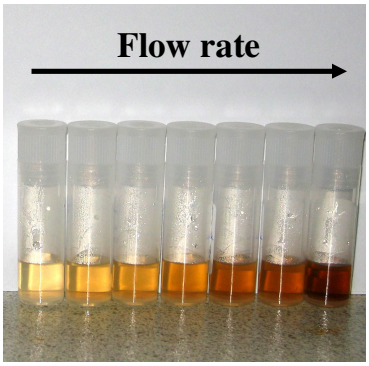

Figure 5.19. Typical aqueous suspensions of magnetoliposomes following magnetic filtration at various flow rates. All samples shown were collected as eluent fractions at increasing flow rates.

Because the expected morphology of AMLs includes an aqueous core of an unknown volume, the hydrodynamic diameter immediately after magnetic filtration does not initially provide an accurate representation of the diameter of the iron-oxide core size which has determined its behaviour under magnetic filtration. However, as seen previously, the diameter consistently decreases over time. In Figure 5.20, the hydrodynamic diameter of freshly filtered AML sample is compared with the diameter of the same samples upon ageing. Upon ageing, the general size trend more closely resembles the trend that would be expected for a SML sample; i.e., a monotonic increase in particle size is observed with

increased flow rate. This observation provides further evidence that AMLs resemble SMLs upon ageing.

It is very interesting to note that the decrease in D_{PCS} over time for AMLs after magnetic filtration indicates that the aqueous core and presumed morphology of AMLs is preserved upon exposure to the magnetic fields and relatively high flow rates used in this study.

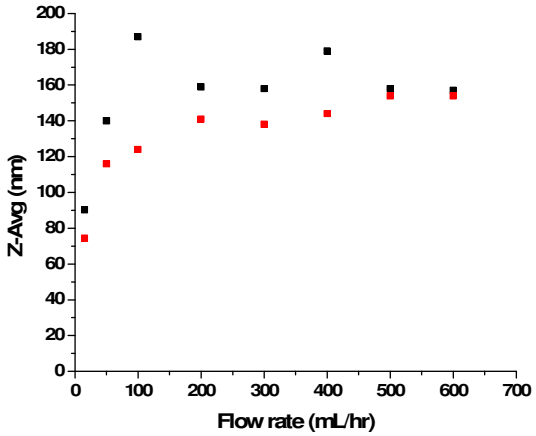

Figure 5.20. The effect of ageing on the hydrodynamic diameter of the eluent; ■ fresh and ■ aged eluent samples. A constant magnetic field of 0.5 T was used, and the flow rate was varied from 15 to 600 mL/hr.

5.4.4 Formation of SMLs

The two-step 'solid'-type physisorption preparation method used to prepare SMLs as well as the expected morphology of the particles resulting from each step is illustrated in Figure 5.21.

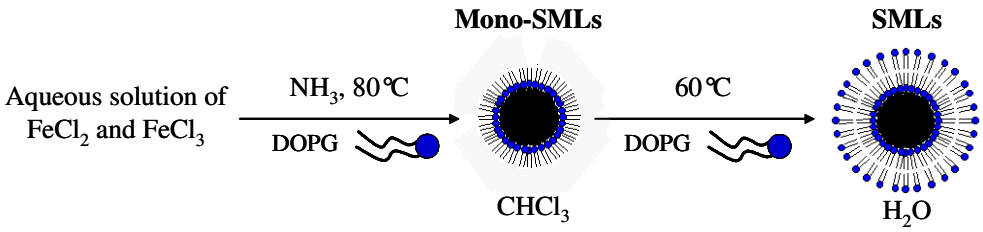

Figure 5.21. Schematic representation of the preparation of 'solid'-type, bilayer stabilised DOPG magnetoliposomes.

There were clear differences in the ATR-IR spectra of mono-SML and SML, which suggests that both the phosphate and hydroxyl groups of DOPG are involved in the bonding of phospholipid to the iron-oxide surface in mono-SML samples. This is consistent with the expected morphology considering the previous studies by Shen et al. and Giri et al., which have demonstrated that coprecipitation in the presence of fatty acids [81,82] or phospholipids [99] results in the chemisorption of a primary surfactant layer onto the nanoparticle surface. Thus, in the present work, the phospholipids in the mono-SML samples are expected to coat the iron-oxide particles through chemisorption of polar headgroups, with the non-polar C18 chains extending away from the cores. This orientation provides efficient steric stabilisation and renders the particles stable in non-polar solvents. As expected, the mono-SML nanoparticles were readily dispersible in $CHCl_3$.

Infrared analysis suggests that the chemisorption of DOPG onto the magnetite surface is through the phosphate-containing headgroups. This is as expected considering the well-known affinity of phosphate for iron-oxide surfaces [205,223]. There are many examples in the literature of the phosphate coatings on iron-oxide surfaces; however, the specific mode of interaction currently remains under investigation. Several bonding schemes have been proposed. For example, Mohapatara et al. reported IR analysis which showed strong bonding of poly(vinylalcohol phosphate) (PVAP) on magnetite surfaces through Fe – O – P bonds; these authors suggested bonding through two oxygen atoms [225]. Yee and co-workers proposed two different bonding schemes between Fe_2O_3 and phosphonate ions of diprotic phosphonic acid; through one or two oxygen atoms of the phosphonate group [226].

Based on the ATR-IR analysis, which suggests the absence of hydroxyl group stretching modes and weaker PO_2^- stretching modes, we propose tridentate bonding of DOPG to the nanoparticle surface (Figure 5.22). Further analysis would be necessary to confirm the proposed structure, however, tridentate bonding of organophosphorous molecules to metal surfaces is not unusual, and has been reported for titanium dioxide [227] and aluminium oxide [228].

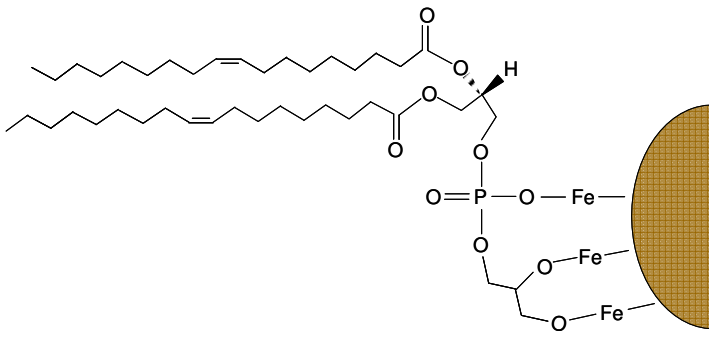

Figure 5.22. Proposed bonding scheme of DOPG to the iron-oxide nanoparticle surface in mono-SML samples.

In contrast to the mono-SML ATR-IR spectrum, the asymmetric PO_2^- stretching mode and the hydroxyl group O-H stretching mode are present in the SML spectrum, indicating the presence of non-bonded DOPG molecules in the sample. It is generally accepted that the non-bonded DOPG molecules form a partially complete, secondary layer physisorbed onto the primary layer. This orientation sequesters the hydrocarbon chains into regions where the contact with water is reduced, while allowing the hydrophilic headgroups to interact with the bulk aqueous solvent (Figure 5.21) [229-231]. Indeed SMLs are observed to be stable for extended periods in H_2O. Further support can be found in the literature. Sahoo et al. reported a quasi-bilayer formation of phosphate and phosphonate ligands covering the surface of magnetite nanoparticles, with the primary layer bound to the surface of the nanoparticles, as suggested by DSC and TGA measurements [84]. A schematic representation of the proposed bilayer formation of DOPG around the magnetite surface for SMLs is provided in Figure 5.23. The ATR-IR spectrum is also shown to clarify the discussion.

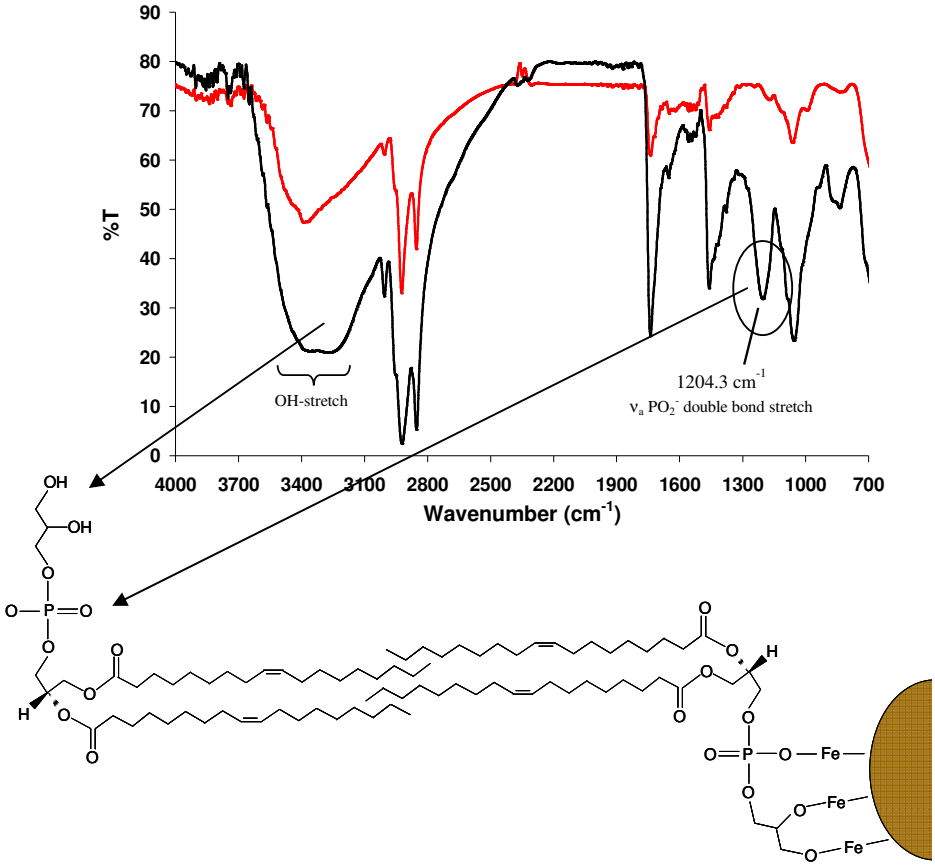

Figure 5.23. Above; ATR-IR spectrum of — Mono-SMLs, and — SMLs. Below; schematic representation of the proposed bilayer formation of DOPG around the magnetite surface for SMLs. Shen and Laibinis have proposed an interpenetration depth of about four methylene/methyl groups for oleic acid [82].

It is unclear, from IR analysis alone, whether this type of bonding is also present in AMLs. The presence of the asymmetric PO_2^- stretching mode and the hydroxyl group O-H stretching mode in the AML sample spectrum (Figure 5.5) confirms the presence of non-bonded DOPG in the AML sample. However, it cannot be determined whether these bands arise due to the vibrations of DOPG molecules located on the inner or outer leaflet of the phospholipid bilayer. In other words, the spectral features arising from outer leaflet phospholipid vibrations can potentially prevent the observation of the absence of modes that are diagnostic of DOPG-magnetite bonding.

5.4.5 Stability of SMLs

Unlike AML suspensions, the hydrodynamic size of SMLs remained relatively stable for 4 – 5 months, with only a ~ 7% increase in the average diameter. The diameter also remained stable to dilution, as indicated by PCS and NMRD measurements. In this type of structure, there is no aqueous lumen, and therefore, no potential for a change in size without desorption of the primary or secondary phospholipids.

5.4.6 Magnetic filtration of SMLs

It can be assumed, therefore, that the hydrodynamic diameter of SMLs is representative of the iron-oxide core size. Thus, fractionation of a SML suspension based on magnetic size is expected to be reflected in the PCS measurements immediately following filtration. Indeed, this is observed in Figure 5.24 where the hydrodynamic diameter of a freshly filtered SML sample is shown as a function of flow rate. The general size trend is as expected for a SML sample; there is an increase in particle size with an increase in flow rate.

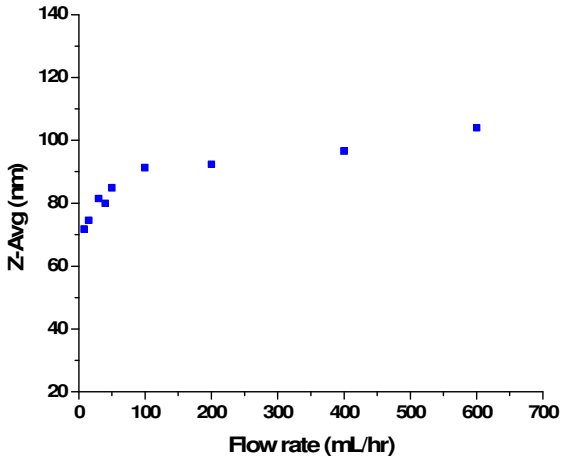

Figure 5.24. The effect of magnetic filtration on the hydrodynamic diameter of SMLs. A constant magnetic field of 0.5 T was used, and the flow rate was varied from 8 to 600 mL/hr.

5.4.7 NMRD of magnetoliposome suspensions

Magnetic filtration allows the fractionation of magnetoliposome suspensions into samples with selected core sizes, and therefore potentially allows separation into

samples with desired magnetic properties. Two approaches were assessed for analysing the magnetic resonance properties of magnetoliposomes.

First, relaxivity profiles were simulated for typical SML and AML suspensions using Muller's relaxation theory for superparamagnetic particles [151], Figure 5.25. The simulated profiles do not entirely conform to the experimental data for either sample. The τ_N values obtained are suspiciously high, and the M_s values are quite low [153].

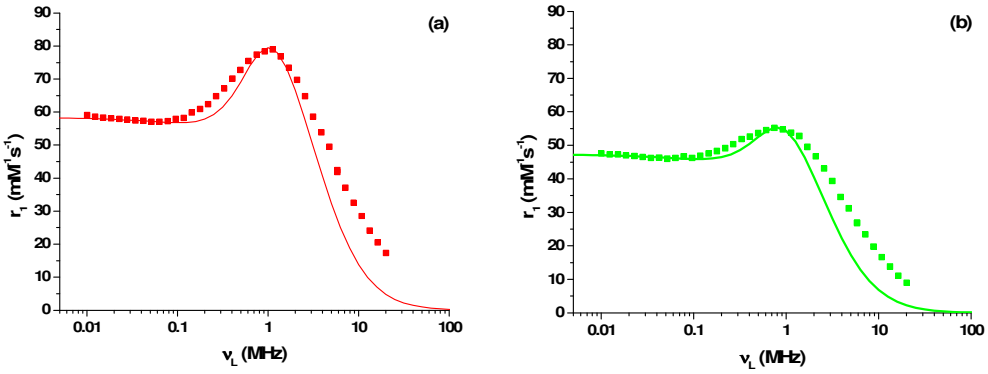

Figure 5.25. (a) ■ Relaxivity profile, at 295K, of a SML suspension. Z-Avg = 108 nm, PDI = 0.125; ▬ Simulated profile using Muller's SPM theory for an 18.6 nm particle using the parameters, M_s = 22.5 emu g^{-1}, τ_N = 90 ns, ν_{anis} = 2 GHz. (b) ■ Relaxivity profile, at 295K, of an AML suspension. Z-Avg = 131 nm, PDI = 0.248; ▬ Simulated profile using Muller's SPM theory for an 21 nm particle using the parameters, M_s = 16.7 emu g^{-1}, τ_N = 147 ns, ΔE_{anis} = 2 GHz;

The experimental data does display some features characteristic of the presence of superparamagnetic nanoparticles for both types of magnetoliposome suspensions, but the absence of a mid-frequency dispersion in the profiles suggests the samples may contain aggregated particles. Aggregation causes an increase in the anisotropy energy due to intercrystal interactions [151], which increases the low frequency relaxivity and eliminates the mid-frequency dispersion. For instance, this effect has been observed in our group in the case of poly(sodium-4-styrene)sulfonate stabilised iron-oxide [110].

Recently, Muller et al. presented an extension of his original theory which takes into account the effects arising from the aggregation of superparamagnetic crystals within a permeable coating [74], we shall call this SPM-cluster theory. This model considers the relaxation of the ^{1}H magnetisation as arising from diffusion of water into the agglomerate, which is considered a large magnetised sphere. The longitudinal relaxation is modelled using an analogy to chemical exchange in which there is exchange between the slowly relaxing bulk water molecules and the water molecules bound to different sites within the aggregate. The contribution to the relaxation arising from individual cores within the aggregate is assumed to be superparamagnetic. The residence time of the water molecules inside the agglomerate increases with an increase in cluster size, which results in a decrease in relaxation rates. The result is that the NMRD profiles gradually become broader and flatter upon increased aggregation [74]. Simulations generated with this approach are shown in Figure 5.26 for agglomerates with radii between 50 – 350 nm [74]. Use of this model is appropriate for particle clusters with weak inter-core interactions.

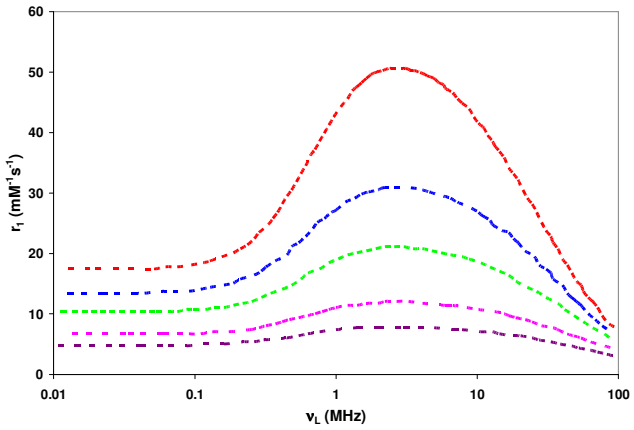

Figure 5.26. Simulated longitudinal NMRD profiles for aggregated magnetic crystals of iron-oxide, using SPM cluster theory, showing the affect of an increased agglomerate radius (R_a). —50 nm, —100 nm, —150 nm, —250 nm, — 350 nm. The parameters characterising the elementary grains are as follows: τ_N = 1.8 ns, Ms = 49 emu g^{-1}, grain radius = 8.2 nm, and a volume fraction occupied inside the agglomerate of 0.02.

It is important to note that SPM-cluster theory predicts that r_1 should decrease as the size of the agglomerate increases, as we observed for SMLs. However, the shape of the simulated profiles for 50 – 350 nm clusters differs significantly from the profiles of SML suspensions, Figure 5.10. In particular, the increased low frequency relaxivity is not predicted.

Simulated profiles for SML and AML suspensions using the SPM cluster model are shown below in Figure 5.27. The magnetic parameters obtained from the cluster model simulations of the experimental profiles are presented in Table 5.11.

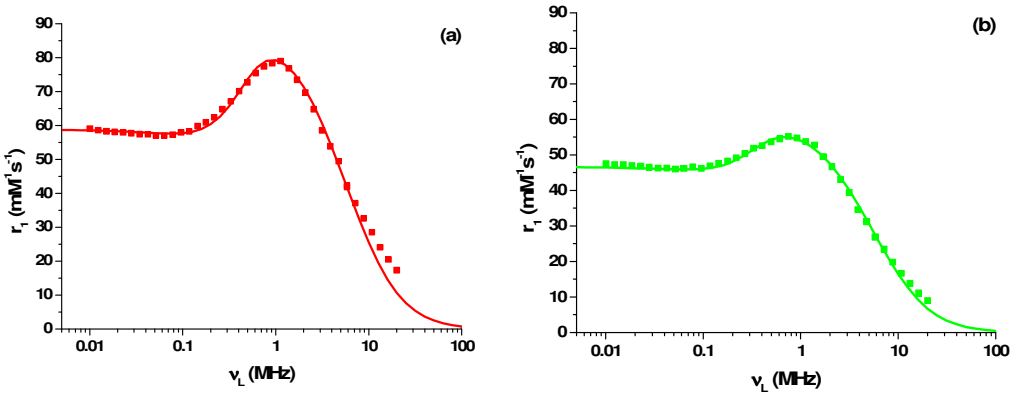

Figure 5.27. (a) ■ Relaxivity profile, at 295K, of a SML suspension. D_{PCS} = 108 nm, PDI = 0.125; ▬ Simulated profile using Muller's cluster theory for a 14.8 nm primary particle using the parameters, M_s = 58 emu g^{-1}, τ_N = 39 ns, ΔE_{anis} = 5 GHz, cluster diameter = 100 nm, scaling factor = 0.112. (b) ■ Relaxivity profile, at 295K, of an AML suspension. D_{PCS} = 131 nm, PDI = 0.248; ▬ Simulated profile using Muller's cluster theory for a 17 nm primary particle using the parameters, M_s = 48 emu g^{-1}, τ_N = 60 ns, ΔE_{anis} = 5 GHz, cluster diameter = 50 nm, scaling factor = 0.080.

Table 5.11. The parameters obtained from SPM theory and cluster theory simulations of SMLs and AMLs. The diffusion coefficient of water was taken to be $4.02 \cdot 10^{-5}$ cm^2s^{-1}. The D_{PCS} values are included for comparison.

NMR parameters	SPM theory		Cluster theory	
	SMLs	AMLs	SMLs	AMLs
D_{NMR}, primary (nm)	18.6	21	14.8	17
$D_{cluster}$ (nm)			100	50
D_{PCS} (nm)	108	131	108	131
M_s (emu/g)	22.5	16.7	58	48
τ_N (ns)	90	147	39	60
ΔE_{anis} (GHz)	2.0	2.0	5.0	5.0

Although the simulations show reasonable agreement with the experimental profiles, it was not possible to fit the SML size data, Figure 5.10, suggesting the good fits, shown above, are somewhat fortuitous. Thus, the encouraging agreement between $D_{cluster}$ and D_{PCS} for the SML sample and the larger $D_{cluster}$ value obtained for the AML sample must be dismissed. Another disadvantage of this approach is the large number of parameters required to fit the data.

Tilcock et al. [232] reported that for liposome encapsulated gadolinium diethylenetriaminepentaacetic acid (Gd-DTPA), prepared by a thin film-hydration method, the relaxivity increased linearly with the surface area to volume ratio of the liposomes, for vesicles 70 – 400 nm in diameter. In this case, the vesicle membrane imposes a permeability barrier to the bulk water, and the linear dependence of the relaxivity can be explained by considering the water flux across the vesicle membrane. For a lipid vesicle of area A and volume V containing n water molecules at concentration C, the flux (J) across the membrane per unit time (t) can be described by Equation 5.2.

$$J \propto \frac{dn(t)}{dt} \cdot \left(\frac{1}{A}\right) \equiv \frac{dC(t)}{dt} \cdot \left(\frac{V}{A}\right) \qquad \text{Equation 5.2}$$

As smaller vesicles have a larger surface-area-to-volume ratio, it follows from this equation that at a given lipid concentration, smaller vesicles will have a greater flux across the membrane per unit time.

We have observed a decrease in the measured relaxivity with particle size, which equates to an approximately linear increase of r_1 and the surface area-to-volume ratio, for our SML suspensions, as shown in Figure 5.28.

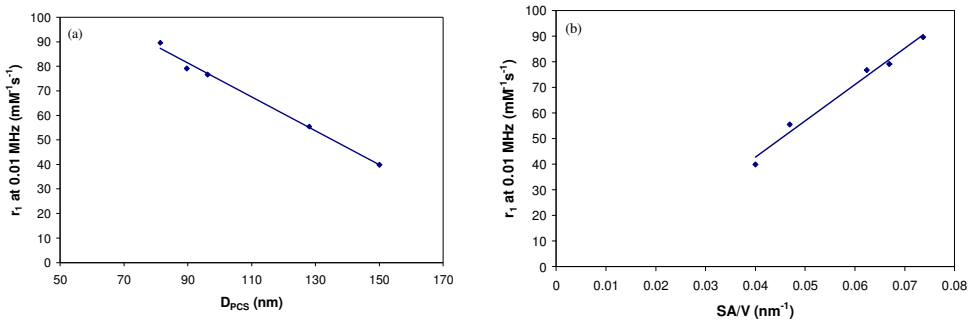

Figure 5.28. Relaxivity at 0.01 MHz as a function of (a) hydrodynamic size and (b) surface-area-to-volume ratio (SA/V) of SMLs with diameters of 81.4 nm, 89.7 nm, 128 nm, and 150 nm (profiles shown in Figure 5.10). The solid lines are linear fits with equations (a) $y = -0.692x + 143.6$, $R^2 = 0.993$; (b) $y = 1414x - 13.82$, $R^2 = 0.984$.

In the case of SMLs, it is unlikely that the relationship between r_1 and the surface area-to-volume ratio can be explained in terms of the water flux across the vesicle membrane, as the aqueous lumen is minimal in these magnetoliposomes. However, it does seem that the relaxivity is determined by the available surface area of the SML. This is a surprising result, particularly as the r_1 values, at all frequencies, exhibit this behaviour. The implication is that both the inner-sphere contribution to the low frequency relaxation, which is modulated by τ_N, and the outer-sphere contribution to the high frequency relaxation, which is driven by the diffusion of water (Chapter 1, section 1.5), scale with the surface area of the SML. This is not currently fully understood.

We suggest a relaxation mechanism whereby bulk water is retained in the proximity of the SML, during which time it experiences relaxation due to the clustered (i.e. non-superparamagnetic) magnetic cores in the SML. The relaxation profile due to the individual sites in the agglomerate are therefore SPM-like but with elevated low frequency relaxivity [110]. As in the case of SPM-cluster theory, extended residence times in the environment of the larger (greater surface area) aggregates, result in a decrease in r_1. This arises due to an increase in the number of water molecules hydrogen bonded to the phospholipid molecules of the bilayer with an increase in particle size. This is a result of an increase in the average lipid-lipid distance, which creates more space for water molecules [233]. Unfortunately, given the large number of parameters that further extension of SPM theory to incorporate non-SPM relaxation in a chemical exchange model would require, it is not possible to analyse the SML profiles quantitatively.

Nonetheless, Figures 5.10 and 5.28 are interesting results, as they demonstrate that the relaxivity, in particular the low-frequency relaxivity, of these stable magnetic fluids can be controlled over a wide range by the use of magnetic filtration. Given the importance of lipids and the broad application of liposomes as carrier systems, this finding may be of interest to the nanotechnology and MRI communities.

On the other hand, the absence of a correlation between D_{PCS} and r_1 for AMLs means that relaxivity measurements are not useful for studying these suspensions. This is probably due in part to the gradual loss of water from the lumen, a process that will have progressed to an unknown extent for any given AML suspension.

5.4.8 Implications for magnetoliposome formulation

5.4.8.1 SMLs

The ‘solid’-type physisorption preparation method used in this work to synthesise SMLs offers several advantages over the dialysis method described by De Cuyper et al. [205,206]. Firstly, the total preparation time is only 3 – 4 hours,

which is much shorter than the three day dialysis reported by De Cuyper. Secondly, the *in-situ* coating of the nanoparticles with DOPG ensures direct interaction of DOPG with the bare magnetite surface. De Cuyper's method is dependent upon on the successful displacement of the fatty acid molecules by phospholipid molecules, and therefore requires a stable aqueous nanoparticle dispersion to ensure the surface is available to the phospholipid molecules. In practice, we found that a stable suspension of magnetite nanoparticles could not be maintained for the duration of the three day dialysis. Thirdly, De Cuyper's dialysis method requires an additional analysis step to assess the residual fatty acid content in the magnetoliposome suspensions. *In-situ* coating with DOPG eliminates the need for this additional step.

The SML preparation method we used was also found to be adaptable to other lipids. We were able to use the method to form SMLs using 1,2-dioleyoyl-*sn*-glycero-3-phosphocholine (DOPC). Successful coating of the nanoparticles with DOPC was also confirmed by ATR-IR spectroscopy (data not shown). As the phospholipids are expected to coat the magnetite through the polar headgroup, these findings suggest that the method may be used for other phosphatidylcholine lipids, such as dipalmitoyl- and dimyristoylphosphatidylcholine (DPPC and DMPC).

The advantage of an adaptable preparation method lies in the ability to tailor the liposome formulation to obtain desired properties, particularly thermodynamic properties. There are numerous reports of heating thermosensitive liposomes, with and without encapsulated magnetic nanoparticles, above the Tm of the phospholipid in order to induce the release of entrapped pharmaceutical agents [54,234,235]. As the release temperature is governed by the Tm of the phospholipid, this strategy is limited to the use of phospholipids with a Tm around or above physiological temperature, which greatly restricts the number of phospholipids suitable for the preparation of thermosensitive systems. Differential scanning calorimetry (DSC) studies of mixed phospholipid bilayer systems have shown that for compound formulations, Tm can occur at intermediate, or average temperatures [236]. Thus, with an adaptable preparation

method, it may be possible to prepare multi-component phospholipid magnetoliposomes with tailored release temperatures.

5.4.8.2 AMLs

In contrast to SML preparation, the approach to the preparation of AMLs could not be adapted for use with other classes of phospholipids, specifically phosphatidylcholines. Neither DOPC, nor DMPC successfully encapsulated the magnetite particles. In all cases the solid magnetite precipitated from suspension. Considering phosphatidylglycerol carries a negative charge, while phosphatidylcholine is a neutral phospholipid, the ability of the phospholipid to encapsulate the nanoparticles is presumably determined by the pH of the magnetic fluid. Future work could involve adjustment of the magnetic fluid pH before the hydration step in the AML preparation method.

5.4.8.3 Magnetic filtration in the preparation of AMLs

The size selection capability of magnetic filtration was investigated as a potential replacement for extrusion in the final step of AML preparation. While extrusion has proven to be a useful, reproducible, and widely accepted means of producing homogenous samples of liposomes with unimodal particle size distributions, it does have limitations. During extrusion, a sample is passed several times through a polycarbonate membrane with a defined pore size. If a sample is too concentrated, it may not be possible to pass the sample through the delicate membranes without causing them to rupture. Magnetic filtration, however, has no concentration limitations. In fact, it allows some control over the final sample concentration, which is determined by the volume of dispersant used to collect the retained magnetic fraction. Extrusion offers no such control over the final sample concentration. The use of extrusion is also limited by sample volume, while there is no upper limit to the volume that can be used with magnetic filtration.

Magnetic filtration and extrusion were performed separately on an aqueous suspension of multilamellar AMLs, to assess their performance as the final preparative step. The intensity size distributions were measured by PCS at each

stage of the AML preparation. The results for the preparation involving extrusion are shown in Figure 5.29, while the results for the preparation involving magnetic filtration are presented in Figure 5.30.

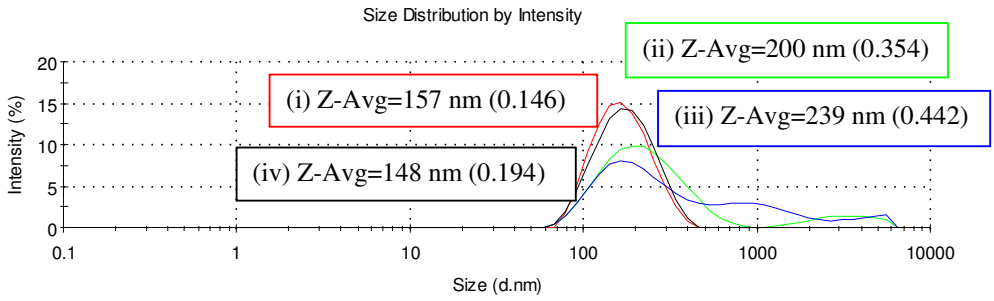

Figure 5.29. PCS results obtained during each of the four main steps of a typical AML preparation: — Uncoated magnetite, — Hydration only, — Hydration + freeze-thaw, — Hydration + freeze-thaw + extrusion.

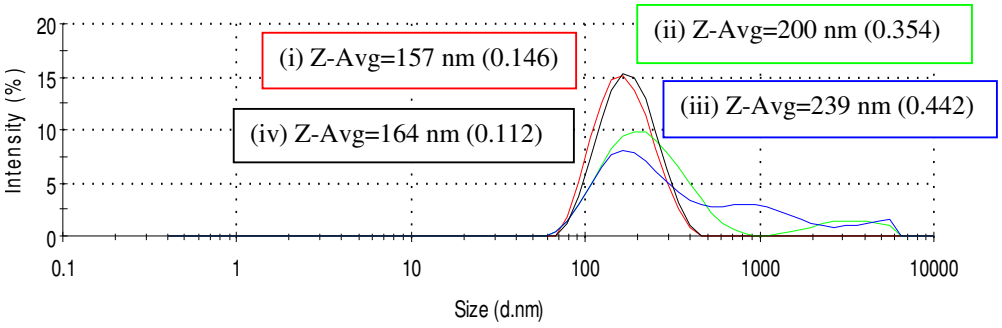

Figure 5.30. PCS results obtained during each of the four steps of an AML preparation in which extrusion was replaced by magnetic filtration: — Uncoated magnetite, — Hydration only, — Hydration + freeze-thaw, — Hydration + freeze-thaw + magnetic filtration.

Figures 5.29 and 5.30 clearly show that both extrusion and magnetic filtration produce lipid stabilised particles with PCS characteristics similar to the uncoated suspensions, although with slightly improved PDIs in the case of magnetic filtration. This is probably due to the fact that the filtered sample only contains magnetoliposomes, the nonencapsulating vesicles having been removed, a further advantage of magnetic filtration.

5.5 Conclusions

We have reported the synthesis of magnetic iron-oxide nanoparticles and their successful stabilisation inside phospholipid membranes by two different methods. A novel 'solid'-type physisorption method was introduced, which offers significant advantages over the widely accepted deCuyper method. The SML and AML structures resulting from the two preparation methods were compared and evaluated in terms of the physical properties and particle morphology of the resulting suspensions.

We have shown that SMLs contain a solid iron-oxide core coated with a phospholipid bilayer, in which the inner phospholipid layer is chemisorbed directly onto the particle surface. SMLs exhibited more consistent relaxivity behaviour, and their hydrodynamic diameter closely reflects their magnetic core diameter. Additionally, SMLs demonstrated a decrease in r_1 with an increase in D_{PCS}, which has been interpreted as a result of extended residence times of bulk water in the proximity of larger magnetoliposomes. The potential to tune the low-frequency relaxivity of SMLs is an interesting finding considering the ubiquity of liposomes in biotechnology and given recent advances in low-frequency MRI [237]. We have demonstrated that AMLs, on the other hand, are liposomal structures in which solid iron-oxide particles are contained within the internal aqueous compartment of the liposome. AMLs appear to lose their aqueous lumen on ageing and dilution, and hence to behave more like SMLs.

Finally, we have successfully developed a magnetic filtration method for selective particle size control, and have demonstrated the ability to fractionate magnetoliposome suspensions into samples with average particle sizes ranging from 50 – 250 nm with relatively narrow size distributions as demonstrated by PCS and NMRD. We have demonstrated the utility of magnetic filtration as an alternative to extrusion in the preparation of AMLs, as it allows particle size homogenisation, elimination of empty liposomes, and selective particle size control, with no sample volume or concentration limitations.

CHAPTER 6

NMRD investigation of molecular and collective motions of liposomes

6.1 Introduction

This chapter presents a field-cycling NMR and dynamic light-scattering study into molecular and collective motions in liposomes. Liposomes were introduced in Chapter 5 as carrier systems for MRI contrast agents and drug delivery vehicles, but the interest in these systems extends beyond their clinical and diagnostic potential. Liposomes resemble cell membranes in both structure and composition and are therefore an ideal model to study membrane functions and dynamics. Membrane function is related to bilayer dynamics [238,239], which includes an array of motional processes occurring over a broad time scale. Amongst the motions of interest are collective membrane motions known as order fluctuations, and individual phospholipid motions such as translational diffusion, and molecular rotation. The characteristic time scales over which these motions are generally accepted to occur are summarised in Table 6.1. An understanding of these processes can provide insight into the role of dynamics in determining the properties of cell membranes, with a view toward allowing the preparation of liposomal carrier systems with selected membrane permeability and thermal stability.

Table 6.1. Summary of the time scales over which membrane motions are generally accepted to occur [203,240,241].

Dynamic process	Time scale (s)
Molecular vibrations	$10^{-15} – 10^{-12}$
Molecular rotation	$10^{-11} – 10^{-8}$
Lateral diffusion	$10^{-8} – 10^{-6}$
Order fluctuations	$10^{-5} – 10^{-3}$
Liposome tumbling	$10^{-4} – 10^{-1}$
Lipid 'flip-flop'	hours or days

Many physical methods are routinely and effectively used to study and characterise the motion of molecules in biological systems. However, it is imperative to consider the time scale of the motions of interest before selecting a

method. Different spectroscopic techniques are sensitive to molecular motions over different time scales. Vibrational spectroscopy, both infrared absorption and Raman scattering, has been used to investigate the influence of cholesterol on the physical properties of membranes and lipid bilayers [242]. As the time scales of the events monitored by these techniques are on the order of 10^{-12} s, they are not suitable for investigating motions slower than molecular vibrations. Fluorescence polarisation techniques can be used to study motions on the nanosecond to microsecond time scale, allowing the investigation of molecular rotation and lateral diffusion [243,244]. The NMR spectroscopic time scale, however, ranges from the nanosecond to the second scale, depending on the experiment used and the magnetic field strength, making it a versatile method for studying dynamics on different time scales for the same sample. NMR relaxation experiments can be performed to study molecular dynamics covering time scales from 10^{-9} to 10 s, or longer [244-246]. The great breadth of this range means that NMR provides a unique perspective on molecular motion in partially ordered systems.

The NMR analysis presented in this chapter differs from previous chapters due to the absence of superparamagnetic relaxation. Instead, the relaxation is of dipolar nature, driven by the individual and collective motions of the model membranes. The quality of the NMRD data presented here necessarily is of poorer quality than that presented in previous chapters due to the low ^1H concentration of the liposome samples (~ 5 M) suspended in D_2O, thus resulting in a lower measurable signal. The overall lipid concentrations were ~ 76 mM.

As introduced in Chapter 1, the NMRD profile provides information concerning the details of the motions that occur in a dynamic system, as it effectively maps out the spectral density function, $J(\omega)$ (Equation 1.10, Chapter 1). Spectral density functions are the Fourier transforms of the time correlation functions, with random motions giving rise to exponential correlation functions (Equation 1.12, Chapter 1). Slow motions result in long correlation times, whereas short correlation times are a result of faster motions. The Fourier transform of an exponential function is a Lorentzian function (Equation 1.13, Chapter 1). The

rate of the motion, τ_c^{-1}, can be obtained directly at a single temperature from the half width of the Lorentzian spectral density function.

By fitting theoretical spectral density functions, numerically or analytically, to experimental relaxation rates, we can investigate the dynamics of model membrane systems. Determining the form of the spectral density function, however, can be nontrivial. In general, nuclear spin relaxation rates (R_1) are expressed as a sum of the spectral densities evaluated at specific frequencies, ω (Equation 6.1).

$$R_1(\omega) = \sum_i J_i(\omega) \qquad \text{Equation 6.1}$$

The number of terms in the sum depends on the details of the motion, the interactions that are being modulated, and the relaxation rate being measured [247]. To link the spectral densities to the macroscopic properties of the system, it is necessary to employ mathematical descriptions of the relevant motional modes [248].

Several approaches exist for the analysis of the nuclear magnetic relaxation data. In this chapter, we have chosen to evaluate two different methods; specifically, we compare a model-free approach (MFA) and a physical model-based analysis, which we will refer to as a defined motions model (DMM). In the MFA, model-free parameters are extracted from the data prior to interpretation within the framework of a model [249,250]. The experimental relaxation dispersion data is fit to an optimal sum of Lorentzian spectral density functions. The form of the spectral density is shown in Equation 6.2.

$$R_1 = \sum_{n=1}^{N} \alpha + \beta[0.2\,J(\omega) + 0.8\,J(2\varpi)]$$

Equation 6.2

$$J(\omega) = \frac{\tau_c}{1 + (\omega\tau_c)^2}$$

The number of Lorentzians that can be used, without unreasonably increasing the number of parameters, can be objectively determined by means of a merit function analysis. The resulting model-free parameters extracted from the data are interpreted in terms of the expected motions of the system. The inherent problem with this approach is the assumption that all of the spectral density functions are Lorentzian, corresponding to random processes. This may or may not always be the case. Thus, we turn our attention toward model-based analysis.

Over the years several quantitative models have been developed for the underlying molecular motions of model membranes. One widely recognised interpretation was reported by Noack et al. in 1988 [203] in which he assumed that four, non-interacting mechanisms contributed to the overall relaxation process for phospholipid bilayers in the liquid crystalline phase. These mechanisms included smectic order fluctuations of the membrane (OF), internal and overall molecular rotations of individual molecules (MR), lateral diffusion of molecules in the bilayer plane (LD), and translationally induced rotations of molecules on curved bilayer regions (TR), Figure 6.2. The form of the spectral density functions reported by Noack for each of the individual relaxation contributions, OF, MR, LD, and TR, respectively, are shown by Equations 6.3 – 6.6. For order fluctuations, the spectral density is not Lorentzian.

$$J_p^{(OF)}(p\omega) = pA^{(OF)}(1/\omega)$$

Equation 6.3

$$A^{(OF)} = \frac{(1/5)k_B TS^2}{Kxr^6}$$

The amplitude factors are denoted by A^{ij}, k_B is the Boltzmann constant, S is the effective order parameter of the proton-proton vector, K denotes the coherence length of the order, and r is the effective proton-proton separation. For molecular rotations:

$$J_p^{(MR)}(p\omega) = p^2 \left[\begin{array}{l} A_1^{(MR)} \dfrac{\tau_{R\perp}}{1+(p\omega\tau_{R\perp})^2} + A_2^{(MR)} \dfrac{\tau_{R//}}{1+(p\omega\tau_{R//})^2} \\ + A_3^{(MR)} \dfrac{\tau_{1R}}{1+(p\omega\tau_{1R})^2} \end{array} \right] \qquad \text{Equation 6.4}$$

where $\tau_{R\perp}$ and $\tau_{R//}$ are the rotational correlation times for anisotropic overall motions perpendicular ($\perp$) and parallel (//) to the main molecular axis, respectively, and τ_{1R} is the effective correlation time for internal rotations. For lateral diffusion:

$$J_p^{(LD)}(p\omega) = p^2 A^{(LD)} \tau_{LD} \left[\begin{array}{l} \sum_{j=1}^{5} B_{0j} \dfrac{\xi_{0j}}{{\xi_{0j}}^2 + \beta^2} + 3\sum_{j=1}^{3} B_{2j} \dfrac{\xi_{2j}}{{\xi_{2j}}^2 + \beta^2} \\ {B_{05}}^2 \dfrac{\exp(-100\xi_{05})}{{\xi_{05}}^2 + \beta^2} \left[\beta \sin 100\beta - \xi_{05} \cos 100\beta\right] - \\ 2\,\mathrm{Re}\left[Ei(-100i\beta)\right] \end{array} \right] \qquad \text{Equation 6.5}$$

where τ_{LD} denotes the time constant for translational molecular jumps, B_{ij} are the numerically evaluated geometry factors, ξ_{ij} are the damping constants, n denotes the surface spin density, and d is the translational closest approach distance for neighbouring spins. Finally, the form of the spectral density function for translationally induced rotations is shown in Equation 6.6:

$$J_p^{(TR)}(p\omega) = p^2 A^{(TR)} \frac{\tau_{TR}}{1+(p\omega\tau_{TR})^2}$$

$$A^{(TR)} = \frac{(4/15)S^2}{r^6} \qquad \text{Equation 6.6}$$

where τ_{TR} is the correlation time for translationally induced rotations. These theoretical expressions were combined using Equation 6.7 to express the overall relaxation.

$$1/T_1(\omega) = \sum_{ij} C^{(if)} J^{(if)}(\omega, \tau_{ij})$$

Equation 6.7

$$C^{(if)} = (9/8)\gamma^4 \hbar^2 (\mu_0 / 4\pi)^2 A^{(if)}$$

In Equation 6.7, the constants γ, ħ, and μ_0 denote the magnetogyric ratio, Planck's constant, and the magnetic permeability of vacuum, respectively. The adjustable parameters are the amplitude factors, $C^{(if)}$, and the motional correlation times, $\tau^{(ij)}$, which were optimised to minimise the deviations between the theoretical predictions and the experimental data. While Noack's model provides a reasonable starting point, and is a useful introduction into a physical model-based analysis, like the MFA, it again results in a very high number of free parameters.

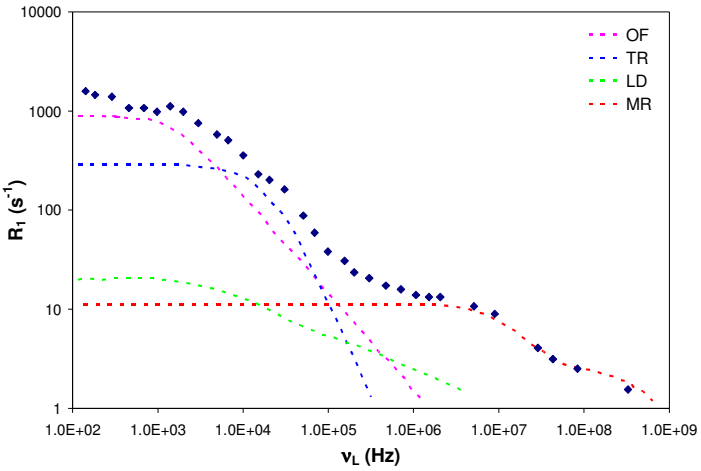

Figure 6.2. Digitised experimental (■) and calculated relaxation dispersion data for multilamellar DMPC bilayers at 30ºC from Noack et al [203]. The dashed lines are the individual relaxation contributions given by Equations 6.3 – 6.6.

The defined motions model utilised in this chapter relates the spectral density functions to previously studied systems, and seeks to fix as many parameters as possible using values determined experimentally or reported in the literature. The experimental profile is compared with the model in order to check the consistency between the analysis and the data. Such an approach significantly

reduces the number of free parameters compared to both the MFA, and Noack's model. The details of the DMM will be discussed at length in the discussion section.

Following an evaluation and comparison of the MFA and DMM for the interpretation of our nuclear magnetic dispersion data, the DMM was selected and utilised to investigate the bilayer dynamics of liposomes. The relaxometric behaviour of DOPC and DMPC liposomes was modelled with a good degree of accuracy for samples with different vesicle sizes. The effect of sample temperature and the addition of cholesterol on the overall relaxation rate were investigated, and the DMM analysis is underway. The inclusion of cholesterol was studied as it is commonly used in drug carrying vesicles, where it offers advantages including structural support and improved stability.

6.2 Experimental

6.2.1 Reagents

1,2-Dioleoyl-*sn*-glycero-3-phosphocholine (DOPC) and 1,2-dimyristoyl-*sn*-glycero-3-phosphocholine (DMPC) were purchased as lyophilised powders (>99%) from Avanti Polar Lipids (Alabaster, AL) and stored at -20°C. Deuterium oxide (D_2O, purity 99.9%) was obtained from Apollo Scientific Limited (UK), and cholesterol (>99%) was purchased from Aldrich Chemical Co. (Milwaukee, WI). All reagents were used without further purification.

6.2.2 Liposome preparation

Uniform mixtures of phospholipid and cholesterol were prepared by dissolving 70.2 mg DOPC or 70.6 mg DMPC and 0-25 mol% cholesterol in 2 mL $CHCl_3$. The solvent was removed under a slow stream of N_2 over 24 hours. Vesicles were prepared by hydrating the mixtures in 1.5 mL deuterium oxide (5 M proton, 0.06M lipid) under a constant flow of Ar. The suspensions were heated above Tm to ~22°C for DOPC and ~35°C for DMPC for 24 hours, followed by 3 heating/cooling/shaking cycles to ensure a homogenous preparation. Following hydration, the vesicle solutions were exposed to 6 freeze-thaw cycles using liquid N_2 and warm water (40°C), then passed through an Avanti Polar Lipids

mini extruder (Alabaster, AL) containing polycarbonate membranes with a pore size of 0.2 or 0.1 μm (Whatman Nuclepore; Clifton, NJ). The extrusion process was carried out above Tm in an AtmosBag glove bag (Aldrich Chemical Co.; Milwaukee, WI).

6.2.3 Characterisation

The liposome suspensions were characterised by PCS and NMRD as described in Chapter 2.

6.2.4 Analysis

Model-free analysis was performed utilising (with permission) a script file written in MATLAB 5.2.1 (LMDISP v 4) by Halle, B. [251] which uses the Levenberg-Marquardt algorithm to fit microscopic parameters to a set of relaxation dispersion data.

The defined motions model, developed by our collaborator Esteban Anoardo of the National University of Córdoba in Argentina [252], was implemented in Excel in Dublin City University.

6.3 Results

6.3.1 Effect of vesicle size on nuclear spin relaxation

6.3.1.1 Unilamellar DOPC vesicles

NMRD profiles for three different unilamellar DOPC liposome samples in the liquid crystalline phase are compared in Figure 6.3, each with a different mean diameter as measured by PCS. The profiles were recorded at 25ºC, Tm for DOPC is -18.3 ± 3.6ºC [253]. It is clear that the size of the DOPC vesicles has an effect on the nuclear spin relaxation below 0.2 MHz. This region is associated with slow motions on the 10^{-4} - 10^{-6} s timescale. The structure of DOPC is shown in Figure 6.4.

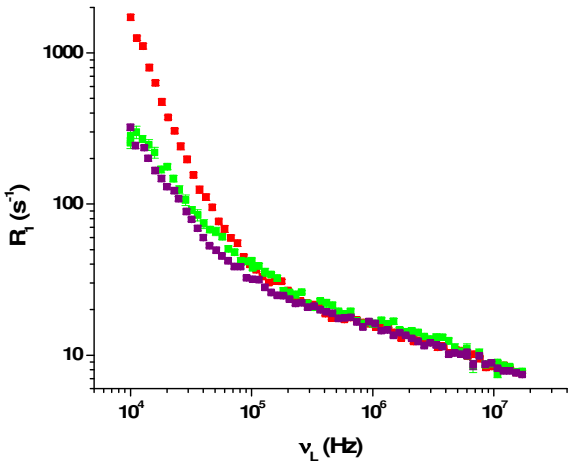

Figure 6.3. Frequency dependence of the ^{1}H spin-lattice relaxation rates at 25°C of unilamellar DOPC vesicles with Z-Avg diameter and PDI values of ■ ~100 nm, ■ 152 nm (0.287), and ■ 240 nm (0.264). The reported Z-Average diameters are from PCS measurements.

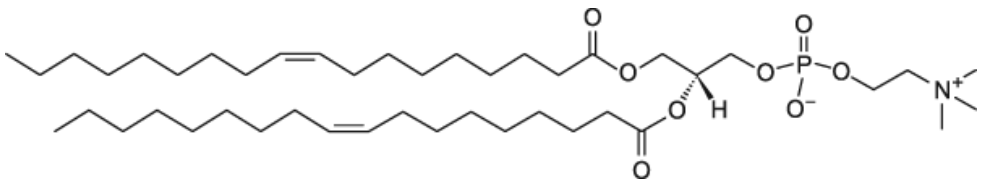

Figure 6.4. The structure 1,2-dioleoyl-*sn*-glycero-3-phosphocholine (DOPC).

6.3.1.2 Unilamellar DMPC vesicles

NMRD profiles for two unilamellar DMPC liposome samples with Z-Avg diameters of 108 and 195 nm are compared in Figure 6.5. The profiles were recorded at 37°C to ensure that the vesicles were in the liquid crystalline (LC) phase, as the Tm of DMPC is known to be 23.6°C ± 1.5°C [253]. The structure of DMPC is shown in Figure 6.6.

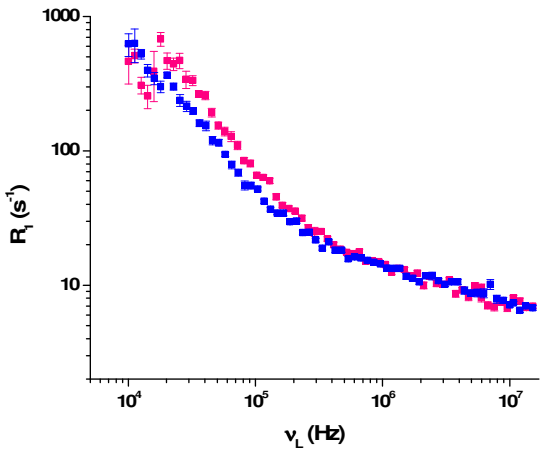

Figure 6.5. Frequency dependence of the ^{1}H spin-lattice relaxation rates at 37°C of unilamellar DMPC vesicles with Z-Avg diameters and PDI values of ■ 108 nm (0.114), and ■ 195 nm (0.207). The reported Z-Average diameters are from PCS measurements.

If the data below 2 x 10^4 Hz is excluded, it is again apparent that, as in the case of unilamellar DOPC vesicles (at 25°C), there is a decrease in the low frequency relaxation rate as the liposome size is increased.

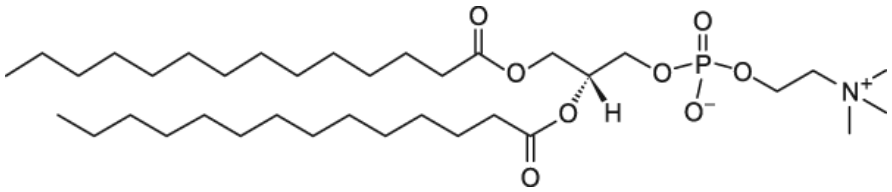

Figure 6.6. The structure 1,2-dimyristoyl-*sn*-glycero-3-phosphocholine (DMPC).

6.3.2 Effect of temperature on nuclear spin relaxation

6.3.2.1 Unilamellar DOPC vesicles

In Figure 6.7 (a), NMRD profiles recorded for a 240 nm unilamellar DOPC liposome sample at 18, 25, and 37°C are presented. The vesicles were in the LC phase at all three temperatures, as the Tm of DOPC is known to be -18.3°C ±

3.6°C [253]. The experiment was repeated using an extended temperature range. Figure 6.7 (b) shows NMRD profiles for a unilamellar DOPC liposome sample in the LC phase at 10, 25, and 45°C. PCS data could not be obtained for this sample due to instrument unavailability, but previous experiments suggest a vesicle diameter of ~230 nm.

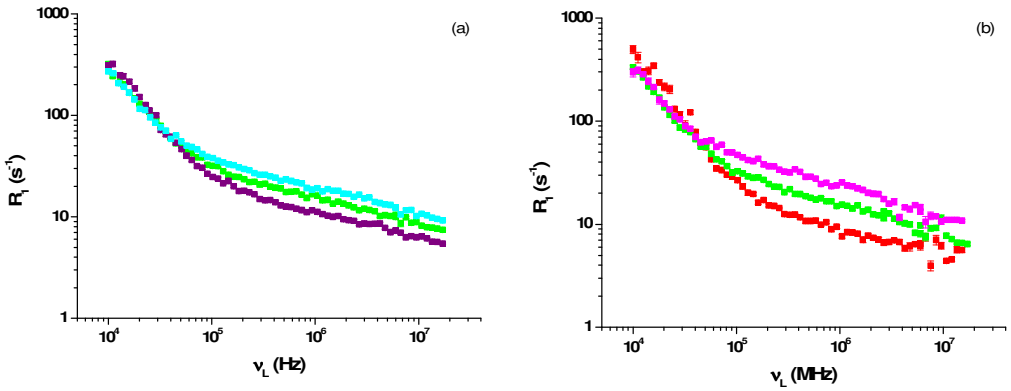

Figure 6.7. Frequency dependence of the ^{1}H spin-lattice relaxation rates of unilamellar DOPC vesicles at (a) ■ 18°, ■ 25°C, and ■ 37°C (Z-Avg = 240 nm), and (b) ■ 10°C, ■ 25°C, and ■ 45°C. The vesicle diameter is ~230 nm, as suggested by previous experiments.

In both experiments, there are clear differences in the profiles as a function of temperature above ~ 0.1 MHz. While the second sample is of poorer quality, these experiments have allowed us to establish that R_1 increases with decreasing temperature between 10 – 45°C, for ν_L > 0.1 MHz. This observation suggests that these motions are in the fast-exchange limit at the relevant frequencies.

6.3.2.2 Unilamellar DMPC vesicles

Figure 6.8 displays NMRD profiles for a unilamellar DMPC liposome sample at 25, 28, 32, 37, and 50°C. DMPC exhibits multiple phases as a function of temperature between 22 – 50°C: a rippled gel ($P_{\beta'}$) phase below Tm (23.6°C ± 1.5°C), an intermediate phase between the gel and fluid phases, and the liquid crystalline fluid phase above Tm. The relaxation mechanism in the liquid crystalline phase has been shown to be different from that in the intermediate

phase [203], and indeed, at 25°C, differences in the profile can be observed over the entire frequency range when compared with those obtained at 28 – 50°C. PCS data could not be obtained for this sample due to instrument unavailability, but previous experiments suggest a vesicle diameter of ~200 nm. As in the case of DOPC, R_1 decreases with an increase in temperature above 0.1 MHz in the temperature range of 28 – 50°C.

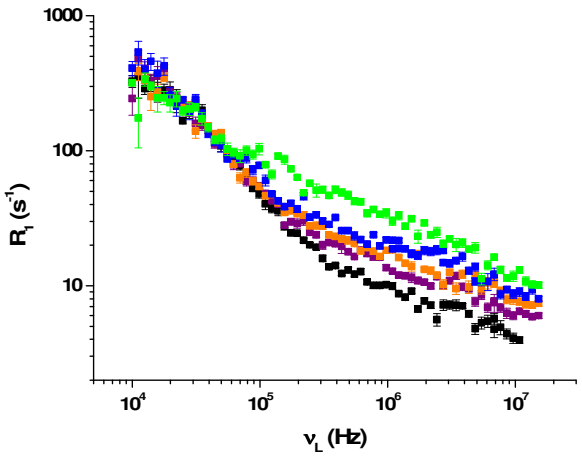

Figure 6.8. Frequency dependence of the ^{1}H spin-lattice relaxation rates of unilamellar DMPC vesicles at ■ 25°C, ■ 28°, ■ 32°C, ■ 37°C, and ■ 50°C. The vesicle diameter is ~200 nm, as suggested by previous experiments.

6.3.3 Effect of cholesterol on nuclear spin relaxation

6.3.3.1 Unilamellar DOPC vesicles

The relaxation curves in Figure 6.9 were recorded for three DOPC liposome samples with differing cholesterol content. Structurally, when cholesterol is added to the membrane, the rigid part of the molecule extends into the bilayer to a depth approximately equal to carbon atom 12 or 13 of the phospholipid acyl chain [240]. Its presence between the phospholipid molecules helps to 'pack' the fatty acid chains, thereby reducing their flexibility and stiffening the membranes, thus providing structural stability. The structure of cholesterol is shown in Figure 6.10.

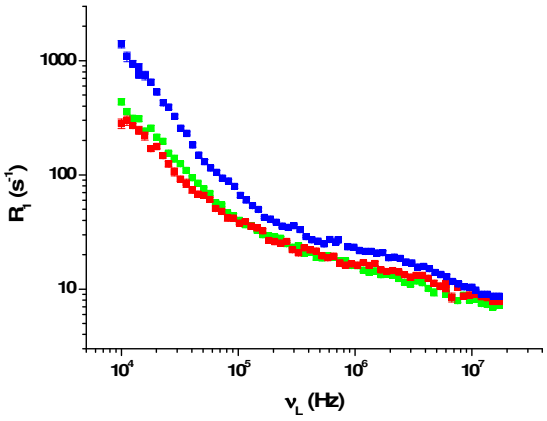

Figure 6.9. Frequency dependence of the ^{1}H spin-lattice relaxation rates at 25°C of DOPC vesicles in D_2O with varying cholesterol content, and similar vesicle sizes. ■ 0% cholesterol: D_{PCS} = 153 nm, ■ 10% cholesterol: D_{PCS} = 160 nm, ■ 25% cholesterol: D_{PCS} = 135 nm**.**

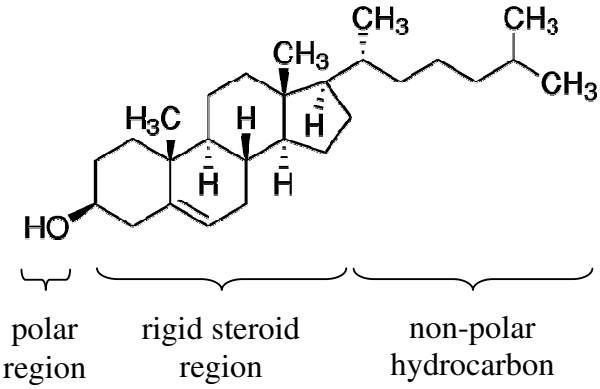

Figure 6.10. The structure of cholesterol.

It is clear that cholesterol affects the shape of the relaxation profile, most notably for ν_L below ~ 0.25 MHz where slower collective motions are known to be a significant contributing mechanism. While the slight change in the average vesicle size probably contributes to the change in the relaxation rate at low frequencies below 0.2 MHz, the magnitude of difference is too great to be attributed to a size effect alone (Figure 6.3)**.** Thus, the increase in the relaxation rate is probably associated with an increase in membrane rigidity due to the presence of higher amounts of cholesterol [231,254,255]. Additionally, there appear to be differences in R_1 as a function of cholesterol content above ~ 0.2

MHz, a region of the profile previously shown to be unaffected by changes in vesicle size.

6.4 Discussion

6.4.1 Effect of vesicle size on nuclear spin relaxation

6.4.1.2 Model-free analysis

The magnetic resonance data obtained for DOPC liposome samples of different sizes (Figure 6.3) were analysed using the MFA. This approach indicated that the experimental relaxation curves can be expressed as a sum of three Lorentzian spectral densities of the form shown in Equation 6.2, corresponding to slow, medium, and fast motions. Thus, three correlation times and three coefficients can be extracted from the experimental data. The individual Lorentzian function contributions to the overall relaxation of DOPC vesicles for ~100 nm, 152 nm, and 240 nm vesicles are shown in Figures 6.11 – 6.13, respectively. The extracted parameters for each motion as a function of vesicle size are summarised in Table 6.2.

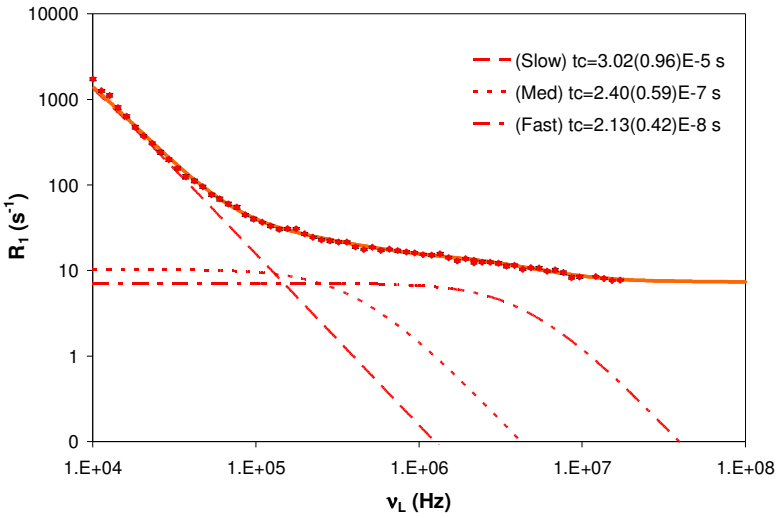

Figure 6.11. Individual contributions to the overall relaxation of unilamellar DOPC vesicles (~100 nm) in D_2O at 25°C. τ_c(Slow) = 3.02(0.96)E-5 s, τ_c(Med) = 2.40(0.59)E-7 s, τ_c(Fast) = 2.13(0.42)E-8 s. α = 7.38 s^{-1}, β_1 = 4.65(1.33)E8 s^{-2}, β_2 = 4.28(0.96)E7 s^{-2}, β_3 = 3.31(0.49)E7 s^{-2}.

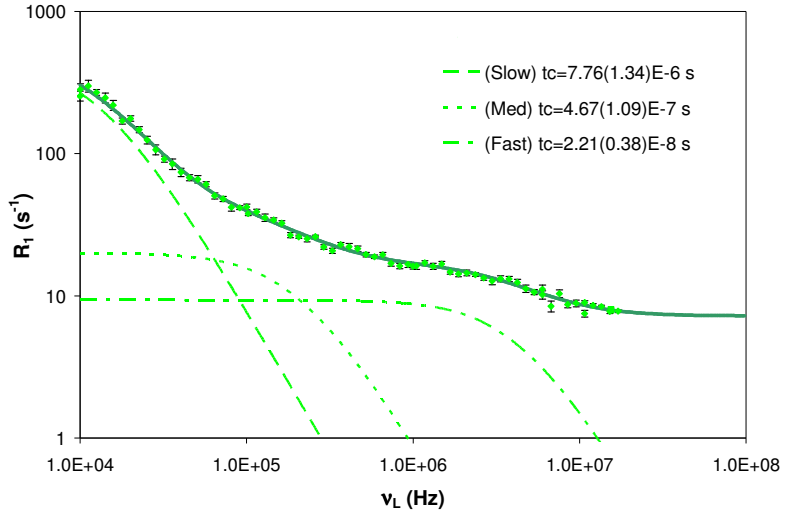

Figure 6.12. Individual contributions to the overall relaxation of unilamellar DOPC vesicles (152 nm) in D_2O at 25°C. τ_c(Slow) = 7.76(1.34)E-6 s, τ_c(Med) = 4.67(1.09)E-7 s, τ_c(Fast) = 2.21(0.38)E-8 s. The reported Z-Average diameter is from PCS measurements. $\alpha = 7.22\ s^{-1}$, $\beta_1 = 6.02(0.34)E7\ s^{-2}$, $\beta_2 = 4.27(0.53)E6\ s^{-2}$, $\beta_3 = 4.22(0.63)E7\ s^{-2}$.

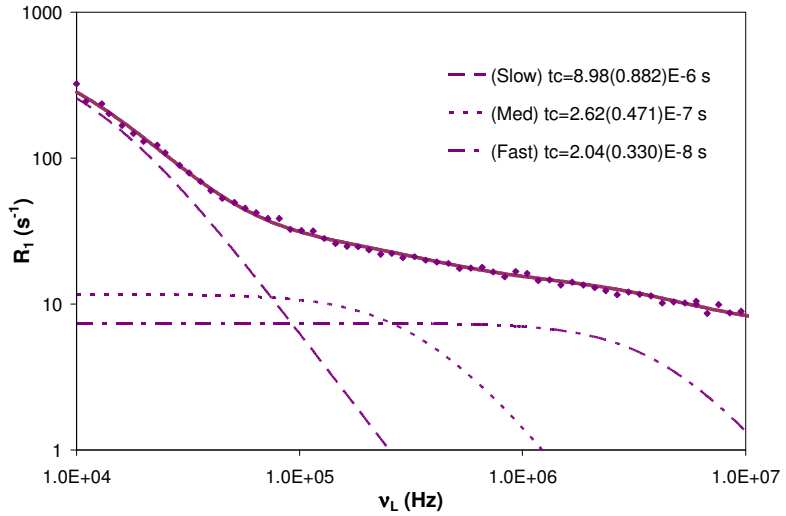

Figure 6.13. Individual contributions to the overall relaxation of unilamellar DOPC vesicles (240 nm) in D_2O at 25°C. τ_c(Slow) = 8.98(0.88)E-6 s, τ_c(Med) = 2.62(0.47)E-7 s, τ_c(Fast) = 2.04(0.33)E-8 s. The reported Z-Average diameter is from PCS measurements. $\alpha = 6.99\ s^{-1}$, $\beta_1 = 5.67(0.25)E7\ s^{-2}$, $\beta_2 = 4.44(0.71)E7\ s^{-2}$, $\beta_3 = 3.62(0.48)E8\ s^{-2}$.

Table 6.2. Summary of free parameters extracted using the MFA from experimental relaxation data at 25°C for 100 nm, 152 nm, and 240 nm unilamellar DOPC vesicles.

D_{PCS} (nm)	α (s^{-1})	β_1 (s^{-2})	τ_c Slow (s)	β_2 (s^{-2})	τ_c Med (s)	β_3 (s^{-2})	τ_c Fast (s)
~100	7.38	4.7(1.3)E8	3.0(1.0)E-5	4.3(1.0)E7	2.4(0.6)E-7	3.3(0.5)E7	2.1(0.4)E-8
152	7.22	6.0(0.3)E7	7.8(1.3)E-6	4.3(0.5)E6	4.7(1.1)E-7	4.2(0.6)E7	2.2(0.4)E-8
240	6.99	5.7(0.3)E7	8.9(0.9)E-6	4.4(0.7)E7	2.6(0.5)E-7	3.6(0.5)E8	2.0(0.3)E-8

While model-free analysis resulted in high quality fits to the data, it required the use of 7 free parameters. Although MFA avoids the potential for overinterpretation, the extracted fitting parameters only have general meaning, and the large number of free parameters is far from ideal.

Ideally, a fitting procedure should have as few free parameters as possible and it should be possible to connect some of the parameters with accepted values from independent measurements or at least for the parameters to be physically consistent. Thus, for instance there is no clear systematic change in the τ_c values with liposome size. This strongly suggests over-sensitivity of the extracted parameters to minor variations, and noise, in the data. Similar problems were encountered when the temperature dependence of the MFA parameters were analysed. Given the apparent limitations of the model-free approach for analysis of our data, we have turned instead to a physical model-based analysis, which allows a reduction in the number of free parameters by utilising known physical quantities.

6.4.1.3 Defined motions model analysis

We have applied an approach developed by Prof. Esteban Anoardo and his group from the National University of Córdoba in Argentina, made available to our group through our current collaboration. In his interpretation, Anoardo assumes there are four statistically independent contributions to R_1; order fluctuations (OF), diffusion (D), molecular rotations (MR), and fast motions (FM). The latter only contribute as a frequency dependent term (A_{FM}) because the dispersion for

such fast motions lies above our highest measurement frequency; i.e., we are in the low frequency plateau for fast motions. The overall relaxation is expressed by Equation 6.8

$$\frac{1}{T_1} = \frac{\alpha_{OF}}{T_1^{OF}} + \frac{\alpha_D}{T_1^D} + \frac{\alpha_{MR}}{T_1^{MR}} + A_{FM} \qquad \text{Equation 6.8}$$

where α_{OF}, α_D, α_{MR}, and A_{FM} are constants representing the relative contribution of each process to the relaxation rate. In the following four sections, we will take a closer look at each of the individual relaxation contributions.

6.4.1.3.1 Order fluctuations

Modelling of the order fluctuations assumes a flaccid, quasi-spherical vesicle with a fixed radius R_0. The spin-lattice relaxation time due to order fluctuations is given by Equation 6.9. A_{OF} is a constant representing the amplitude of the contribution, and can be calculated using Equation 6.10, where r is the effective proton-proton separation, and the remaining parameters are well known quantities. The spectral density function, J(ω), is given by Equation 6.11 [256].

$$\frac{1}{T_1^{OF}} = A_{OF} J(\omega) \qquad \text{Equation 6.9}$$

$$A_{OF} = \frac{9}{8}\left(\frac{\gamma^2\hbar}{r^3}\right)^2\left(\frac{\mu_0}{4\pi}\right)^2 \qquad \text{Equation 6.10}$$

$$J(\omega) = \frac{K_B T}{4\pi\kappa}\sum_{l=2}^{l_{max}} \frac{l(l+1)(2l+1)}{(l^2+l-2)(l^2+l+\sigma)} \frac{2\tau_l}{(1+\omega^2\tau_l^2)} \qquad \text{Equation 6.11}$$

In Equation 6.11 κ is the bending elastic modulus, $l_{max} \sim \pi R_0/a$ the maximum normal mode where a is the average distance between neighbouring molecules in

the lateral direction, σ denotes an effective lateral tension, and τ_l is the correlation time, given by Equation 6.12, where η is the viscosity of D_2O.

$$\tau_l = \frac{\eta R_0^3}{\kappa} \frac{(2l+1)(l^2+2l-1)}{l(l+1)(l+2)(l-1)(l^2+l+\sigma)} \qquad \text{Equation 6.12}$$

Thus, T_1^{OF} can be completely determined using Equations 6.9 – 6.12, and is only a function of vesicle diameter, via l_{max}, for a single given lipid at a constant temperature. The simulated frequency dependence of J(ω) for order fluctuations for three different vesicle diameters is shown in Figure 6.14. This simulation was performed by implementing Equation 6.11 in Excel.

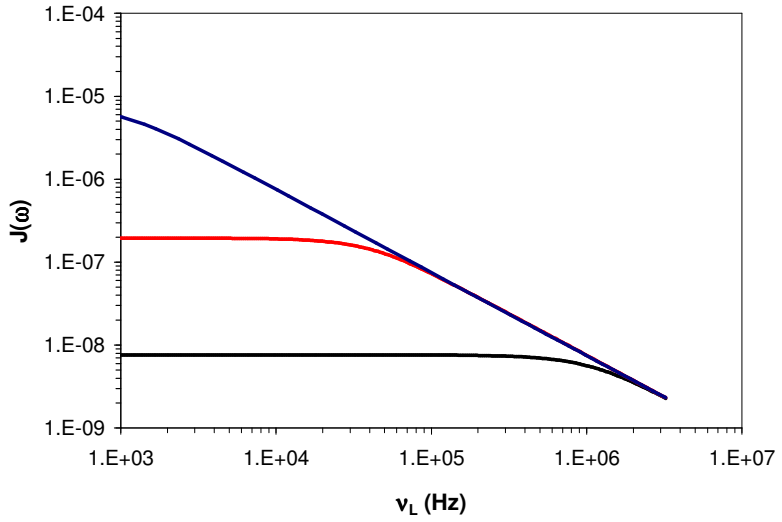

Figure 6.14. Frequency dependence of the spectral density function J(ω) for order fluctuations (Equation 6.11) for three vesicle diameters, d: — d = 400 nm, — d = 118 nm, — d= 40 nm. The other parameters used in the simulation are: η = 8.3025E-4 kg·m^{-1}s^{-1}, s = 0, κ = 1.5E-20 kg·m^{2}s^{-2}, and T = 310 K.

This simulation predicts the presence of a range of linear frequency dependence, $1/T_1 \sim \omega^{-1}$, for each of the vesicle diameters. The range over which this behaviour dominates increases with an increase in diameter, as the larger vesicles more

closely resemble a planar structure. Thus this result is consistent with the results of Marqusee et al. [257] in which it was demonstrated that the low frequency Larmor motions in lipid bilayer membranes may be modelled as fluctuations of the director of a planar structure, with a ~ ω_0^{-1} dependence, as opposed to a 3-dimensional nematic liquid crystal.

6.4.1.3.2 Diffusion

Anoardo's approach to the contribution of diffusion to the spin-lattice relaxation is based on the theory of spin relaxation due to molecular diffusion on curved surfaces, proposed by Halle [258]. The spin-lattice relaxation time for diffusion is given by Equation 6.13; A_D is an adjustable parameter. J(ω) is given by Equation 6.14, where τ_D is a fixed parameter which can be calculated by Equation 6.15.

$$\frac{1}{T_1^D} = A_D(J(\omega) + 4J(2\omega)) \qquad \text{Equation 6.13}$$

$$J(\omega) = \frac{1}{5}\frac{\tau_D}{1+(\omega\tau_D)^2} \qquad \text{Equation 6.14}$$

$$\tau_D = \frac{2\pi\eta R_0^5}{9k_BTD_T}\left(\frac{4\pi\eta R_0^3}{3k_BT} + \frac{R_0^2}{6D_T}\right)^{-1} \qquad \text{Equation 6.15}$$

In Equation 6.15, D_T is the translational diffusion coefficient on the surface of the molecules and the remaining parameters are well known quantities.

6.4.1.3.3 Molecular rotations

The longitudinal relaxation rate for molecular rotation is given by Equation 6.16; A_{MR} is an adjustable parameter. J(ω) is given by Equation 6.17, where the value of τ_{MR} can be fixed based on the results of proton spin-lattice relaxation

experiments reported in the literature [259]. Once again, this spectral density contribution has a Lorentzian form.

$$\frac{1}{T_1^{MR}} = A_{MR} J(\omega) \qquad \text{Equation 6.16}$$

$$J(\omega)_{MR} = \tau_{MR}\left(\frac{1}{1+(\omega\,\tau_{MR})^2} + 4\frac{1}{1+(2\omega\,\tau_{MR})^2}\right) \qquad \text{Equation 6.17}$$

6.4.1.3.4 T_1 dispersion analysis

The function used for the dispersion analysis, the sum of contributions for order fluctuations, diffusion, molecular rotations, and fast motions, is given by Equation 6.18. A list of the free and fixed parameters is given in Table 6.3.

$$\begin{aligned}\frac{1}{T_1} &= A_{OF}\left(\frac{K_B T}{4\pi\kappa}\sum_{l=2}^{l_{max}}\frac{l(l+1)(2l+1)}{(l^2+l-2)(l^2+l+\sigma)}\frac{2\tau_l}{(1+\omega^2\tau_l^2)}\right)\\ &+ A_D\tau_D\left(\frac{1}{5}\frac{1}{1+(\omega\tau_D)^2}+\frac{4}{5}\frac{1}{1+(2\omega\tau_D)^2}\right)\\ &+ A_{MR}\tau_{MR}\left(\frac{1}{1+(\omega\tau_{MR})^2}+4\frac{1}{1+(2\omega\tau_{MR})^2}\right)+A_{FM}\end{aligned} \qquad \text{Equation 6.18}$$

Table 6.3. Summary of parameters used in the PBA analysis of the overall relaxation of unilamellar vesicles.

Adjustable parameters	Fixed parameters
A_D	A_{OF}[(a)]
A_{MR}	τ_L
A_{FM}	τ_D
	τ_{MR}

[(a)] A_{OF} is fixed for a given lipid by Equation 6.10

The DMM reduces the number of free parameters from 7 to 3 when compared to the model-free approach. In order to investigate whether the model is consistent with our experimental data, we have used it to analyse the relaxation data reported here for unilamellar 108 nm and 195 nm DMPC vesicles at 37°C. The individual contributions to the overall relaxation rate, as well as the sum of the four contributions, for the 108 nm and 195 nm vesicles, respectively, are shown in Figures 6.15 – 6.16. The approach is found to result in good agreement with the experimental data, especially when the small number of free parameters is considered. A summary of the parameters used for the profiles at each vesicle size is presented in Table 6.4.

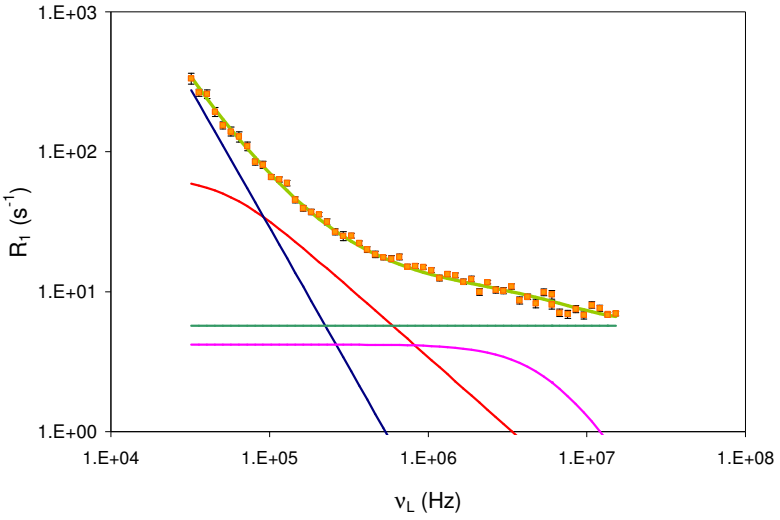

Figure 6.15. Individual contributions, from DMM analysis, to the overall relaxation of 108 nm unilamellar DMPC vesicles in D_2O at 37°C. — OF, — D, — MR, — FM, — sum of the four individual contributions resulting in the overall relaxation.

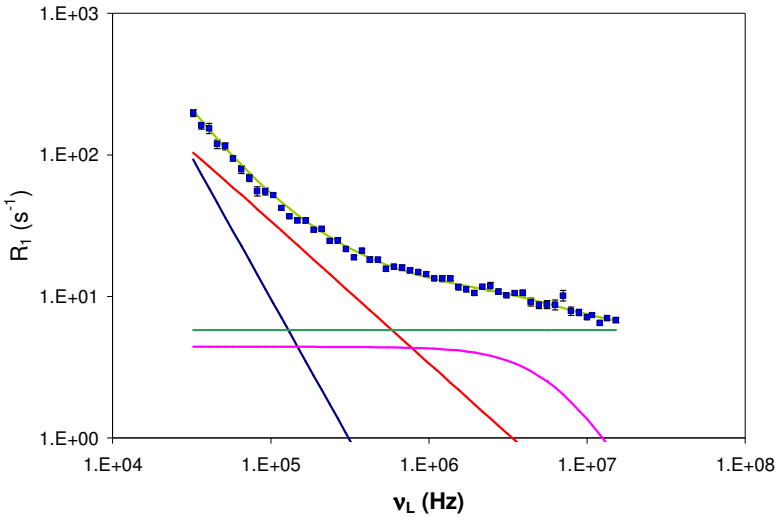

Figure 6.16. Individual contributions, from DMM analysis, to the overall relaxation of 195 nm unilamellar DMPC vesicles in D_2O at 37°C. — OF, — D, — MR, — FM, — sum of the four individual contributions resulting in the overall relaxation.

Table 6.4. Summary of parameters used in the DMM approach to analysing the experimental relaxation data recorded for 108 nm and 195 nm unilamellar DMPC vesicles at 37°C.

Vesicle size (nm)	**A_D (s^{-2})**	**A_{MR} (s^{-2})**	**A_{FM} (s^{-2})**	**A_{OF} (s^{-2})**	**τ_D (s)**	**τ_{MR} (s)**
108 nm	8.5E+08	6.0E+07	5.7	4.5E+08	2.98E-05	1.40E-08
195 nm	1.0E+09	6.3E+07	5.8	4.5E+08	1.05E-04	1.40E-08

6.4.1.3.5 Validity of the DMM for the interpretation of DOPC data

The defined motions model, while originally developed for DMPC, has been extended to interpret DOPC relaxation data by modification of the fixed parameters to account for the structural differences between DMPC and DOPC. The fundamental structural difference between DMPC and DOPC is the presence of a double bond on C9 in each of the acyl chains of DOPC (Figure 6.4). The introduction of the unsaturation causes a disruption of the acyl chain packing and introduces a kink into the chain structure. This increases the average interfacial area per lipid [260], and therefore the average lipid-lipid distance within each

leaflet of the bilayer. The average interfacial area per lipid for DMPC and DOPC is 59.6 and 72.5 $Å^2$, respectively [230]. This has several effects on membrane dynamics. For instance, the phospholipid rotational motion has been reported to increase, at a given temperature, with an increase in the average area per lipid [261]. Similarly, the rate of lipid lateral diffusion has been shown to increase as a result of an increase in the area per molecule caused by unsaturation [262].

The interpretation of the DOPC relaxation data using the DMM approach required changes in three of the fixed parameters; κ, which reflects the membrane rigidity (Equations 6.11 and 6.12), τ_{MR} (Equation 6.17), and D_T (Equation 6.15). The κ value was increased by 50% from that used for DMPC, based on the results of a study by Rawicz et al. [263], in which κ values were obtained by a micropipette pressurisation technique. Previous proton spin-lattice relaxation time experiments suggest a value for τ_{MR} on the order of $2x10^{-8}$ s [259], and the value for D_T was taken directly from the results of a pulsed field gradient (pfg) NMR study by Filippov et al. [202].

As a first step toward the interpretation of DOPC data, we analysed the relaxation data for unilamellar 182 nm DOPC vesicles. The individual contributions to the overall relaxation rate, as well as the sum of the four contributions are shown in Figure 6.17. A summary of the parameters used in the analysis are shown in Table 6.5, where they are also compared with those used in the analysis of the 195 nm unilamellar DMPC vesicles.

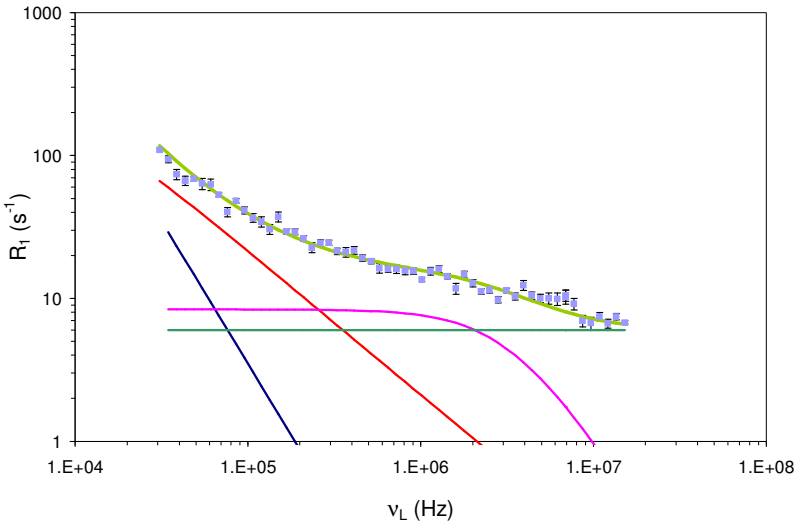

Figure 6.17. Individual contributions, from DMM analysis, to the overall relaxation of 182 nm unilamellar DOPC vesicles in D_2O at 25°C. — OF, — D, — MR, — FM, — sum of the four individual contributions resulting in the overall relaxation.

Table 6.5. Summary of parameters used in the DMM approach to analysing the experimental relaxation data at of 195 nm DMPC vesicles and 182 nm DOPC vesicles at 37 and 25°C, respectively. Both liposome samples were in the liquid crystalline phase when their relaxation profiles were recorded.

Lipid	**Temp** (°C)	**Diameter** (nm)	A_D (s^{-2})	A_{MR} (s^{-2})	A_{FM} (s^{-2})	A_{OF} (s^{-2})	τ_D (s)	τ_{MR} (s)
DMPC	37	195	1.0E+09	6.3E+07	5.8	4.5E+08	1.1E-04	1.4E-08
DOPC	25	182	4.8E+08	6.2E+07	6.0	4.5E+08	1.4E-04	1.2E-08

The DMM approach proves to be capable of reproducing the experimental data for DOPC liposomes. The consistency between the analysis and the experimental data appears to be of similar quality to that previously observed for DMPC (Figures 6.15 and 6.16). As the profiles were not recorded at the same temperature for these two samples, we will not attempt to make any further comparisons.

We can now attempt to utilise the DMM to analyse the DOPC data obtained for vesicles of different sizes (Figure 6.3) in order to investigate the effect of vesicle size on nuclear spin relaxation.

The DMM was used to analyse the relaxation data of unilamellar DOPC liposome samples of different sizes. The individual contributions to the overall relaxation rate, as well as the sum of the four contributions, for each vesicle size are shown in Figures 6.18 – 6.20. A summary of the parameters used to interpret the data for each vesicle size is summarised in Table 6.6.

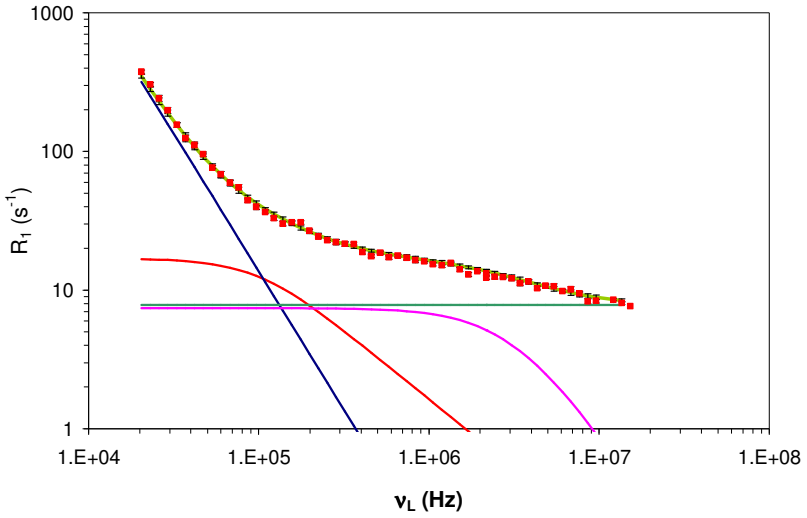

Figure 6.18. Individual contributions, from DMM analysis, to the overall relaxation of ~ 100 nm unilamellar DOPC vesicles in D_2O at 25°C. — OF, — D, — MR, — FM, — sum of the four individual contributions resulting in the overall relaxation.

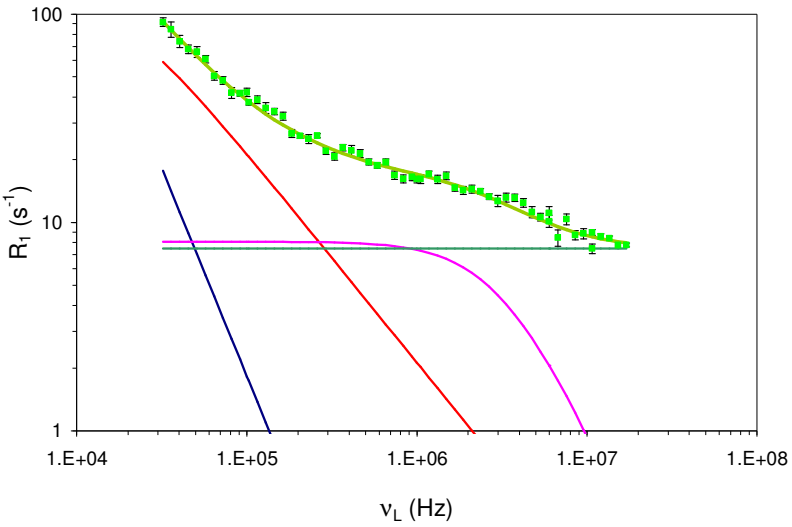

Figure 6.19. Individual contributions, from DMM analysis, to the overall relaxation of 152 nm unilamellar DOPC vesicles in D_2O at 25°C. — OF, — D, — MR, — FM, — sum of the four individual contributions resulting in the overall relaxation.

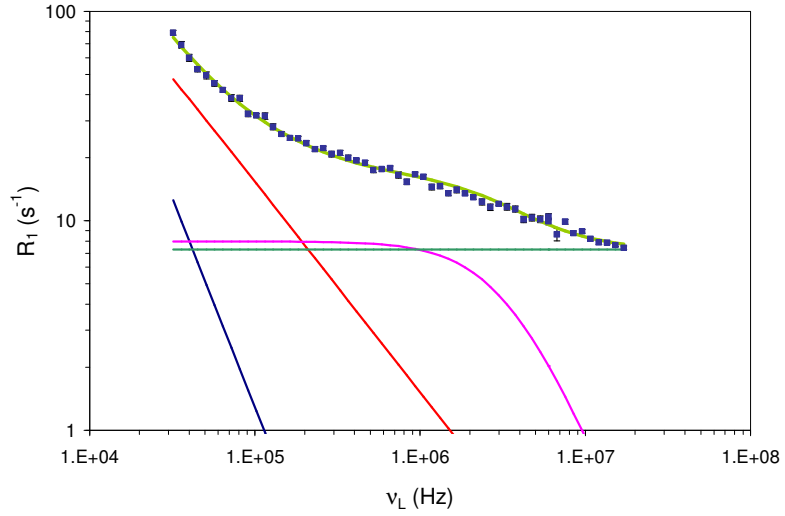

Figure 6.20. Individual contributions, from DMM analysis, to the overall relaxation of 240 nm unilamellar DOPC vesicles in D_2O at 25°C. — OF, — D, — MR, — FM, — sum of the four individual contributions resulting in the overall relaxation.

Table 6.6. A summary of the parameters used in the DMM approach to interpret the experimental relaxation data, at 25°C, of DOPC liposomes samples of three different sizes.

Diameter (nm)	A_D (s^{-2})	A_{MR} (s^{-2})	A_{FM} (s^{-2})	A_{OF} (s^{-2})	τ_D (s)	τ_{MR} (s)
~ 100	5.0E+08	5.5E+07	7.8	4.5E+08	3.7E-05	2.7E-08
152	1.7E+08	6.0E+07	7.5	4.5E+08	9.4E-05	2.7E-08
240	3.6E+08	5.9E+07	7.3	4.5E+08	2.8E-04	2.7E-08

The DMM approach proves to be capable of reproducing the experimental data for DOPC liposomes of different sizes with only three adjustable parameters. The consistency between the analysis and the experimental data appears to be of similar quality for each vesicle size.

6.4.2 Effect of temperature on nuclear spin relaxation

The interpretation of liposome relaxation data at different temperatures using the DMM requires further changes in the fixed parameters. It is known that both D_T and τ_{MR} should be temperature dependent [202,264]. A comprehensive literature review is currently underway in order to identify appropriate parameters for DMM analysis. In the meantime, however, the relaxation data presented can be used to make some more general observations regarding the effect of temperature on nuclear spin relaxation. There are two distinct dispersion regimes apparent in the profiles of both DOPC and DMPC UVs at all temperatures (Figures 6.21 and 6.22, respectively). If we take the alternative approach of fitting power law spectral densities of the form shown in Equation 6.19, below ~ 0.1 – 0.3 MHz where order fluctuations are known to contribute to the proton T_1 relaxation time, a good fit is obtained, as expected for smectic-type collective motions of lipid bilayers. Above 0.1 – 0.3 MHz however, there are clear differences in the profiles at all temperatures. For motions in the fast motion (extreme narrowing) limit (see left hand side of Figure 1.11, Chapter 1), it is anticipated that T_1 should increase (R_1 decrease) with temperature [203], and this is clearly seen in Figures 6.20 and 6.21. A summary of the fitting parameters for DOPC and DMPC samples at all temperatures is presented in Table 6.7 and 6.8, respectively.

$$R_1 = A\nu_L^{\,k} \qquad \text{Equation 6.19}$$

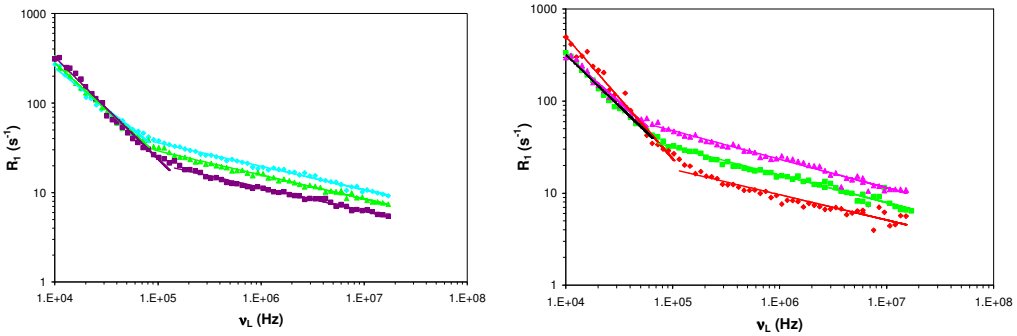

Figure 6.21. Power law fits to the profiles of unilamellar DOPC vesicles at (a) ■ 18°, ■ 25°C, and ■ 37°C (Z-Avg = 240 nm), and (b) ■ 10°C, ■ 25°C, and ■ 45°C. The vesicle diameter is ~230 nm, as suggested by previous experiments.

Table 6.7. A summary of the fitting parameters from the power law fits to the NMRD profiles of unilamellar DOPC vesicles at different temperatures.

Temp (ºC)	Vesicle size (nm)	Low frequency regime			High frequency regime		
		A	k	R^2	A	k	R^2
18	240	1.16E+06	-0.92	0.976	752	-0.26	0.991
25		4.08E+06	-1.0	0.987	646	-0.27	0.989
37		1.20E+07	-1.1	0.987	426	-0.26	0.983
10	~230	4.54E+07	-1.0	0.975	1718	-0.31	0.980
25		9.80E+06	-1.1	0.988	1012	-0.30	0.971
45		1.09E+08	-1.3	0.980	437	-0.28	0.902

There are no clear trends in the powers or intensity parameters obtained from this simplistic approach, for these very two similarly sized DOPC UV suspensions.

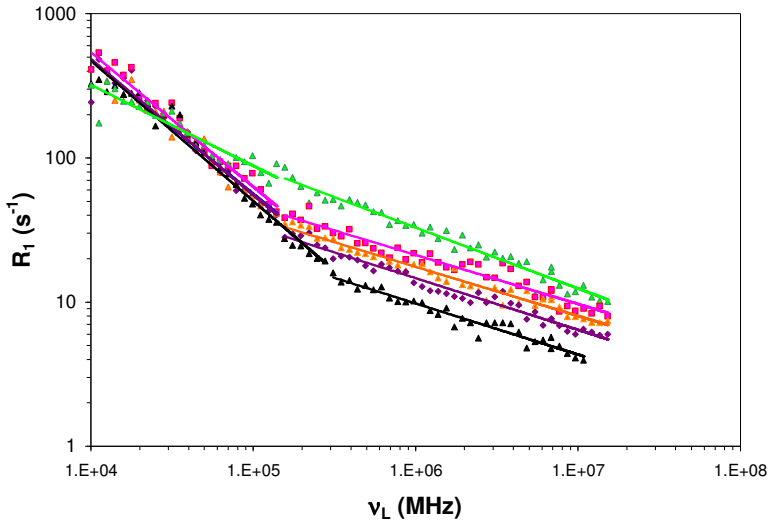

Figure 6.22. Power law fits to the NMRD profiles of unilamellar DMPC vesicles at ■ 25°C, ■ 28°, ■ 32°C, ■ 37°C, and ■ 50°C. The vesicle diameter is ~200 nm, as suggested by previous experiments.

Table 6.8. A summary of the fitting parameters from the power law fits to the NMRD profiles of unilamellar DMPC vesicles at different temperatures.

Temp (ºC)	Low frequency regime			High frequency regime		
	A	k	R^2	A	k	R^2
25	5.69E+04	-0.56	0.879	1.13E+04	-0.42	0.966
28	2.95E+06	-0.93	0.963	2.34E+03	-0.34	0.946
32	2.33E+06	-0.92	0.960	1.96E+03	-0.34	0.963
37	2.91E+06	-0.94	0.948	2.09E+03	-0.36	0.971
50	3.65E+06	-0.97	0.972	1.32E+03	0.36	0.950

For DMPC UV suspensions, this data suggests little change in the power law dependencies at low or high frequencies in the liquid crystalline phase.

For both UV compositions, it appears that no clear trends in the powers or intensity parameters emerge from fitting power law functions. Research to determine whether application of the DMM results in physically consistent trends in the extracted parameters for DOPC and DMPC is ongoing between the two groups.

6.4.3 Conclusions and outlook

We have shown that the DMM has potential for interpretation of the relaxation behaviour of liposomes composed of a single lipid, with fewer parameters than all other published approaches. This is both an interesting result and in one sense, a disappointing one, as it suggests limits to the insight that can be gained, if the relaxation profile can be essentially predicted from knowledge of liposome size and the κ value. However, it can be difficult to measure κ values for liposomes, and a microscopic NMR reporter of an emergent macroscopic property has added value as it can provide insight into the underlying cause of changes in performance.

Our long-term goal is to study more complex systems, such as multi-lipid model membranes and lipid-cholesterol formulations. These systems are obviously more biologically relevant, and an understanding of their behaviour and dynamics offers potential for tailoring membrane properties for improved liposome carrier systems. The work presented in this chapter on DMM analysis of the size dependence on two types of single-lipid liposomes puts us in a position to advance the analysis toward the interpretation of multi-component systems.

Following detailed analysis of the temperature dependence of the relaxation profiles, the next step will be to attempt DMM analysis of the DOPC:cholesterol liposome profiles. The interpretation of this data will require additional changes in the fixed parameters. The increased rigidity of membranes due to the presence of cholesterol should be reflected in a decrease in the rate of the slow collective motions of the bilayer. Additionally, the presence of cholesterol between the phospholipid molecules increases the jump distance for a laterally diffusing lipid molecule, therefore potentially altering D_T. Filippov et al. [202] measured lipid lateral diffusion coefficients as a function of cholesterol in the liquid ordered phase of oriented bilayers of DOPC by pfg-NMR. Their results suggest that the value of the D_T should decrease linearly as the cholesterol concentration is increased from 0 – 40 mol%. ^{2}H-NMR measurements have shown an increase in the rate of molecular rotation in the presence of cholesterol due to improved lipid

chain ordering, resulting in a reduction in the number of chain entanglements [265,266]. An additional complicating factor, that will have to be borne in mind in future work, is the potential for the formation if cholesterol-rich domains, or rafts [267]. This is usually observed at higher cholesterol content, although there is no clear evidence of this in the data presented in Figure 6.9.

Thesis conclusions

Our work with magnetic nanoparticle dispersions, in organic solvents, has demonstrated that it is possible to control the nanoparticle size and to measure the emergent magnetic properties of the suspensions using magnetic resonance techniques. We found that the NMR relaxation enhancement decreases for smaller particles and showed that at the lower end of the size range, increased relative surface area renders the particles more magnetically anisotropic, due to surface defects. We went on to demonstrate that the presence of defects influences the kinetics of surfactant desorption, under conditions where a second phase competes for the stabiliser, resulting in strong size dependence of nanoparticle cluster growth.

The size controlled nanoparticle and nanoparticle clusters we have prepared are coated with hydrophobic stabilisers, so biomedical applications require re-dispersion in water. Work to date suggests that phase transfer of pre-formed assemblies using hydrophilic polymers is unlikely to maintain control over cluster size. On the other hand, detailed kinetic studies have clarified the critical role of maintaining a low concentration of activated nanoparticles in preserving the size dispersity of the growing population. Kinetic modelling of the data already recorded is ongoing, and this will provide insight into the iron-oxide surface coverage required for a self-preserving cluster size distribution. We hope that this approach will allow us to identify suitable stabilisers and competing phases for other manifestations of controlled cluster growth; ideally for magnetic nanoparticles initially dispersed in aqueous media.

In the more immediate term, we demonstrated competition from alkyl stabilised gold nanoparticles for activated sites on iron-oxide nanoparticles and nanoparticle clusters. We have shown that this effect allows the production of iron-oxide-gold core-shell structures of controlled size by the addition of gold nanoparticles to a growing iron-oxide cluster suspension, at a selected time. It can also further improve the size dispersity of the cluster suspension, as compared to iron-oxide alone. The presence of gold on the cluster surface may also provide a means to disperse the suspensions in water, as there is a well-established phase transfer chemistry for gold, involving mecapato-carboxylic acids, amongst many other candidate stabilisers.

Finally, gold also provides opportunities for functionalisation of the clusters with a range of biomolecules. In future work, both of these possibilities could be explored.

We investigated a more direct route to size controlled aqueous magnetic nanoparticle suspensions by adapting accepted methods for the preparation of magnetoliposomes, and obtained limited size selection by magnetic filtration. We adopted approaches to produce magnetoliposomes both with and without an aqueous lumen. The magnetic resonance properties of the former were found to be independent of the degree of hydration, but the latter was found to vary significantly with time. For the magnetoliposomes with no aqueous layer it was found that the low frequency relaxation was dependent on size. As magnetic filtration allows some control over size, this opens up the possibility for tunable and biocompatible low-field contrast agents that may find application with the advent of micro-Tesla MRI. In contrast to dispersed nanoparticle suspensions, we found the NMR relaxation enhancement to decrease for larger magnetoliposomes. This is because less of the iron-oxide is accessible to the bulk water, due to lower relative surface area. Research to apply the formulation methodologies we have developed to magnetoliposomes incorporating cationic lipids, which would have improved bio-compatibility and cellular uptake, is planned. This approach should be feasible given the amphoteric nature of the iron-oxide surface.

Finally, we have made some progress on the related issue of how liposome membrane composition affects both water permeability, which is known to be largely determined by lipid diffusion, and membrane stability, which relates to 'stiffness'. We have demonstrated that a model, where the motions are defined and the critical physico-chemical parameters are taken from the literature, is capable of quantitatively reproducing the NMR relaxation profiles of liposomes of different sizes, which are composed of a single lipid type. In ongoing work we are applying this approach to the interpretation of more biologically relevant systems, including multi-lipid and lipid-cholesterol formulations, for which the relevant parameters are not available. A convenient method for studying permeability and stiffness in liposomes would be a significant step forward in the development of a new generation of pharmacologically useful lipid-based formulations for both diagnostic, and in particular for therapeutic applications as drug delivery vehicles.

References

[1] Gerlach, W. and Stern, O. Der Experimentelle Nachweis des magnetischen Moments des Silberatoms. Zeitschrift für Physik A Hadrons and Nuclei (1922) 8, 110 - 111.

[2] Uhlenbeck, G.E. and Goudsmit, S. Spinning Electrons and the Structure of Spectra. Nature (1926) 117, 264 - 265.

[3] Dirac, P.A.M. The Quantum Theory of the Electron. Proceedings of the Royal Society A (1928) 117, 610.

[4] Pauli, W. Zur Frage der theoretischen Deutung der Satelliten einiger Spektrallinien und ihrer Beeinflussung durch magnetische Felder. Naturwissenschaften (1924) 12, 741 - 743.

[5] Hahn, E.L. Spin Echoes. Physical Review (1950) 80, 580 LP - 594.

[6] Carr, H.Y. and Purcell, E.M. Effects of Diffusion on Free Precession in Nuclear Magnetic Resonance Experiments. Physical Review (1954) 94, 630 - 638.

[7] Callaghan, P.T. Principles of Nuclear Magnetic Resonance Microscopy. Oxford: Oxford University Press Inc., 1991, p. 492.

[8] Meiboom, S. and Gill, D. Modified Spin-Echo Method for Measuring Nuclear Relaxation Times. The Review of Scientific Instruments (1958) 29, 688 - 691.

[9] Rajan, S.S. MRI: A Conceptual Overview. New York: Springer-Verlag, 1997, p. 167.

[10] Jones, G.P. Spin-Lattice Relaxation in the Rotating Frame: Weak-Collision Case. Physical Review (1966) 148, 332 LP - 335.

[11] Puddephat, M. Principles of Magnetic Resonance Imaging. Electronic source, 2008.

[12] Damadian, R. Tumor Detection by Nuclear Magnetic Resonance. Science (1971) 171, 1151 - 1153.

[13] Lauterbur, P.C. Image Formation by Induced Local Interactions; Examples Employing Nuclear Magnetic Resonance. Nature (1973) 242, 190 - 191.

[14] Moon, R.B. and Richards, J.H. Determination of Intracellular pH by ^{31}P Magnetic Resonance. Journal of Biological Chemistry (1973) 248, 7276 - 7278.

[15] Hoult, D.I., Busby, S.J.W., Gadian, D.G., Richards, R.E. and Seeley, P.H. Observation of Tissue Metabolites Using ^{31}P Nuclear Magnetic Resonance. Nature (1974) 252, 285 - 287.

[16] Kumar, A., Welti, D. and Ernst, R.R. NMR Fourier Zeugmatography. Journal of Magnetic Resonance (1975) 18, 69 - 83.

[17] Kumar, A., Welti, D. and Ernst, R.R. Imaging of Macroscopic Objects by NMR Fourier Zeugmatography. Naturwissenschaften (1975) 62, 34.

[18] Buxton, R.B. Introduction to Functional Magnetic Resonance Imaging: Principles and Techniques: Cambridge University Press, 2002, p. 536.

[19] Bushberg, J.T., Seibert, A., Leidholdt, E.M. and Boone, J.M. The Essential Physics of Medical Imaging: Lippincott Williams & Wilkins, 2002, p. 933.

[20] Markisz, J.A. and Aquilia, M. Technical Magnetic Resonance Imaging. Stamford: Appleton & Lange, 1996, p. 287.

[21] Watson, J.K. Applications of Magnetism. New York: John Wiley & Sons, Inc., 1980, p. 480.

[22] Carlin, R.L. and van Duyneveldt, A.J. Magnetic Properties of Transition Metal Compounds. New York: Springer-Verlag New York Inc., 1977, p. 264.

[23] Schwarz, J.A., Contescu, C.I. and Putyera, K. Dekker Encyclopedia of Nanoscience and Nanotechnology: CRC Press, 2004, p. 3200.

[24] Cornell, R.M. and Schertmann, U. The Iron Oxides: Structure, Properties, Reactions, Occurrences and Uses. Weinheim: Wiley-VCH, 1996, p. 703.

[25] Banerjee, S.K. and Moskowitz, B.M. in: Magnetite Biomineralization and Magnetoreception in Organisms. Ferrimagnetic Properties of Magnetite (J.L. Kirschvink, D.S. Jones and B.J. Mac Fadden, Eds.). New York: Plenum Press, 1985, p. 17 - 41.

[26] Zboril, R., Mashlan, M. and Petridis, D. Iron(III) Oxides from Thermal Processes-Synthesis, Structural and Magnetic Properties, Mössbauer Spectroscopy Characterization, and Applications. Chemistry of Materials (2002) 14, 969-982.

[27] Lu, A-H., Salabas, E.L. and Schüth, F. Angewandte Chemie International Edition (2007) 46, 1222-1244.

[28] Leslie-Pelecky, D.L. and Rieke, R.D. Magnetic Properties of Nanostructured Materials. Chemistry of Materials (1996) 8, 1770-1783.

[29] Bean, C.P. and Livingston, J.D. Superparamagnetism. Journal of Applied Physics (1959) 30, 120S - 129S.

[30] Sun, S., Murray, C.B., Weller, D., Folks, L. and Moser, A. Monodisperse FePt Nanoparticles and Ferromagnetic FePt Nanocrystal Superlattices. Science (2000) 287, 1989-1992.

[31] Goldman, A. in: Electronic Ceramics: Properties, Devices, and Applications. Magnetic Ceramics: CRC Press, 1987, p. 533.

[32] Desvaux, C., Amiens, C., Fejes, P., Renaud, P., Respaud, M., Lecante, P., Snoeck, E. and Chaudret, B. Multimillimetre-Large Superlattices of Air-Stable Iron-Cobalt Nanoparticles. Nature Materials (2005) 4, 750-753.

[33] Ceylan, S., Friese, C., Lammel, C., Mazac, K. and Kirschning, A. Inductive Heating for Organic Synthesis by Using Functionalized Magnetic nanoparticles Inside Microreactors. Angewandte Chemie International Edition (2008) 47, 8950-8953.

[34] Weissleder, R., Stark, D.D., Engelstad, B.L., Bacon, B.R., Compton, C.C., White, D.L., Jacobs, P. and Lewis, J. Superparamagnetic Iron Oxide: Pharmacokinetics and Toxicity. American Journal of Roentgenology (1989) 152, 167-173.

[35] Lübbe, A.S., Bergemann, C., Riess, H., Schriever, F., Reichardt, P., Possinger, K., Matthias, M., Dörken, B., Herrmann, F., Gürtler, R., Hohenberger, P., Haas, N., Sohr, R., Sander, B., Lemke, A.-J., Ohlendorf, D., Huhnt, W. and Huhn, D. Clinical Experiences with Magnetic Drug Targeting: A Phase I Study with 4'-Epidoxorubicin in 14 Patients with Advanced Solid Tumors. Cancer Research (1996) 56, 4686-4693.

[36] Bonnemain, B. Superparamagnetic Agents in Magnetic Resonance Imaging: Physiochemical Characteristics and Clinical Applications – A Review. Journal of Drug Targeting (1998) 6, 167 – 174.

[37] Lübbe, A.S., Alexiou, C. and Bergemann, C. Clinical Applications of Magnetic Drug Targeting. Journal of Surgical Research (2001) 95, 200-206.

[38] Neuberger, T., Schöpf, B., Hofmann, H., Hofmann, M. and von Rechenberg, B. Superparamagnetic Nanoparticles for Biomedical Applications: Possibilities and Limitations of a New Drug Delivery System. Journal of Magnetism and Magnetic Materials: Proceedings of the Fifth International Conference on Scientific and Clinical Applications of Magnetic Carriers (2005) 293, 483-496.

[39] Reszka, R., Beck, P., Fichtner, I., Hentschel, M., Richter, J. and Kreuter, J. Body Distribution of Free, Liposomal and Nanoparticle-Associated Mitoxantrone in B16-Melanoma-Bearing Mice. Journal of Pharmacology and Experimental Therapeutics (1997) 280, 232-237.

[40] Alexiou, C., Arnold, W., Klein, R.J., Parak, F.G., Hulin, P., Bergemann, C., Erhardt, W., Wagenpfeil, S. and Lubbe, A.S. Locoregional Cancer Treatment with Magnetic Drug Targeting. Cancer Res (2000) 60, 6641-6648.

[41] Kohler, N., Sun, C., Wang, J. and Zhang, M. Methotrexate-Modified Superparamagnetic Nanoparticles and Their Intracellular Uptake into Human Cancer Cells. Langmuir (2005) 21, 8858-8864.

[42] Zhang, Y., Kohler, N. and Zhang, M. Surface Modification of Superparamagnetic Magnetite Nanoparticles and their Intracellular Uptake. Biomaterials (2002) 23, 1553-1561.

[43] Yu, M.K., Jeong, Y.Y., Park, J., Park, S., Kim, J.W., Min, J.J., Kim, K. and Jon, S. Drug-Loaded Superparamagnetic Iron Oxide Nanoparticles for Combined Cancer Imaging and Therapy In Vivo. Angewandte Chemie (2008) 120, 5442-5445.

[44] Yu, M.K., Jeong, Y.Y., Park, J., Park, S., Kim, J.W., Min, J.J., Kim, K. and Jon, S. Drug-Loaded Superparamagnetic Iron Oxide Nanoparticles for Combined Cancer Imaging and Therapy In Vivo. Angewandte Chemie International Edition (2008) 47, 5362-5365.

[45] Babincová, M., Sourivong, P., Chorvát, D. and Babinec, P. Laser Triggered Drug Release From Magnetoliposomes. Journal of Magnetism and Magnetic Materials (1999) 194, 163-166.

[46] Kuznetsov, A.A., Filippov, V.I., Alyautdin, R.N., Torshina, N.L. and Kuznetsov, O.A. Application of magnetic liposomes for magnetically

guided transport of muscle relaxants and anti-cancer photodynamic drugs. Journal of Magnetism and Magnetic Materials (2001) 225, 95-100.

[47] Viroonchatapan, E., Sato, H., Ueno, M., Adachi, I., Tazawa, K. and Horikoshi, I. Release of 5-fluorouracil from thermosensitive magnetoliposomes induced by an electromagnetic field. Journal of Controlled Release (1997) 46, 263-271.

[48] Rudge, S., Peterson, C., Vessely, C., Koda, J., Stevens, S. and Catterall, L. Adsorption and Desorption of Chemotherapeutic Drugs From a Magnetically Targeted Carrier (MTC). Journal of Controlled Release (2001) 74, 335-340.

[49] Gref, R., Minamitake, Y., Peracchia, M.T., Trubetskoy, V., Torchilin, V. and Langer, R. Biodegradable Long-Circulating Polymeric Nanospheres. Science (1994) 263, 1600-1603.

[50] Kong, G., Anyarambhatla, G., Petros, W.P., Braun, R.D., Colvin, O.M., Needham, D. and Dewhirst, M.W. Efficacy of Liposomes and Hyperthermia in a Human Tumor Xenograft Model: Importance of Triggered Drug Release. Cancer Research (2000) 60, 6950-6957.

[51] Chilkoti, A., Dreher, M.R., Meyer, D.E. and Raucher, D. Targeted Drug Delivery by Thermally Responsive Polymers. Advanced Drug Delivery Reviews: Polymer Conjugates for Cancer Therapy (2002) 54, 613-630.

[52] Mathiowitz, E. and Cohen, M.D. Polyamide Microcapsules for Controlled Release. V. Photochemical Release. Journal of Membrane Science (1989) 40, 67-86.

[53] Kost, J., Leong, K. and Langer, R. Ultrasound-Enhanced Polymer Degradation and Release of Incorporated Substances. Proceedings of the National Academy of Sciences of the United States of America (1989) 86, 7663-7666.

[54] Babincová, M., Èièmanec, P., Altanerová, V., Altaner, È. and Babinec, P. AC-Magnetic Field Controlled Drug Release From Magnetoliposomes: Design of a Method for Site-Specific Chemotherapy. Bioelectrochemistry (2002) 55, 17-19.

[55] Derfus, A.M., von Maltzahn, G., Harris, T.J., Duza, T., Vecchio, K.S., Ruoslahti, E. and Bhatia, S.N. Remotely Triggered Release from Magnetic Nanoparticles. Advanced Materials (2007) 19, 3932-3936.

[56] Jordan, A., Scholz, R., Wust, P., Fähling, H. and F., R. Magnetic Fluid Hyperthermia (MFH): Cancer Treatment with AC Magnetic Field Induced Excitation of Biocompatible Superparamagnetic Nanoparticles. Journal of Magnetism and Magnetic Materials (1999) 201, 413-419.

[57] Mornet, S., Vasseur, S., Grasset, F. and Duguet, E. Magnetic Nanoparticle Design for Medical Diagnosis and Therapy. Journal of Materials Chemistry (2004) 14, 2161-2175.

[58] Gardner, R.A., Vargas, H.I., Block, J.B., Vogel, C.L., Fenn, A.J., Kuehl, G.V. and Doval, M. Focused Microwave Phased Array Thermotherapy for Primary Breast Cancer. Annals of Surgical Oncology (2002) 9, 326-332.

[59] Harari, P.M., Hynynen, K.H., Roemer, R.B., Anhalt, D.P., Shimm, D.S., Stea, B. and Cassady, J.R. Development of Scanned Focused Ultrasound Hyperthermia - Clinical-Response Evaluation. International Journal of Radiation Oncology Biology Physics (1991) 21, 831-840.

[60] Oosterhuis, J.A., Journee-deKorver, H.G. and Keunen, J.E.E. Transpupillary Thermotherapy - Results in 50 Patients with Choroidal Melanoma. Archives of Ophthalmology (1998) 116, 157-162.

[61] van der Zee, J. Heating the Patient: A Promising Approach? Annals of Oncology (2002) 13, 1173-1184.

[62] Mumtaz, H., HallCraggs, M.A., Wotherspoon, A., Paley, M., Buonaccorsi, G., Amin, Z., Wilkinson, I., Kissin, M.W., Davidson, I., Taylor, I. and Bown, S.G. Laser Therapy for Breast Cancer: MR Imaging and Histopathologic Correlation. Radiology (1996) 200, 651-658.

[63] Jeffrey, S.S., Birdwell, R.L., Ikeda, D.M., Daniel, B.L., Nowels, K.W., Dirbas, F.M. and Griffey, S.M. Radiofrequency Ablation of Breast Cancer - First Report of an Emerging Technology. Archives of Surgery (1999) 134, 1064-1068.

[64] Saito, K., Yoshimura, H., Ito, K., Aoyagi, Y. and Horita, H. Clinical Trials of Interstitial Microwave Hyperthermia by Use of Coaxial-Slot Antenna With Two Slots. IEEE Transactions on Microwave Theory and Techniques (2004) 52, 1987 - 1991.

[65] Gilchrist, R.K., Medal, R., Shorey, W.D., Hannselman, R.C., Parrott, J.C. and Taylor, C.B. Selective Inductive Heating of Lymph Nodes. Annals of Surgery (1957) 146, 596 - 606.

[66] Fortin, J.-P., Gazeau, F. and Wilhelm, C. Intracellular Heating of Living Cells Through Néel Relaxation of Magnetic Nanoparticles. European Biophysics Journal (2008) 37, 223-228.

[67] Fannin, P.C. and Charles, S.W. Rapid Measurement of the Néel Relaxation of Magnetic Particles in the Frequency Range 1 kHz to 160 MHz. Journal of Physics D: Applied Physics (1991) 24, 76 - 77.

[68] Hergt, R., Andra, W., d'Ambly, C.G., Hilger, I., Kaiser, W.A., Richter, U. and Schmidt, H.-G. Physical Limits of Hyperthermia Using Magnetite Fine Particles. IEEE Transactions on Magnetics (1998) 34, 3745-3754.

[69] Jordan, A., Scholz, R., Maier-Hauff, K., Johannsen, M., Wust, P., Nadobny, J., Schirra, H., Schmidt, H., Deger, S., Loening, S., Lanksch, W. and Felix, R. Presentation of a New Magnetic Field Therapy System for the Treatment of Human Solid Tumors with Magnetic Fluid Hyperthemia. Journal of Magnetism and Magnetic Materials (2001) 225, 118 - 126.

[70] Tilcock, C. Delivery of Contrast Agents for Magnetic Resonance Imaging, Computed Tomography, Nuclear Medicine, and Ultrasound. Advanced Drug Delivery Reviews (1999) 37, 33-51.

[71] Aime, S., Botta, M., Fasano, M. and Terreno, E. Lanthanide(III) chelates for NMR biomedical applications. Chemical Society Reviews (1998) 27, 19-29.

[72] Rinck, P.A. and Muller, R.N. Field Strength and Dose Dependence of Contrast Enhancement by Gadolinium-Based MR Contrast Agents. European Radiology (1999) 9, 998-1004.

[73] Tóth, E., Helm, L. and Merbach, A.E. in: The Chemistry of Contrast Agnets in Medical Magnetic Resonance Imaging. Relaxivity of Gadolinium(III) Complexes: Theory and Mechanism (A.E. Merbach and E. Tóth, Eds.). Chichester: John Wiley & Sons, Ltd, 2001, p. 46-119.

[74] Roch, A., Gossuin, Y., Muller, R.N. and Gillis, P. Superparamagnetic Colloid Suspensions: Water Magnetic Relaxation and Clustering. Journal of Magnetism and Magnetic Materials (2005) 293, 532-539.

[75] Berry, C.C. and Curtis, A.S.G. Functionalization of Magnetic Nanoparticles for Applications in Biomedicine. Journal of Physics D: Applied Physics (2003) 36, R198-R206.

[76] Ouakssim, A., Roch, A., Pierart, C. and Muller, R.N. Characterization of Polydisperse Superparamagnetic Particles by Nuclear Magnetic Resonance Dispersion (NMRD) Profiles. Journal of Magnetism and Magnetic Materials (2002) 252, 49-52.

[77] Taboada, E., Rodríguez, E., Roig, A., Oró, J., Roch, A. and Muller, R.N. Nanoparticles with High Magnetization. Evaluation as Potential T1 Magnetic Resonance Imaging Contrast Agents for Molecular Imaging. Langmuir (2007) 23, 4583-4588.

[78] Miguel, O.B., Gossuin, Y., Morales, M.P., Gillis, P. and Muller, R.N. Comparative Analysis of the H-1 NMR Relaxation Enhancement Produced by Iron Oxide and Core-Shell Iron-Iron Oxide Nanoparticles. Magnetic Resonance Imaging (2007) 25, 1437-1441.

[79] Muller, R.N., Roch, A., Colet, J.-M., Ouakssim, A. and Gillis, P. The Chemistry of Contrast Agents in Medical Magnetic Resonance Imaging (A.E. Merbach and E. Toth, Eds.). New York: John Wiley and Sons, 2001, p. 417-435.

[80] Khalafalla, S.E. and Reimers, G.W. Preparation of Dilution-Stable Aqueous Magnetic Fluids. IEEE Transactions on Magnetics (1980) 16, 178-183.

[81] Shen, L., Laibinis, P.E. and Hatton, T.A. Aqueous Magnetic Fluids Stabilized by Surfactant Bilayers. Journal of Magnetism and Magnetic Materials (1999) 194, 37-44.

[82] Shen, L., Laibinis, P.E. and Hatton, T.A. Bilayer Surfactant Stabilized Magnetic Fluids: Synthesis and Interactions at Interfaces. Langmuir (1999) 15, 447-453.

[83] Kim, D.K., Zhang, Y., Voit, W., Rao, K.V. and Muhammed, M. Synthesis and characterization of surfactant-coated superparamagnetic monodispersed iron oxide nanoparticles. Journal of Magnetism and Magnetic Materials (2001) 225, 30-36.

[84] Sahoo, Y., Pizem, H., Fried, T., Golodnitsky, D., Burstein, L., Sukenik, C.N. and Markovich, G. Alkyl Phosphonate/Phosphate Coating on

Magnetite Nanoparticles: A Comparison with Fatty Acids. Langmuir (2001) 17, 7907-7911.

[85] Morales, M.P., Veintemillas-Verdaguer, S., Montero, M.I., Serna, C.J., Roig, A., Casas, L., Martinez, B. and Sandiumenge, F. Surface and Internal Spin Canting in Gamma-Fe_2O_3 Nanoparticles. Chemistry of Materials (1999) 11, 3058-3064.

[86] López-Quintela, M.A. and Rivas, J. Chemical Reactions in Microemulsions: A powerful Method to Obtain Ultrafine Particles. Journal of Colloid and Interface Science (1993) 158, 446-451.

[87] Lee, H.S., Lee, W.C. and Furubayashi, T. A comparison of coprecipitation with microemulsion methods in the preparation of magnetite. Journal of Applied Physics (1999) 85, 5231-5233.

[88] Capek, I. Preparation of Metal Nanoparticles in Water-in-Oil (W/O) Microemulsions. Advances in Colloid and Interface Science (2004) 110, 49-74.

[89] Vidal-Vidal, J., Rivas, J. and López-Quintela, M.A. Synthesis of Monodisperse Maghemite Nanoparticles by the Microemulsion Method. Colloids and Surfaces A: Physiochemical and Engineering Aspects (2006) 288, 44 - 51.

[90] Sun, S. and Zeng, H. Size-Controlled Synthesis of Magnetite Nanoparticles. Journal of the American Chemical Society (2002) 124, 8204-8205.

[91] Park, J., An, K.J., Hwang, Y.S., Park, J.G., Noh, H.J., Kim, J.Y., Park, J.H., Hwang, N.M. and Hyeon, T. Ultra-Large-Scale Syntheses of Monodisperse Nanocrystals. Nature Materials (2004) 3, 891-895.

[92] Laurent, S., Forge, D., Port, M., Roch, A., Robic, C., Vander Elst, L. and Muller, R.N. Magnetic Iron Oxide Nanoparticles: Synthesis, Stabilization, Vectorization, Physiochemical Characterizations, and Biological Applications. Chemical Reviews (2008) 108, 2064 - 2110.

[93] Gupta, A.K. and Gupta, M. Synthesis and Surface Engineering of Iron Oxide Nanoparticles for Biomedical Applications. Biomaterials (2005) 26, 3995-4021.

[94] Lu, A.H., Salabas, E.L. and Schüth, F. Magnetic Nanoparticles: Synthesis, Protection, Functionalization, and Application. Angewandte Chemie International Edition (2007) 46, 1222 - 1244.

[95] Park, J., Joo, J., Kwon, S.G., Jang, Y. and Hyeon, T. Synthesis of Monodisperse Spherical Nanocrystals. Angewandte Chemie International Edition (2007) 46, 4630-4660.

[96] Kim, D.K., Zhang, Y., Voit, W., Rao, K.V. and Muhammed, M. Synthesis and Characterization of Surfactant-Coated Superparamagnetic Monodispersed Iron Oxide Nanoparticles. Journal of Magnetism and Magnetic Materials (2001) 225, 30-36.

[97] Lin, C.-L., Lee, C.-F. and Chiu, W.-Y. Preparation and Properties of Poly(acrylic acid) Oligomer Stabilized Superparamagnetic Ferrofluid. Journal of Colloid and Interface Science (2005) 291, 411-420.

[98] Pardoe, H., Chua-anusorn, W., St. Pierre, T.G. and Dobson, J. Structural and magnetic properties of nanoscale iron oxide particles synthesized in the presence of dextran or polyvinyl alcohol. Journal of Magnetism and Magnetic Materials (2001) 225, 41-46.

[99] Giri, J., Thakurta, S.G., Bellare, J., Nigam, A.K. and Bahadur, D. Preparation and Characterization of Phospholipid Stabilized Uniform Sized Magnetite Nanoparticles. Journal of Magnetism and Magnetic Materials (2005) 293, 62-68.

[100] Vayssières, L., Chanéac, C., Tronc, E. and Jolivet, J.P. Size Tailoring of Magnetite Particles Formed by Aqueous Precipitation: An Example of Thermodynamic Stability of Nanometric Oxide Particles. Journal of Colloid and Interface Science (1998) 205, 205-212.

[101] Sun, S., Zeng, H., Robinson, D.B., Raoux, S., Rice, P.M., Wang, S.X. and Li, G. Monodisperse MFe2O4 (M = Fe, Co, Mn) Nanoparticles. Journal of the American Chemical Society (2004) 126, 273-279.

[102] Kwon, S.G., Piao, Y., Park, J., Angappane, S., Jo, Y., Hwang, N.-M., Park, J.-G. and Hyeon, T. Kinetics of Monodisperse Iron Oxide Nanocrystal Formation by the "Heating-Up" Process. Journal of the American Chemical Society (2007) 129, 12571-12584.

[103] Jun, Y.-w., Huh, Y.-M., Choi, J.-s., Lee, J.-H., Song, H.-T., Kim, S., Yoon, S., Kim, K.-S., Shin, J.-S., Suh, J.-S. and Cheon, J. Nanoscale Size

Effect of Magnetic Nanocrystals and Their Utilization for Cancer Diagnosis via Magnetic Resonance Imaging. Journal of the American Chemical Society (2005) 127, 5732-5733.

[104] Lee, S.-Y. and Harris, M.T. Surface Modification of Magnetic Nanoparticles Capped by Oleic Acids: Characterization and Colloidal Stability in Polar Solvents. Journal of Colloid and Interface Science (2006) 293, 401-408.

[105] Wang, Y., Wong, J.F., Teng, X., Lin, X.Z. and Yang, H. Pulling Nanoparticles into Water: Phase Transfer of Oleic Acid Stabilized Monodisperse Nanoparticles into Aqueous Solutions of α-Cyclodextrin. Nano Letters (2003) 3, 1555-1559.

[106] Qin, J., Laurent, S., Jo, Y.S., Roch, A., Mikhaylova, M., Bhujwalla, Z.M., Muller, R.N. and Muhammed, M. A High-Performance Magnetic Resonance Imaging T_2 Contrast Agent. Advanced Materials (2007) 19, 1874-1878.

[107] Gonzales, M. and Krishnan, K.M. Phase Transfer of Highly Monodisperse Iron Oxide Nanocrystals with Pluronic F127 for Biomedical Applications. Journal of Magnetism and Magnetic Materials (2007) 311, 59-62.

[108] Moeser, G.D., Roach, K.A., Green, W.H., Laibinis, P.E. and Hatton, T.A. Water-Based Magnetic Fluids as Extractants for Synthetic Organic Compounds. Industrial & Engineering Chemistry Research (2002) 41, 4739-4749.

[109] Corr, S.A., Byrne, S.J., Tekoriute, R., Meledandri, C.J., Brougham, D.F., Lynch, M., Kerskens, C., O'Dwyer, L. and Gun'ko, Y.K. Linear Assemblies of Magnetic Nanoparticles as MRI Contrast Agents. Journal of the American Chemical Society (2008) 130, 4214 - 4215.

[110] Corr, S.A., Gun'ko, Y.K., Tekoriute, R., Meledandri, C.J. and Brougham, D.F. Poly(sodium-4-styrene)sulfonate - Iron-oxide Nanocomposite Dispersions with Controlled Magnetic Resonance Properties. Journal of Physical Chemistry C (2008) 112, 13324 - 13327.

[111] Harris, L.A., Goff, J.D., Carmichael, A.Y., Riffle, J.S., Harburn, J.J., St. Pierre, T.G. and Saunders, M. Magnetite Nanoparticle Dispersions

Stabilized with Triblock Copolymers. Chemistry of Materials (2003) 15, 1367-1377.

[112] Mendenhall, G.D., Geng, Y. and Hwang, J. Optimization of Long-Term Stability of Magnetic Fluids from Magnetite and Synthetic Polyelectrolytes. Journal of Colloid and Interface Science (1996) 184, 519-526.

[113] Lattuada, M. and Hatton, T.A. Functionalization of Monodisperse Magnetic Nanoparticles. Langmuir (2007) 23, 2158-2168.

[114] Anoardo, E., Galli, G. and Ferrante, G. Fast-field-cycling NMR: Applications and instrumentation. Applied Magnetic Resonance (2001) 20, 365-404.

[115] Kimmich, R. and Anoardo, E. Field-Cycling NMR Relaxometry. Progress in Nuclear Magnetic Resonance Spectroscopy (2004) 44, 257-320.

[116] Malvern Instruments, Dynamic Light Scattering: An Introduction in 30 Minutes. Technical report.

[117] Svanberg, C. and Bergman, R., Chalmers University of Technology, Photon Correlation Spectroscopy. Technical report. 1998.

[118] Koppel, D.E. Analysis of Macromolecular Polydispersity in Intensity Correlation Spectroscopy: The Method of Cumulants. Journal of Chemical Physics (1972) 57, 4814-4820.

[119] International Organization for Standardization (ISO), INTERNATIONAL STANDARD ISO13321, Methods for Determination of Particle Size Distribution Part 8: Photon Correlation Spectroscopy. 1996.

[120] Twomey, S. Introduction to the Mathematics of Inversion of Remote Sensing and Indirect Measurements: Dover Publications, 1997, p. 237.

[121] Lawson, C.L. and Hanson, R.J. Solving Least Squares Problems: SIAM Society for Industrial & Applied Mathematics, 1995, p. 350.

[122] Kaszuba, M., McKnight, D., Connah, M.T., McNeil-Watson, F.K. and Nobbmann, U. Measuring Sub Nanometre Sizes Using Dynamic Light Scattering. Journal of Nanoparticle Research (2008) 10, 823 - 829.

[123] Fringeli, U.P. and Günthard, H.H. in: Membrane Spectroscopy. Infrared Membrane Spectroscopy (E. Gell, Ed.). New York, 1981, p. 270-332.

[124] Nishikida, K., Nishikida, Nishio, E. and Hannah, R.W. Selected Applications of Modern FT-IR Techniques: CRC Press, 1996, p. 280.

[125] Harrick, N.J. Internal Reflection Spectroscopy. New York: John Wiley & Sons Inc., 1967, p. 342.

[126] Stuart, B.H. Infrared Spectroscopy: Fundamentals and Applications. Chichester: John Wiley and Sons Inc., 2004, p. 242.

[127] Cantle, J.E. (1982) in: Techniques and Instrumentation in Analytical Chemistry Vol. 5, Elsevier Scientific Publishing Company, Amsterdam.

[128] Ebdon, L. An Introduction to Atomic Absorption Spectroscopy. A Self-Teaching Approach. London: Heyden & Son Ltd, 1982, p. 1089.

[129] Williams, D.B. and Carter, C.B. Transmission Electron Microscopy: A Textbook for Materials Science. New York: Plenum Press, 1996, p. 729.

[130] Hayat, M.A. Stains and Cytochemical Methods. New York: Springer, 1993, p. 455.

[131] Prasad, P.N. Nanophotonics. New Jersey: Wiley-IEEE, 2004, p. 415.

[132] Lee, S.-J., Jeong, J.-R., Shin, S.-C., Kim, J.-C., Chang, Y.-H., Chang, Y.-M. and Kim, J.-D.J.-D. Nanoparticles of Magnetic Ferric Oxides Encapsulated with Poly(D,L latide-co-glyceride) and their Applications to Magnetic Resonance Imaging Contrast Agent. Journal of Magnetism and Magnetic Materials (2004) 272-276, 2432-2433.

[133] Ferrari, M. Cancer Nanotechnology: Opportunities and Challenges. Nature Reviews Cancer (2005) 5, 161-171.

[134] Babincová, M., Sourivong, P., Leszczynska, D. and Babinec, P. Blood-Specific Whole-Body Electromagnetic Hyperthermia. Medical Hypotheses (2000) 55, 459-460.

[135] Alexiou, C., Schmid, R.J., Jurgons, R., Kremer, M., Wanner, G., Bergemann, C., Huenges, E., Nawroth, T., Arnold, W. and Parak, F.G. Targeting Cancer Cells: Magnetic Nanoparticles as Drug Carriers. European Biophysics Journal (2006) 35, 446-450.

[136] Bronstein, L.M., Huang, X., Retrum, J., Schmucker, A., Pink, M., Stein, B.D. and Dragnea, B. Influence of Iron Oleate Complex Structure on Iron Oxide Nanoparticle Formation. Chemistry of Materials (2007) 19, 3624-3632.

[137] Roca, A.G., Marco, J.F., Morales, M.D. and Serna, C.J. Effect of Nature and Particle Size on Properties of Uniform Magnetite and Maghemite Nanoparticles. Journal of Physical Chemistry C (2007) 111, 18577-18584.

[138] Corot, C., Robert, P., Idée, J.-M. and Port, M. Recent Advances in Iron Oxide Nanocrystal Technology for Medical Imaging. Advanced Drug Delivery Reviews: Particulate Nanomedicines (2006) 58, 1471-1504.

[139] López-Pérez, J.A., López-Quintela, M.A., Mira, J. and Rivas, J. Preparation of Magnetic Fluids with Particles Obtained in Microemulsions. IEEE Transactions on Magnetics (1997) 33, 4359-4362.

[140] Veintemillas-Verdaguer, S., Morales, M.P. and Serna, C.J. Continuous Production of γ-Fe_2O_3 Ultrafine Powders by Laser Pyrolysis. Materials Letters (1998) 35, 227-231.

[141] Zhang, T., Ge, J., Hu, Y. and Yin, Y. A General Approach for Transferring Hydrophobic Nanocrystals into Water. Nano Lett. (2007) 7, 3203-3207.

[142] Wu, H., Zhu, H., Zhuang, J., Yang, S., Liu, C. and Cao, Y.C. Water-Soluble Nanocrystals Through Dual-Interaction Ligands. Angewandte Chemie International Edition (2008) 47, 3730-3734.

[143] Pyenson, H. and Tracy, P.H. A 1,10 Phenanthroline Method for the Determination of Iron in Powdered Milk. Journal of Dairy Science (1945) 28, 401-412.

[144] Fritz, S.F. and Popp, R.K. A Single-Dissolution Technique for Determining FeO and Fe_2O_3 in Rock and Mineral Samples. American Mineralogist (1985) 70, 961-968.

[145] Bruce, I.J., Taylor, J., Todd, M., Davies, M.J., Borioni, E., Sangregorio, C. and Sen, T. Synthesis, Characterisation, and Application of Silica-Magnetite Nanocomposites. Journal of Magnetism and Magnetic Materials (2004) 284, 145-160.

[146] Chantrell, R.W., Popplewell, J. and Charles, S.W. Effect of a Particle-Size Distribution on Coercivity and Remanence of a Fine Particle System. Physica B & C (1977) 86, 1421-1422.

[147] Popplewell, J. and Sakhnini, L. The Dependence of the Physical and Magnetic Properties of Magnetic Fluids on Particle Size. Journal of Magnetism and Magnetic Materials (1995) 149, 72-78.

[148] Feltin, N. and Pileni, M.P. New Technique for Synthesizing Iron Ferrite Magnetic Nanosized Particles. Langmuir (1997) 13, 3927-3933.

[149] Vargas, J.M. Tailoring the Size in Colloidal Iron Oxide Magnetic Nanoparticles. Nanotechnology (2005) 16, 1474 - 1476.

[150] Yu, W.W., Falkner, J.C., Yavuz, C.T. and Colvin, V.L. Synthesis of Monodisperse Iron Oxide Nanocrystals by Thermal Decomposition of Iron Carboxylate Salts. Chemical Communications (2004), 2306 - 2307.

[151] Roch, A., Muller, R. and Gillis, P. Theory of Proton Relaxation Induced by Superparamagnetic Particles. Journal of Chemical Physics (1999) 110, 5403-5411.

[152] Xie, J., Xu, C., Xu, Z., Hou, Y., Young, K.L., Wang, S.X., Pourmand, N. and Sun, S. Linking Hydrophilic Macromolecules to Monodisperse Magnetite (Fe_3O_4) Nanoparticles via Trichloro-s-triazine. Chemistry of Materials (2006) 18, 5401-5403.

[153] Lu, H.M., Zheng, W.T. and Jiang, Q. Saturation Magnetism of Ferromagnetic and Ferrimagnetic Nanocrystals at Room Temperature. Journal of Physics D: Applied Physics (2007) 40, 320-325.

[154] Berkowitz, A.E., Schuele, W.J. and Flanders, P.J. Influence of Crystallite Size on Magnetic Properties of Acicular Gamma-Fe_2O_3 Particles. Journal of Applied Physics (1968) 39, 1261-1263.

[155] Joumaa, N., Toussay, P., Lansalot, M. and Elaissari, A. Surface Modification of Iron Oxide Nanoparticles by a Phosphate-Based Macromonomer and Further Encapsulation Into Submicrometer Polystyrene Particles by Miniemulsion Polymerization. Journal of Polymer Science Part A (2008) 46, 327-340.

[156] Martínez, B., Obradors, X., Balcells, L.I., Rouanet, A. and Monty, C. Low Temperature Surface Spin-Glass Transition in Gamma-Fe_2O_3 Nanoparticles. Physical Review Letters (1998) 80, 181-184.

[157] Moore, J.W. and Wellek, R.M. Diffusion Coefficients of n-Heptane and n-Decane in n-Alkanes at Several Temperatures. Journal of Chemical and Engineering Data (1974) 19, 136-140.

[158] Lefebure, S., Menager, C., Cabuil, V., Assenheimer, M., Gallet, F. and Flament, C. Langmuir Monolayers of Monodispersed Magnetic Nanoparticles Coated with a Surfactant. Journal of Physical Chemistry B (1998) 102, 2733-2738.

[159] Wooding, A., Kilner, M. and Lambrick, D.B. Studies of the Double Surfactant Layer Stabilization of Water-Based Magnetic Fluids. Journal of Colloid and Interface Science (1991) 144, 236-242.

[160] Mulder, W.J.M., Strijkers, G.J., van Tilborg, G.A.F., Griffioen, A.W. and Nicolay, K. Lipid-Based Nanoparticles for Contrast-Enhanced MRI and Molecular Imaging. NMR in Biomedicine (2006) 19, 142-164.

[161] Gaumet, M., Vargas, A., Gurny, R. and Delie, F. Nanoparticles for Drug Delivery: The Need for Precision in Reporting Particle Size Parameters. European Journal of Pharmaceutics and Biopharmaceutics (2008) 69, 1 - 9.

[162] Minchin, R. Nanomedicine: Sizing Up Targets With Nanoparticles. Nature Nanotechnology (2008) 3, 12-13.

[163] Ito, A., Shinkai, M., Honda, H. and Kobayashi, T. Medical Application of Functionalized Magnetic Nanoparticles. Journal of Bioscience and Bioengineering (2005) 100, 1-11.

[164] Choi, H.S., Liu, W., Misra, P., Tanaka, E., Zimmer, J.P., Ipe, B.I., Bawendi, M.G. and Frangioni, J.V. Renal Clearance of Quantum Dots. Nature Biotechnology (2007) 25, 1165 - 1170.

[165] Berret, J.-F., Schonbeck, N., Gazeau, F., El Kharrat, D., Sandre, O., Vacher, A. and Airiau, M. Controlled Clustering of Superparamagnetic Nanoparticles Using Block Copolymers: Design of New Contrast Agents for Magnetic Resonance Imaging. Journal of the American Chemical Society (2006) 128, 1755 - 1761.

[166] Ditsch, A., Laibinis, P.E., Wang, D.I.C. and Hatton, T.A. Controlled Clustering and Enhanced Stability of Polymer-Coated Magnetic Nanoparticles. Langmuir (2005) 21, 6006 - 6018.

[167] Ge, J., Hu, Y., Biasini, M., Beyermann, W.P. and Yin, Y. Superparamagnetic Magnetite Colloidal Nanocrystal Clusters. Angewandte Chemie (2007) 119, 4420 - 4423.

[168] Ghosh, S. PhD Thesis: The Preparation of Magnetic Nanoparticle Assemblies for Biomedical Applications. Dublin City University, 2006.

[169] Stolarczyk, J.K., Ghosh, S.K. and Brougham, D.F. Controlled Growth of Nanoparticle Clusters Through Competitive Stabilizer Desorption. Accepted for publication in Angewandte Chemie International Edition (2008). DOI: 10.1002/anie.200803895.

[170] Lim, I.-I.S., Njoki, P.N., Park, H.-Y., Wang, X., Wang, L., Mott, D. and Zhong, C.-J. Gold and Magnetic Oxide/Gold Core/Shell Nanoparticles as Bio-Functional Nanoprobes. Nanotechnology (2008) 19, 305102 - 350512.

[171] Daniel, M.-C. and Astruc, D. Gold Nanoparticles: Assembly, Supermolecular Chemistry, Quantum-Size-Related Properties, and Applications Toward Biology, Catalysis, and Nanotechnology. Chemical Reviews (2004) 104, 293 - 346.

[172] Larson, T.A., Bankson, J., Aaron, J. and Sokolov, K. Hybrid Plasmonic Magnetic Nanoparticles as Molecular Specific Agents for MRI/Optical Imaging and Photothermal Therapy of Cancer Cells. Nanotechnology (2007) 18.

[173] Kim, J., Park, S., Lee, J.E., Jin, S.M., Lee, J.H., Lee, I.S., Yang, I., Kim, J.-S., Kim, S.K., Cho, M.-H. and Hyeon, T. Designed Fabrication of Multifunctional Magnetic Gold Nanoshells and Their Application to Magnetic Resonance Imaging and Photothermal Therapy. Angewandte Chemie (2006) 118, 7918 - 7922.

[174] Hirsch, L.R., Stafford, R.J., Bankson, J.A., Sershen, S.R., Rivera, B., Price, R.E., Hazle, J.D., Halas, N.J. and West, J.L. Nanoshell-Mediated Near-Infrared Thermal Therapy of Tumors Under Magnetic Resonance Guidance. Proceedings of the National Academy of Sciences of the United States of America (2003) 100, 13549-13554.

[175] Park, H.-Y., Schadt, M.J., Wang, L., Lim, I.-I.S., Njoki, P.N., Kim, S.H., Jang, M.-Y., Luo, J. and Zhong, C.-J. Fabrication of Magnetic Core@Shell Fe Oxide@Au Nanoparticles for Interfacial Bioactivity and Bio-Separation. Langmuir (2007) 23, 9050 - 9056.

[176] Caruntu, D., Cushing, B.L., Caruntu, G. and O'Connor, C.J. Attachment of Gold Nanograins onto Colloidal Magnetite Nanocrystals. Chemistry of Materials (2005) 17, 3398 - 3402.

[177] Lyon, J.L., Fleming, D.A., Stone, M.B., Schiffer, P. and Williams, M.E. Synthesis of Fe Oxide Core/Au Shell Nanoparticles by Iterative Hydroxylamine Seeding. Nano Letters (2004) 4, 719 - 723.

[178] Wang, L., Luo, J., Fan, Q., Suzuki, M., Suzuki, I.S., Engelhard, M.H., Lin, Y., Kim, N., Wang, J.Q. and Zhong, C.-J. Monodispersed Core-Shell Fe_3O_4@Au Nanoparticles. Journal of Physical Chemistry B (2005) 109, 21593 - 21601.

[179] Brust, M., Walker, M., Bethell, D., Schiffrin, D.J. and Whyman, R. Synthesis of Thiol-derivatised Gold Nanoparticles in a Two-phase Liquid-Liquid System. Journal of the Chemical Society. Chemical Communications (1994), 801-802.

[180] Teng, X. and Yang, H. Effects of Surfactants and Synthetic Conditions on the Sizes and Self-Assembly of Monodisperse Iron Oxide Nanoparticles. Journal of Materials Chemistry (2004) 14, 774-779.

[181] López-López, M.T., Durán, J.D.G., Delgado, A.V. and González-Caballero, F. Stability and Magnetic Characterization of Oleate-Covered Magnetite Ferrofluids in Different Nonpolar Carriers. Journal of Colloid and Interface Science (2005) 291, 144-151.

[182] van Ewijk, G.A. and Philipse, A.P. Anomalous Attraction Between Colloidal Magnetite and Silica Spheres in Apolar Solvents. Langmuir (2001) 17, 7204 - 7209.

[183] Friedlander, S.K. in: Smoke, Dust, and Haze: Fundamentals of Aerosol Dynamics. Dynamics of Agglomerate Formation and Restructuring: Oxford University Press, 2000, p. 222 - 248.

[184] Tirado-Miranda, M., Schmitt, A., Callejas-Fernández, J. and Fernández-Barbero, A. Aggregation of Protein-Coated Colloidal Particles: Interaction Energy, Cluster Morphology, and Aggregation Kinetics. Journal of Chemical Physics (2003) 119, 9251 - 9259.

[185] Min, Y., Akbulut, M., Kristiansen, K., Golan, Y. and Israelachvili, J. The Role of Interparticle and External Forces in Nanoparticle Assembly. Nature Materials (2008) 7, 527 - 538.

[186] Israelachvili, J.N. Intermolecular and Surface Forces. Burlington: Academic Press, 2007, p. 600.

[187] Nuzzo, R.G., Zegarski, B.R. and Dubois, L.H. Fundamental Studies of the Chemisorption of Organosulfur Compounds on Gold(111). Implications for Molecular Self-Assembly on Gold Surfaces. Journal of the American Chemical Society (1987) 109, 733-740.

[188] Ulman, A. Formation and Structure of Self-Assembled Monolayers. Chemical Reviews (1996) 96, 1533 - 1554.

[189] Smoluchowski, M.V. Drei Vortrage Uber Diffusion, Brownsche Molekularbewegung und Koagulation von Kolloidteilchen. Physik. Zeitschr (1916) 17, 557 - 599.

[190] Chakraborty, S. and Padhy, S. Anomalous Electrical Conductivity of Nanoscale Colloidal Suspensions. ACS Nano (2008) 2, 2029 - 2036.

[191] Lin, M.Y., Lindsay, H.M., Weitz, D.A., Ball, R.C., Klein, R. and Meakin, P. Universality in Colloid Aggregation. (1989) 339, 360-362.

[192] Kitchens, C.L., McLeod, M.C. and Roberts, C.B. Solvent Effects on the Growth and Steric Stabilization of Copper Metallic Nanoparticles in AOT Reverse Micelle Systems. The Journal of Physical Chemistry B (2003) 107, 11331-11338.

[193] Shah, P.S., Husain, S., Johnston, K.P. and Korgel, B.A. Role of Steric Stabilization on the Arrested Growth of Silver Nanocrystals in Supercritical Carbon Dioxide. Journal of Physical Chemistry B (2002) 106, 12178 - 12185.

[194] Bangham, A.D., Standish, M.M. and Watkins, J.C. Diffusion of Univalent Ions Across the Lamellae of Swollen Phospholipids. Journal of Molecular Biology (1965) 13, 238-252.

[195] Martina, M.-S., Fortin, J.-P., Ménager, C., Clément, O., Barratt, G., Grabielle-Madelmont, C., Gazeau, F., Cabuil, V. and Lesieur, S. Generation of Superparamagnetic Liposomes Revealed as Highly Efficient MRI Contrast Agents for in Vivo Imaging. Journal of the American Chemical Society (2005) 127, 10676-10685.

[196] Bulte, J.W.M., de Cuyper, M., Despres, D. and Frank, J.A. Preparation, Relaxometry, and Biokinetics of PEGylated Magnetoliposomes as MR

Contrast Agent. Journal of Magnetism and Magnetic Materials (1999) 194, 204-209.

[197] Müller-Schulte, D., Füssl, F., Lueken, H. and De Cuyper, M. in: Scientific and Clinical Applications of Magnetic Carriers. A New Aids Therapy Approach Using Magnetoliposomes (U. Häfeli, W. Schutt, J. Teller and M. Zborowski, Eds.). New York: Plenum, 1997, p. 517 - 526.

[198] Lasic, D.D. Novel Applications of Liposomes. Tibtech (1998) 16.

[199] Magin, R. and Weinstein, J.N. in: Liposome Technology: Targeted Drug Delivery and Biological Interaction. The Design and Characterization of Temperature-Sensitive Liposomes (G. Gregoriadis, Ed.), Vol. 3. Boca Raton: CRC Press, Inc., 1984, p. 137-153.

[200] Yatvin, M.B., Cree, T.C. and Tegmo-Larsson, I.-M. in: Liposome Technology: Targeted Drug Delivery and Biological Interaction. Theoretical and Practical Considerations in Preparing Liposomes for the Purpose of Releasing Drug in Response to Changes in Temperature and pH (G. Gregoriadis, Ed.), Vol. 3. Boca Raton: CRC Press, Inc., 1984, p. 159-174.

[201] Gaede, H.C. and Gawrisch, K. Lateral Diffusion Rates of Lipid, Water, and a Hydrophobic Drug in a Multilamellar Liposome. Biophysical Journal (2003) 85, 1734 - 1740.

[202] Filippov, A., Orädd, G. and Lindblom, G. The Effect of Cholesterol on the Lateral Diffusion of Phospholipids in Oriented Bilayers. Biophysical Journal (2003) 84, 3079-3086.

[203] Rommel, E., Noack, F., Meier, P. and Kothe, G. Proton Spin Relaxation Dispersion Studies of Phospholipid Membranes. Journal of Physical Chemistry (1988) 92, 2981-2987.

[204] Riviere, C., Martina, M.-S., Tomita, Y., Wilhelm, C., Tran Dinh, A., Menager, C., Pinard, E., Lesieur, S., Gazeau, F. and Seylaz, J. Magnetic Targeting of Nanometric Magnetic Fluid loaded Liposomes to Specific Brain Intravascular Areas: A Dynamic Imaging Study in Mice. Radiology (2007) 244, 439-448.

[205] De Cuyper, M. and Joniau, M. Magnetoliposomes - Formation and Structural Characterization. European Biophysics Journal with Biophysics Letters (1988) 15, 311-319.

[206] De Cuyper, M., Muller, P., Lueken, H. and Hodenius, M. Synthesis of magnetic Fe_3O_4 particles covered with a modifiable phospholipid coat. Journal of Physics-Condensed Matter (2003) 15, S1425-S1436.

[207] Bulte, J.W.M., Ma, L.D., Magin, R.L., Kamman, R.L., Hulstaert, C.E., Go, K.G., The, T.H. and Leij, L.D. Selective MR Imaging of Labeled Human Peripheral Blood Mononuclear Cells by Liposome Mediated Incorporation of Dextran-Magnetite Particles. Magnetic Resonance in Medicine (1993) 29, 32 - 37.

[208] Lesieur, S., Grabielle-Madelmont, C., Menager, C., Cabuil, V., Dadhi, D., Pierrot, P. and Edwards, K. Evidence of Surfactant-Induced Formation of Transient Pores in Lipid Bilayers by Using Magnetic-Fluid-Loaded Liposomes. Journal of the American Chemical Society (2003) 125, 5266-5267.

[209] Sjögren, C.E., Johansson, C., Nævestad, A., Sontum, P.C., Briley-Sæbø, K. and Fahlvik, A.K. Crystal Size and Properties of Superparamagnetic Iron Oxide (SPIO) Particles. Magnetic Resonance Imaging (1997) 15, 55-67.

[210] Yavuz, C.T., Mayo, J.T., Yu, W.W., Prakash, A., Falkner, J.C., Yean, S., Cong, L., Shipley, H.J., Kan, A., Tomson, M., Natelson, D. and Colvin, V.L. Low-Field Magnetic Separation of Monodisperse Fe_3O_4 Nanocrystals. Science (2006) 314, 964-967.

[211] Sangregorio, C., Wiemann, J.K., O'Connor, C.J. and Rosenzweig, Z. A New Method for the Synthesis of Magnetoliposomes. Journal of Applied Physics (1999) 85, 5699-5701.

[212] Moeser, G.D., Roach, K.A., Green, W.H., Hatton, T.A. and Laibinis, P.E. High-Gradient Magnetic Separation of Coated Magnetic Nanoparticles. AIChE Journal (2004) 50, 2835.

[213] Lasic, D.D. Liposomes: From Physics to Applications: Elsevier, 1993, p.

[214] Silvius, J.R. in: Lipid-Protein Interactions. Thermotropic Phase Transitions of Pure Lipids in Model Membranes and Their Modifications by Membrane Proteins (P.C. Jost and O.H. Griffiths, Eds.), Vol. 2. New York: John Wiley & Sons, Inc., 1982, p. 239 - 281.

[215] Maity, D. and Agrawal, D.C. Synthesis of Iron Oxide Nanoparticles Under Oxidizing Environment and Their Stabilization in Aqueous and

Non-Aqueous Media. Journal of Magnetism and Magnetic Materials (2007) 308, 46 - 55.

[216] Parker, F.S. Applications of Infrared, Raman, and Resonance Raman Spectroscopy in Biochemistry: Springer, 1983, p. 550.

[217] Socrates, G. Infrared and Raman Characteristic Group Frequencies: John Wiley and Sons, 2001, p. 347.

[218] Cevc, G. and Seddon, J.M. in: Phospholipids Handbook. Physical Characterization (G. Cevc, Ed.): CRC Press, 1993, p. 351 - 402.

[219] Hauser, H. in: Phospholipids Handbook. Phospholipid Vesicles (G. Cevc, Ed.). New York: Marcel Dekker, Inc., 1993, p. 603 - 637.

[220] Watwe, R.M. and Bellare, J.R. Manufacture of Liposomes - a Review. Current Science (1995) 68, 715-724.

[221] Traikia, M., Warschawski, D.E., Recouvreur, M., Cartaud, J. and Devaux, P.F. Formation of Unilamellar Vesicles by Repetitive Freeze-Thaw Cycles: Characterization by Electron Microscopy and P-31-Nuclear Magnetic Resonance. European Biophysics Journal with Biophysics Letters (2000) 29, 184-195.

[222] Knight, C.G. (1981) in: Research Monographs in Cell and Tissue Physiology (J.T. Dingle and J.L. Gordon, Eds.) Vol. 7, Elsevier, Amsterdam.

[223] Daou, T.J., Begin-Colin, S., Greneche, J.M., Thomas, F., Derory, A., Bernhardt, P., Legare, P. and Pourroy, G. Phosphate Adsorption Properties of Magnetite-Based Nanoparticles. Chem. Mater. (2007) 19, 4494-4505.

[224] Rheinländer, T., Roessner, D., Weitschies, W. and Semmler, W. Comparison of Size-Selective Techniques for the Fractionation of Magnetic Fluids. Journal of Magnetism and Magnetic Materials (2000) 214, 269-275.

[225] Mohapatra, S., Pramanik, N., Ghosh, S.K. and Pramanik, P. Synthesis and Characterization of Ultrafine Poly(vinylalcohol phosphate) Coated Magnetite Nanoparticles. Journal of Nanoscience and Nanotechnology (2006) 6, 823 - 829.

[226] Yee, C., Kataby, G., Ulman, A., Prozorov, T., White, H., King, A., Rafailovich, M., Sokolov, J. and Gedanken, A. Self-Assembled

Monolayers of Alkanesulfonic and -phosphonic Acids on Amorphous Iron Oxide Nanoparticles. Langmuir (1999) 15, 7111-7115.

[227] Mutin, P.H., Guerrero, G. and Vioux, A. Hybrid Materials From Organophosphorus Coupling Molecules. Journal of Materials Chemistry (2005) 15, 3761 - 3768.

[228] Gurerrero, G., Mutin, P.H. and Vioux, A. Organically Modified Aluminas by Grafting and Sol-Gel Processes Involving Phosphonate Derivatives. Journal of Materials Chemistry (2001) 11, 3161 - 3165.

[229] Vance, D.E. and Vance, J.E. (1985), The Benjamin/Cummings Publishing Company, Inc., Menlo Park.

[230] Nagle, J.F. and Tristram-Nagle, S. Structure of Lipid Bilayers. Biochimica et Biophysica Acta (2000) 1469, 159-195.

[231] Finegold, L. and Singer, M.A. in: Cholesterol in Membrane Models. Cholesterol/Phospholipid Interactions Studied by Differential Scanning Calorimetry: Effect of Acyl Chain Length and Role of the C(17) Sterol Side Group (L. Finegold, Ed.). Boca Raton: CRC Press, 1993, p.

[232] Tilcock, C., Unger, E., Cullis, P. and MacDougall, P. Liposomal Gd-DTPA: Preparation and Characterization of Relaxivity. Radiology (1989) 171, 77-80.

[233] Niemelä, P.S., Hyvönen, M.T. and Vattulainen, I. Influence of Chain Length and Unsaturation on Sphingomyelin Bilayers. Biophysical Journal (2006) 90, 851-863.

[234] Yatvin, M.B., Weinstein, J.N., Dennis, W.H. and Blumenthal, R. Design of Liposomes for Enhanced Local Release of Drugs by Hyperthermia. Science (1978) 202, 1290 - 1293.

[235] Sullivan, S.M. and Huang, L. Enhanced Delivery to Target Cells by Heat-Sensitive Immunoliposomes. Proceedings of the National Academy of Sciences of the United States of America (1986) 83, 6117 - 6121.

[236] Mabrey, S. and Sturtevant, J.M. Investigation of Phase-Transitions of Lipids and Lipid Mixtures by High Sensitivity Differential Scanning Calorimetry. Proceedings of the National Academy of Sciences of the United States of America (1976) 73, 3862-3866.

[237] McDermott, R., Lee, S.K., ten Haken, B., Trabesinger, A.H., Pines, A. and Clarke, J. Microtesla MRI with a Superconducting Quantum

Interference Device. Proceedings of the National Academy of Sciences of the United States of America (2004) 101, 7857 - 7861.

[238] Gawrisch, K. in: The Structure of Biological Membranes. The Dynamics of Membrane Lipids (P.L. Yeagle, Ed.): CRC Press, 2005, p. 540.

[239] Lee, G.M. and Jacobson, K. in: Cell Lipids. Lateral Mobility of Lipids in Membranes (D. Hoekstra, Ed.): Academic Press, 1994, p. 638.

[240] Sim, E. Membrane Biochemistry. London: Chapman and Hall, 1982, p.

[241] Stockton, G.W., Polnaszek, C.F., Tulloch, A.P., Hasan, F. and Smith, I.C.P. Molecular-Motion and Order in Single-Bilayer Vesicles and Multilamellar Dispersions of Egg Lecithin and Lecithin-Cholesterol Mixtures - Deuterium Nuclear Magnetic-Resonance Study of Specifically Labeled Lipids. Biochemistry (1976) 15, 954-966.

[242] O'Leary, T.J. in: Cholesterol in Membrane Models. Vibrational Spectroscopy of Cholesterol-Lipid Interactions (L. Finegold, Ed.). Boca Raton: CRC Press, 1993, p. 137 - 158.

[243] Meyvis, T.K.L., De Smedt, S.C., Van Oostveldt, P. and Demeester, J. Fluorescence Recovery After Photobleaching: A Versatile Tool for Mobility and Interaction Measurements in Pharmaceutical Research. Pharmaceutical Research (1999) 16, 1153 - 1162.

[244] Blume, A. in: Phospholipids Handbook. Dynamic Properties (G. Cevc, Ed.). New York: Marcel Dekker, Inc., 1993, p. 455 - 510.

[245] Smith, R.L. and Oldfield, E. Dynamic Structure of Membranes by Deuterium NMR. Science (1984) 225, 280 - 288.

[246] Bloom, M., Burnell, E.E., Mackay, A.L., Nichol, C.P., Valic, M.I. and Weeks, G. Fatty Acyl Chain Order in Lecithin Model Membranes Determined from Proton Magnetic-Resonance. Biochemistry (1978) 17, 5750-5762.

[247] Beckmann, P. Spectral Densities and Nuclear Spin Relaxation in Solids. Physics Reports (Review Section of Physics Letters) (1988) 171, 85-128.

[248] Wilschut, J. in: Méthodologie des Liposomes. Preparation and Properties of Phospholipid Vesicles (L.D. Leserman and J. Barbet, Eds.), Vol. 107. Paris: INSERM, 1982, p. 9 - 24.

[249] Lipari, G. and Szabo, A. Model-Free Approach to the Interpretation of Nuclear Magnetic Resonance Relaxation in Macromolecules. 1. Theory

and Range of Validity. Journal of the American Chemical Society (1982) 104, 4546-4559.

[250] Halle, B., Jóhannesson, H. and Venu, K. Model-Free Analysis of Stretched Relaxation Dispersions. Journal of Magnetic Resonance (1998) 135, MN981534.

[251] Halle, B. Computer program: LMDISP, v.4, Lund, 2002.

[252] Anoardo, E. Private Communication (2008).

[253] Koynova, R. and Caffrey, M. Phases and Phase Transitions of the Phosphatidylcholines. Biochimica et Biophysica Acta (1998) 1376, 91-145.

[254] De Kruijff, B., Demel, R.A., Slotboom, A.J., Van Deenen, L.L.M. and Rosenthal, A.F. Effect of the Polar Headgroup in the Lipid-Cholesterol Interaction: A Monolayer and Differential Scanning Calorimetry Study. Biochimica et Biophysica Acta (1973) 307, 1-19.

[255] Ulmius, J., Wennerstrom, H., Lindblom, G. and Arvidson, G. Proton NMR bandshape studies of lamellar liquid crystals and gel phases containing lecithins and cholesterol. Biochimica et Biophysica Acta (BBA) - Biomembranes (1975) 389, 197-202.

[256] Vilfan, M., Althoff, G., Vilfan, I. and Kothe, G. Nuclear-Spin Relaxation Induced by Shape Fluctuations in Membrane Vesicles. Physical Review E (2001) 64, 022902.

[257] Marqusee, J.A., Warner, M. and Dill, K.A. Frequency Dependence of NMR Spin Lattice Relaxation in Bilayer Membranes. Journal of Chemical Physics (1984) 81, 6404-6405.

[258] Halle, B. Theory of Spin Relaxation by Diffusion on Curved Surfaces. Journal of Chemical Physics (1991) 94, 3150-3168.

[259] Petersen, N.O. and Chan, S.I. More on the Motional State of Lipid Bilayer Membranes: Interpretation of Order Parameters Obtained from Nuclear Magnetic Resonance Experiments. Biochemistry (1977) 16, 2657-2667.

[260] Holte, L.L., Peter, S.A., Sinnwell, T.M. and Gawrisch, K. 2H Nuclear Magnetic Resonance Order Parameter Profiles Suggest a Change of Molecular Shape for Phosphatidylcholines Containing a Polyunsaturated Acyl Chain. Biophysical Journal (1995) 68, 2396 - 2403.

[261] Alves, M. and Peric, M. An EPR Study of the Interfacial Properties of Phosphatidylcholine Vesicles with Different Lipid Chain Lengths. Biophysical Chemistry (2006) 122, 66 - 73.

[262] Filippov, A., Oradd, G. and Lindblom, G. Domain Formation in Model Membranes Studied by Pulsed-Field Gradient-NMR: The Role of Lipid Polyunsaturation. Biophysical Journal (2007) 93, 3182 - 3190.

[263] Rawicz, W., Olbrich, K.C., McIntosh, T., Needham, D. and Evans, E. Effect of Chain Length and Unsaturation on Elasticity of Lipid Bilayers. Biophysical Journal (2000) 79, 328 - 339.

[264] Mitchell, D.C. and Litman, B.J. Molecular Order and Dynamics in Bilayers Consisting of Highly Polyunsaturated Phospholipids. Biophysical Journal (1998) 74, 879 - 891.

[265] Weisz, K., Gröbner, G., Mayer, C., Stohrer, J. and Kothe, G. Deuteron Nuclear Magnetic Resonance Study of the Dynamic Organization of Phospholipid/Cholesterol Bilayer Membranes: Molecular Properties and Viscoelastic Behavior. Biochemistry (1992) 31, 1100 - 1112.

[266] Trouard, T.P., Nevzorov, A.A., Alam, T.M., Job, C., Zajicek, J. and Brown, M.F. Influence of cholesterol on dynamics of dimyristoylphosphatidylcholine bilayers as studied by deuterium NMR relaxation. Journal of Chemical Physics (1999) 110, 8802-8818.

[267] Crane, J.M. and Tamm, L.K. Role of Cholesterol in the Formation and Nature of Lipid Rafts in Planar and Spherical Model Membranes. Biophysical Journal (2004) 86, 2965-2979.

[268] Coates, J. in: Encyclopedia of Analytical Chemistry. Interpretation of Infrared Spectra, A Practical Approach (R.A. Meyers, Ed.). Chichester: John Wiley & Sons Ltd, 2000, p. 10815 - 10837.

[269] Zhang, L., He, R. and Gu, H.-C. Oleic Acid Coating on the Monodisperse Magnetite Nanoparticles. Applied Surface Science (2006) 253, 2611 - 2617.

[270] Chandaroy, P., Sen, A., Alexandridis, P. and Hui, S.W. Utilizing Temperature-Sensitive Association of Pluronic F-127 with Lipid Bilayers to Control Liposome-Cell Adhesion. Biochimica et Biophysica Acta (BBA) - Biomembranes (2002) 1559, 32-42.

[271] Liu, P., Tian, J., Liu, W. and Xue, Q. Surface-Initiated Atom Transfer Radical Polymerization (ATRP) of Styrene from Silica Nanoparticles Under UV Irradiation. Polymer International (2004) 53, 127-130.

[272] Pyun, J. and Matyjaszewski, K. Synthesis of Nanocomposite Organic/Inorganic Hybrid Materials Using Controlled/"Living" Radical Polymerization. Chemistry of Materials (2001) 13, 3436-3448.

[273] Patten, T.E. and Matyjaszewski, K. Copper(I)-Catalyzed Atom Transfer Radical Polymerization. Accounts of Chemical Research (1999) 32, 895-903.

APPENDIX A

Published Work

A.1 List of papers

1. **Meledandri C.J**, Stolarczyk J.K, Ghosh S.K, Brougham D.F. Non-aqueous magnetic nanoparticle suspensions with controlled particle size and nuclear magnetic resonance properties. Langmuir 2008, 24, 14159-14165.

2. Corr S.A, Gun'ko Y.K, Tekoriute R, **Meledandri C.J**, Brougham D.F. Poly(sodium-4-styrene)sulfonate – iron-oxide nanocomposite dispersions with controlled magnetic resonance properties. J. Phys. Chem. C 2008, 112, 13324-13327.

3. Corr S.A, Byrne S.J, Tekoriute R, **Meledandri C.J**, Brougham D.F, Lynch M, Kerskens C, O'Dwyer L, Gun'ko Y.K. Linear assemblies of magnetic nanoparticles as MRI contrast agents. J. Am. Chem. Soc. 2008, 130, 4214-4215.

Contributions of the author

Paper 1. Performed all experiments, characterised the samples, contributed to the interpretation of the results, and wrote the main portion of the manuscript.

Paper 2. Performed magnetic resonance measurements and iron determination, and contributed to the analysis of the results.

Paper 3. Performed magnetic resonance measurements and iron determination, and contributed to the interpretation of the results.

A.2 Conference presentations

1. Poster presentation: Stolarczyk, J.K, Clarke, S., **Meledandri, C.J**, Brougham D.F. "Towards stabilised magnetic nanoparticle clusters for MRI and drug-delivery applications," SFI Science Summit, 17 – 18 Nov 2008, Kilkenny, Ireland.

2. Oral presentation: **Meledandri C.J**, Brougham D.F. "Synthesis of maghemite nanoparticles of controlled size and evaluation of their magnetic properties," The 60th Irish Universities Chemistry Research Colloquium, 11-13 June 2008, Cork, Ireland.

3. Poster presentation: **Meledandri C.J**, Brougham D.F. "Optimisation of magnetoliposomes for biomedical multi-tasking; potential dual contrast agents and drug delivery vehicles," 5th Conference on Field Cycling NMR Relaxometry, 31 May – 2 June, 2007, Torino, Italy.

4. Poster presentation: **Meledandri C.J**, Brougham D.F. "Optimisation of magnetoliposomes for biomedical multi-tasking; potential dual contrast agents and drug delivery vehicles," Nanotech 2007, The Nanotechnology Conference and Trade Show, 20-24 May 2007, Santa Clara, CA, USA.

A.3 Published work

This content has been removed due to third party copyright.
This content has been removed due to third party copyright.
This content has been removed due to third party copyright.

This content has been removed due to third party copyright.
This content has been removed due to third party copyright.
This content has been removed due to third party copyright.

This content has been removed due to third party copyright.
This content has been removed due to third party copyright.
This content has been removed due to third party copyright.

This content has been removed due to third party copyright.
This content has been removed due to third party copyright.
This content has been removed due to third party copyright.

This content has been removed due to third party copyright.
This content has been removed due to third party copyright.
This content has been removed due to third party copyright.

APPENDIX B

Supplementary information for Chapter 4:

Polymer-mediated phase transfer of primary NPs into aqueous media

B.1 Experimental

B.1.1 Materials

Pluronic acid (PF127), citric acid (≥ 99%), 2-bromo-2-methylpropionic acid (BMPA; 98%), 2-bromo-2-methylpropionyl bromide (BMPB; 98%), 4-styrenesulfonic acid sodium salt hydrate (SSNa), N,N'-dimethylformamide (DMF; 99%), triethylamine (≥ 99.5%), copper (I) bromide (CuBr; 98%), N,N,N,N',N',N'-hexamethyltriethyltetramine (HMTETA; 97%), and 1,2-dichlorobenzene (DCB; ≥ 99%) were purchased from Sigma-Aldrich.

B.1.2 Polymer-mediated phase transfer of primary NPs into aqueous media

B.1.2.1 Pluronic acid

Surface modification of C18-stabilised γ-Fe_2O_3 NPs, prepared as described in Chapter 3, was carried out through the formation of a hierarchical surface structure using a preformed, tri-block copolymer, Pluronic acid (PF127). A suspension of PF127 in DI H_2O (2 mL, 10 mg/mL) was added to a small 6-mL glass vial. An equal volume of ferrofluid was added to the vial. The vial was covered and vigorously agitated on a vortex mixer for 25 minutes. Phase separation was apparent upon termination of the vortex mixing. The open vial was placed under a slow and steady flow of N_2 overnight to evaporate the heptane. The following day, a dark brown, thick, viscous liquid remained in the vial. The N_2 flow was continued for an additional few hours until the particles were almost completely dry. A small volume (4 mL) DI H_2O was then added to the vial containing the particles, and the mixture was vortexed for 3 minutes. A large amount of black solid remained unsuspended in the water, and settled to the bottom of the vial. The system was sonicated for 30 minutes in a bath-type sonicator. The solid was not visible after sonication. The vial was placed over a bar magnet for 2 minutes in order to sediment and remove any larger or aggregated particles. The supernatant was separated from a small amount of sedimented particles by magnetic decantation, transferred to a clean vial, then sonicated for an additional 15 minutes in a bath-type sonicator to produce the final aqueous suspension of PF127/C18-coated nanoparticles. Non-associated

PF127 micelles were removed by magnetic filtration (Chapter 5, section 5.2.4), performed at one flow rate with a constant magnetic field. The eluent was discarded and the retentate was retained for characterisation.

B.1.2.2 PSSNa

Aqueous suspensions of PSSNa-stabilised iron-oxide nanoparticles were prepared through a multi-step, surface functionalisation procedure described by Hatton et al. [113]. For clarity, the reaction scheme is shown in Figure B.1.

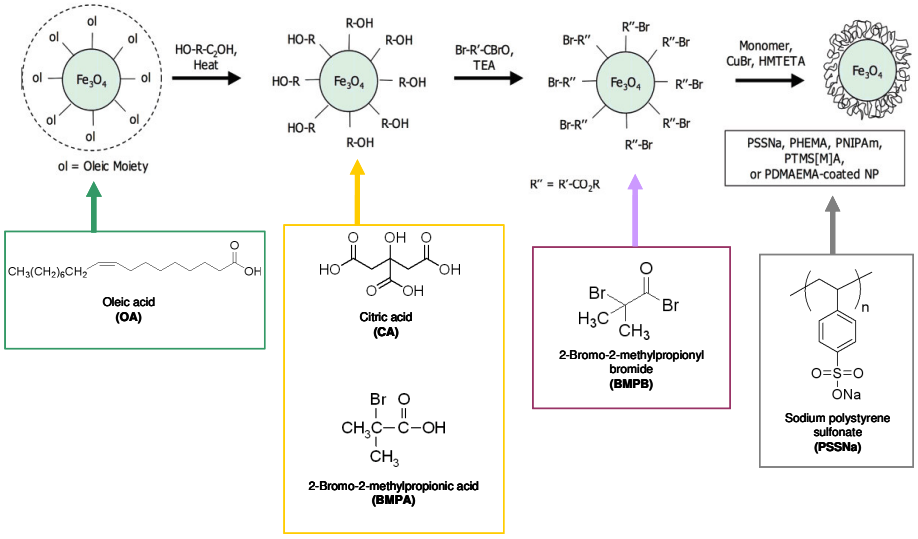

Figure B.1. Reaction scheme for nanoparticle functionalisation and polymerisation, as proposed by Lattuada, Hatton, et al. [113].

(i) Preparation of CA/BMPA-coated iron-oxide nanoparticles.

Ethanol (50 mL) was added to a 100 mL round-bottomed flask containing a heptane suspension of OA/OAm-stabilised γ-Fe_2O_3 nanoparticles to precipitate the solid; the flask was placed over a bar magnet to isolate the NPs. The solvent was decanted from the iron-oxide and 470 mg of the wet nanoparticles were transferred to a pre-weighed 3-neck, 100 mL round-bottomed flask. The NPs were dried in an oven at 80°C for 20 minutes. The final mass of the cooled, dry solid was 148.5 mg. A 50/50 mixture (18 mL total volume) of 1,2-dichlorobenzene and N,N'-dimethylformamide was added to the nanoparticles.

Citric acid (0.0303 g) and BMPA (0.4813 g) were combined and added to the flask. The mixture was stirred by magnetic means under a constant flow of N_2, and heated to 100°C. Heating was continued for 24 hours. During the reaction, a colour change from dark red-brown to dark red was observed. After 24 hours, the suspension was removed from heat and allowed to cool naturally to room temperature. Diethyl ether (50 mL) was added to the suspension to precipitate the iron-oxide, and the flask was placed over a bar magnet to isolate the NPs. This was a slow process and required the flask to remain over the magnet overnight. The dark red supernatant was decanted from the red-brown coloured NPs, which had an appearance resembling that of red clay. The particles were washed three times with ~40 mL acetone; during each wash, the precipitate was immobilised using a bar magnet, and the orange-coloured supernatant was decanted. One final acetone wash was carried out, and the flask was placed over a bar magnet overnight for the final isolation of the NPs. The solvent was decanted, and the flask was placed in an 80°C oven for 20 minutes. The final mass of the cooled, dry CA/BMPA-coated NPs was 45.3 mg.

A small amount (5.3 mg) of CA/BMPA-coated NPs were removed from the flask and transferred to a clean vial. Deionised H_2O (5 mL) was added. The solid nanoparticles did not readily disperse in H_2O; 90 minutes of sonication in a bath-type sonicator was required. Following sonication, the bright orange suspension was placed over a bar magnet for 2 minutes. A small amount of larger particles settled over the magnet. The supernatant was collected and utilised for all characterisation. The remaining 40 mg CA/BMPA-coated nanoparticles was used for the preparation of CA-BMPA/BMPB-coated NPs.

(ii) Preparation of CA-BMPA/BMPB-coated iron-oxide NPs.

N,N'-dimethylformamide (5 mL) was added to the flask containing 40 mg of dry CA/BMPA-coated NPs, and the mixture was stirred vigorously to disperse the particles. Before the addition of triethylamine, a low, continuous flow of N_2 was started through one neck of the flask, and a condenser was attached to the middle neck. The condenser was left open to the atmosphere to prevent the potential hazardous accumulation of triethylamine vapour during the experiment. Triethylamine (0.33 mL) was then carefully added to the flask through the

remaining open neck using a syringe. BMPB (0.17 mL) was slowly added dropwise to the flask. The acylation reaction was allowed to proceed for 3 hours at room temperature. Upon completion of the reaction, the particles were precipitated through the addition of 30 mL acetone, and the flask was placed over a bar magnet to isolate the particles. The orange-red supernatant was decanted, and the NPs were washed three times with ~30 mL acetone; during each wash, the precipitate was immobilised using a bar magnet, and the supernatant was decanted. One final acetone wash was carried out, and the flask was placed over a bar magnet for the final isolation of the NPs. The solvent was decanted, and the flask was placed in an 80°C oven for 20 minutes. The final mass of the cooled, dry CA-BMPA/BMPB-coated NPs was ~22 mg.

A small amount (1.8 mg) of CA-BMPA/BMPB-coated NPs were removed from the flask and transferred to a clean vial. Deionised H_2O (2 mL) was added. The dispersion was sonicated in a bath-type sonicator for 15 minutes and retained for future characterisation. The remaining 20 mg CA-BMPA/BMPB-coated nanoparticles was used for the preparation of PSSNa-coated NPs.

(iii) Preparation of PSSNa-coated iron-oxide nanoparticles

A 3/1 (v/v) mixture of deionised H_2O (2.81 mL) and methanol (0.94 mL) were added to the 3-neck round bottomed flask containing 20 mg CA-BMPA/BMPB-coated NPs. Vigorous magnetic stirring for > 60 min was required to disperse the majority of the solid particles, and a small amount of solid remained dried on the wall of the flask. A mixture of 1.0447 g SSNa and 0.0487 g CuBr was prepared, then added to the flask. Nitrogen was purged through the reactor for 30 minutes and the vigorous stirring was continued. HMTETA (~0.1 mL) was injected into the reaction mixture with a syringe. The reaction was allowed to proceed for 22 hours at room temperature; after 2 hours, a light blue-green colour was observed. The reaction was stopped after 22 hours. The magnetic stir bar had become lodged in the hardened, tan-coloured solid material that had formed at the bottom of the flask. A mixture of tan, orange-brown, and light blue-green material had splattered on the walls of the flask. Acetone (30 mL) was added to the flask and the mixture was agitated by vortex mixing to disrupt and dislodge this solid material. The flask was placed over a bar magnet overnight. The blue-green

supernatant was decanted, and the tan coloured solid material was washed three times with 30 mL acetone. The amount of solid material remaining at the bottom of the flask appeared much greater than the original 20 mg of CA-BMPA/BMPB-coated NPs. The solid was washed two more times with 30 mL acetone. After the final wash, the acetone was decanted, and 5 mL of DI H_2O were added to the tan coloured solid. The suspension turned dark green and was placed over a bar magnet for 15-20 minutes. Dark red-brown solid particles settled over the magnet, and the supernatant remained dark green in colour. The supernatant was decanted and 5 mL of DI H_2O were added to the red-brown coloured nanoparticles. This was followed by 30 minutes of sonication in a bath-type sonicator. The suspension was placed over a bar magnet for 10 minutes in order to sediment the largest particles. The red-brown coloured aqueous supernatant, presumably containing PSSNa-coated NPs, was collected and retained for characterisation.

B.1.3 Characterisation

The aqueous and non-aqueous ferrofluids were characterised by PCS and NMRD as described in Chapter 2.

Attenuated total reflectance (ATR)-infrared spectra were recorded on a Spectrum GX FT-IR System (Perkin Elmer; Norwalk, CT, USA). Liquid suspensions were placed on the face of a ZnSe trough-plate crystal and the solvent was evaporated under N_2. Eight scans were recorded over a 4000 – 650 cm^{-1} spectral range with 2 cm^{-1} spatial resolution. ATR and baseline corrections were applied (Spectrum software v.3.01; Perkin Elmer LLC; Norwalk, CT, USA).

B.2 Results

B.2.1 Pluronic acid

Pluronic F127 triblock copolymer was used to phase transfer C18-coated iron-oxide NPs synthesised by the thermal decomposition method from heptane to water. The results of PCS measurements carried out before and after phase transfer are shown in Table B.1. Both of the suspensions were relatively monodisperse, and the low PDI values indicate unimodal size distributions. An

increase of 49 nm was observed in the hydrodynamic diameter upon phase transfer.

Table B.1. The average hydrodynamic diameter and polydispersity index, at 25°C, of C18- and PF127- stabilised maghemite NPs.

Stabiliser	Dispersant	Z-Avg (nm)	PDI
C18	Heptane	9.2	0.159
PF127	H_2O	58.2	0.096

The relaxivity curves of the maghemite suspensions are compared in Figure B.2. The appearance of the curves is consistent with dispersed superparamagnetic NPs in suspension. The high-frequency r_1 maximum for the heptane suspension of C18-stabilised nanoparticles presumably lies above 20 MHz, indicating ultra-small primary particles < 10 nm [151]. This result is consistent with the hydrodynamic diameter of 9.2 nm obtained from PCS measurements (Table B.1). The r_1 maximum for the water dispersion of PF127-coated particles is observed at a lower frequency, around 10 MHz, indicating a primary particle size of ~ 10 nm. Thus, there is a large discrepancy between D_{NMR} and the D_{PCS} value of 58.2 nm obtained for PF127-coated NPs.

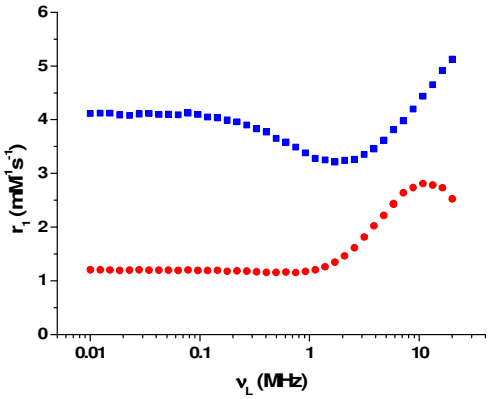

Figure B.2. Relaxivity profiles, measured at 25°C, of ■ a heptane suspension of C18-stabilised maghemite NPs (D_{PCS} = 9.2 nm), and ● a water suspension of PF127-stabilised maghemite NPs (D_{PCS} = 58.2 nm).

B.2.2 PSSNa

Attenuated total reflectance-infrared (ATR-IR) was used to qualitatively monitor the extent of ligand exchange throughout the multi-step polymerisation phase transfer procedure (Figure B.1). The spectra are shown in Figure B.3. Clear changes in the spectra can be observed upon ligand exchange and surface modification. Distinct features in the spectrum of the final suspension confirmed the presence of PSSNa. Similar spectral features were reported by Corr et al. for PSSNa-stabilised magnetite NPs [109]. It should be noted that a very small quantity (22 mg) of the CA-BMPA/BMPB-coated nanoparticles was recovered after the acylation step (step ii); therefore, we opted to forgo ATR-IR analysis at this stage in order to maximise the amount of material available for PSSNa-coating.

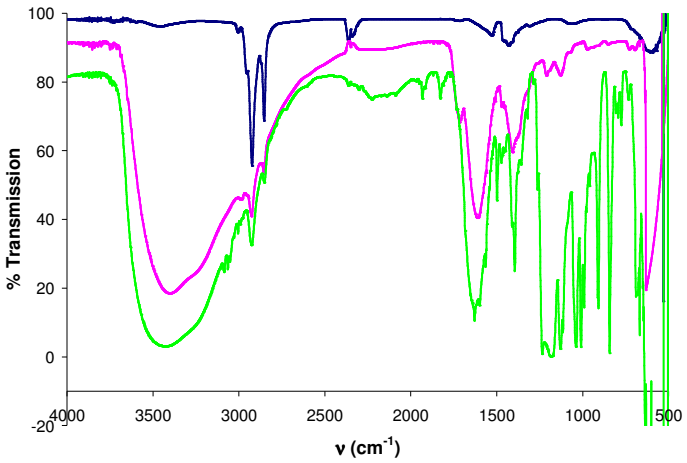

Figure B.3. ATR-IR spectra of γ-Fe_2O_3 NPs coated with — C18, — CA-BMPA, and — PSSNa.

The band assignments for CA-BMPA- and PSSNa-functionalised maghemite NPs are reported in Tables B.2 and B.3, respectively. Considering first the spectrum for the C18-stabilised iron-oxide NPs, there are two predominant bands in the 2850 – 3040 cm^{-1} frequency region which originate from asymmetric and symmetric C – H stretching modes. This confirms the presence of the alkyl

chains of the C18 surfactant molecules. There is a noted absence of vibrational modes typically present for carboxylic acids; namely C=O stretching (1725 – 1700 cm^{-1} frequency range), C – O stretching (1320 – 1210 cm^{-1}), O – H stretching (3300 – 2500 cm^{-1}), and O – H bending (960 – 850 cm^{-1}) [268]. Instead, two bands are observed at 1420 cm^{-1} and 1529 cm^{-1}, which can be attributed to asymmetric and symmetric stretching of a carboxylate group [268,269]. This suggests that the carboxyl group of the oleic acid is chemisorbed to the nanoparticle surface in the form of a carboxylate group. This is consistent with other reported studies in which a chelating bidentate interaction has been predicted between the COO^- group of oleic acid and the trivalent iron atom [269].

There are several notable features in the spectrum of the CA-BMPA-modified particles signifying an effective ligand exchange. The strong absorbance band at 632 cm^{-1} originates from the C-Br stretch of the BMPA. The band at 1610 cm^{-1} exhibits the presence of C=O stretching (shifted to lower frequency due to strong intramolecular H-bonding), and The R-O-H in plane bending and O-H stretching modes appear at 1406 cm^{-1} and 3399 cm^{-1}, respectively.

The spectrum of PSSNa-modified particles is distinctly different from the spectrum of the CA/BMPA-coated particles. Most notably, the asymmetric and symmetric S=O stretching is observed at 1396 cm^{-1} and 1183 cm^{-1}, respectively, and C=C ring stretches appear at 1600 cm^{-1} and 1630 cm^{-1}.

Table B.2. Summary of IR band assignments for CA-BMPA-coated maghemite nanoparticles.

ν (cm^{-1})	**Assignment**
3399	OH stretch
2999	sp^2 CH stretch
2926	ν_a CH_2 stretch
2855	ν_s CH_2 stretch
1610	C=O stretch (w/strong intramolecular H-bonding)
1406	R-O-H in-plane bend
632	C-Br stretch

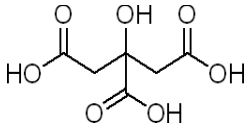

Citric acid
(CA)

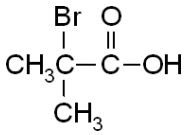

2-Bromo-2-methylpropionic acid
(BMPA)

Table B.3. Summary of IR band assignments for PSSNa-coated maghemite NPs.

ν (cm^{-1})	**Assignment**
3085	sp^2 CH stretch (aromatic ring)
3005	sp^2 CH stretch (aromatic ring)
2926	sp^3 ν_a CH_2 stretch
2852	sp^3 ν_s CH_2 stretch
1630	C=C ring stretch (ν_{8a})
1600	C=C ring stretch (ν_{8b})
1396	ν_a S=O stretch
1183	ν_s S=O stretch
1010	benzene in-plane ring deformation
844	C-H out of plane bend (2 adjacent C-H groups)

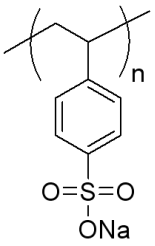

Sodium polystyrene sulfonate
(PSSNa)

The results of PCS measurements carried out after each stage of surface modification are shown in Table B.4. A significant increase in the average hydrodynamic diameter of the particles was observed upon the replacement of the OA/OAm coating and phase transfer into water. All of the suspensions were reasonably monodisperse.

Table B.4. The average hydrodynamic diameter and polydispersity index, at 25°C, of surface modified maghemite NPs.

Surface coating	Dispersant	Z-Avg (nm)	PDI
OA/OAm	Heptane	9.2	0.159
CA-BMPA	H_2O	132	0.203
CA-BMPA/BMPB	H_2O	161	0.241
PSSNa	H_2O	121	0.261

The relaxivity profiles of C18-stabilised and PSSNa-stabilised maghemite NPs are compared in Figure B.4. The shape of the profiles is as expected for dispersed superparamagnetic NPs in suspension. A high-frequency r_1 maximum is observed above 10 MHz in both cases, indicating very small primary particles, of size < 10 nm [151]. While this result is consistent with the diameter obtained from PCS measurements for C18-stabilised particles, there is a large discrepancy between the estimated D_{NMR} and D_{PCS} (Table B.4) for PSSNa-coated particles. The value of r_1 was significantly higher after PSSNa-mediated phase transfer at all measured frequencies > 1 MHz.

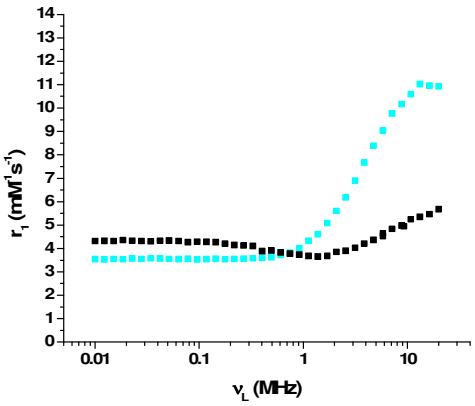

Figure B.4. Relaxivity profiles, measured at 25°C, of ■ C18-stabilised maghemite NPs suspended in heptane (D_{PCS} = 9.2 nm), and ■ PSSNa-functionalised maghemite NPs suspended in H_2O (D_{PCS} = 121 nm).

B.3 Discussion

The aim of the polymer-mediated transfer was to attempt a transfer of dispersed primary particles from organic to aqueous media without aggregation. If successful, these methods could then be used to phase transfer size-controlled NPCs. A large number of techniques have been developed to modify the hydrophobic surfaces of NPs and transfer them into water [103-105,113]. We have carried out two methods of polymer-mediated phase transfer and investigated the effect of the surface modification on the size and magnetic resonance properties of iron-oxide NPs.

B.3.1 Pluronic acid

Monodisperse C18-stabilised iron-oxide NPs were transferred from organic to aqueous phase through surface modification using PF127. PF127, made from two A-chains of polyethylene oxide (PEO) and one B-chain of polypropylene oxide (PPO) in an ABA configuration, has been shown to surround surface-bound oleic acid molecules, forming a hierarchical surface structure [106] (Figure B.5). The hydrophobic PPO chains are thought to interact with the hydrocarbon chains of the C18 surfactant coating on the iron-oxide particles, while the hydrophilic PEO chains extend away from the core to stabilise the particles in aqueous suspension.

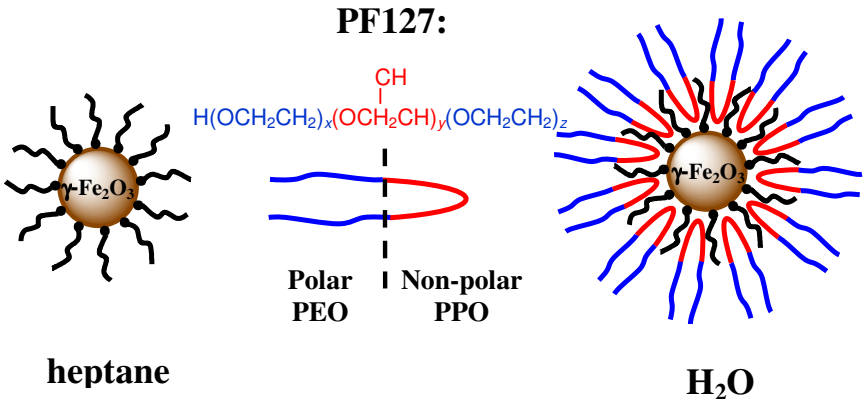

Figure B.5. Schematic representation of PF127-mediated transfer of OA-coated maghemite NPs from the non-aqueous to the aqueous phase. (a) γ-Fe_2O_3 NPs coated with a monolayer of OA and suspended in heptane. (b) PF127-coated NPs with a hierarchical surface structure, suspended in H_2O.

PCS measurements indicate a difference of 49.0 nm in the average hydrodynamic diameter of C18-stabilised- and PF127-coated iron-oxide NPs. The average diameter of PF127 micelles, as determined by light scattering techniques, is 23 nm [270]. It is unlikely that the difference in the hydrodynamic diameter is due to the presence of non-associated PF127 micelles, as the applied magnetic filtration technique (Chapter 5, section 5.2.4) would have prevented the retention of any non-magnetic particles in the suspension. There are two possibilities for the increase in the hydrodynamic diameter. Firstly, the increase may be a result of NPCs coated within a polymer shell of PF127. The hydrodynamic diameter did not decrease upon ultrasonic treatment of the aqueous suspensions. Thus, any aggregates present resisted ultrasonic disruption. Secondly, the application of magnetic filtration, carried out at one flow rate with a constant magnetic field, may have resulted in the unintentional selective retention of the larger magnetic cores present in the heptane suspension before phase transfer. However, the PDI value of 0.159 from PCS measurements indicate a reasonably monodisperse heptane suspension of C18-stabilised magnetic nanoparticles.

In Chapter 3 we demonstrated that SPM theory, originally developed for aqueous suspensions, can be extended to interpret heptane suspensions of superparamagnetic NPs. Interpretation of the relaxivity profile of PF127-coated particles with this theory can provide a very reasonable estimate of the magnetic core diameter contained within the PF127 coating. A clear shift in the r_1 maximum to lower frequencies after coating the C18-stabilised particles with PF127 is observed in Figure B.2. In general, an increase in the diameter of the magnetic core due to NP aggregation would result in a broadening and flattening of the NMRD profile [74] (Chapter 5, section 5.4.7). Such a broadening is not evident in the profile of PF127-coated particles. However, the mid-frequency dispersion, often present for suspensions of small crystals (typically < 20 nm) [151], and quite obvious in the profile of C18-stabilised particles, does not appear in the profile of PF127-coated particles. Furthermore, we observed a marked decrease in the relaxivity of the magnetic suspension at all measured frequencies after PF127-mediated phase transfer. As reported in Chapter 3, SPM

theory predicts that, for monodisperse iron-oxide nanoparticles of a given size, the NMRD profiles of fully dispersed heptane suspensions will have r_1 values approximately 15% higher than the equivalent water suspensions, in the range below 100 MHz. Taking this into consideration, there is still a large decrease in the relaxivity of the magnetic suspension of PF127-stabilised nanoparticles when compared to the simulated equivalent water suspension of C18-stabilised nanoparticles (Figure B.6). In summary, the method of PF127 does not appear to allow controlled phase transfer of single iron-oxide nanocrystals, or the preservation of magnetic resonance properties.

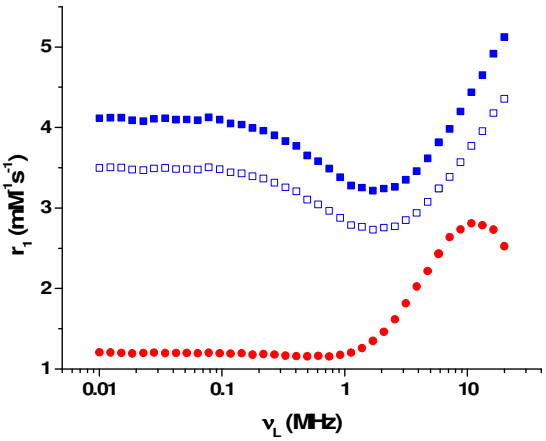

Figure B.6. Relaxivity profiles, measured at 25°C, of ■ a heptane suspension of C18-stabilised maghemite NPs (D_{PCS} = 9.2 nm), and ● a water suspension of PF127-stabilised maghemite NPs (D_{PCS} = 58.2 nm). The open blue squares show the result of the heptane profile scaled down by a factor of 1.15.

B.3.2 PSSNa

In recent years, there has been increasing interest in the use of atom transfer radical polymerisations (ATRP) to enable controlled growth of well-defined polymer chains from the surface of inorganic nanoparticles [113,271,272]. This 'grafting from' technique is thought to prevent the type of nanoparticle agglomeration observed during the PF127 surface modification. ATRP uses reversible metal-catalysed atom transfer to generate the propagating polymer radicals [273]. Several steps were required to transform our C18-stabilised iron-oxide NPs into initiators for ATRP; the detailed strategy of which was recently

described by Hatton et al. [113]. First, the surface OA/OAm surfactant molecules were replaced with CA/BMPA ligands containing reactive hydroxyl groups through a ligand exchange reaction. The hydroxyl groups were reacted with an acylating agent (BMPB) in the presence of triethylamine, forming ester bonds and transforming the hydroxyl groups into ester moieties containing a highly efficient ATRP initiator (α-haloester) [113]. The initiator induces polymerisation through the generation of radicals, and the PSSNa polymer brush is grown from, or "grafted from," the NP surface.

Distinct features in the ATR-IR spectrum of PSSNa-functionalised maghemite NPs confirmed the presence of the polymer (Figure B.3). The average hydrodynamic diameter of the PSSNa-coated particles was 121 nm, an increase of ~112 nm from the diameter of C18-stabilised maghemite NPs. Hatton et al [113] reported an increase of ~ 39 nm upon coating primary NPs with PSSNa. While the relaxivity profile of the aqueous suspension of PSSNa-coated maghemite NPs does display some features characteristic of the presence of superparamagnetic NPs (Figure B.4), the absence of a mid-frequency dispersion in the profile after polymer coating suggests the samples may contain aggregated particles. Aggregation causes an increase in the anisotropy energy due to intercrystal interactions [151], which increases the low frequency relaxivity and eliminates the mid-frequency dispersion. This is not entirely surprising, as this effect has previously been observed in our group in the case of PSSNa-stabilised iron-oxide prepared by an *in-situ* approach [110].

B.4 Conclusions

We have evaluated two distinct methods of polymer-mediated stabilisation of dispersed NPs, and have characterised the resulting aqueous suspensions by dynamic light scattering and relaxivity measurements. The approaches assessed were a limited success. While the surface chemistries were demonstrated to be compatible with iron-oxide and phase transfer was successful in all cases, some aggregation could not be avoided, thus affecting the emergent magnetic properties of the aqueous suspensions.